Galaxy Formation and Evolution with Machine Learning

from CORRELATION to CAUSATION

Sunil Mucesh

A dissertation submitted in partial fulfillment
of the requirements for the degree of
Doctor of Philosophy
of
University College London.

Supervisors:
Prof. Ofer Lahav
Dr. William Hartley
Prof. Timothy Scanlon

Examiners:
Prof. Carlton Baugh
Dr. Nikos Nikolaou

Department of Physics and Astronomy
University College London

July 5, 2024

To my mum, dad, and brother.

Thank you.

I, Sunil Mucesh, confirm that the work presented in this thesis is my own. Where information has been derived from other sources, I confirm that this has been indicated in the work.

Abstract

Understanding how galaxies form and evolve is at the heart of modern astronomy. With the advent of large-scale surveys, remarkable progress has been made in the last few decades as the overall picture has been established. Nevertheless, the importance of the physical processes behind the phenomena are far from known, as primarily correlations have been identified rather than the underlying causality. While simulations are inherently causal by nature, the causal effect itself is intractable given meaningful complexity. In this thesis, the causal inference framework is applied to move beyond correlations to causation, in an effort to truly understand the galaxy formation and evolution process.

First—before inference (i.e., the why)—the equally important task of prediction (i.e., the what) is tackled as machine learning (ML) is utilised to predict galaxy properties. Concretely, a novel method based on the random forest (RF) algorithm is developed to generate joint probability distribution functions (PDFs). As a demonstration, joint redshift–stellar mass PDFs are estimated, which have many science applications. Compared to a traditional SED-fitting approach, the ML-based method has superior performance in terms of accuracy (based on predefined metrics) and speed (by ~ 5 orders of magnitude).

Then, combining causal inference and ML, causal ML is applied to infer the causal effect of environment on galaxies, specifically on their star-formation rate (SFR). To achieve this, a comprehensive causal model of galaxy formation and evolution is constructed, and the long-outstanding problem of disentangling nature and nurture is tackled. The causal effect is found to be negative and substantial, with environment suppressing the SFR by a factor of ~ 100. While the overall effect at $z = 0$ is negative, in the early Universe, environment is discovered to have a positive impact, boosting star formation by a factor of ~ 10 at $z \sim 1$ and by even greater

amounts at higher redshifts.

Impact Statement

Broadly, the work in this thesis contributes to advancing our understanding of galaxy formation and evolution, with potential applications to other fields. The estimation of galaxy properties with machine learning (ML) is hugely significant, as traditional methods are unlikely to scale to the billions of galaxies that will be observed by the next generation of large-scale surveys, such as Euclid, LSST, and Roman.

Delving deeper, moving beyond point estimates to probability distribution functions (PDFs) enables more accurate analyses since the latter fully characterise uncertainties. The joint PDF, in particular, is more informative than the marginal as it captures any potential correlations between galaxy properties, so their incorporation could reduce bias. This work directly contributes to the LSST DESC Science Roadmap (SRM), as estimating joint PDFs of redshift and an ancillary property is one of its enhanced objectives. Furthermore, methods have been introduced to validate multivariate PDFs, and they have already been implemented in studies to validate posterior distributions of the reionisation parameters obtained from the 21-cm power spectrum (Zhao et al., 2022, 2023).

I have developed and published `GALPRO`—an open-source, state-of-the-art Python package for estimating multivariate PDFs of galaxy properties. `GALPRO` is fast and efficient, able to compute joint PDFs for a million galaxies in just under 6 minutes with consumer computer hardware. Moreover, it can generate PDFs on the fly once trained, thus solving the potential challenge of data storage. The package has already been employed to estimate joint redshift–luminosity and redshift–stellar mass PDFs in order to estimate the Hubble constant using gravitational waves (Palmese et al., 2023) and constrain the stellar-to-halo mass relation (SHMR) with galaxy clustering and weak lensing (Zacharegkas et al., in prep), respectively. Overall, `GALPRO` will facilitate galaxy formation and evolution and cosmological studies in the era of "Big

Data".

Estimating the causal effect of environment on star-formation rate (SFR) by tackling the key challenge of disentangling nature and nurture propels the field to a deeper understanding. With the introduction of a principled framework (to the field) to infer causality, this work paves the way towards potentially unravelling some of the biggest mysteries in galaxy formation and evolution, such as: why do galaxies quench, what is responsible for morphological transformations of galaxies, what is the impact of supermassive black holes (SMBHs) on their host galaxies, and the long-outstanding question, which is more important: nature or nurture?

Causality is at the heart of many sciences, so this work has broad applications. In particular, it is pertinent to dynamical systems with feedback loops (here being galaxies), and they are ubiquitous. One of the most complex and important is the Earth's climate system. The method utilised in this work can be applied to determine, for example, the anthropogenic activity that most contributes to global warming, which is critical to tackling climate change.

Acknowledgements

From a young boy on a small Indian island who first saw thousands of twinkling stars in the night sky during a blackout and became fascinated—to eventually pursuing a PhD in astronomy, it has been quite a journey—a journey that would have been impossible without the support of many people.

First and foremost, I would like to express my deepest gratitude to my supervisors: Prof. Ofer Lahav, Dr. William Hartley, and Prof. Timothy Scanlon. Ofer, thank you for your guidance and wisdom. You gave me the freedom to explore and follow my interests whilst gently nudging me in the right direction and always being there for support. I take with me your immense curiosity and insatiable desire for learning. Will, thank you for nurturing me as a scientist, with seemingly infinite patience and humility. Knowing that I could make mistakes and that you would explain without judgement allowed me to grow and learn. Your gentle reassurance and support helped me push through the difficult periods. Thank you for being so kind and understanding.

A massive thank you to Prof. Ciarán Gilligan-Lee for introducing me to the world of causal inference and ultimately inspiring me to apply it to the field of galaxy formation and evolution. It was amazing to collaborate with you on the project. Also, thank you to Prof. Antonella Palmese for guiding and working with me right from the beginning of my PhD. Thanks to also Prof. Chihway Chang, Prof. Clécio Roque De Bom, Dr. Lorne Whiteway, Dr. Judit Prat, and Dr. Georgios Zacharegkas for collaborating with me, and Prof. Asa Black and Dr. Alex Alarcon-Gonzalez for examining and providing valuable feedback on my first paper.

Rewinding back the time, thank you Mr. Jack Harrison. Your A-level Physics lectures all those years ago truly inspired me and cemented my interest in the subject. You played a big role in me choosing to study physics at university and, to a certain

degree, my path thereafter. Also, I would like to acknowledge Prof. Hartmut Boesch and Dr. Hilke Oetjen for giving me the opportunity to conduct research at the National Centre for Earth Observation (NCEO) at University of Leicester. This first experience of researching in a professional environment was truly invaluable. Thank you also to Prof. Richard Ambrosi and Prof. Mervyn Roy for highlighting the opportunity.

My deepest gratitude to Prof. Mark Wilkinson. Mark, I count myself lucky to have had you as my supervisor (for 3rd year and Master's projects). I had so much fun researching, and it was then that I realised I could aim for a PhD. However, it felt out of reach for multiple reasons. You gave me the confidence and courage to pursue it. You really went above and beyond to support me, especially after the setback. All I can say is thank you for believing in me. I will forever be grateful.

Finally, from the bottom of my heart, thank you to my family. Mum and Dad, words cannot really express how grateful I am for everything you have done for me. You gave me every opportunity to pursue what I wanted despite our circumstances and have always trusted and believed in me. Thank you for your unconditional love and support. I hope I have made you proud. Sonu, thank you for listening to my endless ramblings about everything and especially for trying your hardest not to fall asleep during my practice presentations. Jokes aside, I could not have asked for a better brother. Thank you for always having my back. Also, a big thank you to my uncles, aunts, and extended family. A special mention also to my lovely and caring grandma, or Baa. I really could not have done this without all of you. Thank you.

UCL Research Paper Declaration Form: referencing the doctoral candidate's own published work(s)

1. **1. For a research manuscript that has already been published** (if not yet published, please skip to section 2)**:**

   (a) **What is the title of the manuscript?**

   A machine learning approach to galaxy properties: joint redshift–stellar mass probability distributions with Random Forest

   (b) **Please include a link to or doi for the work:**

   https://doi.org/10.1093/mnras/stab164

   (c) **Where was the work published?**

   Monthly Notices of the Royal Astronomical Society

   (d) **Who published the work?**

   Oxford University Press

   (e) **When was the work published?**

   January 2021

   (f) **List the manuscript's authors in the order they appear on the publication:**

   S. Mucesh, W. G. Hartley, A. Palmese, O. Lahav, L. Whiteway, A. F. L. Bluck, A. Alarcon, A. Amon, K. Bechtol, G. M. Bernstein, A. Carnero Rosell, M. Carrasco Kind, A. Choi, K. Eckert, S. Everett, D. Gruen, R. A. Gruendl, I. Harrison, E. M. Huff, N. Kuropatkin, I. Sevilla-Noarbe, E. Sheldon, B. Yanny, M. Aguena, S. Allam, D. Bacon, E. Bertin, S. Bhargava, D. Brooks, J. Carretero, F. J. Castander, C. Conselice, M. Costanzi, M. Crocce, L. N. da Costa, M. E. S. Pereira, J. De Vicente, S. Desai, H. T. Diehl, A. Drlica-Wagner, A. E. Evrard, I. Ferrero, B. Flaugher, P. Fosalba, J. Frieman, J. García-Bellido, E. Gaztanaga, D. W. Gerdes, J. Gschwend, G. Gutierrez, S. R. Hinton, D. L. Hollowood, K. Honscheid, D. J. James, K. Kuehn, M. Lima, H. Lin, M. A. G. Maia, P. Melchior, F. Menanteau, R. Miquel, R. Morgan, F. Paz-Chinchón, A. A. Plazas, E. Sanchez, V. Scarpine, M. Schubnell, S. Serrano, M. Smith, E. Suchyta, G. Tarle, D. Thomas, C. To, T. N. Varga, and R.D. Wilkinson

(DES Collaboration)

(g) **Was the work peer reviewed?**

Yes

(h) **Have you retained the copyright?**

Yes

(i) **Was an earlier form of the manuscript uploaded to a preprint server (e.g. medRxiv)? If 'Yes', please give a link or doi**

https://doi.org/10.48550/arXiv.2012.05928

If 'No', please seek permission from the relevant publisher and check the box next to the below statement:

☐ *I acknowledge permission of the publisher named under 1d to include in this thesis portions of the publication named as included in 1c.*

2. **For a research manuscript prepared for publication but that has not yet been published** (if already published, please skip to section 3)**:**

(a) **What is the current title of the manuscript?**

(b) **Has the manuscript been uploaded to a preprint server 'e.g. medRxiv'?**

If 'Yes', please please give a link or doi:

(c) **Where is the work intended to be published?**

(d) **List the manuscript's authors in the intended authorship order:**

(e) **Stage of publication:**

3. **For multi-authored work, please give a statement of contribution covering all authors** (if single-author, please skip to section 4)**:**

S. Mucesh: investigation, methodology, data curation, formal analysis, validation, interpretation, writing, visualisation, software

W. G. Hartley: supervision, conceptualisation, methodology, validation, interpretation, writing (review and editing)

A. Palmese: supervision, conceptualisation, writing (review)

O. Lahav: supervision, writing (review)

4. **In which chapter(s) of your thesis can this material be found?**
   Chapters 2 and 4

e-Signatures confirming that the information above is accurate (this form should be co-signed by the supervisor/ senior author unless this is not appropriate, e.g. if the paper was a single-author work)**:**

Candidate: Sunil Mucesh
Date: 02/02/2024
Supervisor/Senior Author signature (where appropriate)**:** Ofer Lahav
Date: 02/02/2024

UCL Research Paper Declaration Form: referencing the doctoral candidate's own published work(s)

1. **1. For a research manuscript that has already been published** (if not yet published, please skip to section 2)**:**

   (a) **What is the title of the manuscript?**

   (b) **Please include a link to or doi for the work:**

   (c) **Where was the work published?**

   (d) **Who published the work?**

   (e) **When was the work published?**

   (f) **List the manuscript's authors in the order they appear on the publication:**

   (g) **Was the work peer reviewed?**

   (h) **Have you retained the copyright?**

   (i) **Was an earlier form of the manuscript uploaded to a preprint server (e.g. medRxiv)? If 'Yes', please give a link or doi**
   If 'No', please seek permission from the relevant publisher and check the box next to the below statement:

   ☐ *I acknowledge permission of the publisher named under 1d to include in this thesis portions of the publication named as included in 1c.*

2. **For a research manuscript prepared for publication but that has not yet been published** (if already published, please skip to section 3)**:**

   (a) **What is the current title of the manuscript?**
   The Causal Effect of Environment on Star Formation with Causal Machine Learning

   (b) **Has the manuscript been uploaded to a preprint server 'e.g. medRxiv'?**
   If 'Yes', please please give a link or doi:

   (c) **Where is the work intended to be published?**
   Nature Astronomy or Communications

(d) **List the manuscript's authors in the intended authorship order:**
S. Mucesh, W. G. Hartley, C. M. Gilligan-Lee, O. Lahav,

(e) **Stage of publication:**
In Preparation

3. **For multi-authored work, please give a statement of contribution covering all authors** (if single-author, please skip to section 4)**:**
S. Mucesh: conceptualisation, investigation, methodology, data curation, formal analysis, validation, interpretation, writing, visualisation, software
W. G. Hartley: supervision, interpretation, writing (review and editing)
C. M. Gilligan-Lee: supervision, methodology, interpretation, writing (review)
O. Lahav: supervision, writing (review)

4. **In which chapter(s) of your thesis can this material be found?**
Chapters 3 and 5

e-Signatures confirming that the information above is accurate (this form should be co-signed by the supervisor/ senior author unless this is not appropriate, e.g. if the paper was a single-author work)**:**

Candidate: Sunil Mucesh
Date: 02/02/2024

Supervisor/Senior Author signature (where appropriate)**:** Ofer Lahav
Date: 02/02/2024

Contents

1 Introduction **29**

1.1 The Cosmological Framework 30

1.1.1 The Standard Model of Cosmology 30

1.1.2 Friedmann-Lemaître-Robertson-Walker Metric 30

1.1.3 Friedmann Equations 31

1.1.4 Redshift, Distance and Lookback Time 32

1.2 Measuring Galaxy Properties 36

1.2.1 Spectral Energy Distribution 36

1.2.2 Redshift 36

1.2.3 Stellar Population Synthesis 39

1.2.4 SED Fitting 44

1.2.5 Uncertainties, PDFs and Big Data 45

1.3 The Galaxy Population 47

1.3.1 Physical Properties 47

1.3.2 Environment and Correlations 50

1.3.3 High Redshift and Evolution 55

1.3.4 Nature versus Nurture 58

1.4 Thesis Outline 60

2 Machine Learning **62**

2.1 Decision Trees 64

2.1.1 Classification and Regression Trees 64

2.2 Random Forests 67

2.2.1 Hyperparameters 69

3 Causal Inference **70**

3.1 Causal Models and Graphs 71

3.2 Causal Framework 73

3.3 Causal Assumptions 74

3.4 Biases and Adjustments 76

3.4.1 Confounding Bias 76

3.4.2 Selection Bias 78

3.5 Causal Machine Learning 80

4 Galaxy Properties with Machine Learning **82**

4.1 Introduction 84

4.2 Method 87

4.3 Data 88

4.3.1 Cosmological Evolution Survey 89

4.3.2 Dark Energy Survey 89

4.3.3 Preprocessing 91

4.4 Models and Implementation 94

4.5 Results and Discussion 96

4.5.1 Point Estimates 96

4.5.2 Marginal Probability Distributions 98

4.5.3 Joint Probability Distributions 104

4.6 Comparison: ML versus SED Fitting 108

4.7 Conclusions 113

5 The Causal Effect of Environment on Galaxies with Causal Machine Learning **115**

5.1 Introduction 117

5.2 Causal Model of Galaxy Formation and Evolution 121

5.2.1 Galaxy Formation 122

5.2.2 Galaxy Evolution 125

5.2.3 Causal DAG and Effects 135

5.3 Data 138

5.3.1 IllustrisTNG 138

5.3.2 The Galaxy Sample . . . 139
5.4 Method . . . 145
5.4.1 Propensity Scores . . . 147
5.4.2 Inverse Probability Weighting . . . 148
5.5 Estimation . . . 152
5.5.1 Overview . . . 154
5.5.2 Application . . . 154
5.6 Validation . . . 157
5.6.1 Diagnostic Tests . . . 158
5.7 Results and Discussion . . . 162
5.7.1 Overall Causal Effect of Environment . . . 162
5.7.2 Role of Environment over Time . . . 164
5.7.3 Model Comparison . . . 168
5.8 Conclusions . . . 176

6 Conclusions **180**
6.1 Summary . . . 181
6.2 Future Prospects . . . 183

Appendices **185**

A GALPRO **185**
A.1 Training Model . . . 186
A.2 Testing Model . . . 186
A.3 On-the-fly PDFs . . . 187
A.4 Validating Model . . . 187
A.5 Plotting . . . 188
A.6 Configuration . . . 188

List of Figures

1.1 Redshifted rest-frame spectral energy distribution (SED) anticipated from a galaxy at $z = 7$, showing the Lyman, Balmer, and 4000 Å breaks. The Lyman break is sampled by the optical (F775W and F850LP) and near-infrared (NIR) filters (F105W, F125W and F160W) on-board the Hubble Space Telescope (HST), while the Balmer and 4000 Å breaks are sampled by infrared (IR) filters (3.6µm, 4.5µm) on the Spitzer Space Telescope. Reproduced from Dunlop (2013). . . . 38

1.2 Overview of the stellar population synthesis (SPS) technique. The upper panels highlight the ingredients necessary for constructing simple stellar populations (SSPs): an initial mass function (IMF), isochrones, and stellar spectra. The middle panels highlight the ingredients necessary for constructing composite stellar populations (CSPs): star formation histories (SFHs), chemical evolution, SSPs, and a model for dust attenuation and emission. The bottom row shows the final CSPs both before and after a dust model is applied. Reproduced from Conroy (2013). 43

1.3 Tuning-fork style diagram of the Hubble sequence (Hubble, 1936). The visual classification scheme designates galaxies into three Hubble types: ellipticals (E), lenticulars (S0), and spirals (S). The spirals are further separated into normal (S) and barred (SB). Note that the location of galaxies on the sequence does not indicate the temporal evolution of galaxies. Reproduced from Hubble (1936). 48

1.4 Distribution of galaxy colours and colour–magnitude relation of $\sim$ 365,000 galaxies in the Sloan Digital Sky Survey (SDSS; York et al. 2000). The colour distribution is bimodal, with most galaxies being either blue or red. In the colour–magnitude diagram, the blue galaxies dominate the faint end, while the red galaxies the bright end. These two populations are dubbed the "blue sequence" (also known as the "blue cloud") and the "red sequence", respectively (Bell et al., 2004). The sparse population between the two is in the so-called "green valley" (Wyder et al., 2007; Martin et al., 2007; Salim et al., 2007; Schiminovich et al., 2007). Reproduced from Mo et al. (2010). 49

1.5 Colour distribution of SDSS galaxies overlaid with early versus late morphology type. The black triangles and open squares represent early-type and late-type galaxies, respectively. In the left panel, there are 500 galaxies, which are classified spectroscopically. In the right panel, there are 287 bright galaxies, which are classified by visual inspection. Reproduced from Strateva et al. (2001). 50

1.6 The star-formation rate (SFR)–stellar mass ($M_\star$) relation of SDSS galaxies. The galaxies separate into star-forming (upper contours) and quenched (lower contours). The star-forming main sequence (MS) fit to the star-forming galaxies is from Renzini and Peng (2015) and is shown as a solid magenta line. The minimum of the bimodal density contours is shown as a dashed magenta line. The plot is colour coded by the mean logarithmic distance to the MS. The solid black line indicates the median SFR $- M_\star$ relationship, which shows a rapid transition from the star forming to the quenched density peak at $\log(M_\star/M_\odot) \sim 10.5$. Adapted from Bluck et al. (2020a). 51

1.7 Spatial distribution of $\sim$ 80,000 galaxies in the 2dF Galaxy Redshift Survey (2dFGRS; Colless et al. 2001) in a 4° slice projected onto the redshift/right ascension plane. The galaxies are not randomly distributed but are part of the cosmic web (Bond et al., 1996), consisting of voids, sheets or walls, filaments, and nodes. Reproduced from Peacock et al. (2002). 52

1.8 The morphology–density relation (Dressler, 1980). The fraction of ellipticals (E), lenticulars (S0), and spirals (S) and irregulars (Irr) as a function of environmental density (log of the projected density), in a sample of 55 rich clusters at $z \sim 0$. The fraction of the different morphological types in the field is also indicated for comparison. The upper panel shows the number of galaxies in each density bin. Reproduced from Dressler (1980). 53

1.9 The colour–density relation (Kodama et al., 2001). The colour $(V - I)$ as a function of environmental density (10th nearest neighbour density) of galaxies brighter than $I = 23.4$ in the rich cluster $A851$ at $z = 0.41$. The open circles and filled triangles show the galaxies brighter or fainter than $I = 21.4$ $(M_v^\star + 2)$, respectively. The three red lines represent the loci of the 25th, 50th, and 75th percentile colours. Reproduced from Kodama et al. (2001). 54

1.10 The star-formation rate (SFR)–density relation (Gómez et al., 2003). The SFRs of SDSS galaxies as a function of environmental density (10th nearest neighbour density). The shaded area represents the distribution of corrected SFRs (Hopkins et al., 2001). The median is the solid line, and the top and bottom are the 25th and 75th percentiles, respectively. There is an abrupt transition in the SFR at surface density $\sim 1\ h_{75}^{-2}$ Mpc^{-2}. Reproduced from Gómez et al. (2003). 55

1.11 The fraction of ellipticals (E), lenticulars (S0), ellipticals and lenticulars (E + S0), and spirals and irregulars (Sp + Irr) in clusters over time. The open and filled circles denote clusters in the ESO Distant Cluster Survey (EDisCS; White et al. 2005) and Fasano et al. (2000), respectively. Reproduced from Desai et al. (2007). 56

1.12 The fraction of galaxies with luminosities greater than $(M_B - 5\log h) < -20$ in four rest-frame colour bins as a function of environment (δ on $R = 5h^{-1}$Mpc) in four different redshift intervals. The horizontal bars indicate the amplitude of the bins in δ (i.e., the range spanned by the lower 5% and upper 95% percentile of the objected contained in each bin), while the vertical error bars represent a Poissonian 1σ uncertainty. The shaded areas are obtained by smoothing the red (blue) fraction with an adaptive sliding box containing the same number of objects in each bin as the point marked explicitly. Reproduced from Cucciati et al. (2006). 57

2.1 Binary decision tree in a radial layout, spanning out from the root node close to the centre. The root and decision nodes are represented as circles, and the leaf nodes are grey triangles. The colour of the root and decision nodes identifies the unique variable on which data is split. The subpanel shows a zoomed in region from the tree. Reproduced from Carrasco Kind and Brunner (2013). 65

2.2 Overview of the random forest (RF) prediction process. The predictions of all N decision trees are aggregated in a final result. For classification, the final prediction is the mode, and for regression, it is the average. Adapted from https://www.spotfire.com/glossary/what-is-a-random-forest. 68

3.1 Causal graph representing the causal relationship between two variables, T and Y. The direct edge (black arrow) from T to Y implies that T directly causes Y. The causal association (i.e., the association due to causation) 'flows' asymmetrically from T to Y (represented by the blue dashed line arrow), while association 'flows' symmetrically (represented by the red dashed line). The causal graph is an example of a directed acyclic graph (DAG). A DAG is a graph that is: (i) directed (i.e., has edges that imply a direction) and (ii) acyclic (i.e., a variable does not cause itself either directly or through another variable). 72

3.2 Illustration of confounding bias. DAGs representing the causal relationships between treatment T, outcome Y, and their common cause or confounder X. (a) There are two paths for association to flow between T and Y: (i) the direct path between T and Y and (ii) the backdoor path linking T and Y via X. The causal association (depicted with the blue dashed line arrow) flows through the former, while the non-causal confounding association (depicted with the red dashed line arrow) flows through the latter. The admixture of the causal and non-causal associations means association is not causation. (b) The act of conditioning on X (visualised with the greyed-out node) blocks the non-causal confounding association from flowing via the backdoor path. 77

3.3 Illustration of selection (or collider) bias. DAGs representing the causal relationships between treatment T, outcome Y, and their common effect or collider X. (a) Similar to Figure 3.2, there is a direct path and a backdoor path between T and Y for association to flow. As before, the causal association (depicted with the blue dashed line arrow) flows through the former. However, the non-causal association (depicted with the red dashed line arrow) cannot flow through the latter as it is now blocked because of the collider. (b) The act of conditioning on X (visualised with the greyed-out node) unblocks the previously blocked backdoor path, allowing once again the non-causal association to flow. As a result, association is not causation as it is once again an admixture of the causal and non-causal associations. 79

4.1 Marginal and joint distributions of redshifts and stellar masses of galaxies in the DF dataset and the distributions of *griz* luptitudes. The colours in the joint distribution indicate the density of points. The DF dataset is created by cross-matching galaxies in the DES Y3 Deep Fields (DF) and the COSMOS2015 catalogues. All galaxies with unreliable or missing redshift and stellar mass are discarded from the dataset, and a magnitude-limited sample is produced by selecting galaxies with $i < 23.5$. The *griz* luptitudes in the dataset are computed from fluxes in the Y3 DF catalogue, while the redshifts and stellar masses are from the COSMOS2015 catalogue. 93

4.2 'True' redshifts and stellar masses of test galaxies versus the predictions made by the DES-DF and DES-WF models. The colours indicate the density of points. The normalized median absolute deviation (NMAD; Hoaglin and Mosteller 2000) metric values are stated for redshift and stellar mass, respectively. For redshift, the bias $\hat{y} - \tilde{y}$ is divided by $1 + \tilde{y}$ in Equation 4.4. 97

4.3 Redshift and stellar mass PIT distributions for the DES-DF and DES-WF models. These distributions are used to assess the probabilistic calibration of marginal PDFs of test galaxies produced by the models. They are overlaid with Q–Q plots to highlight deviations from uniformity. The black-dashed and solid blue lines represent the quantiles of $U(0, 1)$ and PIT distributions, respectively. The percentage of catastrophic outliers along with the values of the Kullback–Leibler (KL) divergence, Kolmogorov–Smirnov (KS) test, and Cramér-von Mises (CvM) metrics are also stated to quantify uniformity of the PIT distributions. We define a catastrophic outlier to be any galaxy with a redshift or stellar mass completely outside the support of its marginal PDF. 103

4.4 The difference between the average predictive CDF ($\hat{F}_I$) and the true empirical CDF ($\tilde{G}_I$) of redshift and stellar mass plotted at different intervals in their respective ranges. These diagnostic plots are used to assess the marginal calibration of marginal PDFs of test galaxies produced by the DES-DF and DES-WF models. 103

4.5 Examples of joint redshift–stellar mass PDFs produced by the DES-DF and DES-WF models of the same test galaxies (in rows). The gold and white stars alongside the dashed lines represent the 'true' and predicted redshifts and stellar masses of the galaxies, respectively. The predicted redshifts and stellar masses are computed by averaging the predictions from all the decision trees in the individual RFs. The green circles indicate the values of redshift and stellar mass in the leaf nodes that are representative of the test galaxies. 105

4.6 copPIT distributions for the DES-DF and DES-WF models. They are overlaid with Q–Q plots to aid in visually assessing the probabilistic copula calibration of joint redshift–stellar mass PDFs of test galaxies. The black-dashed and solid blue lines represent the quantiles of $U(0, 1)$ and copPIT distributions, respectively. The percentage of catastrophic outliers along with the values of the Kullback–Leibler (KL) divergence, Kolmogorov–Smirnov (KS) test, and Cramér-von Mises (CvM) metrics is also stated to quantify uniformity of the copPIT distributions. We define a catastrophic outlier to be any galaxy that is completely outside the support of its marginal PDFs. Probabilistic copula calibration is the multivariate analogue of probabilistic calibration. 107

4.7 The difference between the "average Kendall distribution function" ($\hat{\mathcal{K}}_{H_I}$) and the empirical CDF of the predicted joint CDFs evaluated at the 'true' redshifts and stellar masses ($\tilde{J}_I$), plotted at regular intervals in the probability space $w \in [0, 1]$. This diagnostic plot is used to assess the Kendall calibration of the joint PDFs produced by the DES-DF and DES-WF models. Kendall calibration is the multivariate analogue of marginal calibration. 107

4.8 Comparison diagnostic plots for benchmarking the performance of GALPRO on test galaxies in the DF dataset against that of BAGPIPES on a comparable dataset, which is composed of the same galaxies but with Subaru photometry in four bands (V, r, $i+$, and $z++$) from the COSMOS2015 catalogue. The marginal and joint PDFs of redshift and stellar mass produced by BAGPIPES are validated using a 'truth' catalogue constructed by running BAGPIPES on photometry in 22 COSMOS bands listed in Table 4.1. 112

5.1 Mini causal models of different stages of galaxy formation and standard physical processes occurring in galaxies. For visual clarity, all the possible causal connections of a variable with others are not drawn. . 124

5.2 Mini causal models of different internal processes of galaxy evolution. For visual clarity, all the possible causal connections of a variable with others are not drawn. 127

5.3 Mini causal models of different external processes of galaxy evolution. For visual clarity, all the possible causal connections of a variable with others are not drawn. 133

5.4 Causal model of galaxy formation and evolution, with all the mini causal models and variables connected. 134

5.5 Directed acyclic graph (DAG) of the causal model of galaxy formation and evolution (Figure 5.4). It is constructed from carefully tracing the causal chains and unravelling the feedback loops between halo mass (H), environment (E), and star-formation rate (SFR). The subscripts indicate time, increasing from left to right (with zero marking the present). The DAG is the causal model unless otherwise specified. . 136

5.6 Distributions of fundamental halo and galaxy properties, such as host halo mass, halo mass, stellar mass, and star-formation rate (SFR), as well as the average environmental density (10th nearest neighbour density), of the galaxy sample at $z = 0$. 143

5.7 Evolutionary history of a galaxy (following the main progenitor branch) in terms of its host halo mass, halo mass, stellar mass, star-formation rate (SFR), and environmental density (10th nearest neighbour density), from $z \sim 6$ to $z = 0$. The various histories are min-max normalised to allow for comparison on the same scale. 144

5.8 Average absolute correlation coefficients ($AACC$) at different redshifts in the original population before weighting and in the pseudo-population after weighting. 160

5.9 Weight distributions at different redshifts, assuming the causal model. The black and blue dashed lines indicate the reference mean (1) and the mean of the distribution (stated), respectively. 161

5.10 Causal dose-response curves (CDRCs) of the marginal and joint causal effects of environment on the SFR (i.e., causal SFR–density relations) at $z = 0$. The bottom panel shows the average causal effects τ of different density environments (comparing to the lowest-density environment). The shaded regions represent the 68% confidence interval, estimated with bootstrapping. 163

5.11 Causal dose-response curves (CDRCs) of the causal effects of environment on the SFR (i.e., causal SFR–density relations) at $z = 0$ and at different redshifts going back to $z \sim 3$. The bottom panel of $z = 0$ shows the average causal effects τ of different density environments (comparing to the lowest-density environment). The shaded regions represent the 68% confidence interval, estimated with bootstrapping. 165

5.12 The causal model assumed implicitly in the literature to estimate the effect of environment. We refer to it as the traditional model. 169

5.13 Causal dose-response curves (CDRCs) of the causal effects of environment on the SFR (i.e., causal SFR–density relations) at $z = 0$ and at different redshifts going back to $z \sim 3$, of the naïve, traditional, and causal models (with stellar mass and halo mass as the confounder, respectively). The bottom panel of $z = 0$ shows the difference in the average SFRs between the different causal models and the causal model (i.e., causal model (halo mass)). The shaded regions represent the 68% confidence interval, estimated with bootstrapping. 171

5.14 Causal dose-response curves (CDRCs) of the marginal causal effects of environment on the SFR (i.e., causal SFR–density relations) at $z = 0$ and at different redshifts going back to $z \sim 3$, assuming the traditional model. The bottom panel of $z = 0$ shows the average causal effects τ of different density environments (comparing to the lowest-density environment). The shaded regions represent the 68% confidence interval, estimated with bootstrapping. 174

5.15 Weight distributions at different redshifts, assuming the traditional model. The black and blue dashed lines indicate the reference mean (1) and the mean of the distribution (stated), respectively. 175

List of Tables

4.1 List of 22 COSMOS bands used to build a 'truth' catalogue to validate the marginal and the joint PDFs of redshift and stellar mass produced by `BAGPIPES` using the four-band (V, r, $i+$, and $z++$) Subaru photometry. 110

4.2 Fixed and fitted parameters with their associated priors for the delayed exponentially declining ($\tau^{-2}te^{-t/\tau}$) star-formation history (SFH) model used in the `BAGPIPES` runs. The model is not readily available in `BAGPIPES`, so we lightly modify the code to meet our requirements. We adopt the Calzetti et al. (2000) attenuation curve, stellar population synthesis (SPS) models of Bruzual and Charlot (2003), and a Kroupa and Boily (2002) initial mass function (IMF). A_V is the attenuation in the V-band, τ is the star formation time-scale, Z is the metallicity, U is the ionisation parameter, a_{BC} is the lifetime of HII regions, and ϵ is a constant that controls the extra attenuation towards them. . . 110

Chapter 1

Introduction

Galaxies are islands of stars in the vast and dark cosmic ocean. They are fascinating entities, exhibiting various colours, sizes, and morphologies, but above all, they are the fundamental building blocks of the visible Universe.

In the current paradigm, galaxies form and evolve in haloes of dark matter (White and Rees, 1978; Efstathiou and Silk, 1983; Blumenthal et al., 1984). The overall scenario is as follows. Quantum fluctuations in the very early Universe generate density perturbations in the primordial matter density field (Guth and Pi, 1982; Hawking, 1982; Linde, 1982; Starobinsky, 1982; Bardeen et al., 1983). These initial perturbations grow and evolve under gravitational instability until they reach over-density, at which point they decouple from the cosmic expansion and collapse to form dark matter haloes. Baryonic matter falls into the gravitational potential wells of these haloes and subsequently cools and condenses into a gas cloud. Finally, the cloud collapses into stars, giving rise to a galaxy. Over time, galaxies grow and evolve as they accrete new matter from their surroundings and merge with neighbouring galaxies via their haloes.

This chapter is organised as follows. Section 1.1 briefly overviews the cosmological framework within which galaxy formation and evolution unfolds. Section 1.2 covers how the properties of galaxies are derived from their light. Section 1.3 describes the galaxy population along with a discussion on how galaxies have formed and evolved. Finally, Section 1.4 provides the outline of this thesis.

1.1 The Cosmological Framework

Modern cosmology is founded on the cosmological principle, which states that the Universe is spatially homogeneous (i.e., it looks the same from any location) and isotropic (i.e., it looks the same in all directions) on large scales, and Einstein's theory of general relativity (GR; Einstein 1916), which describes gravity as a geometric property of spacetime.

1.1.1 The Standard Model of Cosmology

The Universe is composed of three main components: dark energy, dark matter, and baryonic matter. The nature of dark energy and dark matter is unknown, but their roles are reasonably well understood. Dark energy is driving the accelerated cosmic expansion, as inferred from observations of distant Type Ia supernovae (Riess et al., 1998; Perlmutter et al., 1999). And dark matter is responsible for structure formation in the Universe. Indirect evidence of this invisible matter has come from velocity dispersions of galaxy clusters (Oort, 1932; Zwicky, 1933, 1937), rotation curves of galaxies (Freeman, 1970; Rubin and Ford, 1970), gravitational lensing (see Massey et al., 2010, for a review), and the cosmic microwave background (CMB). This leads to the standard model of cosmology—Lambda cold dark matter (ΛCDM). The cosmological model describes a flat universe of $\sim 68\%$ dark energy (described by the cosmological constant Λ), $\sim 27\%$ cold dark matter (CDM), and only $\sim 5\%$ baryonic matter that constitutes the visible Universe (i.e., planets, stars, galaxies, etc.) (Planck Collaboration et al., 2020).

1.1.2 Friedmann-Lemaître-Robertson-Walker Metric

The matter distribution in the Universe governs the geometry of spacetime according to the Einstein field equations,

$$G_{\mu\nu} = R_{\mu\nu} - \frac{1}{2} g_{\mu\nu} R = \frac{8\pi G}{c^4} T_{\mu\nu} + \Lambda g_{\mu\nu}. \tag{1.1}$$

On the left-hand side, $G_{\mu\nu}$ is the Einstein tensor, $R_{\mu\nu}$ and R are the Ricci tensor and Ricci scalar respectively, and $g_{\mu\nu}$ is the metric tensor. On the right-hand side, $T_{\mu\nu}$ is the energy–momentum tensor, and Λ is the cosmological constant.

Assuming the cosmological principle, the exact solution of the Einstein field equations is the Friedmann-Lemaître-Robertson-Walker (FLRW) metric,

$$ds^2 = c^2dt^2 - a^2(t)\left[\frac{dr^2}{1-kr^2} + r^2(d\theta^2 + \sin^2\theta d\phi^2)\right], \tag{1.2}$$

where ds is the spacetime interval, c is the speed of light, dt is the proper time interval, $a(t)$ is the scale factor, k is the spatial curvature constant, and (r, θ, ϕ) are comoving coordinates. The scale factor and spatial curvature constants characterise the expansion (or contraction) and curvature of the Universe, respectively. The scale factor is 1 at the present time, and the values of -1, 0, $+1$ for the spatial curvature constant correspond to open, flat, and closed geometries, respectively.

1.1.3 Friedmann Equations

The expansion of a homogeneous and isotropic universe is described by the Friedmann equations (Friedmann, 1922). The expansion rate $\dot{a}$ is given by the Friedmann equation,

$$\left(\frac{\dot{a}}{a}\right)^2 = \frac{8\pi G}{3}\rho - \frac{kc^2}{a^2} + \frac{\Lambda c^2}{3}, \tag{1.3}$$

and the acceleration of the Universe $\ddot{a}$ is given by the Friedmann acceleration equation,

$$\frac{\ddot{a}}{a} = -\frac{4\pi G}{3}\left(\rho + \frac{3P}{c^2}\right) + \frac{\Lambda c^2}{3}, \tag{1.4}$$

where G is the gravitational constant, and ρ and P are the energy density and pressure of the fluid, respectively. The expansion rate divided by the scale factor is the Hubble parameter,

$$H(t) = \frac{\dot{a}(t)}{a(t)}. \tag{1.5}$$

The Hubble parameter at the present time is called the Hubble constant and is denoted by H_0.

The Friedmann equation is usually written in terms of the density parameter,

$$\Omega = \frac{\rho}{\rho_c}, \tag{1.6}$$

where the critical density,

$$\rho_c = \frac{3H^2}{8\pi G}, \tag{1.7}$$

is the density of a spatially flat universe. The Friedmann equation is then simply:

$$1 = \Omega_m + \Omega_k + \Omega_\Lambda, \tag{1.8}$$

where

$$\Omega_m = \frac{8\pi G\rho}{3H^2}, \tag{1.9}$$

$$\Omega_k = \frac{-kc^2}{a^2H^2}, \tag{1.10}$$

$$\Omega_\Lambda = \frac{\Lambda c^2}{3H^2}, \tag{1.11}$$

are the matter, spatial curvature, and cosmological constant (or vacuum) densities, respectively. In terms of the present-day density parameters, the Friedmann equation is:

$$H^2 = H_0^2(\Omega_{r,0}a^{-4} + \Omega_{m,0}a^{-3} + \Omega_{k,0}a^{-2} + \Omega_{\Lambda,0}), \tag{1.12}$$

where the additional component $\Omega_{r,0}$ is the radiation density. The values of these cosmological parameters are: $H_0 = 67.4 \pm 0.5$ kms^{-1}Mpc^{-1}, $\Omega_{m,0} = 0.315 \pm 0.007$, $\Omega_{\Lambda,0} = 0.6847 \pm 0.0073$, and $\Omega_{k,0} = 0.001 \pm 0.002$ (Planck Collaboration et al., 2020). The uncertainties are 68% confidence intervals.

1.1.4 Redshift, Distance and Lookback Time

As light travels in an expanding universe, it loses energy and its wavelength increases and frequency decreases. This phenomenon is called redshift (z) since the light shifts towards the red end of the spectrum, and it is determined by the ratio of the scale factors at the time of observation (a_{obs}) and emission (a_{emit}).

$$1 + z = \frac{\lambda_{obs}}{\lambda_{emit}} = \frac{a_{obs}}{a_{emit}}, \tag{1.13}$$

where λ_{obs} and λ_{emit} are the observed and emitted wavelengths, respectively.

There are two fundamental distance measures in an expanding universe: comoving and proper. The comoving distance is the distance in the comoving reference

frame. In other words, the comoving distance between two objects moving with the Hubble flow is constant over time. Conversely, the proper distance is the distance between two objects at a specific moment in cosmological time, which does change over time due to the expansion of the Universe.

The light from an object travels on a null geodesic ($ds = 0$), so the comoving distance χ from the FLRW metric is:

$$\chi = \int_{t_{emit}}^{t_{obs}} c\frac{dt}{a(t)}, \tag{1.14}$$

where t_{emit} and t_{obs} are the times of emission and observation, respectively. The scale factor converts the comoving distance to the proper distance,

$$d = a(t)\chi. \tag{1.15}$$

In a spatially flat universe ($k = 0$), the comoving distance is equal to the radial comoving distance r.

The comoving and proper distances are not directly observable. However, if the size or luminosity of an object is known then its distance can be measured. These objects are called standard rulers and standard candles, respectively. The angular diameter distance,

$$d_A = \frac{D}{\theta} = \frac{\chi}{1+z}, \tag{1.16}$$

where D and θ are the physical and angular sizes, respectively. The luminosity distance,

$$d_L = \sqrt{\frac{L}{4\pi F}} = \chi(1+z), \tag{1.17}$$

where L is the luminosity and F is the flux. Combining the previous two equations, the luminosity distance is related to the angular diameter distance via:

$$d_L = d_A(1+z)^2. \tag{1.18}$$

The different distance measures are only equal to each other in a static universe. At small redshifts ($z \ll 1$), the luminosity distance,

$$d_L \simeq \frac{c}{H_0}\left[z + \frac{1}{2}(1 - q_0)z^2 + ...\right], \tag{1.19}$$

where the deceleration parameter,

$$q_0 = -\frac{\ddot{a}_0 a_0}{\dot{a}_0^2}. \tag{1.20}$$

To the first-order approximation,

$$cz = H_0 d_L. \tag{1.21}$$

When the recessional velocity is much less than the speed of light, the redshift $z \simeq v/c$. Thus,

$$v = H_0 d. \tag{1.22}$$

This is Hubble's law, also known as the Hubble–Lemaître law (Lemaître, 1927; Hubble, 1929), which states that the recessional velocity of an object is directly proportional to its distance.

Finally, the time taken for light to travel from an object at redshift z, or the lookback time,

$$t_L = \frac{1}{H_0}\int_0^z \frac{dz}{(1+z)\ E(z)}, \tag{1.23}$$

where $E(z) = H(z)/H_0$ is the dimensionless Hubble parameter.

The connection between redshift, distance, and lookback time makes redshifts crucial for both cosmology and galaxy formation and evolution. Distances are necessary to map the large-scale structure (LSS) of the Universe, which is heavily dependent on cosmology. Specifically, the spatial distribution of galaxies can constrain the nature of dark energy via probes such as galaxy cluster counts (Haiman et al., 2001), weak lensing tomography (Hu, 1999), and baryonic acoustic oscillations (BAO; Eisenstein 2005). On the other hand, the lookback time is important as it pinpoints galaxies in time. Due to the timescales involved, it is impossible to witness the evolution of individual galaxies. However, the finite speed of light provides an opportunity, as galaxies at larger distances are observed when the Universe

was younger. In this regard, redshifts are fundamental because by comparing the properties of the galaxy population at different epochs, it is possible to infer how galaxies form and evolve.

1.2 Measuring Galaxy Properties

Galaxies are diverse entities and are thus characterised by a large number of properties, with stellar mass, star-formation rate (SFR), metallicity, and age being among the most important. Before describing the galaxy population, this section covers how to estimate such physical properties and redshift from the light of a galaxy.

1.2.1 Spectral Energy Distribution

Galaxies emit light across the electromagnetic (EM) spectrum, characterised by the spectral energy distribution (SED), i.e., the energy emitted as a function of wavelength or frequency. The majority of the stellar population emits in the optical and near-infrared (NIR), with the exception being young, massive stars that emit in the near-ultraviolet (NUV). The galactic starlight is processed by the gas and dust lying between the stars in the interstellar medium (ISM). Specifically, the gas (primarily atomic hydrogen) absorbs extreme-UV (EUV) photons and emits at specific wavelengths, producing absorption and emission lines such as the Hα. On the other hand, the dust radiates in the mid-infrared (MIR) to far-infrared (FIR) range. Lastly, an active galactic nucleus (AGN) powered by an accreting supermassive black hole (SMBH) emits in most, if not all, wavebands and produces strong emission lines.

1.2.2 Redshift

From the previous section, redshift is defined as the ratio between the shift in wavelength and the emitted wavelength.

$$z = \frac{\lambda_{obs} - \lambda_{emit}}{\lambda_{emit}}. \tag{1.24}$$

The redshift of a galaxy consists of: (i) cosmological redshift due to the expansion of the Universe, (ii) Doppler redshift due to peculiar motions separate from the Hubble flow as a result of local gravitational effects, and (iii) gravitational redshift due to light travelling from a strong to a weak gravitational potential. Of the three, the cosmological redshift is the most relevant and significant. The Doppler redshift is only important at low redshifts ($z < 0.01$) and in rich clusters, which can have velocity dispersions over 1000 km/s (Girardi et al., 1993). Lastly, the gravitational redshift is usually negligible. It is important to measure redshifts because they can be converted into distances to galaxies, for example, through Hubble's law. The

caveat is that the redshift must be the cosmological redshift.

1.2.2.1 Spectroscopic Redshifts

Measuring redshifts from SEDs is straightforward as the task reduces to identifying strong absorption and emission lines in the spectra and determining the shift in their positions from known rest-frame wavelengths. These so-called spectroscopic redshifts (spec-zs) are highly accurate with relative errors of less than 0.1% (Mo et al., 2010). The downside is that long exposures are necessary to achieve a sufficient signal-to-noise (S/N) ratio, especially for faint galaxies. For this reason, it is not feasible to obtain redshifts with spectroscopy for anything above tens of millions of galaxies with the current technology. For example, the ongoing Dark Energy Spectroscopic Instrument (DESI; DESI Collaboration et al. 2016) will record spectra of some 30 million galaxies.

1.2.2.2 Photometric Redshifts

The alternative to spec-zs are photometric redshifts (photo-zs), i.e., redshifts estimated from photometry. With photometry, the amount of light is measured in several wavebands rather than at specific wavelengths. This rough sampling of the underlying SED makes it impossible to pinpoint individual absorption and emission lines to obtain redshifts, so the photo-z estimation method relies on the detection of the overall shape and strong broad features such as:

- The Lyman break at 912 Å due to the absorption of photons of wavelengths shorter than the Lyman limit by neutral atomic hydrogen (HI) gas within the galaxy or in the intergalactic medium (IGM).
- The Balmer break at 3646 Å due to the absorption of photons more energetic than the Balmer limit.
- The 4000 Å break due to absorption by ionised metals in stellar atmospheres. This break is enhanced by a deficiency in young, blue stars (Hamilton, 1985).

The breaks are associated with a rapid rise/drop in light intensity, as can be observed in Figure 1.1. As a result, they are easy to detect by comparing the fluxes/magnitudes between two bands, i.e., the colour. Given that the features are sampled by filters only at specific redshifts, a single colour predicts a galaxy's redshift

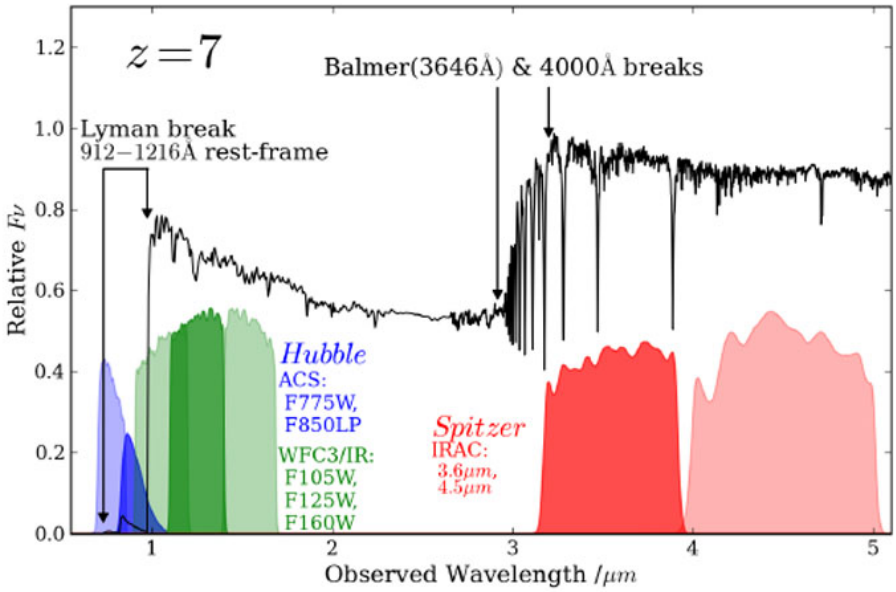

Figure 1.1: Redshifted rest-frame spectral energy distribution (SED) anticipated from a galaxy at $z = 7$, showing the Lyman, Balmer, and 4000 Å breaks. The Lyman break is sampled by the optical (F775W and F850LP) and near-infrared (NIR) filters (F105W, F125W and F160W) on-board the Hubble Space Telescope (HST), while the Balmer and 4000 Å breaks are sampled by infrared (IR) filters (3.6µm, 4.5µm) on the Spitzer Space Telescope. Reproduced from Dunlop (2013).

to within a range. The combination of multiple colours narrows this range further since the multi-dimensional colour space is small at a given redshift.

Photo-zs can be estimated for a large sample because photometry is quicker to obtain than the spectra of galaxies. Additionally, the method can be extended to much fainter galaxies. However, photo-zs are less reliable than spec-zs due to colour–redshift degeneracies (beside filter widths). Indeed, these degeneracies are broken by the detection of breaks, so the number and type of filters utilised determines the magnitude of errors. For example, IR filters (JHK) are necessary to bracket the Balmer break as it moves out of the visible range at $z = 1.2 - 2.2$. Also, the U filter is required for galaxies at $z \leq 0.4$ because none of the other filters can detect a strong break. The method is also fundamentally limited because if there are no breaks in the first place, then the error will always be significant. This is the case for star-forming galaxies, which lack a pronounced 4000 Å break. Generally, photo-z errors are in the order of $3 - 10\%$ (Mo et al., 2010). Despite the larger uncertainty, some analyses such as weak lensing, benefit more from the increased statistical power

of a larger sample size than from precision (Palmese, 2018). Consequently, the next generation of surveys, such as Euclid (Laureijs et al., 2011), the Rubin Observatory Legacy Survey of Space and Time (LSST; LSST Science Collaboration et al. 2009), and the Nancy Grace Roman Space Telescope (Roman; Spergel et al. 2015), will primarily be photometric.

There are many approaches to estimating photo-zs, such as colour–colour (Koo, 1985) and colour–redshift (Pello et al., 1996) diagrams, but the most common is SED fitting or template fitting (Baum, 1962; Puschell et al., 1982; Loh and Spillar, 1986). The basic idea is to first compute expected colours (or fluxes/magnitudes) at a given redshift from SED templates (which can be either empirical or theoretical) and then perform a match to the observed colours (or fluxes/magnitudes) to determine the best-fit redshift. Since SEDs are shaped by the different physical processes occurring in galaxies, SED fitting not only provides redshifts but also physical properties. Before laying out the process in more detail, the next section describes how theoretical SEDs are created.

1.2.3 Stellar Population Synthesis

Stellar population synthesis (SPS) or evolutionary population synthesis (EPS) (Tinsley, 1968, 1972; Searle et al., 1973; Tinsley and Gunn, 1976; Larson and Tinsley, 1978; Bruzual A., 1983) is a method for modelling galaxy SEDs. As the light from a galaxy is composed of contributions from different components, the basic premise behind SPS is to model each galaxy component and combine their contributions, beginning with the primary constituent—the stars.

1.2.3.1 Stars

Broadly speaking, a galaxy is a population of stars ranging from the most common, low-luminosity, long-lived, dwarf M-types to the less numerous, high-luminosity, short-lived, massive OB-types. For simplicity, an ensemble of stars of a certain age and metallicity called a simple stellar population (SSP) is modelled rather than individual stars. The galaxy spectrum is then the sum of spectra of many SSPs.

There are two methods for constructing SSPs: isochrone synthesis (Chiosi et al., 1988; Maeder and Meynet, 1988; Charlot and Bruzual A, 1991) and fuel consumption (Renzini and Buzzoni, 1986; Maraston, 1998). The difference between the two lies in the integration variable adopted in the post-main sequence (PMS). The isochrone

synthesis method integrates the spectra of all stars along an isochrone, i.e., a curve on the Hertzsprung-Russell (HR) diagram representing a population of stars of the same age but different masses. A potential problem is that the isochrones are calculated at discrete time steps, so any phases of stellar evolution more rapid than the time step are poorly represented. To circumvent this issue, isochrones are computed up to the end of the early asymptotic giant branch (E-AGB), and later rapid stellar phases like the thermally-pulsating asymptotic giant branch (TP-AGB) are added manually.

On the other hand, the fuel consumption method solves this issue directly by changing the integration variable above the main sequence turnoff (i.e., a point in the HR diagram when a star leaves the main sequence) to the so-called fuel, which is the amount of hydrogen and helium consumed via nuclear burning during a given PMS phase. This is because the luminosity of PMS stars, which are among the most luminous, is directly linked to the fuel available at the turnoff mass (Buzzoni, 1989; Maraston, 1998, 2005).

The spectrum of an SSP at time t and metallicity Z can be written as (Conroy, 2013):

$$f_{\rm SSP}(t, Z) = \int_{m_{lo}}^{m_{up}} f_{\rm star}[T_{\rm eff}(M_\star), \log g(M_\star)|t, Z]\ \Phi(M_\star) dM_\star, \tag{1.25}$$

where $M_\star$ is the stellar mass at the zero-age main sequence, $\Phi(M_\star)$ is the initial mass function (IMF), and $f_{\rm star}$ is the stellar spectrum.

- The IMF is the initial distribution of stellar masses of zero-age main sequence stars. Three known empirical forms are the simple power law (Salpeter, 1955), broken power law (Kroupa, 2001), and lognormal (Chabrier, 2003). These IMFs are derived from observations of stars in the solar neighbourhood. There are also top-heavy and bottom-heavy IMFs, but the most commonly used are the broken power law and lognormal.

- The isochrones are constructed from stellar evolution tracks computed with stellar evolution theory. The most widely used stellar evolution tracks and isochrones are the Padova (Bertelli et al., 1994; Girardi et al., 2000; Marigo and Girardi, 2007; Marigo et al., 2008), Geneva (Schaller et al., 1992; Lejeune and Schaerer, 2001), and BaSTI (Pietrinferni et al., 2004, 2006; Cordier et al.,

2007). The isochrones determine the relation between the effective temperature $T_{\rm eff}$ and surface gravity g for a given stellar mass $M_\star$, at time t and metallicity Z.

- Stellar spectral libraries convert the outputs of stellar evolution into stellar spectra. There are both theoretical libraries, such as BaSel (Lejeune et al., 1997, 1998; Westera et al., 2002), and empirical libraries, such as STELIB (Le Borgne et al., 2003) and MILES (Sánchez-Blázquez et al., 2006; Cenarro et al., 2007).

1.2.3.2 The Interstellar Medium

The stars are embedded in an interstellar medium (ISM) of gas and dust, which processes the starlight. Interstellar gas is primarily composed of hydrogen. It is present in both atomic and molecular forms, but the latter does not contribute significantly to the overall SED (Young and Scoville, 1991; Hollenbach and Tielens, 1997). Any neutral hydrogen (HI) gas near young, massive OB stars is ionised by the Lyman continuum photons they emit, and the recombination of this ionised hydrogen (HII) gas creates various emission lines. As the OB stars have a short lifespan, these HII regions or emission nebulae are strong indicators of recent star formation. Furthermore, the flux of hydrogen emission lines is proportional to the Lyman continuum flux produced by the stars, so they are used to determine the SFR. The most commonly used is the Hα emission line in the optical range. Also, HI gas by itself is responsible for the 21-cm radio emission line. The cause is a spin-flip transition within the atom. Several codes are available that predict the nebular emission as a function of the physical state of the gas, such as CLOUDY (Ferland et al., 1998) and MAPPINGSIII (Groves et al., 2004a,b).

Interstellar dust is believed to be produced by AGB stars and injected into the ISM via stellar winds (Mo et al., 2010). The dust absorbs and scatters galactic starlight in the IR-UV range, thus causing extinction. The effect of extinction is interstellar dimming (i.e., galaxies appear dimmer than expected) and interstellar reddening (i.e., galaxies appear redder than expected) because shorter wavelength light is absorbed and scattered more easily. The radiation absorbed by the dust is re-emitted in the MIR and FIR.

It is hard to accurately model the impact of dust on the final spectrum because

not only does it depend on the star–dust geometry (i.e., the distribution of dust within the galaxy relative to stars) but also the chemical composition and size of the dust grains. Furthermore, light can be scattered into the line of sight as well as out of it. This complexity is usually captured by Calzetti et al. (2000) or Charlot and Fall (2000) attenuation curves. Lastly, the contribution from an AGN must also be modelled for active galaxies.

1.2.3.3 Composite Stellar Populations

The final step of SPS modelling to produce SEDs is evolving the galaxies. Specifically, the stellar population is evolved by specifying a star-formation history (SFH) and chemical evolution model. Combining all the ingredients results in a composite stellar population (CSP), as shown in Figure 1.2. The spectrum of a galaxy at time t can be written as (Conroy, 2013):

$$f_{\rm CSP}(t) = \int_{t'=0}^{t'=t} \int_{Z=0}^{Z=Z_{\rm max}} \psi(t-t')\, P(Z, t-t')\, f_{\rm SSP}(t', Z) e^{-\tau_d(t')} + A f_{\rm dust}(t', Z)\, dt' dZ, \tag{1.26}$$

where ψ is the SFR, P is the metallicity distribution function, τ_d is the optical depth controlling dust attenuation, $f_{\rm dust}$ is the dust emission function, and A is the normalisation constant. All of the functions are time-dependent and metallicity-dependent.

An exponentially-declining SFH is widely adopted as given by the exponential or τ–model (Schmidt, 1959), where $\psi(t) \propto e^{-t/\tau}$. In recent years, rising SFHs have been adopted to explain the SEDs of high-redshift galaxies (Maraston et al., 2010; Papovich et al., 2011), e.g., $\psi(t) \propto t^{\beta} e^{-t/\tau}$. The time-dependent metallicity distribution function is usually a δ-function. In other words, a single metallicity is assumed for the entire composite population.

Some widely known SPS models are PEGASE (Fioc and Rocca-Volmerange, 1997) and PEGASE-HR (Le Borgne et al., 2004), GRASIL (Silva et al., 1998), STARBURST99 (Leitherer et al., 1999), GALAXEV (also known as BCO3; Bruzual and Charlot 2003), M05 (Maraston, 2005), and FSPS (Conroy et al., 2009; Conroy and Gunn, 2010). In summary, SPS generates SEDs by modelling the components and physical processes of galaxies. The ultimate goal is then to invert the process

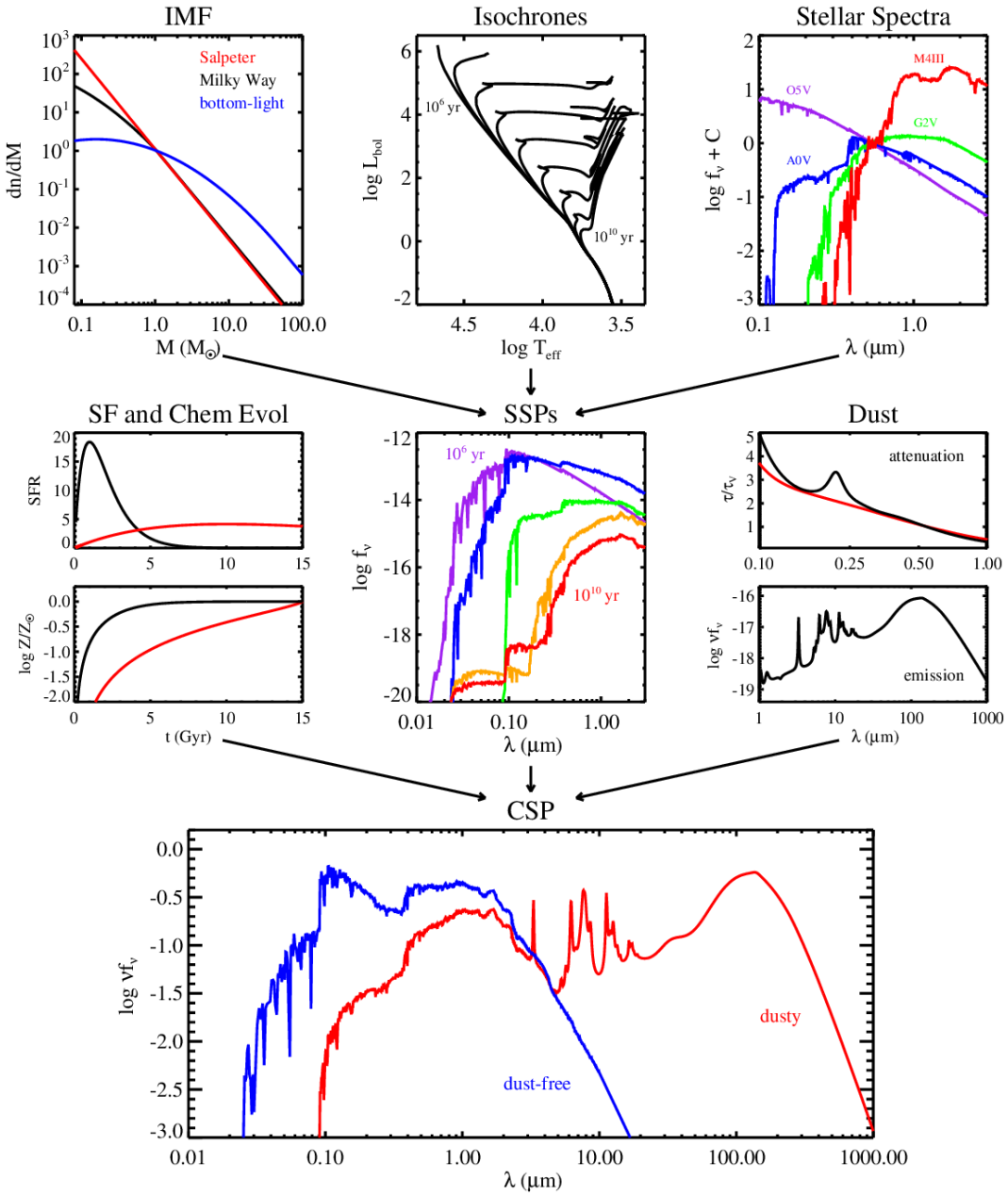

Figure 1.2: Overview of the stellar population synthesis (SPS) technique. The upper panels highlight the ingredients necessary for constructing simple stellar populations (SSPs): an initial mass function (IMF), isochrones, and stellar spectra. The middle panels highlight the ingredients necessary for constructing composite stellar populations (CSPs): star formation histories (SFHs), chemical evolution, SSPs, and a model for dust attenuation and emission. The bottom row shows the final CSPs both before and after a dust model is applied. Reproduced from Conroy (2013).

and derive the physical properties of galaxies from their SEDs.

1.2.4 SED Fitting

SED fitting involves fitting template SEDs to observational data (photometric or spectroscopic) to estimate redshifts and physical properties of galaxies. The general procedure is as follows. First, a library of template SEDs is generated. The templates can be either empirical (Coleman et al., 1980; Kinney et al., 1996; Mannucci et al., 2001; Assef et al., 2010) or theoretical (Bruzual and Charlot, 2003; Conroy et al., 2009; Conroy and Gunn, 2010). With the latter, one typically starts from SSPs and then fits for varying SFHs, metallicities, dust attenuation, etc. Next, the templates are redshifted and then convolved and integrated with the filter transmission curves of a particular survey to produce expected fluxes (or magnitudes) at a given redshift. The observed fluxes O are compared to the expected fluxes E, and the best-fit redshift and best-fit template are usually found by minimising the chi-square statistic,

$$\chi^2 = \sum_{i=1}^{N} \left(\frac{O_i - bE_i}{\sigma_i} \right)^2 , \tag{1.27}$$

where σ_i is the error on the observed fluxes in filter i, and b is the scaling factor between the two sets of data.

The parameters of the best-fitting template can then be used to determine physical properties. One of the most important is stellar mass, which is computed by multiplying the observed luminosity L with the stellar mass-to-light ratio M/L. The M/L ratio is given by (Walcher et al., 2011):

$$\frac{M}{L_\lambda} = \frac{\int \psi(t)\ dt}{\int L_\lambda(t)\ T_\lambda(t)\ dt}, \tag{1.28}$$

where L_λ and T_λ are the luminosity of an SSP and the mean transmission of the ISM at a given wavelength, respectively.

SFRs can also be estimated with SED fitting. However, high-quality data are necessary to break the age-dust-metallicity degeneracy; otherwise, the SFRs can be unreliable. Also, the choice of model priors on the dust model and SFH library often imposes strong biases. For these reasons, SFRs are more commonly derived from monochromatic and hybrid indicators (see Kennicutt, 1998; Kennicutt and Evans, 2012, for reviews). Besides the already mentioned Hα nebular emission line,

there are many others like the 24µm luminosity, UV luminosity, total IR luminosity, radio continuum luminosity, and X-ray flux. The various indicators are sensitive to different SFR timescales.

Examples of well-established SED-fitting codes are `LEPHARE` (Arnouts et al., 1999), `HYPERZ` (Bolzonella et al., 2000), `BPZ` (Benítez, 2000), `CIGALE` (Burgarella et al., 2005; Noll et al., 2009; Boquien et al., 2019), `ZEBRA` (Feldmann et al., 2006), `EAZY` (Brammer et al., 2008), `FAST` (Kriek et al., 2009), and `MAGPHYS` (da Cunha et al., 2011).

1.2.5 Uncertainties, PDFs and Big Data

Out of all the physical properties estimated with SED fitting, stellar mass is the most robust (Papovich et al., 2001; Shapley et al., 2001; Wuyts et al., 2009; Muzzin et al., 2009; Lee et al., 2009). The M/L ratios for most galaxies with 'normal' SEDs are probably accurate to within ~ 0.3 dex, assuming a fixed IMF (Conroy, 2013). The uncertainty is primarily due to incorrect modelling of TP-AGB stars and assumptions about the SFH (Walcher et al., 2011). Also, the treatment of metallicity (often held fixed over the SFH) contributes. Between star-forming and quiescent galaxies, stellar masses of the former are considered to be less accurate. The primary reason is that young stars can outshine the older stellar population and thus obscure the total mass.

Ultimately, the accuracy of redshifts and physical properties estimated with SED fitting depends on the identification of the correct template SED. As such, the template library must be accurate and complete. However, this is unlikely to be the case when using empirical or theoretical spectral libraries. Empirical libraries are constructed from observations of stars in the solar neighbourhood, and as a result, they are likely incomplete. On the other hand, theoretical libraries are probably complete but not entirely accurate because while the theory of stellar evolution is advanced, short-lived and bright stellar phases such as massive stars, TP-AGB stars, extreme horizontal branch (EHB) stars, and blue stragglers are still not fully understood (Walcher et al., 2011).

Mismatches can also arise if the multi-dimensional parameter space is not exhaustively explored when generating templates from SSPs for different combinations of model parameters. Here, Markov Chain Monte Carlo (MCMC) techniques are

efficient (Conroy et al., 2009; Acquaviva et al., 2012). Furthermore, the templates are usually calibrated using galaxies at low redshifts, so there is greater uncertainty on predictions for galaxies at high redshifts (Carrasco Kind and Brunner, 2013).

Even a valid and representative template set does not guarantee accuracy because of the intrinsic degeneracies that exist in the colour–redshift and colour–physical properties spaces. The colour of a galaxy is related to the age and metallicity of its stellar population. For example, redder galaxies are either older, more metal-rich, or both. Moreover, a galaxy may appear red even though it is blue in reality because of dust extinction. This degeneracy in the colour-age-dust-metallicity space means that two or more templates can match the same input colours.

Given the possibility of multi-modal solutions, the standard approach of assuming Gaussian uncertainties is flawed. Hence, the new generation of SED-fitting codes such as `GALMC` (Acquaviva et al., 2011), `BAYESed` (Han and Han, 2012, 2014, 2019), `BEAGLE` (Chevallard and Charlot, 2016), `PROSPECTOR` (Leja et al., 2017; Johnson et al., 2021), and `BAGPIPES` (Carnall et al., 2018) have moved beyond a single-point estimate and a Gaussian error to output probability distribution functions (PDFs). These PDFs fully characterise uncertainties, which translates to more accurate analyses. For example, using PDFs rather than point estimates of redshift has been shown to improve the accuracy of cosmological measurements (Mandelbaum et al., 2008; Myers et al., 2009; Sheldon et al., 2012; Carnero et al., 2012; Jee et al., 2013) without introducing further bias (Bordoloi et al., 2010; Abrahamse et al., 2011). The issue is that it is not feasible to obtain PDFs for a large number of galaxies. For example, `BAGPIPES` takes on average a few minutes to fit each galaxy, making it impractical to fit modern datasets where sample numbers can exceed hundreds of millions. And the situation becomes worse now in the era of "Big Data" when surveys such as Euclid, LSST, and Roman are primed to observe galaxies in the billions. Another separate but equally important challenge is storing and sharing the PDFs (Rau et al., 2015). In this thesis, machine learning (ML) is applied to estimate PDFs of galaxy properties at speed and on the fly, culminating in a highly intuitive and efficient Python package called `GALPRO`.

1.3 The Galaxy Population

This section describes the galaxy population and discusses the implications for how galaxies have formed and evolved based on the observations. First, the salient properties of the population are presented. Next, the correlations between galaxy properties and environment are outlined. Following on, the population as observed at high redshift and its subsequent evolution is described. Lastly, the nature versus nurture debate in the context of galaxy formation and evolution is summarised.

1.3.1 Physical Properties

Galaxies are richly diverse, and one of the most striking properties is their shape or morphology. There are four broad types:

1. *Ellipticals (E)*: ellipsoidal-shaped galaxies with little to no internal structure, supported by the random motion of their stars. Elliptical galaxies are further categorised based on their apparent degree of ellipticity, ranging from highly spherical E0s to flat E7s.

2. *Spirals (S)*: thin, disk-like galaxies with spiral arm structures and a central bulge, mainly supported by rotation. Spiral galaxies come in two types: normal (S) and barred (SB). The latter exhibit an elongated bar-like structure in the central region. Each type is further split into three classes—a, b, and c—according to the following criteria: the brightness of the central bulge, the tightness of the spiral arms, and the degree to which the spiral arms are resolved into stars, HII regions, and ordered dust lanes.

3. *Lenticulars (S0)*: thin, disk-like galaxies with a central bulge like spirals (though more prominent) but a smooth light distribution and no spiral arms like ellipticals. An intermediate class between the two types.

4. *Irregulars (Irr)*: galaxies with no defined shape or structure.

The different morphological types are arranged in the famous Hubble sequence (Hubble, 1936) shown in Figure 1.3, with the ellipticals on the left, lenticulars in the centre, and spirals on the right. Notably, irregular galaxies are missing in the original Hubble sequence, but they are now included as they are considered to be perturbed spiral galaxies (Mo et al., 2010). Ellipticals and lenticulars are referred

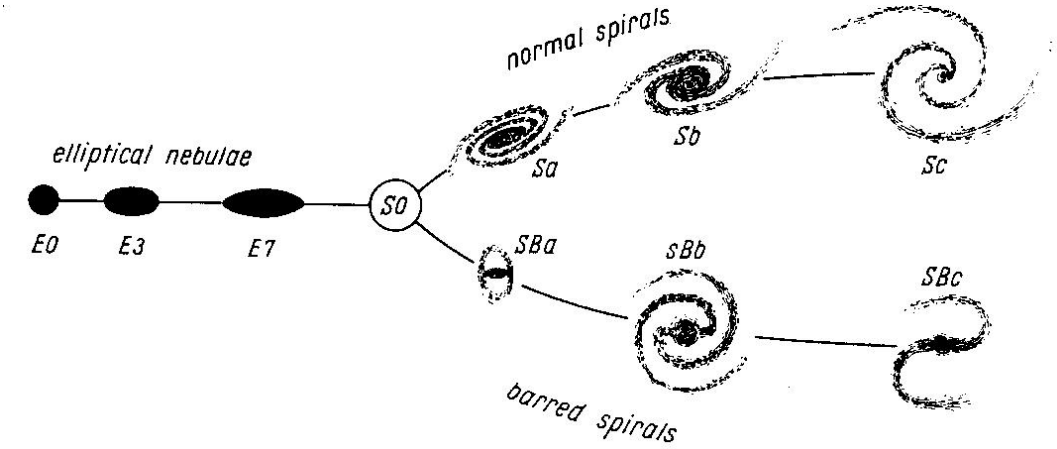

Figure 1.3: Tuning-fork style diagram of the Hubble sequence (Hubble, 1936). The visual classification scheme designates galaxies into three Hubble types: ellipticals (E), lenticulars (S0), and spirals (S). The spirals are further separated into normal (S) and barred (SB). Note that the location of galaxies on the sequence does not indicate the temporal evolution of galaxies. Reproduced from Hubble (1936).

to as early-type galaxies, while spirals and irregulars are called late-type galaxies. Somewhat confusingly, the location of the galaxies on the Hubble sequence and the nomenclature do not relate to their temporal state. The galaxies are simply placed in order of structural complexity from left to right, and this is the connotation behind 'early' and 'late'. In other words, the Hubble sequence is not an evolutionary sequence of galaxies whereby structurally-simple ellipticals evolve into more complex spirals over time. In fact, the polar opposite is now believed to be true: galaxies form disk-like and then transform into elliptical-like over time. Consequently, the diagram may be read from right to left, with some debate over the placement of S0 galaxies (Kormendy and Bender, 1996).

The galaxy population is bimodal in colour (Strateva et al., 2001; Hogg et al., 2002, 2004; Blanton et al., 2003; Bell et al., 2004; Baldry et al., 2004b, 2006; Gallongo et al., 2005; Weiner et al., 2005; Willmer et al., 2006; Brammer et al., 2009). Specifically, most galaxies are either blue or red, according to Figure 1.4. In the colour distribution, there is a broad peak at the blue end of the spectrum and a narrow peak at the red end, so there are more blue galaxies than red. Furthermore, the blue galaxies are predominantly faint, while the majority of the red galaxies are bright, as evident from the colour–magnitude distribution. These two populations are dubbed the "blue sequence" (also known as the "blue cloud") and the "red sequence"

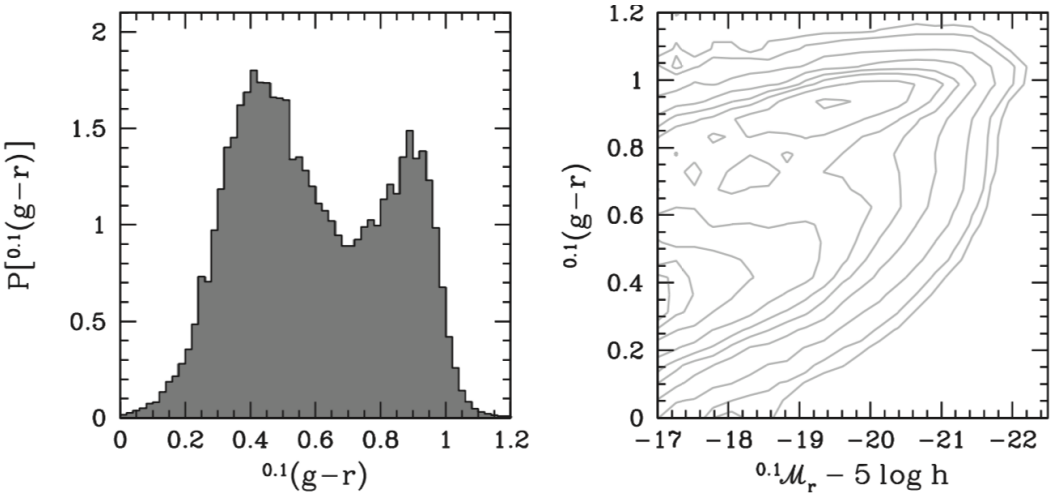

Figure 1.4: Distribution of galaxy colours and colour–magnitude relation of $\sim 365,000$ galaxies in the Sloan Digital Sky Survey (SDSS; York et al. 2000). The colour distribution is bimodal, with most galaxies being either blue or red. In the colour–magnitude diagram, the blue galaxies dominate the faint end, while the red galaxies the bright end. These two populations are dubbed the "blue sequence" (also known as the "blue cloud") and the "red sequence", respectively (Bell et al., 2004). The sparse population between the two is in the so-called "green valley" (Wyder et al., 2007; Martin et al., 2007; Salim et al., 2007; Schiminovich et al., 2007). Reproduced from Mo et al. (2010).

of galaxies, respectively (Bell et al., 2004). There is also a sparse population of galaxies between the two in the so-called "green valley" (Wyder et al., 2007; Martin et al., 2007; Salim et al., 2007; Schiminovich et al., 2007).

The morphology of a galaxy is correlated to its colour: early-type galaxies are redder than late-type galaxies, which are bluer (Humason, 1936; Holmberg, 1958; de Vaucouleurs, 1961; Roberts and Haynes, 1994). However, this relation is not perfect as a significant number of dusty red spirals (van den Bergh, 1976; Wolf et al., 2009; Masters et al., 2010) and blue ellipticals (Schawinski et al., 2009) have also been observed. Overall, late-type galaxies primarily populate the blue cloud, while early-type galaxies occupy the red sequence (see Figure 1.5).

The colour of a galaxy is determined by the age and metallicity of its stellar population. The most important are OB stars because they are very luminous and thus dominate the total light emitted. These hot, blue stars have a short lifespan, which means blue galaxies have ongoing or recent star formation, while red galaxies do not. Nevertheless, dust extinction complicates this basic picture (Whitaker et al., 2012; Taylor et al., 2015). In general, galaxies are either "star-forming" or "quenched".

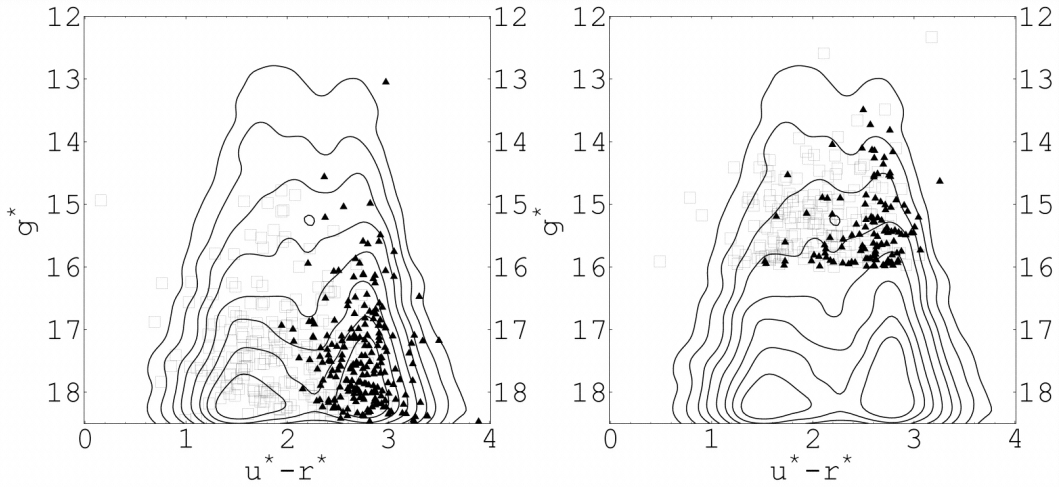

Figure 1.5: Colour distribution of SDSS galaxies overlaid with early versus late morphology type. The black triangles and open squares represent early-type and late-type galaxies, respectively. In the left panel, there are 500 galaxies, which are classified spectroscopically. In the right panel, there are 287 bright galaxies, which are classified by visual inspection. Reproduced from Strateva et al. (2001).

However, whether the SFR distribution is bimodal, like the colour distribution, is subject to debate (Elbaz et al., 2007; McGee et al., 2011; Feldmann, 2017).

The SFR of star-forming galaxies are tightly correlated with their stellar mass (see Figure 1.6). This relation is called the star-forming main sequence (MS; Brinchmann et al. 2004; Salim et al. 2007; Noeske et al. 2007; Daddi et al. 2007), and it exists at least up to $M_\star \sim 10^{10.5} M_\odot$, at which point some observational studies report a flattening (Whitaker et al., 2014; Lee et al., 2015; Schreiber et al., 2015; Tasca et al., 2015; Tomczak et al., 2016; Eales et al., 2017; Popesso et al., 2019).

In summary, galaxy properties are correlated with each other, and there are two distinct populations in the local Universe: one of massive, red, early-type, quiescent galaxies that constitute the red sequence, and the other of less-massive, blue, late-type, star-forming galaxies that occupy the blue cloud. The fundamental question is then: why is the population bimodal?

1.3.2 Environment and Correlations

In a ΛCDM universe, structures form bottom up in a hierarchical manner—starting with galaxies, which merge over time to form galaxy groups, which in turn merge to create clusters and superclusters. Hence, at the present time, a significant fraction of galaxies are located in groups and clusters, consisting of tens and upwards of

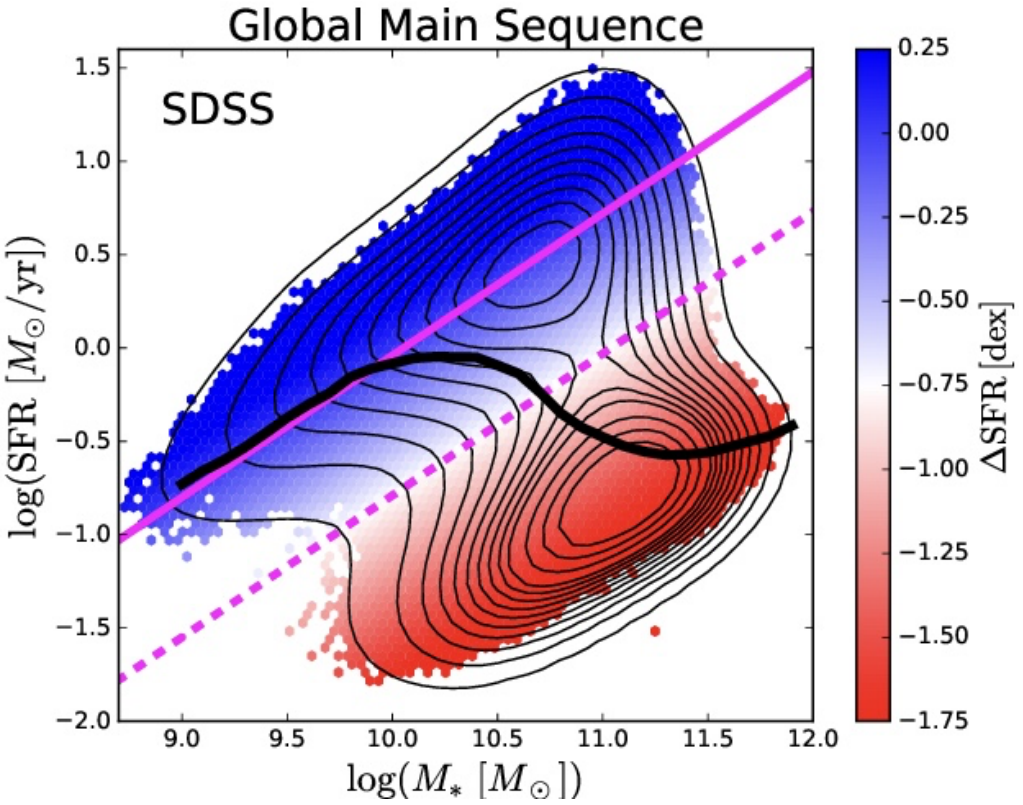

Figure 1.6: The star-formation rate (SFR)–stellar mass ($M_\star$) relation of SDSS galaxies. The galaxies separate into star-forming (upper contours) and quenched (lower contours). The star-forming main sequence (MS) fit to the star-forming galaxies is from Renzini and Peng (2015) and is shown as a solid magenta line. The minimum of the bimodal density contours is shown as a dashed magenta line. The plot is colour coded by the mean logarithmic distance to the MS. The solid black line indicates the median SFR $- M_\star$ relationship, which shows a rapid transition from the star forming to the quenched density peak at $\log(M_\star/M_\odot) \sim 10.5$. Adapted from Bluck et al. (2020a).

hundreds, respectively (Hubble and Humason, 1931; Shapley, 1933; Zwicky, 1937, 1938, 1952; Abell, 1958, 1965). Conversely, some galaxies are relatively isolated in the field. These galaxies were either part of fossil groups where all members eventually merged (Ponman et al., 1994; Jones et al., 2000, 2003) or have been isolated for their entire lifetime. On the largest scales, galaxies are part of a complex "cosmic web" (Bond et al., 1996), composed of voids, sheets or walls, filaments, and nodes (see Figure 1.7). Simply put, galaxies reside in different environments of varying densities. Significantly, the physical properties of a galaxy are correlated to its environment.

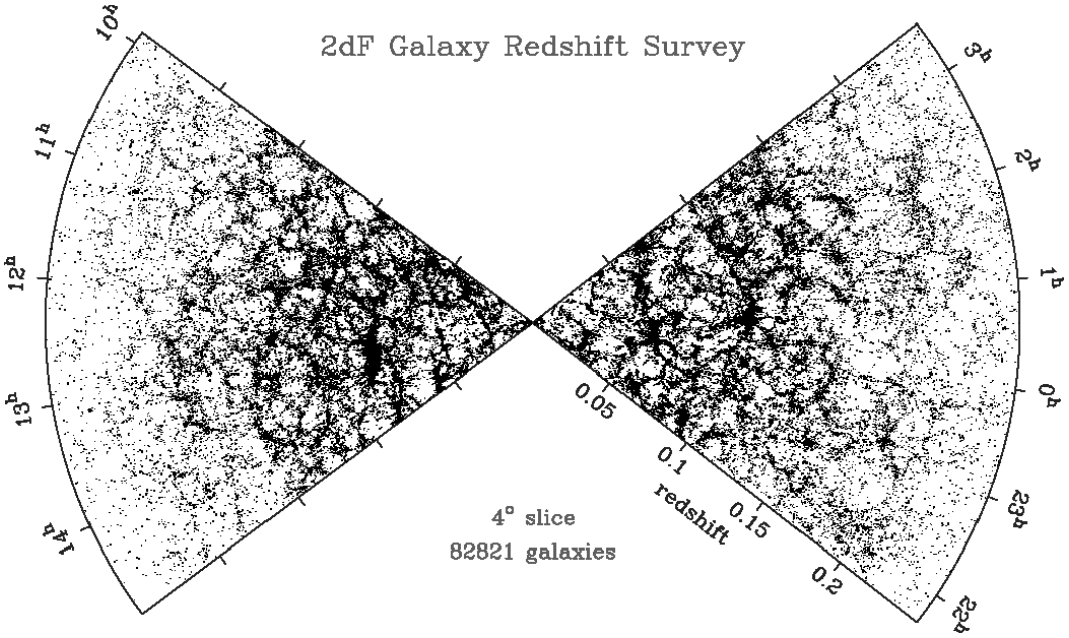

Figure 1.7: Spatial distribution of $\sim 80,000$ galaxies in the 2dF Galaxy Redshift Survey (2dFGRS; Colless et al. 2001) in a 4° slice projected onto the redshift/right ascension plane. The galaxies are not randomly distributed but are part of the cosmic web (Bond et al., 1996), consisting of voids, sheets or walls, filaments, and nodes. Reproduced from Peacock et al. (2002).

The morphology–density relation

The different morphological types are unevenly distributed in the Universe. Typically, early-type galaxies inhabit high-density environments, while late-type galaxies occupy low-density environments (Hubble and Humason, 1931; Abell, 1965; Oemler, 1974; Davis and Geller, 1976). According to the morphology–density relation (Dressler, 1980) in Figure 1.8, the fraction of spirals and irregulars decreases smoothly with increasing environmental density, from $\sim$ 60% in the highest-density region to $\sim$ 10% in the lowest-density region of clusters. Meanwhile, the trend is reversed for ellipticals, which increase from $\sim$ 10% to $\sim$ 40%. The portion of lenticulars also increases, but more modestly, from $\sim$ 30% to $\sim$ 50%.

The colour–density relation

Galaxy colour is also correlated with environment: the colour–density relation (Kodama et al., 2001). As environmental density increases, galaxies tend to become redder (see Figure 1.9).

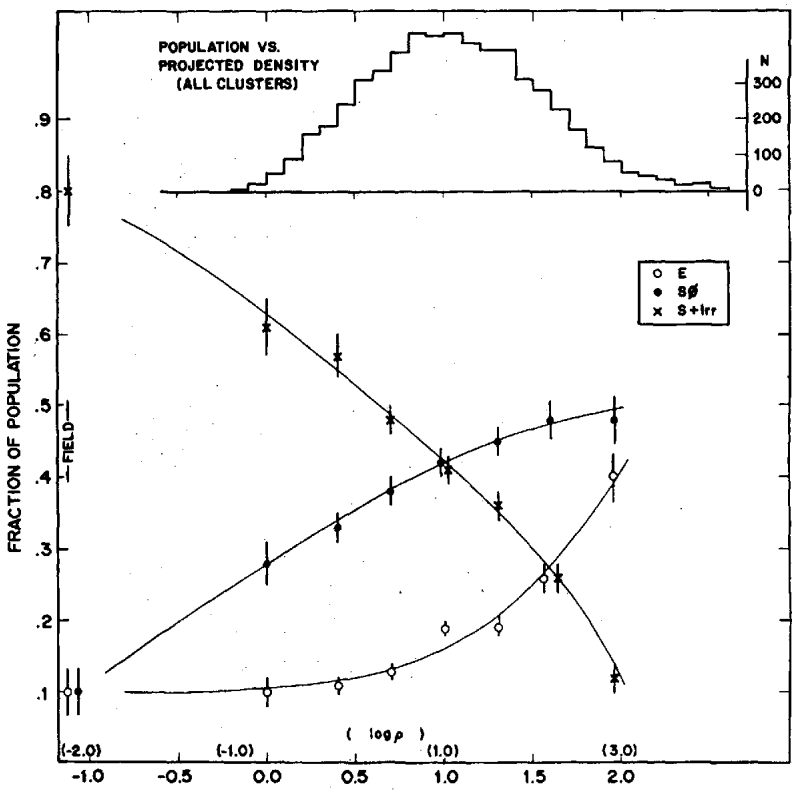

Figure 1.8: The morphology–density relation (Dressler, 1980). The fraction of ellipticals (E), lenticulars (S0), and spirals (S) and irregulars (Irr) as a function of environmental density (log of the projected density), in a sample of 55 rich clusters at $z \sim 0$. The fraction of the different morphological types in the field is also indicated for comparison. The upper panel shows the number of galaxies in each density bin. Reproduced from Dressler (1980).

The star-formation rate–density relation

Given the causal connection between colour and SFR and the colour–density relation, the SFR is also correlated with the galaxy environment. The SFR–density relation (Gómez et al., 2003) in Figure 1.10 shows that SFR decreases with increasing environmental density. This trend is particularly strong for highly star-forming galaxies in the 75th percentile of the SFR distribution (i.e., the top of the shaded area). Furthermore, there seems to be a characteristic density ($\sim 1\ h_{75}^{-2}\ \mathrm{Mpc}^{-2}$) at which the SFR increases (or decreases) rapidly.

In summary, galaxies become redder, form fewer stars, and exhibit more early-type morphologies as environmental density increases. Essentially, the red sequence of the galaxy population is mainly located in high-density environments, while the

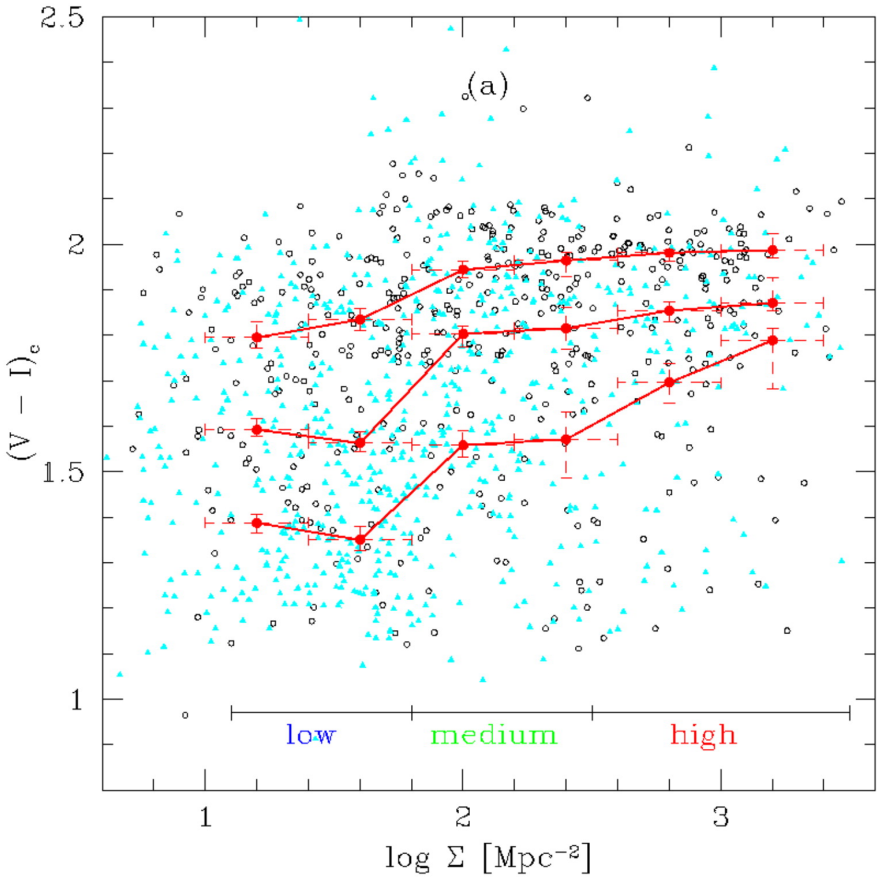

Figure 1.9: The colour–density relation (Kodama et al., 2001). The colour $(V-I)$ as a function of environmental density (10th nearest neighbour density) of galaxies brighter than $I = 23.4$ in the rich cluster $A851$ at $z = 0.41$. The open circles and filled triangles show the galaxies brighter or fainter than $I = 21.4$ $(M_v^\star + 2)$, respectively. The three red lines represent the loci of the 25th, 50th, and 75th percentile colours. Reproduced from Kodama et al. (2001).

blue sequence is found in low-density environments. So, is environment the cause of the bimodal population and are the correlations causal in nature? Also, which of the relations with environment are truly causal, and which are just a result of correlations that exist between galaxy properties? For example, Bamford et al. (2009) and Skibba et al. (2009) disentangled the influence of environment on colour and morphology and found that the colour–density relation is stronger than the morphology–density relation, so the latter may arise as a consequence of the former. There is potential evidence of the correlations being causal from observations of the galaxy population at high redshift.

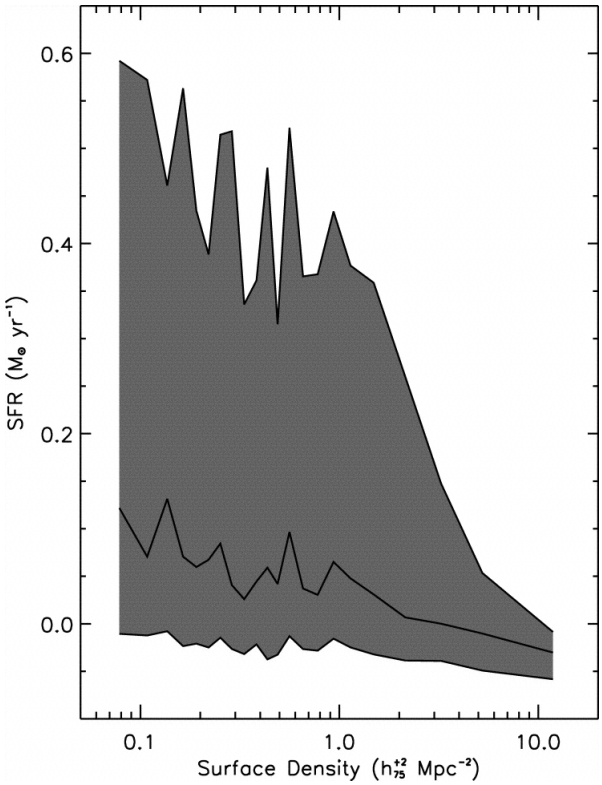

Figure 1.10: The star-formation rate (SFR)–density relation (Gómez et al., 2003). The SFRs of SDSS galaxies as a function of environmental density (10th nearest neighbour density). The shaded area represents the distribution of corrected SFRs (Hopkins et al., 2001). The median is the solid line, and the top and bottom are the 25th and 75th percentiles, respectively. There is an abrupt transition in the SFR at surface density $\sim 1\ h_{75}^{-2}$ Mpc^{-2}. Reproduced from Gómez et al. (2003).

1.3.3 High Redshift and Evolution

At high redshift ($z \gtrsim 0.5$), the fraction of lenticulars in clusters is significantly lower compared to the local Universe, while the spiral fraction is higher (Dressler et al., 1997; Treu et al., 2003; Postman et al., 2005; Guzzo et al., 2007). Tracing the population over time, the portion of lenticulars has increased gradually while that of spirals (and irregulars) has decreased, as shown in Figure 1.11 (Fasano et al., 2000; Smith et al., 2005; Desai et al., 2007; Capak et al., 2007; Just et al., 2010; Cavanagh et al., 2023). On the other hand, the fraction of ellipticals has remained roughly constant. This suggests that spiral galaxies are progenitors of lenticular galaxies and have evolved into the latter over time.

Also in distant clusters, the fraction of blue, star-forming galaxies is higher than in the local clusters (Butcher and Oemler, 1978; Couch and Newell, 1984): the

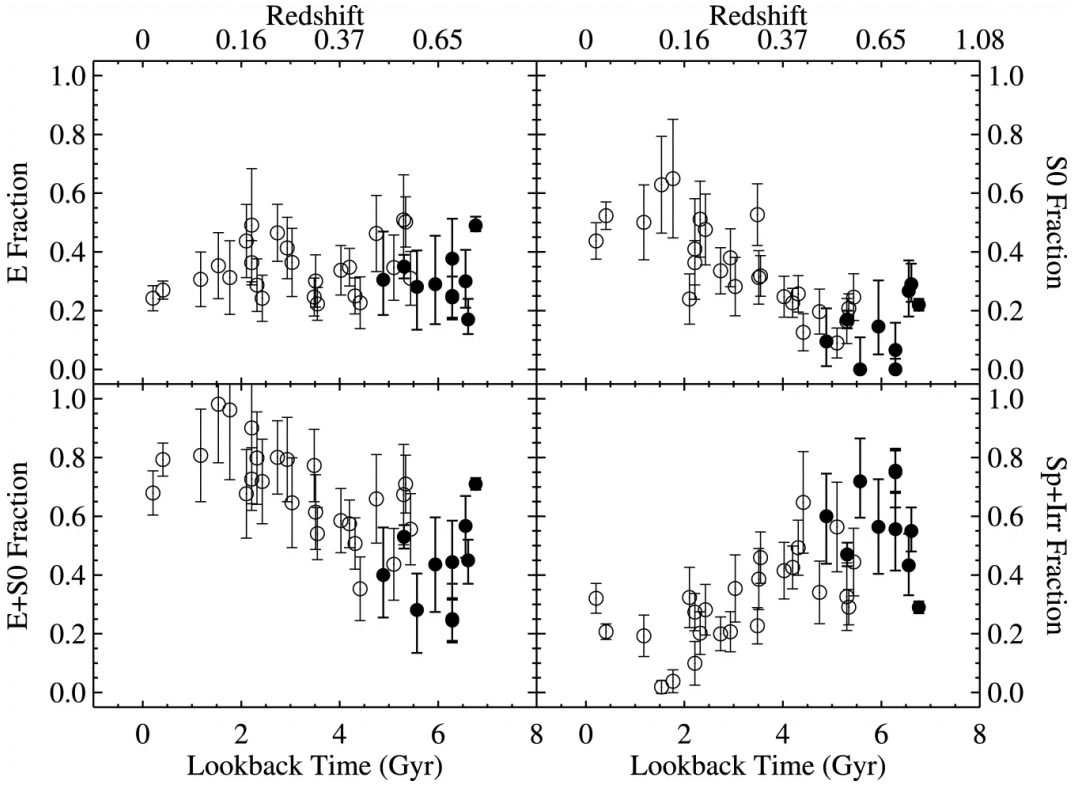

Figure 1.11: The fraction of ellipticals (E), lenticulars (S0), ellipticals and lenticulars (E + S0), and spirals and irregulars (Sp + Irr) in clusters over time. The open and filled circles denote clusters in the ESO Distant Cluster Survey (EDisCS; White et al. 2005) and Fasano et al. (2000), respectively. Reproduced from Desai et al. (2007).

Butcher-Oemler effect. As shown in Figure 1.12, the fraction increases with redshift (Butcher and Oemler, 1984; Aragon-Salamanca et al., 1993; Rakos and Schombert, 1996; Lubin, 1996; Margoniner and de Carvalho, 2000; Margoniner et al., 2001; Ellingson et al., 2001; Kodama and Bower, 2001; Poggianti et al., 2006; Cucciati et al., 2006; Cooper et al., 2007). Unsurprisingly, given the correlation between colour, SFR, and morphology, these galaxies are predominantly spirals (Dressler et al., 1994; Couch et al., 1994, 1998; Oemler et al., 1997). Furthermore, a significant fraction have perturbed morphologies, which further supports the case for the morphological transformation of galaxies.

Lastly, galaxies with strong Balmer lines in absorption but no detectable emission lines have been observed in distant clusters (Dressler and Gunn, 1983; Couch and Sharples, 1987). The absence of emission lines means these galaxies have little to no ongoing star formation, and the presence of strong Balmer absorption lines indicates an excessive population of A-stars, which implies that they had elevated

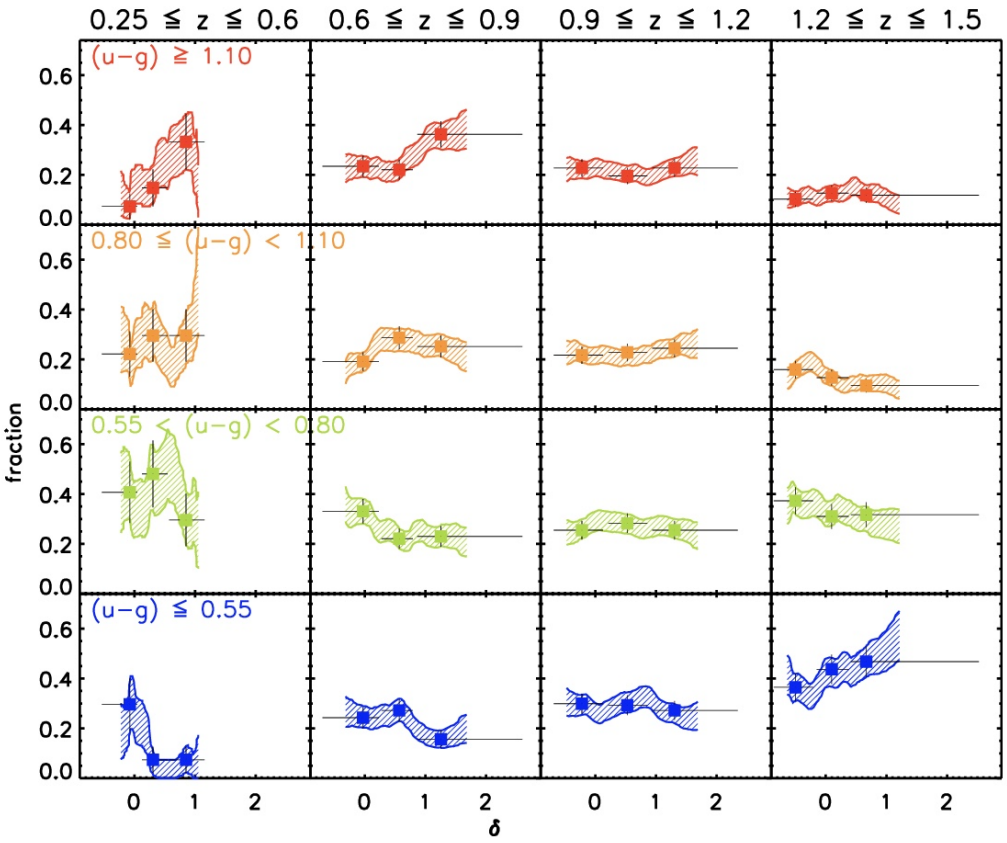

Figure 1.12: The fraction of galaxies with luminosities greater than $(M_B - 5\log h) < -20$ in four rest-frame colour bins as a function of environment (δ on $R = 5h^{-1}$Mpc) in four different redshift intervals. The horizontal bars indicate the amplitude of the bins in δ (i.e., the range spanned by the lower 5% and upper 95% percentile of the objected contained in each bin), while the vertical error bars represent a Poissonian 1σ uncertainty. The shaded areas are obtained by smoothing the red (blue) fraction with an adaptive sliding box containing the same number of objects in each bin as the point marked explicitly. Reproduced from Cucciati et al. (2006).

levels of star formation in the past and have recently quenched in the last $1 - 2$ Gyrs. These post-starburst (PSB, also known as E+A or K+A; see French, 2021, for a review) galaxies at high redshift ($z > 1$) are spheroidally dominated (Whitaker et al., 2012; Yano et al., 2016; Almaini et al., 2017; Maltby et al., 2018). For all these reasons, PSBs are likely galaxies transitioning from the blue cloud to the red sequence (Caldwell et al., 1996; Zabludoff et al., 1996; Norton et al., 2001; Yang et al., 2004, 2008; Pracy et al., 2009; Zwaan et al., 2013; Yesuf et al., 2014; Wu et al., 2014; Pattarakijwanich et al., 2016). Note that PSBs have also been found in the field (Tran et al., 2004), but they are more prevalent in denser environments (Dressler et al., 1999; Poggianti et al., 2009; Vergani et al., 2010; Muzzin et al., 2012;

Socolovsky et al., 2018; Paccagnella et al., 2019; Taylor et al., 2023), with some studies reporting a significant fraction of the galaxy population in clusters (Henry and Lavery, 1987; Fabricant et al., 1991; Tran et al., 2003, 2007).

In conclusion, galaxies have undergone rapid evolution in dense environments whereby blue, star-forming, late-type galaxies at high redshifts have transformed into red-and-dead early-type galaxies at low redshifts. On this basis, environment does seem responsible for the bimodal population in the local Universe, and if so, the correlations are causal. However, one has to be careful because the same correlations between galaxy properties and environment also exist with stellar mass, as massive galaxies are likely to be early types, red, and quenched (Kauffmann et al., 2004; Baldry et al., 2006; Fontana et al., 2009; van Dokkum et al., 2009; Peng et al., 2010; Nayyeri et al., 2014). Furthermore, stellar mass is correlated with environment (Balogh et al., 2001; Hogg et al., 2003; Mo et al., 2004; Croton et al., 2005; Hoyle et al., 2005; Blanton et al., 2005). Consequently, are the correlations with environment mere reflections, and is the observed evolution due to internal processes that scale with stellar mass rather than external processes associated with environment? This is the essence of the nature versus nurture debate in the context of galaxy formation and evolution (Irwin, 1995).

1.3.4 Nature versus Nurture

Galaxies form and evolve as: (i) hot gas cools through radiative cooling, (ii) stars form out of the cold gas, evolve, and eventually die—in a cycle—enriching the ISM in the process, and (iii) SMBHs grow via accretion and mergers and their feedback heats and/or expels the gas. Simultaneously, haloes are accreting matter from their surroundings and merging with their neighbours. In a nutshell, the formation and evolution of galaxies depends on both nature and nurture.

The nature of a galaxy can be associated with its halo mass since galaxies form in dark matter haloes, while nurture is related to its environment. There is complex interplay between nature and nurture as haloes and their environments interact with each other through the processes of accretion and mergers and co-evolve over time. Furthermore, the effects of nature depend on nurture and vice versa, as internal processes driven by halo mass are affected by environment, and external processes linked to environment depend on halo mass. In summary, nature and nurture are

heavily intertwined.

To disentangle nurture from nature, studies have controlled for the stellar mass (a proxy of halo mass) at a snapshot in time, typically by binning galaxies into fixed bins of stellar mass. Nevertheless, this has been demonstrated to be insufficient in disentangling nature and nurture (De Lucia et al., 2012). The problem remains unsolved and therefore, the individual causal effects of nature and nurture on galaxy formation and evolution are unknown.

The principal approach to establish causality has been through simulations. Physical models have been developed and tested by comparing simulations to observations, leading to insights into the galaxy formation and evolution process. Nonetheless, the causal effect itself is intractable in a simulation of any meaningful complexity. A method called genetic modification (GM; Roth et al. 2016) has emerged that estimates the causal effect through controlled experiments (Cadiou et al., 2021), mimicking in effect, a randomised control trial (RCT). However, it is limited to a single object (at a time) and clearly cannot be applied to the real Universe.

In this thesis, the causal inference framework is adopted to infer causality. Specifically, causal inference is combined with ML, and causal machine learning (causal ML) is applied to disentangle nature and nurture and estimate the causal effect of environment on galaxies.

1.4 Thesis Outline

The outline of this thesis is as follows:

Chapter 2 briefly overviews machine learning (ML) and describes random forests (RFs), an ensemble learning method based on decision trees (DTs) that is utilised in this thesis.

Chapter 3 introduces the causal inference framework and core concepts, such as causal models and causal graphs. Additionally, this chapter presents the emerging field of causal machine learning (causal ML), which combines causal inference and ML.

In Chapter 4, ML is applied to estimate galaxy properties. Specifically, a novel method based on the RF algorithm is developed to estimate joint probability distribution functions (PDFs). As an example, joint redshift–stellar mass PDFs are estimated. The outcome of this work is `GALPRO`—a highly intuitive and efficient Python package that rapidly generates multivariate PDFs on the fly. Appendix A provides the documentation for the package.

In Chapter 5, causal ML is applied to disentangle nature and nurture and estimate the causal effect of environment on star-formation rate (SFR). To achieve this, the causal inference method, inverse probability weighting (IPW) of marginal structural models (MSMs), is combined with the RF algorithm.

Finally, Chapter 6 provides a summary of this thesis and discusses potential future prospects.

This thesis is based on the following papers, together with ongoing work:

- **Mucesh, S.**, Hartley, W. G., Palmese, A., Lahav, O., Whiteway, L., Bluck, A. F. L., ... & (DES Collaboration). (2021). A machine learning approach to galaxy properties: joint redshift–stellar mass probability distributions with Random Forest. *Monthly Notices of the Royal Astronomical Society*, 502(2), 2770-2786. (Chapters 2 and 4)

- **Mucesh, S.**, Hartley, W. G., Gilligan-Lee, C. M., & Lahav, O. (in prep). The Causal Effect of Environment on Star Formation with Causal Machine Learning. (Chapters 3 and 5)

Other papers contributed to but not covered in this thesis:

- Palmese, A., Bom, C. R., **Mucesh, S.**, & Hartley, W. G. (2023). A Standard Siren Measurement of the Hubble Constant Using Gravitational-wave Events from the First Three LIGO/Virgo Observing Runs and the DESI Legacy Survey. *The Astrophysical Journal*, 943(1), 56.

- Zacharegkas, G., Chang, C., Prat, J., **Mucesh, S.**, Hartley, W. G., Pandey, S., Ferrero, I., Blazek, J., Jain, B., Crocce, M., DeRose, J., Palmese, A., Seitz, S., Sheldon, E., Wechsler, R. H., Dodelson, S., Fosalba, P., Krause, E., Park, Y., Sánchez, C., ... & (DES Collaboration). (in prep). Constraining the Stellar-mass-to-halo-mass Relation with Galaxy Clustering and Weak Lensing from DES Year 3 Data.

Chapter 2

Machine Learning

This Chapter is based on a section in *Mucesh et al. (2021)*: A machine learning approach to galaxy properties: joint redshift–stellar mass probability distributions with Random Forest. *Monthly Notices of the Royal Astronomical Society*, 502(2), 2770-2786. It has been modified and augmented for the thesis.

Machine learning (ML) is concerned with the development of computer algorithms that can 'learn' from data to make predictions or decisions without being explicitly programmed to do so. It is a subset of the broader field of artificial intelligence (AI). In general, there are three types of learning paradigms:

- *Supervised learning* – the training set consists of input features X and target variables Y. The goal is to learn a mapping $X \to Y$ between the two sets of data. The most common types of supervised learning tasks are classification and regression.

- *Unsupervised learning* – the training set consists of input features but no targets. The goal is to learn some kind of structure of the underlying distribution of data (e.g., model the distribution itself, identify clusters/modes, identify anomalies, learn the underlying lower-dimensional manifold where the data live).

- *Reinforcement learning* – there is no training set. The goal is to interact with a dynamic environment and learn from feedback to achieve a predefined goal (e.g., driving a car).

The first application of ML was to teach a computer to play the game of checkers—Arthur Samuel's checkers-playing program (Samuel, 1959). Since then, ML has been applied to solve a wide range of problems across many fields. In astrophysics, the application of ML began as early as the 1990s with the use of artificial neural networks (ANNs) for star–galaxy separation (e.g., Odewahn et al., 1992) and morphological classification of galaxies (e.g., Storrie-Lombardi et al., 1992; Lahav et al., 1995). With the advent of large-scale surveys such as the Sloan Digital Sky Survey (SDSS; York et al. 2000) and more recently the Dark Energy Survey (DES; The Dark Energy Survey Collaboration 2005; The Dark Energy Survey Collaboration et al. 2016; Lahav et al. 2020), ML algorithms have been widely adopted to cope with the enormous influx of data and to do novel science (see Baron, 2019; Fluke and Jacobs, 2020, for recent reviews). This trend is likely to continue with the next generation of surveys, such as Euclid (Laureijs et al., 2011), the Rubin Observatory Legacy Survey of Space and Time (LSST; LSST Science Collaboration et al. 2009), and the Nancy Grace Roman Space Telescope (Roman; Spergel et al. 2015), as they will produce an order of magnitude more data than the previous. This chapter

describes decision trees and the ensemble learning method based on them: random forests.

2.1 Decision Trees

Decision trees (DTs) are a non-parametric supervised learning method. A decision tree is a type of data structure that allows one to make a decision using a series of yes-or-no questions. There are many different decision tree algorithms, but the most notable are ID3 (Quinlan, 1986), C4.5 (Quinlan, 1993), and Classification and Regression Trees (CART; Breiman et al. 1984). In the following section, the CART algorithm is explained.

2.1.1 Classification and Regression Trees

CART is a recursive algorithm that splits the data into two groups at each step until some predefined condition is achieved. The main components of the decision tree are the root, decision, and leaf nodes. The root node defines the first and optimal split on the full training dataset. The decision nodes describe the subsequent splits, and the leaf nodes contain the final groups. An illustration of a decision tree is shown in Figure 2.1.

The exact process of building a decision tree is as follows. At each step, all possible splits are evaluated in all dimensions of the input feature space. For classification, the data are split to best separate different classes, and this is achieved by maximising the information gain,

$$IG(D, X) = I(D) - \frac{N_L}{N} I(D_L) - \frac{N_R}{N} I(D_R), \tag{2.1}$$

where X is the input feature, D is the parent node containing number of samples N, and D_L and D_R are the child nodes containing number of samples N_L and N_R, respectively.

There are three commonly used criteria for the impurity I: the Shannon entropy (also called the information entropy; Shannon 1948),

$$H = -\sum_{k=1}^{K} p_k \log_2(p_k), \tag{2.2}$$

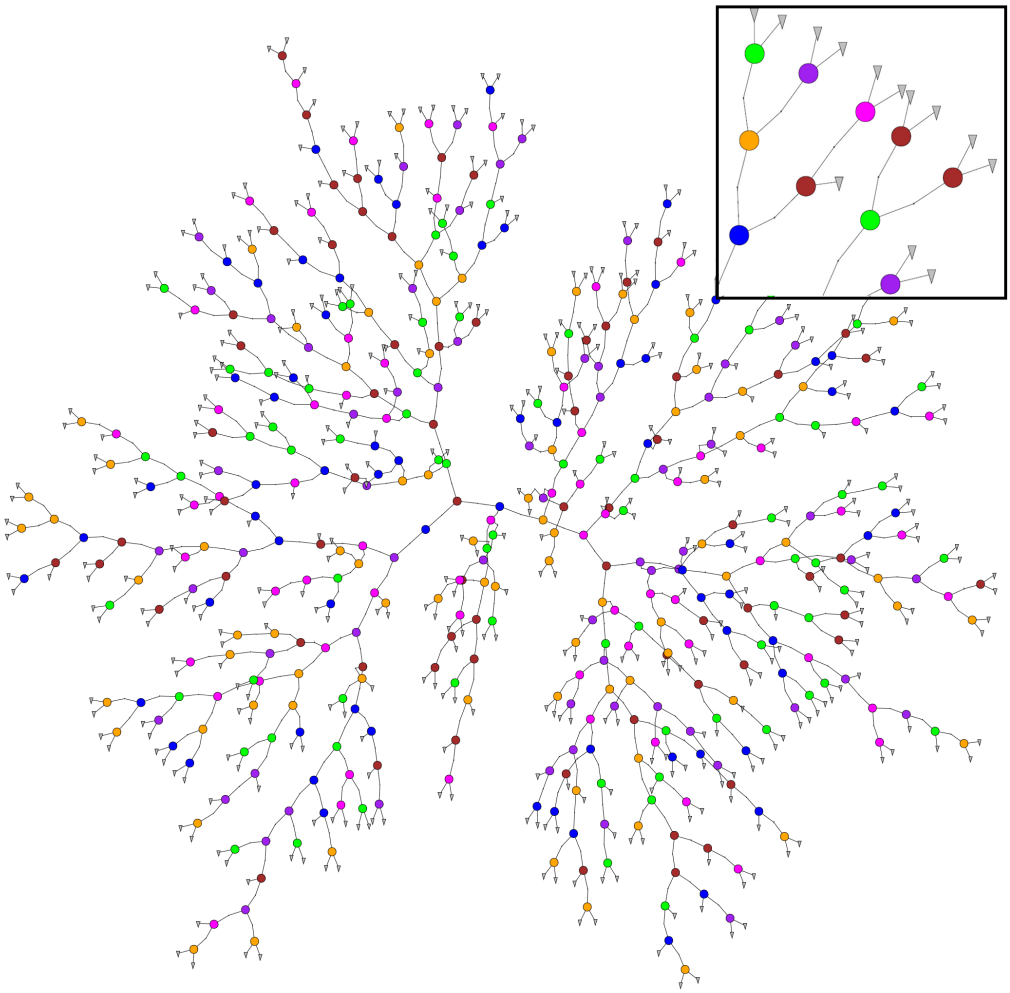

Figure 2.1: Binary decision tree in a radial layout, spanning out from the root node close to the centre. The root and decision nodes are represented as circles, and the leaf nodes are grey triangles. The colour of the root and decision nodes identifies the unique variable on which data is split. The subpanel shows a zoomed in region from the tree. Reproduced from Carrasco Kind and Brunner (2013).

the Gini coefficient (also known as the Gini index or Gini ratio; Gini 1912),

$$G = 1 - \sum_{k=1}^{K} p_k^2, \tag{2.3}$$

and the classification error,

$$C_E = 1 - \max\{p_k\}, \tag{2.4}$$

where p_k is the proportion of samples of class k in a node. The Shannon entropy and Gini coefficient are zero when a node is 'pure' (i.e., all samples belong to the same class) and one when the node is 'balanced' (i.e., there is an even representation of all classes).

For regression, the data are split such that the average values of the target variable are representative of the nodes. Usually, this is accomplished by minimising the sum of squared errors,

$$SSE = \frac{1}{N_L} \sum_{i \epsilon D_L} (\tilde{y}_i - \bar{y}_{D_L})^2 + \frac{1}{N_R} \sum_{i \epsilon D_R} (\tilde{y}_i - \bar{y}_{D_R})^2, \tag{2.5}$$

where $\tilde{y}_i$ are the values of the target variable of samples in a node, and $\bar{y}_{D_L}$ and $\bar{y}_{D_R}$ are the node means of the target variable.

Once the decision tree is built ('trained'), it can be used to make predictions. If the training data used to build the tree are complete and representative, then a new datapoint will end up in a leaf node that is representative of itself. The content of the leaf node can then be used to make a prediction. For classification, the prediction is the mode, and for regression, it is the mean of the leaf node.

Decision trees are easy to interpret and understand. Their "white box" nature combined with the simplicity of the algorithm makes it one of the most popular learning mechanisms. However, there are a few major limitations. Decision trees are not stable due to the manner in which they are constructed. For example, two decision trees can predict different outcomes with only a slight variation in the training data (Gareth et al., 2013). Also, axis-parallel splits may not always effectively (and efficiently) capture decision boundaries, leading to suboptimal performance. Furthermore, decision trees are prone to overfitting and thus do not generalise well to new, unseen data. This problem can be mitigated by reducing the complexity of

trees with "pruning" (i.e., removing redundant parts of the tree). However, a more encompassing yet simple solution is to combine multiple decision trees—the basis of ensemble methods such as random forests.

2.2 Random Forests

Random forests (RFs) are a supervised learning method based on ensemble learning. The first RF algorithm was proposed by Ho (1995), but the de facto is that of Breiman (2001). RFs solve many of the issues associated with decision trees by constructing multiple decision trees and making a few adjustments. For example, when building the decision trees, only a subset of the training data and features is used. This technique is called feature bagging and it injects randomness, making RFs more flexible and better suited to make predictions on data not encountered before. By using multiple decision trees in combination with feature bagging, RFs aim to preserve the low bias of a single decision tree whilst simultaneously reducing variance to successfully navigate the bias-variance tradeoff[1]. In summary, a RF can be built using the following process:

1. Create a bootstrapped dataset by sampling randomly from the training data with replacement.

2. Choose from a random subset of input features to split on at each node when building a decision tree using the bootstrapped data.

3. Repeat the process to build multiple decision trees, thus creating a 'forest'.

The process of predicting with a RF is similar to predicting with a single decision tree. The only difference is that predictions from all the decision trees are aggregated. For classification, the prediction is the most predicted class, and for regression, it is the mean of all the values predicted by the decision trees (see Figure 2.2).

[1]The bias error is an error from erroneous assumptions in the learning process. A high-bias model is an oversimplified model that fails to capture the true relationship between the input features and the target variable (underfitting). It performs poorly both on the training and test sets. The variance is an error from sensitivity to small fluctuations in the training data. A high-variance model captures noise rather than the underlying patterns (overfitting). Such a model performs well on the training data but poorly on unseen data because it fails to generalise. Reducing bias often increases variance and vice versa, i.e., the bias-variance tradeoff. The goal is to strike a balance between the two.

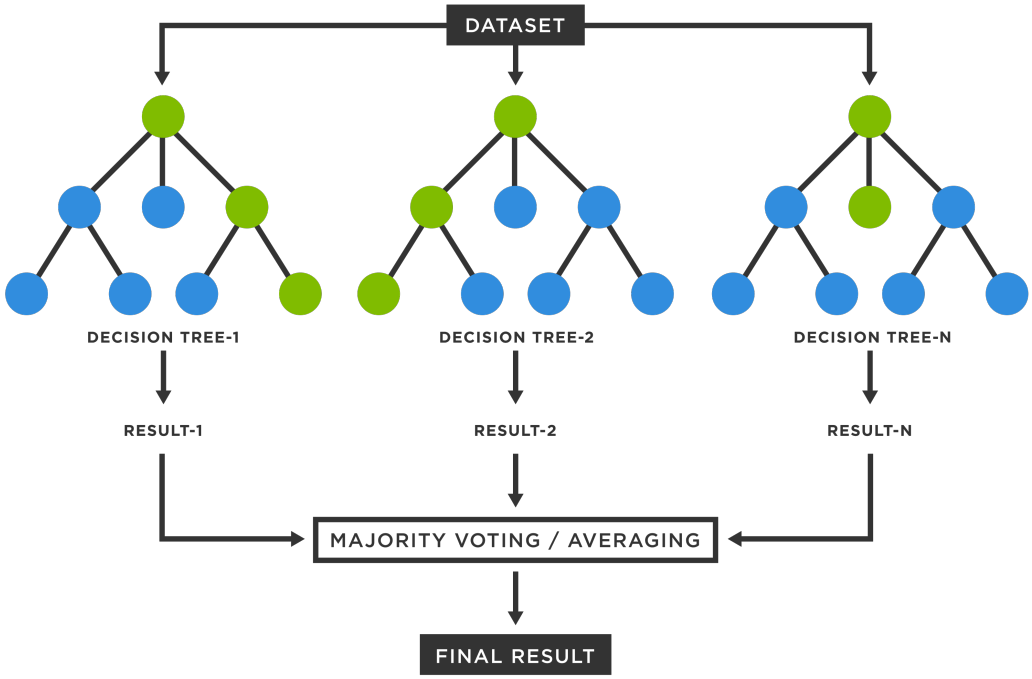

Figure 2.2: Overview of the random forest (RF) prediction process. The predictions of all N decision trees are aggregated in a final result. For classification, the final prediction is the mode, and for regression, it is the average. Adapted from https://www.spotfire.com/glossary/what-is-a-random-forest.

2.2.1 Hyperparameters

Hyperparameters are parameters of an ML algorithm that control the learning process and are specified prior to training. RFs have many hyperparameters, but the most important are:

- `n_estimators` – the number of decision trees used to build the RF determines its effectiveness. Each decision tree is built using a subset of training data. As a result, if the number used is too small, the likelihood of complete coverage of the training data decreases, resulting in poor performance. The performance improves as the number of trees increases, but at a cost, the time taken for training. The key is to find the right balance between performance and training time because the gains become negligible after a certain point.

- `max_features` – the maximum number of features considered at each step when building the decision trees controls the correlation between them and, hence, the flexibility of the RF. Usually, $\sqrt{N}$ features are sufficient to build each decision tree, where N is the total number of input features.

- `max_depth` – the maximum depth defines the number of levels in the decision tree and thus determines how finely or coarsely the training data are grouped. A low depth leads to underfitting, while a high depth may cause overfitting. In essence, the maximum depth provides a stopping criterion for the constituent decision trees. The minimum number of training samples in a leaf node (`min_samples_leaf`) and the minimum number of training samples in a leaf node before the data are split (`min_samples_split`) also serve the same purpose.

Generally, RFs require very little configuration and work well out of the box. Besides their ease of use, RFs are efficient, interpretable, and versatile, performing competitively in many tasks across various fields. Given all these qualities, the algorithm is utilised in this thesis. In Chapter 4, RF is applied to predict redshifts and stellar masses of galaxies. While ML can make predictions, it generally cannot perform inference. This is because ML, broadly, learns the data not the underlying data-generating process (DGP). In the following chapter, a theoretical framework is introduced for inferring causality.

Chapter 3

Causal Inference

This Chapter is based on a section in *Mucesh et al. (in prep)*: The Causal Effect of Environment on Star Formation with Causal Machine Learning. It has been modified and augmented for the thesis.

Causal inference is concerned with inferring cause and effect (see Pearl, 2009a, for an overview). The field is well established, with significant advancements made in recent decades (see Pearl, 2010, for a review). The goal is to identify and quantify the causal effect of one thing on another, e.g., a vaccine on a disease. A correlation[1] between the vaccine and outcome (disease cured or not) hints at its effectiveness but does not guarantee it as "correlation does not imply causation". The observed correlation can be due to a common cause (Reichenbach, 1956) that causes both the vaccine and outcome. For example, age is a potential common cause as it typically influences whether an individual can receive a vaccine and their chance of recovery from a disease. In the extreme case, there may not be a causal connection between the vaccine and outcome, and the correlation may be entirely due to age, which would signify that the vaccine is ineffective. However, if the vaccine has a causal effect on the outcome, the correlation will be partly due to age and the vaccine. Regardless of the situation, the measured effectiveness of the vaccine without considering age will be biased. Herein lies the fundamental difference between statistical and causal inference: the former ascertains a relationship between two quantities (assuming one exists), while the latter can establish the causal nature of the relationship. This chapter describes a mathematical framework of causal inference and key tenets, such as causal models and causal graphs.

3.1 Causal Models and Graphs

The principal component for any causal inference task is a causal model or structural causal model (SCM), i.e., a model that describes causal relationships between variables. Formally, an SCM specifies a set of exogenous, or latent, variables $U = \{u_1, \ldots, u_n\}$ distributed as $P(U)$, a set of endogenous, or observable, variables $V = \{v_1, \ldots, v_m\}$, a directed acyclic graph (DAG), called the causal structure of the model, whose nodes are the variables $U \cup V$, and a collection of functions $F = \{f_1, \ldots, f_n\}$, such that $v_i = f_i(PA_i, u_i)$, for $i = 1, \ldots, n$, where PA denotes the parent observed nodes of an observed variable (Pearl, 2009b). The collection of functions and distribution over latent variables induces a distribution over observable variables: $P(V = v) := \sum_{\{u_i | f_i(PA_i, u_i) = v_i\}} P(u_i)$. We can thus assign uncertainty

[1]Technically, "correlation" only refers to the degree to which a pair of variables are linearly related. Consequently, the broader term "association" is used instead to refer to statistical dependence because it describes any relationship between variables, linear or not.

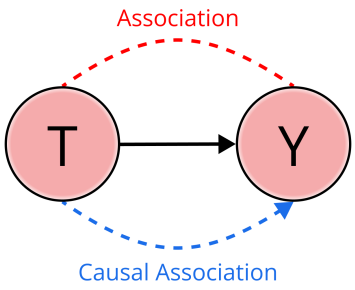

Figure 3.1: Causal graph representing the causal relationship between two variables, T and Y. The direct edge (black arrow) from T to Y implies that T directly causes Y. The causal association (i.e., the association due to causation) 'flows' asymmetrically from T to Y (represented by the blue dashed line arrow), while association 'flows' symmetrically (represented by the red dashed line). The causal graph is an example of a directed acyclic graph (DAG). A DAG is a graph that is: (i) directed (i.e., has edges that imply a direction) and (ii) acyclic (i.e., a variable does not cause itself either directly or through another variable).

over observable variables despite the fact the underlying dynamics are deterministic.

Structural equations (F) fully capture and mathematically describe a causal model. However, a graphical representation of a causal model in the form of causal graphs (also called causal diagrams) is more intuitive for understanding causal relationships. A causal graph is a probabilistic graphical model and consists of a collection of nodes and edges that connect the nodes (Wright, 1921). The nodes represent variables, while the edges communicate the causes of the variables. Figure 3.1 shows the fundamental causal graph between two variables, T and Y. The direct edge (black arrow) from T to Y implies that T directly causes Y. The causal graph is an example of a DAG because it is: (i) directed (i.e., has edges that imply a direction) and (ii) acyclic (i.e., a variable does not cause itself either directly or through another variable).

DAGs make it easy to deduce if two variables share a causal or non-causal relationship. More importantly, they allow one to effortlessly conclude if association is causation with a few basic rules. For example, causal association (i.e., the association due to causation) can be imagined as 'flowing' asymmetrically along directed paths (a sequence of adjacent nodes with direct edges all in the same direction), while

association 'flowing' symmetrically along directed paths. In the DAG in Figure 3.1, the causal association flows in one direction from T to Y along the direct path (as shown by the blue dashed line arrow). However, the association flows in both directions along the same path (as shown by the red dashed line). Hence, association alone does not provide any information on the direction of causality. It does not distinguish between the following possible causal relationships between the two variables:

1. T causes Y (direct causation)
2. Y causes T (reverse causation)
3. T and Y share a common cause (common causation)
4. T and Y cause each other (cyclic causation)

Furthermore, it is also possible that T and Y are not related at all, and the association is spurious. Consequently, association does not imply causation. Nevertheless, the DAG in this instance conveys that all association is causal as there is only a solitary direct path between T and Y. If the DAG represents the true causal model of the vaccine–disease example, where T is the vaccine and Y is the outcome, the observed correlation does imply causation. The following section describes a framework for reasoning and quantifying causality.

3.2 Causal Framework

The Rubin causal model (Holland, 1986), also known as the Neyman–Rubin causal model (Neyman, 1923; Rubin 1974), is a mathematical framework of causal inference based on the idea of potential outcomes (see Yao et al., 2020, for a recent review). The framework is inspired by how humans reason about causality. We compare an outcome Y given an action T with the outcome under no action. If there is a difference in the two outcomes, we reason that the action has had a causal effect on the outcome. The individual causal effect (ICE) on a unit i,

$$\tau_i = Y_i(1) - Y_i(0), \tag{3.1}$$

where $Y_i(1)$ and $Y_i(0)$ are the two potential outcomes under action and no action, respectively. It is impossible to know both potential outcomes given that the two

potential realities, the one in which the action takes place and the other in which it does not, cannot be observed simultaneously. The potential outcome that is observed is "factual", whereas the unobserved potential outcome is "counterfactual". This dilemma is the "fundamental problem of causal inference" (Holland, 1986). The impossible nature of the task is the reason why causality is such a challenging subject to tackle. Nevertheless, it is possible to estimate rather than compute causal effects. Generally, it is difficult to accurately estimate unit-level causal effects, but it is feasible to reliably estimate an average of the causal effect within a population—the average causal effect (ACE; Holland 1986),

$$\tau = \mathbb{E}[\tau_i] = \mathbb{E}[Y_i(1) - Y_i(0)] = \mathbb{E}[Y_i(1)] - \mathbb{E}[Y_i(0)]. \tag{3.2}$$

We make the reader aware of the terminology we use throughout this thesis: the action T is the quantity we are interested in measuring the causal effect of, and the outcome Y is the quantity we want to measure the causal effect on. Furthermore, the action is sometimes referred to as an intervention, an exposure, or a treatment, depending on the scientific nature of the study. We will refer to the action as the treatment from hereon.

3.3 Causal Assumptions

Causal inference necessitates the following assumptions:

1. *Exchangeability* – the potential outcomes are independent of the treatment.

$$Y(t) \perp\!\!\!\perp T \tag{3.3}$$

2. *Positivity* – the probability of receiving treatment is greater than zero but less than one.

$$0 < P(T) < 1 \tag{3.4}$$

3. *Consistency* – the treatment is well-defined such that the observed outcome is equal to the potential outcome under treatment.

$$Y = Y(t) \tag{3.5}$$

4. *No interference* – the potential outcome of a unit only depends on its treatment and not on the treatment of other units (Cox, 1958).

$$Y_i = Y_i(t_i) \tag{3.6}$$

The exchangeability assumption states that potential outcomes must be independent of the treatment. In other words, it must be possible to exchange treatment groups without changing their potential outcomes. To understand why the assumption is essential, consider the aforementioned vaccine–disease example, with age as a common cause. If age influences who receives the vaccine, then the treatment and control groups are not exchangeable because their age distributions are dissimilar. And if age also impacts one's ability to recover from the disease, then the causal effect estimated using the groups is biased as it is an admixture of the causal effects of the vaccine and age. Exchangeability ensures that the causal effect is bias-free because if the treatment groups are similar in all of their characteristics except for the treatment, then any outstanding causal effect must be the result of the treatment only.

Positivity states that there must be a non-zero probability of receiving any treatment. This assumption is important because its violation leads to undefined causal effects. For example, consider the situation where everyone or no one receives the vaccine. In such a scenario, the causal effect of the vaccine would be mathematically impossible to estimate because the counterfactual would always be missing. Intuitively, causal effects are only meaningful if the outcome under "treatment" is contrasted to the outcome under "no treatment" within the potential outcomes framework of causal inference.

Consistency states that the observed outcome must equal the potential outcome under treatment. When this assumption is not met, the causal effect is inconclusive. Following the vaccine–disease example, there must be only one version of the vaccine if the goal is to estimate its efficacy. If multiple versions exist and they are labelled as the treatment, then the causal effect will be a mixture of the individual causal effects of the different vaccines. Furthermore, if the temperature of the vaccine affects the outcome, then all individuals must receive the vaccine at the same temperature. Simply put, the treatment must be well-defined.

Lastly, the no interference assumption states that the potential outcome of a unit must only depend on its treatment. Violation of this assumption makes the causal effect of treatment ill-defined in the strict sense because the treatment is now an admixture of multiple units' treatment and must be redefined. This situation is common in many real-world cases and is referred to as spillover effects. For example, the likelihood of contracting COVID-19 depends not only on one's immunity to the disease but also on the immunity within the population.

The consistency and no interference assumptions are sometimes grouped into the so-called stable unit treatment value assumption (SUTVA; Rubin 1980) because their violation results in ill-defined causal effects. If all of the above assumptions are met, the ACE is identifiable and is the statistical quantity,

$$\tau = \mathbb{E}[Y(1)] - \mathbb{E}[Y(0)] = \mathbb{E}[Y|T=1] - \mathbb{E}[Y|T=0]. \tag{3.7}$$

3.4 Biases and Adjustments

The gold standard for causal inference is a randomised control trial (RCT; Chalmers et al. 1981). A well-conducted RCT always outputs a true measure of the ACE because the causal assumptions are met by construction. However, it is not always possible to perform RCTs because they can be unethical, infeasible, or outright impossible. More often than not, only observational data is available that is prone to many biases, unlike experimental data. The biases violate the causal assumptions and distort the true causal effect. Here, causal graphs truly come into their own as they make it easy to identify such biases and adjust for them such that the causal assumptions hold, resulting in valid estimates of the causal effect. There are many different types of biases, but the primary two are confounding bias and selection (or collider) bias.

3.4.1 Confounding Bias

Confounding bias arises in the presence of a common cause or confounder X that causes both the treatment and the outcome, as illustrated in Figure 3.2. Unlike the DAG in Figure 3.1, there are two paths for association to flow between T and Y: (i) the direct path between T and Y and (ii) the backdoor path linking T and Y via X. The causal association flows through the former, and the non-causal

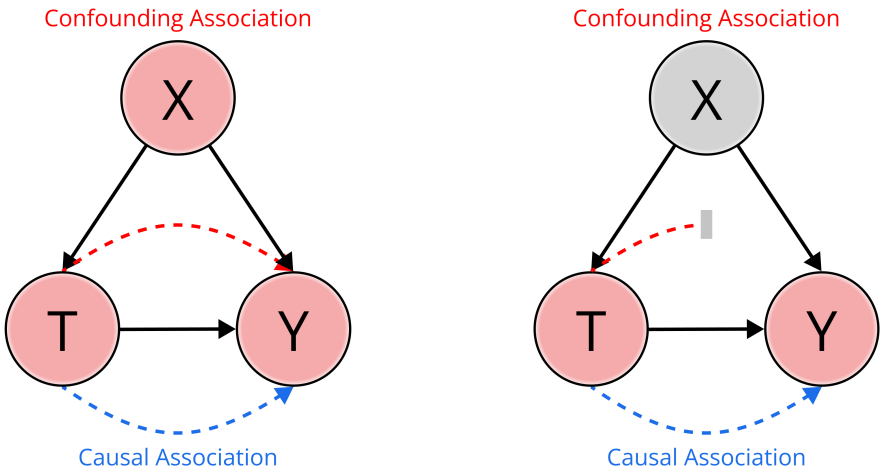

(a) Before conditioning **(b)** After conditioning

Figure 3.2: Illustration of confounding bias. DAGs representing the causal relationships between treatment T, outcome Y, and their common cause or confounder X. (a) There are two paths for association to flow between T and Y: (i) the direct path between T and Y and (ii) the backdoor path linking T and Y via X. The causal association (depicted with the blue dashed line arrow) flows through the former, while the non-causal confounding association (depicted with the red dashed line arrow) flows through the latter. The admixture of the causal and non-causal associations means association is not causation. (b) The act of conditioning on X (visualised with the greyed-out node) blocks the non-causal confounding association from flowing via the backdoor path.

confounding association flows through the latter. The amalgam of causal and non-causal associations means association is not causation, and the causal effect is biased. Specifically, the causal effect is an admixture of the causal effects of the treatment and confounder. Intuitively, if age influences the treatment and outcome in the aforementioned vaccine–disease example, then it is difficult to separate the causal effect that age has on the outcome from the causal effect of the treatment. In terms of the causal assumptions, the presence of confounders violates exchangeability because the treatment is not independent.

In experimental data, confounding is not an issue as RCTs remove its effect via randomisation of the treatment. In DAGs, treatment randomisation translates to removing the direct edge from X to T, making T independent, so confounding association cannot flow via the backdoor path as it does not exist. As a result, association is causation because exchangeability holds, and the causal effect does not suffer from confounding bias. In contrast, confounding is a major issue in observational data because, by its nature, the treatment is not randomised beforehand

via experimentation. The goal with observational data is not to solve the issue directly but rather to negate it by adjusting the data such that the estimates of causal effects are bias-free. The first step is to modify the causal assumptions to be appropriate for observational data. For example, conditional exchangeability must hold for observational data, as the prevalence of confounders will always violate exchangeability. Conditional exchangeability states that potential outcomes are independent of the treatment given confounders.

$$Y(t) \perp\!\!\!\perp T|X. \tag{3.8}$$

Visually, conditioning on a confounder blocks the non-causal confounding association from flowing from T to Y via the backdoor path, as shown in Figure 3.2b, leaving only the causal association. Also, as exchangeability and confounding are intertwined concepts, the conditional exchangeability assumption is sometimes referred to as unconfoundedness. An alteration of the positivity assumption is also necessary to account for confounding. Following on from the original definition, the conditional probability of receiving treatment given confounders must be greater than zero and less than one.

$$0 < P(T|X) < 1. \tag{3.9}$$

Given the prior consistency and no interference assumptions, in addition to conditional exchageability and positivity, the ACE

$$\tau = \mathbb{E}[Y(1)] - \mathbb{E}[Y(0)] = \mathbb{E}_{\mathbb{X}}[\mathbb{E}[Y|T=1,X] - \mathbb{E}[Y|T=0,X]]. \tag{3.10}$$

This is known as the adjustment formula because adjustments are made post-data generation to infer true, unbiased causal effects.

3.4.2 Selection Bias

While confounding bias persists when there is a lack of adjustment of a common cause, selection bias occurs precisely due to adjustment of a common effect X, as illustrated in Figure 3.3. A common effect is a variable that is caused by both the treatment and the outcome. As previously, there is a direct path and a backdoor path between T and Y for association to flow. The causal association flows through the former as

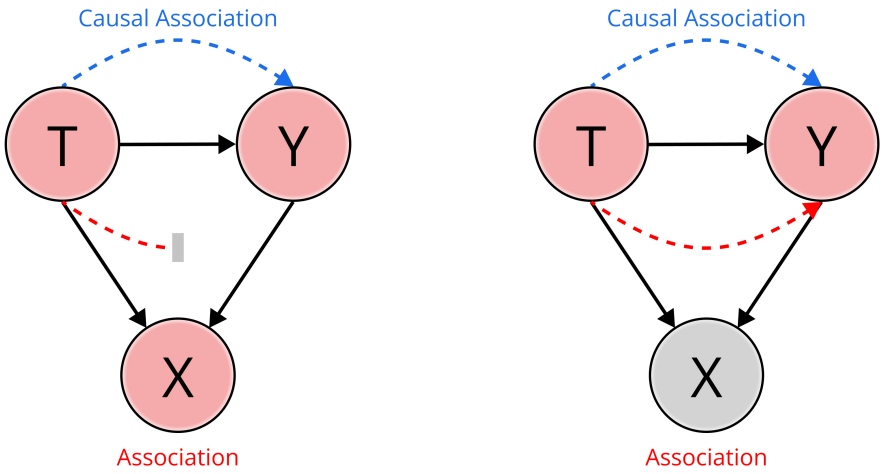

(a) Before conditioning **(b)** After conditioning

Figure 3.3: Illustration of selection (or collider) bias. DAGs representing the causal relationships between treatment T, outcome Y, and their common effect or collider X. (a) Similar to Figure 3.2, there is a direct path and a backdoor path between T and Y for association to flow. As before, the causal association (depicted with the blue dashed line arrow) flows through the former. However, the non-causal association (depicted with the red dashed line arrow) cannot flow through the latter as it is now blocked because of the collider. (b) The act of conditioning on X (visualised with the greyed-out node) unblocks the previously blocked backdoor path, allowing once again the non-causal association to flow. As a result, association is not causation as it is once again an admixture of the causal and non-causal associations.

before, but the non-causal association does not flow through the latter as it is now a blocked path. The flow of association from T and Y 'collides' on X, as shown in Figure 3.3a. Hence, X is also referred to as a collider. In this scenario, association is causation, and the causal effect is not biased. By incorrectly conditioning on X, the backdoor path is unblocked, allowing the non-causal association to flow as shown in Figure 3.3b, which ultimately induces selection bias.

Continuing the vaccine–disease example: assume the vaccine has side effects and can cause hospitalisations in rare cases. The disease can also cause hospitalisations by deteriorating the health of individuals. Figure 3.3 represents this exact situation, where hospitalisation X is the common effect of the vaccine T and disease Y. Conditioning on X by selecting only the hospitalised patients induces a non-causal association between the vaccine and disease. Specifically, a positive association between the vaccine and disease would be observed as the hospitalised population is more likely to be vaccinated or have the disease than the general population. The

conclusion that one would draw from the selected data is that the vaccine causes the disease, which would be detrimental as it would dissuade people from receiving the vaccine. In terms of the causal assumptions, conditioning or selecting on the common effect also violates exchangeability.

3.5 Causal Machine Learning

Causal machine learning (Causal ML) is an emerging field that combines causal inference and machine learning (ML) to leverage the benefits of one for the other (see Kaddour et al., 2022, for a review).

Causal Inference for Machine Learning

Although ML has been successful in a wide range of applications and transformed many fields, there are some major limitations. Traditional ML suffers from:

1. *Generalisability* – ML algorithms rely on training and testing data being identically and independently distributed (i.i.d.). When the i.i.d. assumption does not hold under distributional shifts—a highly likely occurrence in real-world scenarios—the performance drops drastically. Simply put, ML algorithms fail to generalise to out-of-distribution (OOD) data (see Shen et al., 2021, for a recent survey).

2. *Interpretability* – defined as the ability to understand how an ML model makes its decisions (Lipton, 2016). Thus, an interpretable model is one that can be easily understood by humans and readily explained in terms of its underlying logic or rules. ML, and especially deep learning (DL) models, are complex and difficult to interpret. Furthermore, there is a tradeoff between accuracy and interpretability (Kuhn et al., 2013). ML algorithms like linear regression are highly interpretable but often do not achieve outstanding accuracy. Conversely, artificial neural networks (ANNs) generally have great accuracy but are less interpretable.

3. *Explainability* – defined as the ability to explain why an ML model made its particular decision (Miller, 2017). An explainable model is one that can provide human-understandable explanations for its predictions, which is the goal of explainable AI (XAI; see Došilović et al., 2018; Verma et al., 2020; Karimi et al., 2020; Burkart and Huber, 2020, for surveys).

4. *Bias and Fairness* – bias can be introduced at various stages of the ML pipeline, from data collection and preprocessing to the selection of the model and its hyperparameters. A biased ML model is unfair if its decisions discriminate against an individual or group based on their inherent or acquired characteristics (see Mehrabi et al., 2019, for a recent survey).

Many of the shortcomings are believed to stem from ML being correlation-based rather than causal-based. For example, explainability is an inherently causal problem as it is concerned with the question of why. As such, incorporating causality into ML algorithms is argued to be the solution (Pearl, 2019; Ahmed et al., 2020; Goyal and Bengio, 2020; Schölkopf et al., 2021).

Machine Learning for Causal Inference

There are two common causal inference tasks: (i) causal effect estimation (i.e., estimating the causal effect of a treatment on an outcome) and (ii) causal discovery (i.e., identifying the causal relationships between variables to determine the underlying causal model). ML can aid in both with:

1. *Improved modelling of non-linear relationships* – ML algorithms can model non-linear relationships, making it possible to capture more complex causal relationships in the data.

2. *Better handling of high-dimensional data* – ML techniques can handle high-dimensional data, making it possible to estimate causal effects in settings where traditional causal inference methods may struggle.

Traditional ML algorithms redesigned for causal inference include causal k-nearest neighbours (CkNNs; Zhou and Kosorok 2017), causal forests (CRFs; Wager and Athey 2015; Athey et al. 2016), and causal artificial neural networks (CANNs; Shi et al. 2019; Xia et al. 2021). Note, these causal ML algorithms do not perform causal effect estimation and causal discovery on their own. In Chapter 5, causal inference and ML is combined to infer the causal effect of environment on SFR. ML is utilised solely for estimation, and the causal inference framework to infer causality. Specifically, the standard RF algorithm is combined with the causal inference method, inverse probability weighting (IPW) of marginal structural models (MSMs).

Chapter 4

Galaxy Properties with Machine Learning

This Chapter is based on *Mucesh et al. (2021)*: A machine learning approach to galaxy properties: joint redshift–stellar mass probability distributions with Random Forest. *Monthly Notices of the Royal Astronomical Society*, 502(2), 2770-2786.

We demonstrate that highly accurate joint redshift–stellar mass probability distribution functions (PDFs) can be obtained using the random forest (RF) machine learning (ML) algorithm, even with few photometric bands available. As an example, we use the Dark Energy Survey (DES), combined with the COSMOS2015 catalogue for redshifts and stellar masses. We build two ML models: one containing deep photometry in the *griz* bands, and the second reflecting the photometric scatter present in the main DES survey, with carefully constructed representative training data in each case. We validate our joint PDFs for 10,699 test galaxies by utilising the copula probability integral transform and the Kendall distribution function, and their univariate counterparts to validate the marginals. Benchmarked against a basic set-up of the SED-fitting code `BAGPIPES`, our ML-based method outperforms SED fitting on all of our predefined performance metrics. In addition to accuracy, the RF is extremely fast, able to compute joint PDFs for a million galaxies in just under 6 minutes with consumer computer hardware. Such speed enables PDFs to be derived in real-time within analysis codes, solving potential storage issues. As part of this work, we have developed `GALPRO`[1]—a highly intuitive and efficient Python package to rapidly generate multivariate PDFs on the fly. `GALPRO` is documented and available for researchers to use in their cosmological and galaxy evolution studies.

[1] https://galpro.readthedocs.io/

4.1 Introduction

The next generation of photometric surveys, such as the Rubin Observatory Legacy Survey of Space and Time (LSST; LSST Science Collaboration et al. 2009) and Euclid (Laureijs et al., 2011), will observe billions of galaxies. The sheer amount of data generated will enable studies ranging from the cosmic large-scale structure (LSS) to the formation and evolution of galaxies to be conducted in unprecedented detail, ultimately leading to a transformation in our understanding of the Universe. However, one of the key challenges will be developing algorithms that can quickly and reliably extract physical properties and redshifts of galaxies.

The success of many scientific analyses critically hinges on redshift measurements. For example, redshifts are required in weak lensing tomography (Hu, 1999); one of the primary probes to unveil the nature of dark energy. As a result, a large number of methods now exist to estimate redshifts from photometric data, i.e., photo-zs (see Salvato et al., 2019, for a review). In general, they are either physically-motivated or data-driven.

SED-fitting methods fall into the former category as they require prior knowledge in the form of SED templates. These templates are fit to the observed fluxes, and photo-zs are usually determined using chi-square minimisation (e.g., Bolzonella et al., 2000). Baum (1962) originally applied SED fitting to estimate photo-zs of elliptical galaxies. Since then, a plethora of codes have been developed for the task, such as `LEPHARE` (Arnouts et al., 1999), `HYPERZ` (Bolzonella et al., 2000), `BPZ` (Benítez, 2000), `ZEBRA` (Feldmann et al., 2006), `EAZY` (Brammer et al., 2008), and `BCNZ2` (Eriksen et al., 2019).

The fundamental principle behind data-driven methods is to learn a mapping between photometry and redshift using training data. Connolly et al. (1995) used a polynomial function for the mapping. However, since the new millennium, machine learning (ML) methods have become popular as they are able to learn more complex mappings. Once trained, ML algorithms can make predictions on 'new' galaxies. As with SED fitting, a large number of ML algorithms have been used to predict photo-zs. These include artificial neural networks (ANNs; Firth et al. 2003; Collister and Lahav 2004; Sadeh et al. 2016), support vector machines (SVMs; Wadadekar 2005), self-organizing maps (SOMs; Geach 2012; Way and Klose 2012; Carrasco Kind

and Brunner 2014), Gaussian processes (GPs; Way and Srivastava 2006), genetic algorithms (GAs; Hogan et al. 2015), k-nearest neighbours (kNNs; Ball et al. 2007), boosted decision trees (BDTs; Gerdes et al. 2010), random forests (RFs; Carliles et al. 2008, 2010; Carrasco Kind and Brunner 2013; Rau et al. 2015), and sparse Gaussian framework (Almosallam et al., 2016). Furthermore, deep learning (DL) methods have also been implemented (Hoyle, 2016; D'Isanto and Polsterer, 2018; Pasquet et al., 2019).

Galaxies are described by a wide range of physical properties, with stellar mass, star-formation rate, age, and metallicity being among the most important. SED-fitting codes such as `FAST` (Kriek et al., 2009), `CIGALE` (Burgarella et al., 2005; Noll et al., 2009; Boquien et al., 2019), `MAGPHYS` (da Cunha et al., 2011), and `BMASTELLARMASSES` (Palmese et al., 2020a) have been specifically designed to output these quantities. Meanwhile, the application of ML in this field has been fairly limited, but literature has now begun to emerge (Acquaviva, 2016; Stensbo-Smidt et al., 2016; Bonjean et al., 2019; Delli Veneri et al., 2019).

While single-value (point) estimates are useful, probability distribution functions (PDFs) have become increasingly important in recent years as a full characterisation of the uncertainties, beyond a point estimate and an error bar, is required for accurate analyses. This has been particularly true in the role of redshifts for weak lensing cosmology (e.g., Bonnett et al., 2016), where it has been shown that using distributions instead of point estimates can improve the accuracy of cosmological measurements (Mandelbaum et al., 2008; Myers et al., 2009). It is possible to extract redshift PDFs using both SED fitting and ML methods. However, ML methods have recently grown in use due to their efficiency. For example, packages such as `ArborZ` (Gerdes et al., 2010), `TPZ` (Carrasco Kind and Brunner, 2013), `SOMz` (Carrasco Kind and Brunner, 2014), `SkyNet` (Bonnett, 2015), and `ANNz2` (Sadeh et al., 2016) all have foundations in ML. To reach a consensus on the best algorithm in terms of PDF accuracy, Schmidt et al. (2020) and Euclid Collaboration: Desprez et al. (2020) have compared a dozen or more popular algorithms from both approaches.

The redshift and physical properties of a galaxy, measured via modelling its photometry, are correlated, and thus should be described with a multivariate distribution. The commonly used marginal distributions in redshift, stellar mass, etc., constitute a

loss of information and could potentially introduce biases into a scientific analysis as a result. Consequently, a new class of SED-fitting codes has come to the fore, such as `BAYESed` (Han and Han, 2012, 2014, 2019), `BEAGLE` (Chevallard and Charlot, 2016), and `BAGPIPES` (Carnall et al., 2018). They utilise Bayesian statistical techniques such as Markov chain Monte Carlo (Goodman and Weare, 2010; Foreman-Mackey et al., 2013) and nested sampling algorithms (Skilling, 2006; Feroz and Hobson, 2008; Feroz et al., 2009, 2019) to generate multivariate posterior distributions of the most important properties. By estimating redshift and physical properties simultaneously, they allow for any uncertainties on redshift to propagate to the statistical constraints on physical properties, whilst accounting for any potential correlations (Chevallard and Charlot, 2016). The only drawback is that it is not feasible to obtain these distributions for a large number of galaxies. For example, `BAGPIPES` takes on average a few minutes to fit each galaxy, making it prohibitively expensive to fit modern datasets where sample numbers can exceed hundreds of millions, let alone upcoming surveys where the numbers will exceed a billion. Moreover, the results of the fit to each galaxy must somehow be stored in a way that is accessible to scientific analysis routines.

Based on the speed and competitive performance of ML algorithms when used to estimate photo-zs, it is possible that an ML approach to the problem could be promising. With this in mind, we take a significant step towards realising the ultimate goal of extracting full posterior distributions of galaxy properties using ML by first focusing on 2D posterior distributions of redshift and stellar mass. We choose these properties as they are two of the most important and accurate to predict (Walcher et al., 2011; Conroy, 2013). Furthermore, joint PDFs are straightforward to visualise and thus ideal for uncovering any hidden correlations or degeneracies that exist between the properties.

Joint redshift–stellar mass PDFs have many potential science applications, such as determining the evolution of the stellar mass function (SMF; e.g., Papovich et al., 2003; Mortlock et al., 2015; Capozzi et al., 2017), the cross-correlation function between galaxies and galaxy groups (Yang et al., 2005), understanding the connection between stellar mass and dark matter in galaxy clusters (Palmese et al., 2016, 2020a), and the stellar-to-halo mass relation (SHMR; see Wechsler and Tinker, 2018, for

an overview). However, their storage remains a potential issue. Unless there is a revolution in data storage, it will not be feasible to store a large number of multivariate PDFs. To solve this dilemma, we have developed `GALPRO`—a highly intuitive and efficient Python package for rapid, on-the-fly generation of n-dimensional PDFs. `GALPRO` is documented and available for fellow researchers to use in their analyses at https://galpro.readthedocs.io/.

An interesting application of `GALPRO` could be to generate joint redshift–luminosity PDFs for measurements of the Hubble constant from gravitational wave events that lack an electromagnetic counterpart (Schutz 1986; Palmese et al. 2019; Soares-Santos and Palmese et al., 2019). The use of full redshift PDFs rather than point estimates is very important for standard siren measurements (Palmese et al., 2020b), and the inclusion of joint redshift–luminosity PDFs allows one to correctly define the selection function of the galaxy sample at the same time.

The outline of this chapter is as follows. In Section 4.2, we outline the method we use to extract point estimates and marginal and joint posterior probability distributions of redshift and stellar mass using the RF algorithm. In Section 4.3, we describe the preprocessing steps we perform to construct the necessary datasets. In Section 4.4, we describe the different RF models we train and explain the motivation behind them. We compare, discuss, and validate our results in Section 4.5, and place them into a familiar context via a comparison to those achieved by `BAGPIPES` in Section 4.6. Finally, we summarise this work in Section 4.7.

4.2 Method

The RF algorithm has previously been utilised to extract point estimates (Carliles et al., 2008, 2010) and PDFs (Carrasco Kind and Brunner, 2013) of redshift. Recently, Bonjean et al. (2019) used the algorithm to predict stellar masses and star-formation rates of galaxies. They built a single model to predict both target variables simultaneously. The process of building decision trees to achieve this is conceptually similar to building them to predict one target variable. The only difference is that at each step, to decide the best split, the average loss function for two or more variables is minimised. In Equation 2.5, $\tilde{y}_i$, and $\bar{y}_{D_L}$ and $\bar{y}_{D_R}$, are now vectors of target variables and the means, respectively. As this loss function is scale-dependent, the target variables must be transformed to place them on scales with similar ranges.

Otherwise, the variance of one will dominate, resulting in the algorithm expending more effort in getting one target variable correct at the expense of others (Breskvar et al., 2018). Once trained, the leaf nodes in the decision trees contain values of the target variables.

We apply this methodology to predict redshift and stellar mass simultaneously, thus preserving any correlation between the properties. As both variables are continuous, we use regression trees to build the forest. However, it is entirely possible to use classification trees as shown by Gerdes et al. (2010) and Carrasco Kind and Brunner (2013). Another motivation for using regression trees is that they are generally faster to train and better suited to non-uniform data. To summarise the process,

- Galaxies cluster together in n-dimensional space if they have comparable values of input features.
- The algorithm identifies these clusters by minimising the loss function (Equation 2.5), with redshift and stellar mass being the target variables.
- These clusters end up in the leaf nodes of the decision trees. In the end, the leaf nodes contain redshifts and stellar masses of similar galaxies.

We extract point estimates of redshift and stellar mass by running a 'new' galaxy down all the decision trees and using the mean of all the predicted values. To build marginal posterior distributions, we aggregate the values of redshift and stellar mass in the leaf nodes across all the decision trees, respectively. Finally, we combine the aggregated values to build joint posterior distributions. We would like to point out that our method is flexible and can be adapted to generate joint PDFs of any other combination of properties. However, we chose redshift and stellar mass as they are two of the most important and accurate properties to predict. Furthermore, the method is flexible and can be applied to generate n-dimensional PDFs. We describe the implementation of the RF in this work and the input features in Section 4.4.

4.3 Data

We use data from two different surveys to train and test our RF models. These are the Dark Energy Survey (DES; The Dark Energy Survey Collaboration 2005;

The Dark Energy Survey Collaboration et al. 2016; Lahav et al. 2020) and the Cosmological Evolution Survey (COSMOS; Scoville et al. 2007).

4.3.1 Cosmological Evolution Survey

The COSMOS observed a $2\,\mathrm{deg}^2$ equatorial field in the entire spectral range from radio to X-ray with both ground and space-based telescopes, collecting photometric and spectroscopic data. In this field, ~ 2 million galaxies were detected, spanning 75% of the age of the Universe (Scoville et al., 2007).

We use the COSMOS2015 (Laigle et al., 2016) catalogue from the field for its photo-zs and stellar masses. Usually, to train an ML algorithm to predict photo-zs, spectroscopic redshifts (spec-zs) are used. However, the photo-zs in this catalogue have been shown to be precise and accurate. Compared to photo-zs from surveys such as DES and the Sloan Digital Sky Survey (SDSS; York et al. 2000), the COSMOS photo-zs have been computed using more than 30 bands spanning a huge portion of the electromagnetic spectrum, as opposed to four or five optical bands. The most precise photo-zs have been estimated for very bright, low redshift, star-forming galaxies, with a normalized median absolute deviation (NMAD; Hoaglin and Mosteller 2000) of 0.007, of which 0.5% are catastrophic outliers (i.e., objects with $|z_{phot} - z_{spec}|/(1 + z_{spec}) > 0.15$). Furthermore, in the deepest regions of the survey, 90% of galaxies with stellar mass greater than $10^{10} M_{\odot}$ at $z = 4$ have been detected (Laigle et al., 2016). The high photo-z precision and the overall completeness of the survey in stellar mass makes this an exemplary dataset to use in this work.

4.3.2 Dark Energy Survey

The DES is a visible and near-infrared survey that has imaged $\sim 5100\,\mathrm{deg}^2$ of the South Galactic Cap ten times in $grizY$ photometric bands using the Dark Energy Camera (DECam; Flaugher et al. 2015) over a span of six years, starting in 2013. It is expected to have generated ~ 310 million galaxies with photo-zs, once all the data has been processed. In addition, the survey targeted a set of four fields with a total of ten DECam pointings over $27\,\mathrm{deg}^2$ for supernova (SN) science. This SN survey had an approximately weekly cadence and thus many more epochs per pointing than the main survey (Neilsen et al., 2019). We use two datasets from the DES survey, which are discussed in the following sections.

4.3.2.1 DES Deep Fields

As part of the DES Year 3 (Y3) cosmology analysis, observations from the SN survey were combined with community data, additional DES exposures (particularly in u-band) and coincident near-infrared data to form the DES Deep Fields (DF) catalogue (Hartley and Choi et al., 2020). The principal aims of the DF project are to improve calibration of redshift distributions in the main survey and to act as a prior on the population of full multicolour images for `Balrog` (discussed in the next section), to better understand the systematics and selection function of the wide-field (WF) survey. These goals rely on the fact that the DF represents a statistically complete, yet effectively noiseless, population of the galaxies that are found in the WF survey. Other motives include conducting galaxy evolution studies, science with the faintest possible sources, and the properties of the host galaxies of transient events.

The Y3 DF catalogue consists of data from three SN fields plus the COSMOS field, with a total coverage of $5.88\,\mathrm{deg}^2$ and photometry of over 1.7 million objects (after masking for image defects) in DECam $ugriz$ and VIRCam JHK bands. We combine the deep (~ 1.25 mag fainter than the WF data) and precise $griz$ photometry in this catalogue with the accurate redshifts and stellar masses from the COSMOS2015 catalogue to produce a baseline DF dataset. Specifically, we utilise the bulge+disc model-fit magnitudes computed using the Multi-Object Fitting (Drlica-Wagner et al., 2018) algorithm.

Our goal is to produce valid posterior PDFs of galaxies in the main DES survey, and to achieve this, we require a suitable dataset with which to train a RF model. The photometric errors in the DF dataset would not reflect those in the WF and so would lead to biased results if used directly as training data. Furthermore, the COSMOS field does not overlap the main survey area and the redshifts and stellar masses that could be derived from model fitting to the four-band WF data are grossly imprecise compared to those in the COSMOS2015 catalogue. In essence, we require a catalogue of DF galaxies that emulate galaxies in the WF to overcome these issues, and for this, we take advantage of the `Balrog` algorithm.

4.3.2.2 Balrog

`Balrog` is a Python package designed for the purpose of measuring the selection function of imaging surveys (Suchyta et al., 2016; Everett et al., 2020). The process by which it achieves this is as follows. A realistic ensemble of fake stars and galaxies is generated using `GALSIM` (Rowe et al., 2015), including survey characteristics appropriate to their intended sky location, e.g., seeing FWHM. The fake objects are then embedded into real survey images, thus inheriting many of their properties. Finally, the objects are detected and measured using `SExtractor` (Bertin and Arnouts, 1996) in the same way as the original survey images. The output catalogue comprises a Monte Carlo sampling of the selection function and measurement biases and naturally accounts for systematic effects arising from the photometric pipeline, detector defects, seeing, and other sources of observational systematic errors.

The Balrog process requires a prior population of galaxies from which to draw objects. The DES Y3 Balrog catalogue (Everett et al., 2020) was produced by injecting model fits of galaxies drawn randomly from the Y3 DF catalogue into DES Y3 single-epoch images and then measuring their properties. This catalogue contains true and measured *griz* photometry of nearly 4 million objects, and it provides us with ready-made emulated galaxies that reflect our target WF dataset, the DES Y3 GOLD (Sevilla-Noarbe et al., 2020). By combining the Y3 Balrog catalogue with COSMOS2015, we obtain a dataset that closely matches and is representative of the WF data, capturing many of the details of the objects' noise properties, but with the addition of accurate redshifts and stellar masses. From the catalogue, we use composite model magnitudes in this work. In the next section, we outline the preprocessing steps we perform to create the DF and WF datasets.

4.3.3 Preprocessing

To construct the DF dataset, we first cross-match galaxies in the Y3 DF and COSMOS2015 catalogues using `TOPCAT` (Taylor, 2005), with a matching radius of 1 arcsec. This serves the dual purpose of enabling the use of accurate photo-zs (`PHOTOZ`) and stellar masses (`MASS_BEST`) in our analysis and removing galaxies in all the other fields besides the COSMOS field. Next, we discard stars, as well as galaxies with unreliable or missing redshift and stellar mass, by ensuring $0 < z < 9.99$. We produce a magnitude-limited sample by selecting galaxies with $i < 23.5$. These

cuts automatically remove saturated objects and bad areas. We discover that there are some faint galaxies with close to zero or even negative fluxes in the grz bands, resulting in their magnitudes being undefined. To solve this issue, we convert all galaxy fluxes into "asinh" magnitudes or "luptitudes" (Lupton et al., 1999), defined as

$$\mu = \mu_0 - a \sinh^{-1}\left(\frac{f}{2b}\right), \tag{4.1}$$

where $\mu_0 = m_0 - 2.5 \log b$, $a = 2.5 \log e$, f is the flux, b is an arbitrary softening parameter, and m_0 is the magnitude zero point. The authors state that the optimal value of $b = \sqrt{a}\sigma$, where σ is the standard deviation of the flux. We set the value of σ to be the median of the standard deviations. Additionally, we transform flux errors into luptitude errors using

$$\sigma_\mu = \frac{a\sigma}{2b}. \tag{4.2}$$

Luptitudes behave like magnitudes for bright photometry and like fluxes for faint photometry, with the turning point in the behaviour determined by the softening parameter. By converting to luptitudes, we avoid introducing an additional selection effect by not discarding galaxies with negative fluxes.

To produce the WF dataset, we start anew and match "WF" galaxies in the Y3 Balrog catalogue to their counterparts in the Y3 DF using the `ID` column. Next, we cross-match the galaxies in the intermediate catalogue to the COSMOS2015 catalogue. There are multiple scattered WF copies of each DF galaxy in the Balrog catalogue to efficiently sample the DES selection function, and to preserve this, we keep all of the copies. This is an important aspect of our set-up, as it captures the selection function through the galaxy detection probability as a function of true photometry and light profile, as well as the asymmetric scatter between photometry and galaxy properties (redshift and stellar mass) that it induces. We remove any galaxies with erroneous flux measurements by selecting all galaxies with `MEAS_CM_FLAG` $= 0$ (Everett et al., 2020). Finally, we repeat all the aforementioned cuts and steps used in constructing the DF dataset, the only difference being that on this occasion, we apply the i-band cut to the magnitudes of WF galaxies. Thus, we have augmented a completely

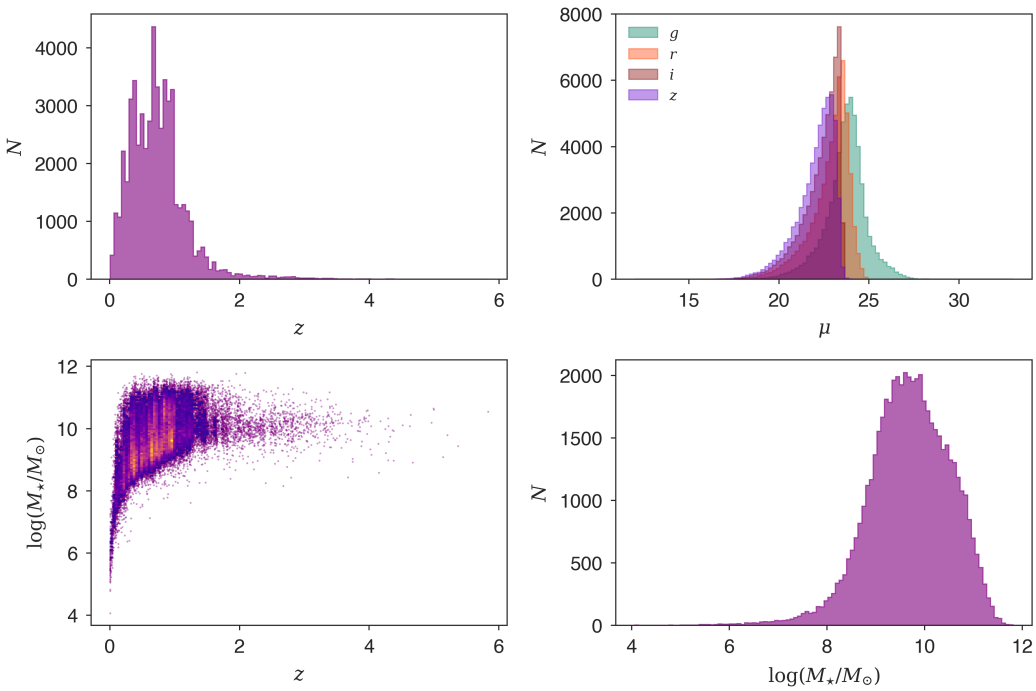

Figure 4.1: Marginal and joint distributions of redshifts and stellar masses of galaxies in the DF dataset and the distributions of *griz* luptitudes. The colours in the joint distribution indicate the density of points. The DF dataset is created by cross-matching galaxies in the DES Y3 Deep Fields (DF) and the COSMOS2015 catalogues. All galaxies with unreliable or missing redshift and stellar mass are discarded from the dataset, and a magnitude-limited sample is produced by selecting galaxies with $i < 23.5$. The *griz* luptitudes in the dataset are computed from fluxes in the Y3 DF catalogue, while the redshifts and stellar masses are from the COSMOS2015 catalogue.

realistic target dataset which effectively replicates the systematics in the WF survey without compromising on the accuracy of redshifts and stellar masses.

After all the preprocessing steps, there are $53,491$ galaxies in the DF dataset and $393,276$ galaxies in the WF dataset. Each dataset contains the following information: *griz* luptitudes and luptitude errors, photo-zs, and stellar masses. Additionally, we compute all the relevant lupticolours, and the associated errors using the standard error propagation formula:

$$\sigma_c = \sqrt{\sigma_{\mu_1}^2 + \sigma_{\mu_2}^2}, \tag{4.3}$$

where σ_{μ_1} and σ_{μ_2} are the errors on the luptitudes, and σ_c is the error on the computed lupticolour. Figure 4.1 shows the marginal and the joint distribution of redshifts and stellar masses of galaxies in the DF dataset, and the distributions of *griz* luptitudes. The average redshift and stellar mass is approximately 0.7 and

$5 \times 10^9 M_\odot$, respectively. For the sake of brevity, we do not show a similar figure for the WF dataset as the distributions are broadly similar.

We perform an $80:20$ split on the DF and WF datasets to create their training and testing datasets, respectively. As there are multiple copies of each galaxy in the WF dataset, we ensure that there is no admixture of unique galaxies in its training and testing datasets. In other words, unique galaxies that exist in the training dataset do not appear in the testing dataset, and vice versa. As a consequence, there are $314,196$ and $79,080$ galaxies in the WF training and testing datasets, respectively. Lastly, we randomly sample $10,699$ galaxies without replacement from the WF testing dataset to construct its final version. We do this to ensure that the number of galaxies in both the DF and WF testing datasets matches, thus enabling us to make a fair comparison when testing our RF models.

The training datasets represent prior information that the RF models utilise in order to make predictions on the test datasets. As a result, one must construct a suitable and representative training dataset (as we have done) when using outputs from an ML model in their scientific analysis. In the next section, we describe the different RF models, explain the motivation behind them, and detail the implementation of the RF algorithm we use in this work.

4.4 Models and Implementation

We train and test two different RF models, with redshift and stellar mass as the target variables and the following as input features:

- $griz$ luptitudes
- $griz$ luptitude errors
- $g-r$, $r-i$, and $i-z$ lupticolours, and their associated errors

We build the first model using the DF dataset and refer to it as DES-DF from here onwards. The high-precision photometry of DF galaxies combined with the accurate redshifts and stellar masses allows us to establish the baseline performance. We build the second model to produce valid posterior PDFs of galaxies in our target dataset (the DES Y3 GOLD) by training on the WF dataset. We refer to this model as DES-WF.

To train and test our RF models, we use the implementation of the algorithm in the Python ML package `scikit-learn` (Pedregosa et al., 2011). In particular, we use the `RANDOMFORESTREGRESSOR` module from the package, which allows us to do regression. Before training, we do not perform feature scaling as the RF algorithm is invariant under monotonic transformations. Furthermore, we do not scale the target variables because redshift and stellar mass (in the logarithmic form) have similar ranges. Besides, `scikit-learn` automatically normalises the variances of individual target variables so that they contribute equally to the loss function.

As previously discussed in Section 2.2, RF has hyperparameters that can be tuned to increase the performance of a model. Therefore, we tune our RF models before training using a combination of random search and grid search, adopting k-fold cross-validation (specifically, 3-fold). We first set up a wide grid of hyperparameters and run the models using 100 different combinations. Next, we use a grid search around the best hyperparameters found in the previous searches. After tuning, we find that the performance of the models, in terms of the root-mean-square error (RMSE), only improves by $1-2\%$. In principle, one could use metrics associated with the validity of PDFs (described in Sections 4.5.2.1 and 4.5.3.1). However, we opted for the simple RMSE as we do not believe that there exists a single metric that can fully characterise the performance of a model. Given the insignificant improvements in the performance of our models, we ultimately resorted to using the following default `scikit-learn` hyperparameters for training both models:

- `n_estimators: 100`
- `max_features: auto`
- `max_depth: none`
- `min_samples_leaf: 1`
- `min_samples_split: 2`
- `max_leaf_nodes: none`
- `min_impurity_decrease: 0.0`
- `min_impurity_split: none`

- `min_weight_fraction_leaf: 0.0`

With these hyperparameters, the decision trees are fully grown until the training data can no longer be split. We set `max_features` to `auto` instead of $\sqrt{N}$, where N is the total number of input features, to ensure that our models have sufficient prior information, given that we are using a limited number of photometric bands to begin with. We train and test both models on a 13" Macbook Pro (2.4 GHz Intel Core i5, 16GB LPDDR3) using `GALPRO`, and it takes less than 1 and 5 minutes respectively, to generate PDFs for $10,699$ galaxies. In the next section, we compare, discuss, and validate the point estimates and marginal and joint posterior PDFs of redshift and stellar mass of test galaxies estimated from the trained models.

4.5 Results and Discussion

4.5.1 Point Estimates

We extract point estimates by averaging predictions from all the decision trees in a given RF model. In order to quantify how the models are performing, we use the NMAD metric for redshift and stellar mass. The NMAD is defined as:

$$\sigma_{\rm NMAD} = 1.4826 \times \text{median} \mid \hat{y}_i - \tilde{y}_i \mid, \tag{4.4}$$

where $\hat{y}_i$ and $\tilde{y}_i$ are the predicted and true values of redshift and stellar mass of galaxies, respectively. For redshift, the bias $\hat{y} - \tilde{y}$ is divided by $1 + \tilde{y}$.

Figure 4.2 shows the redshifts and stellar masses of test galaxies versus the predictions made by DES-DF and DES-WF. Most of the data points lie close to the diagonal, which indicates that the predicted redshifts and stellar masses are accurate. However, there are outliers at low and high redshifts and low stellar masses. There is a lack of training data available in these regions, as can be observed in Figure 4.1. Given the strong correlation between the accuracy of a RF model and the abundance of training data, these outliers are to be expected.

Moreover, the degradation in performance could be due to degeneracies that exist in the colour–redshift space. For example, at $z < 0.2$, there is a lack of strong spectral features that can be detected in the *griz* bands. Using the *u*-band can break the degeneracies. However, we do not use it as an input feature as the band is not available in the DES data. Furthermore, in the redshift range, $1.2 < z < 2.2$, there is

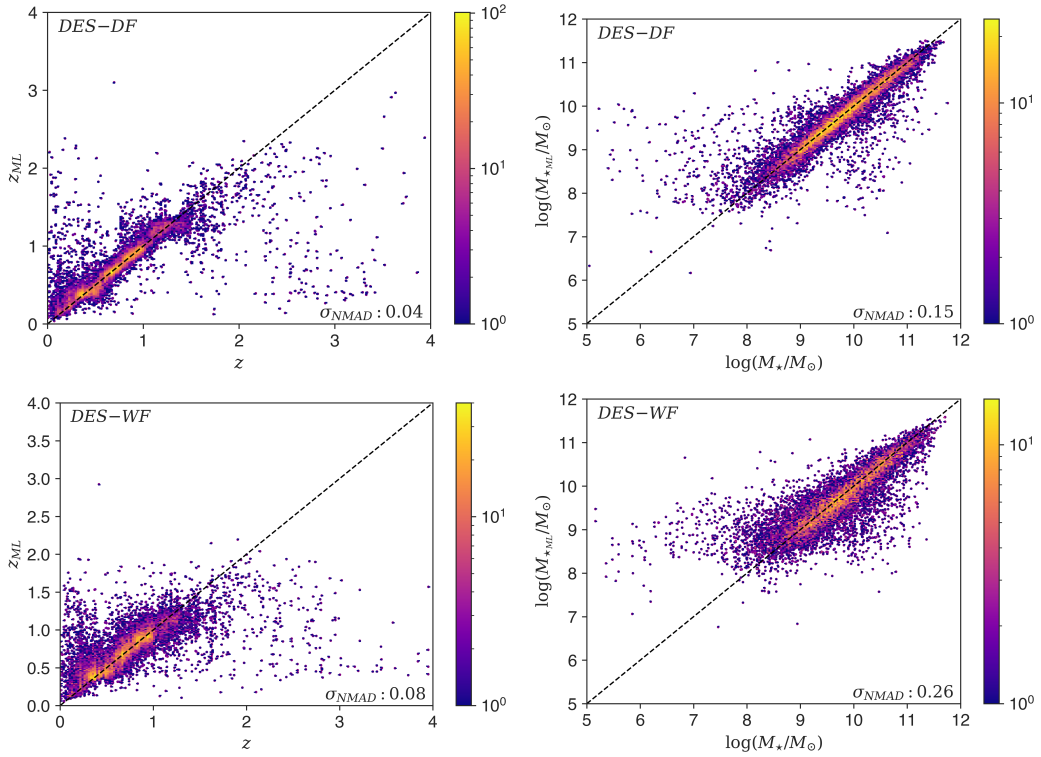

Figure 4.2: 'True' redshifts and stellar masses of test galaxies versus the predictions made by the DES-DF and DES-WF models. The colours indicate the density of points. The normalized median absolute deviation (NMAD; Hoaglin and Mosteller 2000) metric values are stated for redshift and stellar mass, respectively. For redshift, the bias $\hat{y} - \tilde{y}$ is divided by $1 + \tilde{y}$ in Equation 4.4.

a lack of strong spectral features in the visible bands (Bolzonella et al., 2000). These degeneracies can lead to incorrect clustering of training galaxies and thus inaccurate point predictions.

Comparing the two models, the point-estimate performance of DES-DF is better than DES-WF, with $\sigma_{\rm NMAD}$ of 0.04 and 0.15 dex for redshift and stellar mass, respectively. There is a visible increase in the scatter in the DES-WF plots, and this is reflected in the values of the performance metric doubling for redshift to 0.08 and increasing by $\sim 73\%$ to 0.26 dex for stellar mass. This drop in performance is primarily due to the degraded photometric precision, which makes it difficult for the RF to cluster galaxies, resulting in imprecise predictions. Nevertheless, DES-WF still performs well for a significant portion of test galaxies, as can be observed. On a related note, we also explored the impact on the performance when predicting one versus two variables. We built two models each using the DF and WF datasets to predict redshift and stellar mass separately and found that there was an insignificant

improvement in the performance, with σ_{NMAD} decreasing by $0.001 - 0.002$.

4.5.2 Marginal Probability Distributions

The point estimates we extracted are not perfect. In general, inaccuracies can arise from:

- *Incomplete and incorrect information* – the information provided to an ML algorithm may not be sufficient to learn the perfect mapping between the input features and target variables. For example, to estimate redshifts to a high degree of accuracy, spectroscopic data are required. However, we use photometric data that only provides a rough sampling of the underlying SED. Furthermore, the data used for training and testing have to be accurate. In our case, the redshifts and stellar masses we use to train our RF models may contain some errors. They have been estimated using the SED-fitting code `LEPHARE`, which utilises template SEDs, and they may not be a perfect representation of the true SED. Therefore, the mappings learnt by the RFs may not be entirely accurate, and this could lead to the observed errors in the estimates. Furthermore, we predict redshifts and stellar masses using four-band photometry, while those in the COSMOS2015 catalogue are computed using more than 30 bands. Consequently, there will be subtle differences between our predictions and the 'truth'.

- *Unrepresentative and incomplete training data* – the lack of representative and complete training data can also lead to errors. In our case, the training data are highly likely to be representative. However, in some regions, the data are sparse and therefore do not provide a complete sampling of the target population. For example, at low and high redshifts, the number of galaxies available for training reduces dramatically, as can be observed in Figure 4.1, and this causes the performance of the algorithm to suffer. Furthermore, the effect of sample variance from the small COSMOS area can lead to some incompleteness.

- *ML algorithms and hyperparameters* – different ML algorithms learn using different methods. As a result, predictions on the same datapoint can be slightly different. Furthermore, the hyperparameters can also have an effect, as discussed in Section 2.2. However, the performance of ML algorithms suitable

for a specific problem generally converges given sufficient and good quality training data.

In order to characterise uncertainties associated with our point estimates, we extract marginal posterior distributions of redshift and stellar mass. We do this by aggregating the redshift and stellar mass values in the leaf nodes of the decision trees in a RF that are representative of the test galaxy in question. We extract the distributions from the trained models and validate them using several techniques and metrics described in the next section.

4.5.2.1 Marginal PDFs Validation

Unlike point estimates, it is not possible to validate individual redshift and stellar mass PDFs as the true distributions are not available. Consequently, we aim to determine the validity of the marginal PDFs as a whole. We use the framework developed by Gneiting et al. (2007), which is founded on the paradigm of maximising the sharpness of the predictive distributions subject to calibration. Sharpness refers to the concentration of predictive distributions and is a property of the distributions only. The authors describe calibration as the statistical consistency between the distributions and the truth. We refer to this as validation as it better captures the essence of use in our context. However, for consistency, we will use the former when describing the authors' work. In this work, we focus on calibration to validate the marginal PDFs produced by our models, rather than sharpness, as the latter is useful when ranking competing calibrated methods. Furthermore, as demonstrated by Bordoloi et al. (2010), one could use the framework to empirically recalibrate marginal PDFs. However, this can be challenging and could potentially result in unforeseen issues.

Gneiting et al. (2007) introduce three modes of calibration: probabilistic, marginal, and exceedance. The first two modes are the most important, and they can be empirically assessed. As a result, we focus on them to determine if the marginal PDFs produced by our models are valid and exclude exceedance calibration in our analysis. Probabilistic calibration can be assessed using the probability integral transform (PIT; Rosenblatt 1952). It is the cumulative distribution function (CDF) evaluated at its true redshift or stellar mass:

$$PIT = \int_{-\infty}^{\tilde{y}} f(y)dy, \tag{4.5}$$

where $\tilde{y}$ is the true redshift or stellar mass, and $f(y)$ is the marginal PDF. If the marginal PDFs are probabilistically calibrated, then the true redshifts and stellar masses should be random draws from their respective distributions. This statement is equivalent to requiring that the CDF evaluated at the true redshift should not have a preferred value. In this case, for an ensemble of galaxies, the distribution of PIT values should follow the standard uniform distribution ($U(0,1)$; Dawid 1984), i.e., one percent of galaxies should have their spec-zs found within the first percentile of their CDFs, and so on. Deviations from uniformity can be interpreted as follows. If the marginal PDFs are overly broad, then fewer objects will have true redshifts in the tails of their PDF, instead being closer to 0.5, and the PIT distribution will be convex-shaped. Conversely, if they are overly narrow, then the PIT distribution will be concave-shaped. Finally, if the PIT distribution has a gradient, then this means that the marginal PDFs are biased. In the past, the PIT distribution has been utilised to determine the validity of redshift PDFs (e.g., Bordoloi et al., 2010; Polsterer et al., 2016; Tanaka et al., 2018; Schmidt et al., 2020; Euclid Collaboration: Desprez et al., 2020).

The uniformity of the PIT distribution is a necessary condition for marginal PDFs to be valid. However, Hamill (2000) has shown that uniformity can also arise from biased distributions. Therefore, probabilistic calibration may not be sufficient in some cases, and marginal calibration may be required to reach a concrete conclusion. Marginal calibration is associated with the equality of the predicted and true distributions of redshift and stellar mass. Specifically, the average predictive CDF ($\hat{F}_I$) is compared to the true empirical CDF ($\tilde{G}_I$).

$$\hat{F}_I(y) = \frac{1}{N}\sum_{i=1}^{N} F_i(y), \tag{4.6}$$

$$\tilde{G}_I(y) = \frac{1}{N}\sum_{i=1}^{N} \mathbb{1}\{\tilde{y}_i \leq y\}, \tag{4.7}$$

where N is the number of test galaxies, F_i is the predicted CDF, $\tilde{y}_i$ is the true redshift or stellar mass of a galaxy, and $\mathbb{1}$ is the indicator function, defined as:

$$\mathbb{1}\{\tilde{y}_i \leq y\} = \begin{cases} 1 & \text{if True} \\ 0 & \text{if False} \end{cases}. \tag{4.8}$$

If the PDFs are marginally calibrated, then the average predictive CDF should equal the true empirical CDF. To assess probabilistic calibration, we check the uniformity of the PIT distributions visually and use quantile–quantile (Q–Q) plots to highlight deviations. In a Q–Q plot, the quantiles of one distribution are plotted against the quantiles of another distribution. In our case, these are the PIT and $U(0,1)$. If the two distributions are identical, then the quantiles match and lie along the diagonal. Furthermore, we use several metrics to quantitatively determine the uniformity of the PIT distributions (Schmidt et al., 2020), such as the Kullback–Leibler (KL; Kullback and Leibler 1951) divergence, Kolmogorov–Smirnov (KS; Shiryayev 1992) test, and Cramér-von Mises (CvM; Cramér 1928) test. All of these metrics measure the similarity between two distributions in different ways. The KL divergence is defined by the following integral:

$$KL = \int_{-\infty}^{\infty} p(x) \log(\frac{p(x)}{q(x)}) dx, \tag{4.9}$$

where $p(x)$ and $q(x)$ are the reference ($U(0,1)$) and target (PIT) PDFs, respectively. The KS test is a non-parametric test and is the maximum distance between the empirical distribution function ($F_n(x)$) and the CDF ($F(x)$) of the reference distribution.

$$KS = sup_x |F_n(x) - F(x)|, \tag{4.10}$$

where sup_x is the supremum of the set of distances. The CvM is an alternative to KS test and is more sensitive to the edges of a distribution.

$$CvM = \int_{-\infty}^{\infty} (F_n(x) - F(x))^2 dF(x). \tag{4.11}$$

A value of zero for the different metrics indicates that there is a perfect match between the two distributions.

Figure 4.3 shows the redshift and stellar mass PIT distributions and Q–Q plots for the models. The black-dashed line represents the quantiles of $U(0,1)$, and the

quantiles of the PIT distributions are shown using the solid blue curves. The values of the metrics, along with the percentage of catastrophic outliers, are also indicated. We define a catastrophic outlier to be any galaxy for which the true value of redshift or stellar mass is completely outside the support of its marginal PDF.

Visually, the PIT distributions of DES-DF and DES-WF appear to be uniform, and this is reinforced by the quantiles of the PIT distributions lying close to the diagonal in the Q–Q plots, if not on it. Consequently, at first glance, both models seem to be performing equally well. However, on closer inspection, subtle differences can be observed in the PIT distributions. The PIT distributions of DES-DF are more uniform compared to those of DES-WF, and the main difference arises at the edges. Specifically, the PIT distributions of DES-WF are slightly concave-shaped, as indicated by the minor deviations in the Q–Q plots at the extremes and quantitatively confirmed by the significantly larger CvM criterion values. Hence, the marginal PDFs produced by DES-WF are somewhat overly narrow or underdispersed. Taking into account the degraded photometry, DES-WF is still performing admirably, with only small increases in the number of catastrophic outliers compared to DES-DF. Overall, both models are producing probabilistically calibrated marginal PDFs and performing at an unprecedented level.

To assess marginal calibration, we plot the difference between the average predictive and true empirical CDFs of redshift and stellar mass at regular intervals in their respective ranges. If the PDFs are marginally calibrated, then only minor fluctuations about the zero line are expected. Figure 4.4 shows the redshift and stellar mass marginal calibration for the models. There are negligible fluctuations about the zero line, with maximum deviations of ~ 0.005. Therefore, both models are producing marginally calibrated redshift and stellar mass PDFs, with DES-DF performing marginally better with a smaller average deviation compared to DES-WF. To summarise, the marginal PDFs are both probabilistically and marginally calibrated, thus giving us confidence that they are valid. Finally, in the next section, we analyse and perform validation checks of the joint redshift–stellar mass posterior distributions.

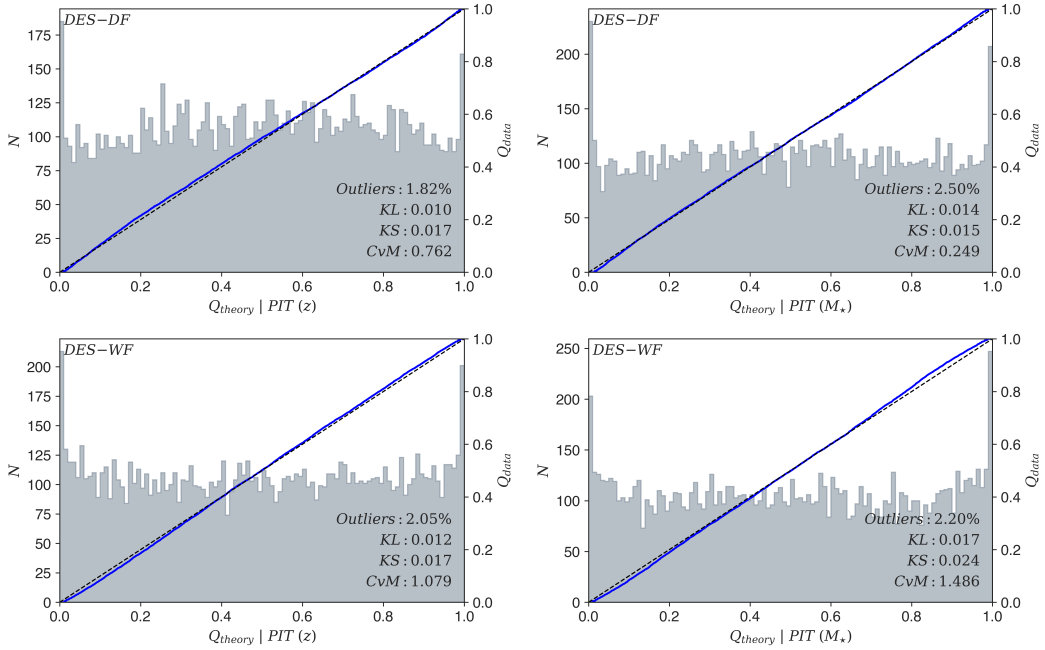

Figure 4.3: Redshift and stellar mass PIT distributions for the DES-DF and DES-WF models. These distributions are used to assess the probabilistic calibration of marginal PDFs of test galaxies produced by the models. They are overlaid with Q–Q plots to highlight deviations from uniformity. The black-dashed and solid blue lines represent the quantiles of $U(0, 1)$ and PIT distributions, respectively. The percentage of catastrophic outliers along with the values of the Kullback–Leibler (KL) divergence, Kolmogorov–Smirnov (KS) test, and Cramér-von Mises (CvM) metrics are also stated to quantify uniformity of the PIT distributions. We define a catastrophic outlier to be any galaxy with a redshift or stellar mass completely outside the support of its marginal PDF.

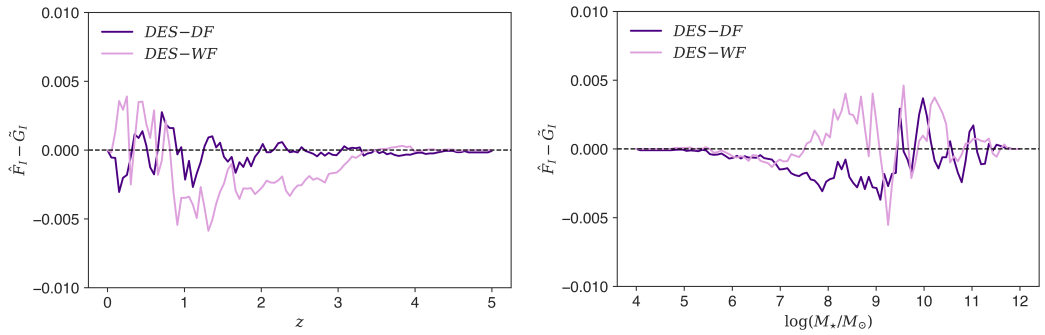

Figure 4.4: The difference between the average predictive CDF ($\hat{F}_I$) and the true empirical CDF ($\tilde{G}_I$) of redshift and stellar mass plotted at different intervals in their respective ranges. These diagnostic plots are used to assess the marginal calibration of marginal PDFs of test galaxies produced by the DES-DF and DES-WF models.

4.5.3 Joint Probability Distributions

In general, a joint PDF encompasses more information than its marginals. Therefore, we extract joint redshift–stellar mass PDFs of test galaxies from DES-DF and DES-WF. We build the distributions by combining the aggregated values of redshift and stellar mass in the leaf nodes across all the decision trees. Figure 4.5 shows some examples of the joint PDFs of the same test galaxies produced by the models. The gold and white stars alongside the dashed lines indicate the 'true' and predicted redshifts and stellar masses, respectively. We remind the reader that the predicted redshifts and stellar masses are computed by averaging the predictions from all the decision trees in a RF. Visually, the joint PDFs of the same test galaxy look alike and occupy similar regions of the redshift–stellar mass space. However, the joint PDFs produced by DES-WF are more spread out compared to the ones produced by DES-DF, or in other words, the probability is more dispersed. This is a reflection of the degraded photometry in the WF dataset. Overall, we do not expect the joint PDFs of the same galaxy to resemble each other perfectly as both models have been trained using different datasets.

4.5.3.1 Joint PDFs Validation

It is more challenging to validate joint PDFs compared to marginal PDFs as the relatively straightforward methods adopted to validate the latter are no longer applicable. As a result, we use the multivariate extensions of probabilistic and marginal calibration developed by Ziegel and Gneiting (2014) to validate joint PDFs in our case. These are probabilistic copula calibration and Kendall calibration, respectively. Probabilistic copula calibration can be empirically assessed by using the copula probability integral transform,

$$copPIT = \mathcal{K}_H(H(\tilde{y})), \tag{4.12}$$

where $H(\tilde{y})$ is the joint CDF evaluated at the true redshift and stellar mass, and $\mathcal{K}_H$ is the Kendall distribution function, defined as:

$$\mathcal{K}_H(w) = P(H(y) \leq w), \tag{4.13}$$

where $H(y)$ is the predicted joint CDF and $w \in [0, 1]$. Simply put, the Kendall

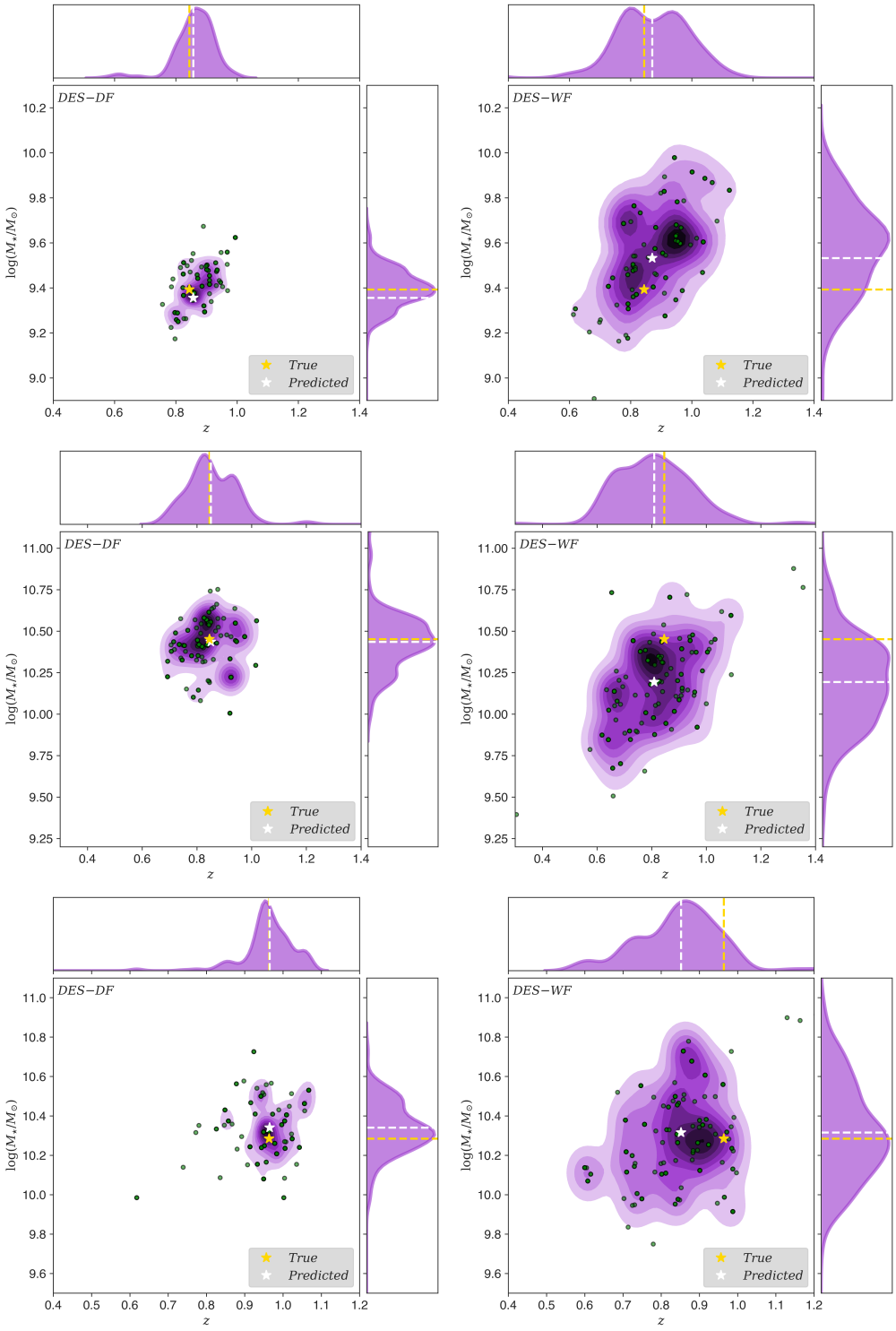

Figure 4.5: Examples of joint redshift–stellar mass PDFs produced by the DES-DF and DES-WF models of the same test galaxies (in rows). The gold and white stars alongside the dashed lines represent the 'true' and predicted redshifts and stellar masses of the galaxies, respectively. The predicted redshifts and stellar masses are computed by averaging the predictions from all the decision trees in the individual RFs. The green circles indicate the values of redshift and stellar mass in the leaf nodes that are representative of the test galaxies.

distribution function is the CDF of $H(y)$. For marginal PDFs, it corresponds to the standard uniform distribution, and the copPIT coincides with the PIT. To assess Kendall calibration, we compare what we refer to as the "average Kendall distribution function" ($\hat{\mathcal{K}}_{H_I}$) to the empirical CDF of the predicted joint CDFs evaluated at the true redshifts and stellar masses ($\tilde{J}_I$):

$$\hat{\mathcal{K}}_{H_I}(w) = \frac{1}{N}\sum_{i=1}^{N}\mathcal{K}_{H_i}(w), \tag{4.14}$$

$$\tilde{J}_I(w) = \frac{1}{N}\sum_{i=1}^{N}\mathbb{1}\{H_i(\tilde{y}_i) \leq w\}. \tag{4.15}$$

Probabilistic copula calibration and Kendall calibration can be interpreted in the same manner as their univariate counterparts. As such, probabilistic copula calibration ascertains if the true redshifts and stellar masses of galaxies are random draws from their corresponding joint PDFs, as they should be. If this is the case, then for an ensemble, the copPIT distribution is uniform, and the joint PDFs are probabilistically copula calibrated. On the other hand, Kendall calibration probes how well the dependence structure between redshift and stellar mass is predicted on average, and can be understood as marginal calibration of the Kendall distribution. If $\hat{\mathcal{K}}_{H_I}$ is comparable to $\tilde{J}_I$, then the joint PDFs are Kendall calibrated. Once again, if both modes of calibration are satisfied, then we can claim with some conviction that the joint PDFs are valid overall. Furthermore, we would like to point out that while we use probabilistic copula calibration and Kendall calibration to validate our joint redshift–stellar mass PDFs, they can be applied to validate higher dimensional PDFs also.

Figure 4.6 shows the copPIT distributions for the DES-DF and DES-WF models. The distributions are uniform with minor deviations, which are more prominent for DES-WF. Overall, both models are performing well with no substantial differentiation and producing joint PDFs that are probabilistically copula calibrated. Furthermore, in comparison to the PIT distributions in Figure 4.3, the copPIT distributions of DES-WF are somewhat less uniform, as primarily reflected by the large CvM value. Hence, the marginal PDFs produced by the model are better probabilistically calibrated than the joint PDFs.

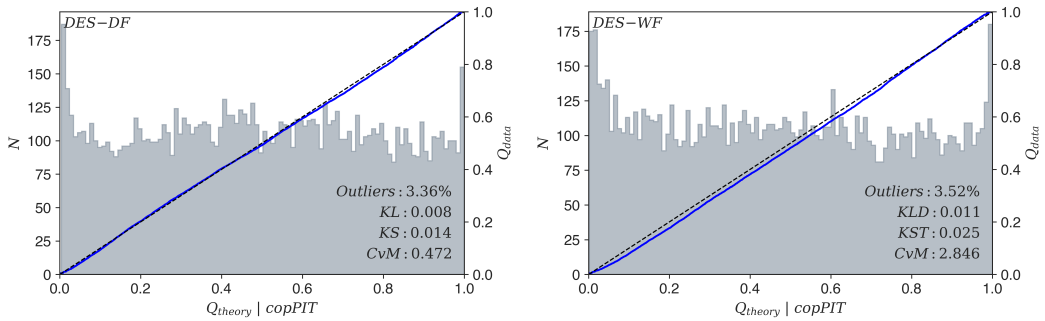

Figure 4.6: copPIT distributions for the DES-DF and DES-WF models. They are overlaid with Q–Q plots to aid in visually assessing the probabilistic copula calibration of joint redshift–stellar mass PDFs of test galaxies. The black-dashed and solid blue lines represent the quantiles of $U(0,1)$ and copPIT distributions, respectively. The percentage of catastrophic outliers along with the values of the Kullback–Leibler (KL) divergence, Kolmogorov–Smirnov (KS) test, and Cramér-von Mises (CvM) metrics is also stated to quantify uniformity of the copPIT distributions. We define a catastrophic outlier to be any galaxy that is completely outside the support of its marginal PDFs. Probabilistic copula calibration is the multivariate analogue of probabilistic calibration.

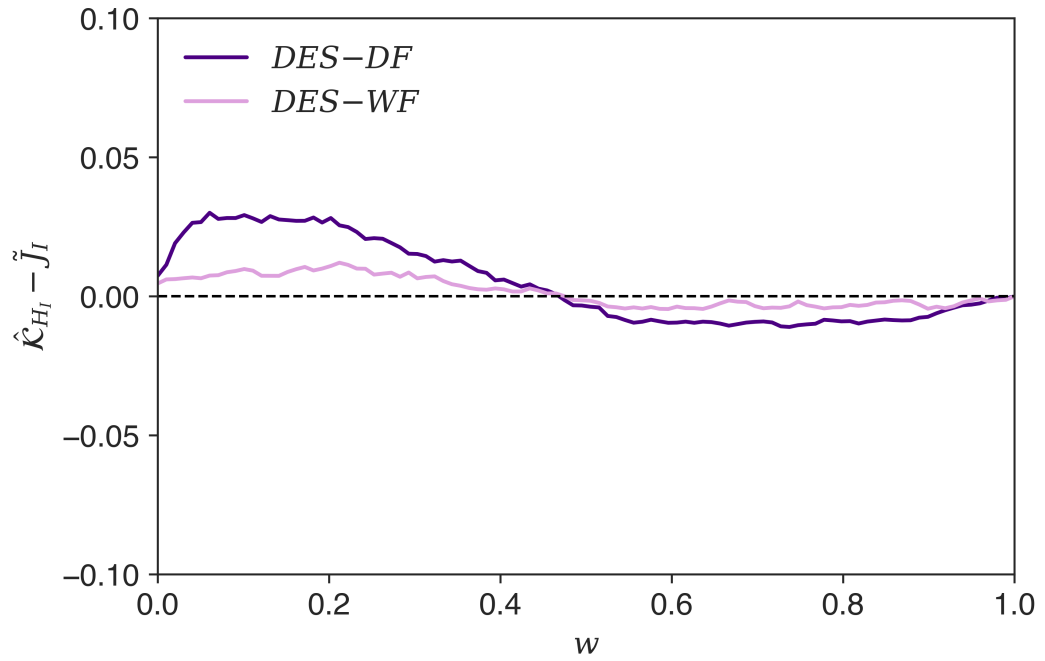

Figure 4.7: The difference between the "average Kendall distribution function" ($\hat{\mathcal{K}}_{H_I}$) and the empirical CDF of the predicted joint CDFs evaluated at the 'true' redshifts and stellar masses ($\tilde{J}_I$), plotted at regular intervals in the probability space $w \in [0,1]$. This diagnostic plot is used to assess the Kendall calibration of the joint PDFs produced by the DES-DF and DES-WF models. Kendall calibration is the multivariate analogue of marginal calibration.

Figure 4.7 shows the difference between $\hat{\mathcal{K}}_{H_I}$ and $\tilde{J}_I$ at regular intervals in the probability space w. For DES-WF, the fluctuations about the zero line are smaller compared to those for DES-DF, thus indicating that the joint PDFs produced by the former are better Kendall calibrated. We believe that DES-WF is better capturing the redshift–stellar mass dependence structure as it is trained using the WF dataset that contains multiple scattered copies of the same DF galaxies, resulting in better incorporation of photometric errors present in the data into the model. Collectively, the joint PDFs are less marginal/Kendall calibrated compared to the marginal PDFs as the deviations are larger in magnitude. However, we hypothesise that the deviations in the Kendall calibration are not significant given the complex nature of joint PDFs, and to prove this, we compare our results to those achieved by the SED-fitting code `BAGPIPES` in the next section.

4.6 Comparison: ML versus SED Fitting

The different diagnostic plots and the metrics we utilise to validate the marginal and joint PDFs produced by our RF models are difficult to fully appreciate without familiar context. Consequently, we utilise Bayesian Analysis of Galaxies for Physical Inference and Parameter EStimation, or `BAGPIPES` (Carnall et al., 2018), to benchmark our results. `BAGPIPES` is a Python package that uses `MultiNest` (Feroz and Hobson, 2008; Feroz et al., 2009, 2019) nested sampling algorithm, accessed through the `PyMultiNest` interface (Buchner et al., 2014), to model the emission from galaxies and to fit these models to any combinations of spectroscopic and photometric data in order to output multivariate posterior distributions of parameters such as redshift and stellar mass, hence making it ideal for comparison.

The photometry in the COSMOS2015 and DES Y3 DF catalogues have been calibrated independently of one another. So, although we can expect them to be broadly consistent, it is possible that small differences in absolute calibration between the two remain. Even minor offsets in the calibration baseline may have a significant impact on the stellar mass posterior PDFs produced using `BAGPIPES` with respect to COSMOS2015, and perhaps also some subtle effects in redshift. Accordingly, validation of the PDFs using the point predictions in the catalogue would not be appropriate. To solve this dilemma, we run `BAGPIPES` on Subaru V, r, $i+$, and $z++$ bands' photometry from the catalogue in place of the DES DF $griz$ bands. We

specifically choose these bands in order to imitate the DES bands as far as possible and therefore allow for an adequate comparison between the SED-fitting method and our ML-based method. Although this does not match exactly the degradation in the information provided to the RF, it is nevertheless very similar as we measure PDFs using four optical bands instead of the 30-plus bands available in the catalogue. Importantly, however, we avoid introducing any possible systematic effects that could arise from inter-dataset calibration differences.

The model SED templates used by Laigle et al. (2016) cannot be exactly reproduced in `BAGPIPES`. It is important for the validity of our comparison that the four-band PDFs and the truth values are constructed under the same set of model assumptions. Therefore, we produce a new set of truth values using the 22 COSMOS bands (including the four aforementioned) listed in Table 4.1. In both the four-band and 22-band runs, we employ the same physical information about the model as outlined in Table 4.2. These choices were made to closely mimic the set-up adopted by Laigle et al. (2016) to compute the redshifts and stellar masses in the COSMOS2015 catalogue, so that we can make a fair comparison. There are, however, slight differences that we cannot negate, and as such, a direct comparison is not possible. Nevertheless, they are mostly similar, and the aggregate metric results should be comparable. We compute total COSMOS flux and flux errors from those measured in a 3 arcsec diameter aperture, correct for photometric and systematic offsets, and foreground galaxy extinction before initiating the runs. We define the true values of redshift and stellar mass from the 22-band run to be the mean predictions for each galaxy. Finally, we extract marginal and joint PDFs of redshift and stellar mass from the four-band run and validate them using these new 'truth' values. We utilise a total of 14 nodes for both runs, with each node consisting of 12 Xeon X5660 cores and 16GB of random-access memory (RAM). The runs take approximately 900 and $1,400$ hours to generate PDFs for $10,699$ galaxies, respectively. Naturally, we only run `BAGPIPES` on test galaxies in the DF dataset.

SED fitting with four bands is known to be difficult due to degeneracies in the parameter space (see Renzini, 2006, for a review). To compensate, authors sometimes restrict the parameter space, for example, by neglecting dust extinction to improve results (e.g., Capozzi et al., 2017), and this amounts to a hard prior in the galaxy

Instrument/Telescope (Survey)	Band
UltraVista	Y, J, H, Ks
CFHT	u
Subaru	B, V, r, i+, z++, IA427, IA464, IA484, IA505 IA527, IA574, IA624, IA479 IA709, IA738, IA767, IA827

Table 4.1: List of 22 COSMOS bands used to build a 'truth' catalogue to validate the marginal and the joint PDFs of redshift and stellar mass produced by `BAGPIPES` using the four-band (V, r, $i+$, and $z++$) Subaru photometry.

Free parameter	Prior	Limits	Fixed parameter	Value
A_V	Uniform	[0, 4]	$\log_{10}(U)$	-3
$\log_{10}(M_\star/M_\odot)$	Uniform	[4, 13]	a_{BC}	0.01 Gyr
z	Uniform	[0, 10]	ϵ	3
τ	Uniform	[0.3, 10]	SPS models	Bruzual and Charlot (2003)
$Z/Z_\odot$	Uniform	[0, 2.5]	IMF	Kroupa and Boily (2002)

Table 4.2: Fixed and fitted parameters with their associated priors for the delayed exponentially declining ($\tau^{-2}te^{-t/\tau}$) star-formation history (SFH) model used in the `BAGPIPES` runs. The model is not readily available in `BAGPIPES`, so we lightly modify the code to meet our requirements. We adopt the Calzetti et al. (2000) attenuation curve, stellar population synthesis (SPS) models of Bruzual and Charlot (2003), and a Kroupa and Boily (2002) initial mass function (IMF). A_V is the attenuation in the V-band, τ is the star formation time-scale, Z is the metallicity, U is the ionisation parameter, a_{BC} is the lifetime of HII regions, and ϵ is a constant that controls the extra attenuation towards them.

population. By design, RF includes an implicit prior built from the training data. We approximate the effect of this prior by applying a 2D population prior formed from the redshifts and stellar masses in the 'truth' catalogue to the PDFs estimated by `BAGPIPES` using the four-band photometry. To apply the prior, we fit a kernel density estimate (KDE) to the 'true' redshifts and stellar masses. We use 1% of the total number of point predictions to fit this prior, which equates to $\sim 200,000$ data points. Next, we compute the prior probability density at each redshift–stellar mass sample point output by the `BAGPIPES` nested sampling (with four-band photometry). We produce a smoothed posterior of these points, weighted by the prior probability, via another KDE. Finally, we draw 1000 importance samples from this smoothed posterior. We repeat this process for all the galaxies.

We explored the possibility of applying a full 6D prior because, in principle, it should further improve the results. However, doing so caused a large number of galaxies to become catastrophic outliers. It is beyond the scope of this work to go through the painstaking process of carefully optimising a high-dimensional prior, as we simply want a comparison that assists the reader's intuition in interpreting the result from our RF models. Nevertheless, we still had a considerable percentage $(6-7\%)$ of catastrophic outliers even with our 2D prior. These outliers can skew the performance in terms of the metrics we have chosen and can often be treated separately in scientific analyses. Hence, we remove these outliers and then perform the different calibration checks to better gauge the performance of the population at large.

Figure 4.8 shows the PIT and the copPIT distributions alongside the marginal and Kendall calibration plots from the analysis, and for comparison, they are overlaid with results from the DES-DF model, labelled as `GALPRO`. The PIT distributions are not uniform and indicate biased marginal PDFs for the galaxy population, which correlates well with the marginal calibration plots that have large fluctuations about the zero line. Nevertheless, the marginal redshift PIT distribution is competitive with SED-fitting approaches used in code comparison works, e.g., Schmidt et al. (2020, Figure 2) and Euclid Collaboration: Desprez et al. (2020, Figure 7). However, these studies use deeper data than in this work. Unsurprisingly, a small number of joint PDFs are also biased, as reflected by the non-uniform copPIT distribution.

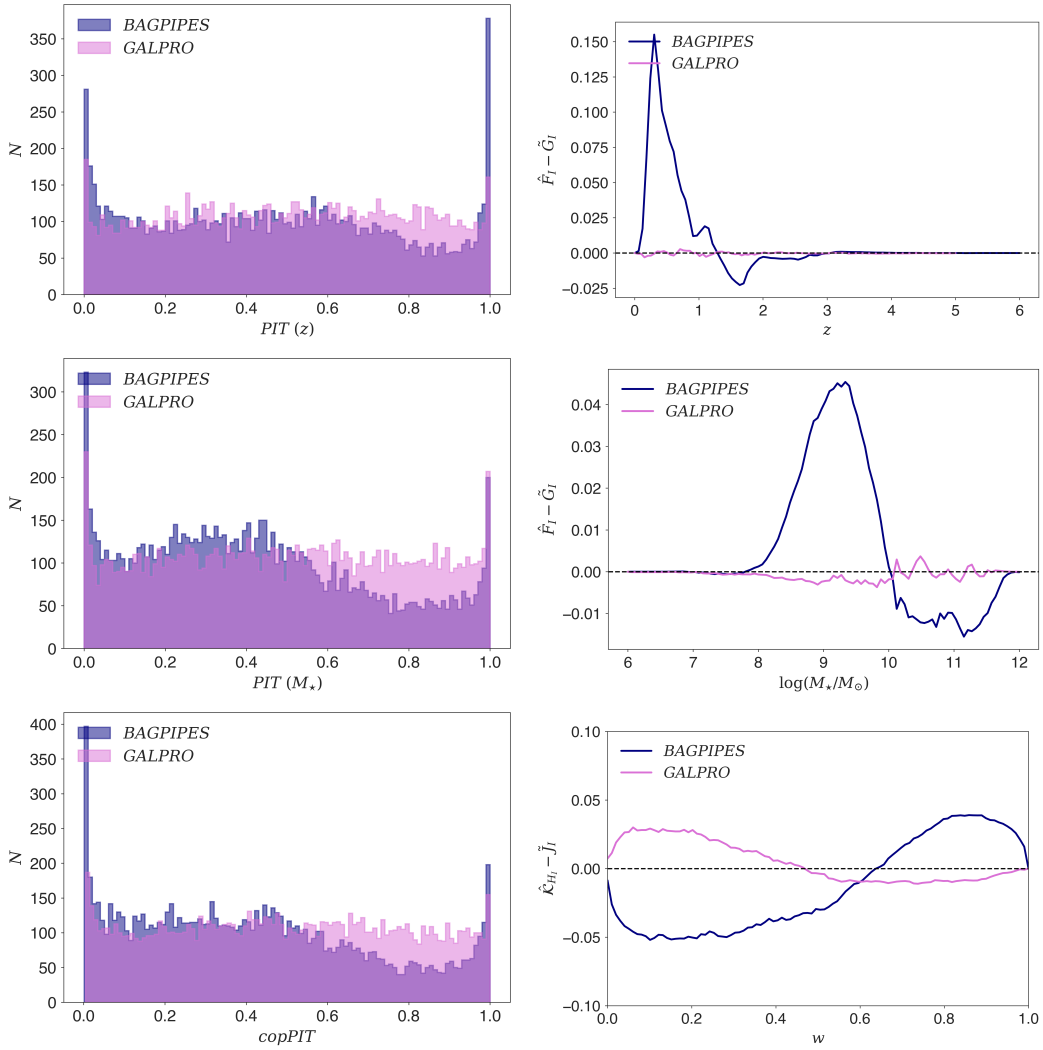

Figure 4.8: Comparison diagnostic plots for benchmarking the performance of `GALPRO` on test galaxies in the DF dataset against that of `BAGPIPES` on a comparable dataset, which is composed of the same galaxies but with Subaru photometry in four bands (V, r, $i+$, and $z++$) from the COSMOS2015 catalogue. The marginal and joint PDFs of redshift and stellar mass produced by `BAGPIPES` are validated using a 'truth' catalogue constructed by running `BAGPIPES` on photometry in 22 COSMOS bands listed in Table 4.1.

Despite the biased PDFs, BAGPIPES does manage to capture the dependence structure between redshift and stellar mass on a similar level to that achieved by the RF. On the whole, RF outperforms BAGPIPES on the metrics we have considered in our analysis. Having said that, it should be possible for BAGPIPES to match the performance of the RF through judicious use of priors and great care in photometric calibration. A great advantage of the RF is that the large effort that would be required to do so is not necessary. An implicit prior is automatically applied, transferring information from the rich training dataset to our target data.

To summarise, we have benchmarked the performance of GALPRO against BAGPIPES, and by doing so, we have been able to place our results into context. We have found that our ML-based method performs better in every aspect compared to a SED-fitting method that employs a fairly standard set-up. Thus, we have confidence that our models are producing valid marginal and joint posterior probability distributions, based on the different calibration modes and metrics we have employed in our analysis.

4.7 Conclusions

The emergence of SED-fitting methods with the capability of generating multivariate PDFs of redshift and physical properties of galaxies represents a paradigm shift. These PDFs account for potential correlations between different galaxy properties and fully characterise uncertainties associated with point estimates of the quantities. However, with their potential benefits, comes the task of generating them quickly, which is difficult given their complexity. For example, the SED-fitting code BAGPIPES takes a few minutes to fit each galaxy. While this may not seem significant, the amount of time required to generate them for hundreds of thousands of galaxies, let alone the billions that will be observed with the upcoming photometric surveys such as LSST and Euclid, quickly becomes impractical. Coupled with the difficulty of storing such PDFs, a solution that enables on-the-fly production at speed is greatly desirable.

In this work, we tackle the problem by using an ML-based approach. We introduce a novel method based on the RF algorithm to generate joint PDFs. As an example, we generate PDFs for the probability space in redshift and stellar mass, as they are two of the most important to accurately predict. Our method can

be generalised to extract n-dimensional PDFs. However, we focus on this specific two-dimensional space as it is easy to visualise and exhibits well-known correlations between the properties.

To demonstrate the method, we train two RF models to produce joint PDFs of galaxies in the DES DF and the main WF DES survey, respectively. We separately combine the COSMOS2015 catalogue, with the DES Y3 DF and the Y3 Balrog to construct the necessary datasets, which contain $53,941$ and $393,276$ galaxies, respectively. From the trained models, we extract point estimates and marginal and joint PDFs of $10,699$ test galaxies. We then proceed to determine the validity of both sets of PDFs, and for this, we utilise the notions of probabilistic copula calibration and Kendall calibration to validate the joint PDFs, and their univariate counterparts to validate the marginals. We highlight in particular the advantage of incorporating realistic photometric errors into the RF on Kendall calibration. We benchmark our results against those achieved by `BAGPIPES`, adopting a basic set-up and simple population-derived prior in redshift and stellar mass, to provide some context to the metric values and guide our intuition. We find that our ML-based method is producing valid PDFs with only small calibration errors and performs at a superior level on every metric we consider in our analysis compared to `BAGPIPES`. Despite the success of our method, SED-fitting approaches such as `BAGPIPES` undoubtedly still have a vital role to play in building the training samples for ML-based codes.

To conclude, joint redshift–stellar mass PDFs have many potential science applications, from determining the evolution of the SMF to constraining the SHMR. Consequently, we have developed `GALPRO`, a highly intuitive and efficient Python package for rapidly generating n-dimensional PDFs on the fly, thus solving the potential issue of storage. We have trained and tested our RF models using `GALPRO` on a 13" Macbook Pro (2.4 GHz Intel Core i5, 16GB LPDDR3) and found that, at best, it takes on average a few milliseconds to generate a PDF. Thus, `GALPRO` can potentially offer a $100,000x$ reduction in run time compared to packages based on SED-fitting methods, making it ideal for the impending era of "Big Data". Of course, one must ensure that the training dataset is representative and suitable for their scientific analysis to fully reap the benefits of `GALPRO`.

Chapter 5

The Causal Effect of Environment on Galaxies with Causal Machine Learning

This Chapter is based on *Mucesh et al. (in prep)*: The Causal Effect of Environment on Star Formation with Causal Machine Learning.

The formation and evolution of galaxies is a consequence of both their nature and nurture. The two components are heavily intertwined, as nature influences nurture and vice versa in a feedback loop as the galaxies and their environments co-evolve over time. This muddling of causality combined with the lack of knowledge of the evolutionary history of galaxies has hindered progress and restricted observational studies to imply a galaxy–environment causal connection without the causal effect.

We aim to make progress with the emerging field of causal machine learning (causal ML). In this work, we establish the causal nature of the star-formation rate (SFR)–density relation in the IllustrisTNG simulations, specifically the TNG100-1 run. We construct a comprehensive causal model of galaxy formation and evolution and employ the g-method, inverse probability weighting (IPW) of marginal structural models (MSMs; Section 5.4), to disentangle nature and nurture. We apply the random forest (RF) algorithm in a two-step estimation process to determine the overall causal effect of environment on the SFR at $z = 0$. Additionally, we estimate the causal effect at different redshifts going back to $z \sim 3$ (with a baseline at $z \sim 6$) to understand how the role of environment has changed over time.

We find the causal effect is negative and substantial, with environment suppressing the SFR by a factor of ~ 100. While the environment has a negative impact on star formation at low-to-intermediate redshifts ($z \lesssim 1$), at high redshifts ($z \gtrsim 1$), the role is reversed as it has a positive impact and boosts the SFR. Furthermore, we reveal that: (i) nature plays a significant role since ignoring its effect results in the causal effect in the densest environment being underestimated by a factor of ~ 6, (ii) controlling for the stellar mass at a snapshot in time (as is common in the literature) is not only insufficient but actually has an adverse effect. The negative effect at low-to-intermediate redshifts is overestimated, while the positive effect at high redshifts is underestimated, by up to a factor $\gtrsim 10$ at specific densities, though (iii) stellar mass is an adequate proxy of the effects of nature. The results are supported by diagnostic tests, which indicate that our causal model is valid and the causal assumptions might be satisfied.

5.1 Introduction

Galaxies are diverse entities, with no two being completely alike. However, the population naturally separates into two distinct, broad classes: the red sequence of massive, red, early-type, quiescent galaxies, and the blue sequence of less-massive, blue, late-type, star-forming galaxies. In the local Universe, the bimodal population is unevenly distributed, with the red sequence mainly found in groups and clusters and the blue sequence located in relative isolation in the field. In other words, galaxy properties are correlated with environment. The fundamental question is then: are the correlations causal?

The well-established morphology–density (Dressler, 1980), colour–density (Kodama et al., 2001), and star-formation rate (SFR)–density (Gómez et al., 2003) relations reveal that as environmental density increases, there is a shift from late-type to early-type morphologies (Hubble and Humason, 1931; Zwicky, 1937; Morgan, 1961; Abell, 1965; Oemler, 1974; Davis and Geller, 1976; Postman and Geller, 1984; Whitmore and Gilmore, 1991; Santiago and Strauss, 1992; Whitmore et al., 1993; Hermit et al., 1996; Guzzo et al., 1997; Domínguez et al., 2001; Giuricin et al., 2001; Treu et al., 2003; Goto et al., 2003), an increase in the fraction of red galaxies (Willmer et al., 1998; Brown et al., 2000; Pimbblet et al., 2002; Zehavi et al., 2002; Hogg et al., 2004; Blanton et al., 2005; Martínez and Muriel, 2006), and a decline in the star-formation activity of galaxies (Balogh et al., 1997, 1998; Hashimoto et al., 1998; Poggianti et al., 1999; Balogh et al., 2000; Couch et al., 2001; Postman et al., 2001; Carter et al., 2001; Lewis et al., 2002; Balogh et al., 2004a; Tanaka et al., 2004; Rines et al., 2005), respectively. The correlations may be causal, but one has to be careful as "correlation does not imply causation". Notably, stellar mass is strongly correlated with most galaxy properties (McGaugh and de Blok, 1997; Blanton et al., 2003; Kauffmann et al., 2003b,a; Baldry et al., 2004b; Hogg et al., 2004) and environment (Balogh et al., 2001; Hogg et al., 2003; Mo et al., 2004; Croton et al., 2005; Hoyle et al., 2005; Blanton et al., 2005). Consequently, are the observed correlations due to internal processes that scale with stellar mass rather than external processes associated with environment? This is the essence of the nature versus nurture debate.

Galaxy formation and evolution is conceivably a result of both nature and nurture.

Typically, analyses have attempted to isolate the effect of nature by controlling for stellar mass. A common approach has been to bin galaxies into fixed bins of stellar mass before drawing conclusions from the residual trends. Most studies have found that galaxy properties still depend on environment (Kauffmann et al., 2004; Balogh et al., 2004b; Baldry et al., 2004a, 2006; Weinmann et al., 2006; Bamford et al., 2009; Skibba et al., 2009). Overall, there is little doubt that environment plays a role in shaping the evolution of a galaxy. But the magnitude of the role is still up for debate (Pasquali et al., 2009; Thomas et al., 2010; Grützbauch et al., 2011).

There is uncertainty on whether controlling stellar mass is sufficient to disentangle the roles of nature and nurture (De Lucia et al., 2012). Furthermore, it is still unclear whether the nature versus nurture debate is sensible in the first place. In biology and many other fields, there is consensus that nature influences nurture and vice versa in a feedback loop. This is arguably true for galaxy evolution as well, as galaxies and their environments interact with each other over time. In this instance, the notion of separating the influence of nature and nurture is muddled and ill-defined.

There is some evidence to suggest that the effects of stellar mass and environment are separable (Peng et al., 2010; Quadri et al., 2012; Kovač et al., 2014). Peng et al. (2010) concluded that there are two processes associated with stellar mass and environment that play a major role in quenching galaxies independently of each other, which they termed "mass quenching" and "environmental quenching", respectively. Simply put, massive galaxies become quiescent independent of their environment, and galaxies located in high-density regions quench independently of their stellar mass. Given the strong possibility of a causal connection between stellar mass and environment (Bolzonella et al., 2010; De Lucia et al., 2012; Mortlock et al., 2015; Darvish et al., 2015; Davidzon et al., 2016), and contradictory studies (Lin et al., 2014; Knobel et al., 2015; Darvish et al., 2016; Kawinwanichakij et al., 2017), the result is puzzling and requires further exploration.

As galaxies and their environments co-evolve over time, consideration of their histories is likely paramount to infer causality. Yet, observational studies in the past have been confined to a sole snapshot in time, predominantly focused on the local Universe due to the limitations of the then-available surveys. The advent of deep surveys, such as COMBO-17 (Wolf et al., 2003), Great Observatories Origins

Deep Survey (GOODS; Giavalisco et al. 2004), Deep Extragalactic Evolutionary Probe (DEEP; Vogt et al. 2005) and DEEP2 Galaxy Redshift Survey (DEEP2; Davis et al. 2003; Newman et al. 2013), and Cosmic Evolution Survey (COSMOS; Scoville et al. 2007) and zCOSMOS (Lilly et al., 2007), has enabled studies to utilise multiple snapshots over time. However, they still suffer from being unable to trace the evolution of an individual galaxy, thereby weakening any evidence of causality (VanderWeele et al., 2016).

In summary, we believe the lack of a theoretical framework to think and reason about causal questions, combined with the limitations of observational data, has hindered progress in the field. The studies have been largely statistical in nature, so they have hinted towards causality but without mathematical conviction. We aim to make progress by: (i) adopting the causal inference framework to comprehend and solve the discussed problems and (ii) using simulations to trace both the evolution of the galaxy population and individual galaxies over time.

Causal inference methods have been applied to answer crucial questions in various fields, such as economics (Angrist and Krueger, 1991; Card and Krueger, 1993; Cengiz et al., 2019), political science (Kam and Palmer, 2008), education (Angrist and Lavy, 1999; Carlsson et al., 2015), policy (Ghosh et al., 2018), public health (Doll and Hill, 1950; Chay and Greenstone, 2003; Clark and Royer, 2013; Desouza et al., 2022), and more recently, astronomy (Schölkopf et al., 2015; Wang et al., 2016). Despite their success, the methods do not scale to handle high-dimensional and unstructured data and non-linear relationships. Conversely, these are the strengths of machine learning (ML) methods. ML has proliferated in most fields, including astrophysics (see Baron, 2019; Fluke and Jacobs, 2020, for recent reviews). And in recent years, ML algorithms have even been utilised for causal insights into galaxy formation and evolution by determining the predictive power (Teimoorinia et al., 2016; Bluck et al., 2019, 2020a,b, 2022; Brownson et al., 2022; Piotrowska et al., 2022; McGibbon and Khochfar, 2022). For example, Bluck et al. (2022) estimated feature importances with the random forest (RF; Breiman 2001) algorithm and demonstrated that it is capable of identifying causal from non-causal parameters (known from simulations). Nonetheless, the predictive power of a variable does not translate to the causal effect and cannot guarantee causality because ML is fundamentally correlation-based. The

missing ingredient is causal inference.

Causal machine learning (Causal ML) aims to empower causal inference with powerful ML techniques and ML with causal reasoning (see Kaddour et al., 2022, for a review). The field is still in its infancy but is developing rapidly and has already shown some promising results (Richens et al., 2020). In this chapter, we apply causal ML to disentangle the roles of nature and nurture and establish the causal nature of the SFR–density relation. We estimate the causal effect of environment on the SFR at $z = 0$ to determine the overall impact and at different redshifts out to $z \sim 3$ to determine how the role of environment has changed over cosmic time. Furthermore, we answer the fundamental questions:

1. Is stellar mass an adequate proxy of the effects of nature?

2. Does controlling for the stellar mass at a snapshot in time disentangle the effects of nature and nurture?

3. Is nature important in the nature–nurture debate? Specifically, is galaxy formation and evolution top-down determined by environment with no reverse influence of nature?

The outline of this chapter is as follows. In Section 5.2, we construct a comprehensive causal model of galaxy formation and evolution. In Section 5.3, we detail the preprocessing steps we follow to prepare the galaxy sample we use in our analysis. In Section 5.4, we describe the causal inference method we employ to disentangle nature and nurture and estimate the causal effect of environment on SFR. In Section 5.5, we outline the overall two-step ML estimation process we apply to estimate the causal effects. In Section 5.6, we validate our results by performing diagnostic tests to ascertain whether the causal assumptions are satisfied and our causal model is correct. In Section 5.7, we discuss and interpret the results, and place them into a wider context via a model comparison. Finally, we summarise this chapter and discuss potential future work in Section 5.8.

5.2 Causal Model of Galaxy Formation and Evolution

Our goal is to estimate the causal effect of environment on SFR. Given that performing an RCT on the Universe is impossible, we must infer the causal effect from observational data[1]. As detailed in Chapter 3, observational data suffers from many biases, which make any direct inference invalid. Causal inference from observational data necessitates identifying and nullifying the biases with expert knowledge and a priori assumptions about the data-generating process (DGP) in the form of causal models. Consequently, we construct a causal model of galaxy formation and evolution.

We assume the cold dark matter (CDM) paradigm, in which galaxies form and evolve hierarchically in dark matter haloes (White and Rees, 1978; Efstathiou and Silk, 1983; Blumenthal et al., 1984). To build our causal model, we review established theories of galaxy formation and evolution, and in particular ideas from semi-analytic modelling (SAM; White and Frenk 1991; Cole 1991; Kauffmann et al. 1993; Cole et al. 1994; Kauffmann et al. 1999; Somerville and Primack 1999; Springel et al. 2001; Hatton et al. 2003; Springel et al. 2005; Kang et al. 2005; Lu et al. 2011; Benson 2012; Henriques et al. 2015; also see Baugh 2006; Benson 2010, for reviews), and express them as causal graphs. We carefully consider all the relevant physical processes and assemble the causal model step-by-step with mini causal models before connecting all the pieces.

We note that a method called genetic modification (GM; Roth et al. 2016) has emerged that can determine the causal effect in simulations. Based on performing controlled experiments, it mimics in effect an RCT and has been applied to estimate the causal effect of environment (Cadiou et al., 2021). While the approach is promising, it is limited to a single object (at a time) and, more importantly, cannot be applied to the real Universe. Also, while we build the causal model, it is conceivable to infer it—the aim of causal discovery. However, identifying causality is not our goal, but rather the question this thesis attempts to address is: given our knowledge of galaxy formation and evolution, how can we estimate the causal effect?

We adopt a straightforward naming convention in the causal model: any variables associated with the halo and galaxy are preceded by them, respectively. Furthermore, halo refers to the dark matter halo that hosts a galaxy, and host halo refers to the

[1]Observational data here refers to data not acquired through experimentation.

parent dark matter halo that hosts other haloes. As such, halo refers to both distinct haloes and subhaloes. In the following section, we describe the galaxy formation process. Figure 5.1 shows the mini causal models of the different stages of galaxy formation and standard physical processes occurring in galaxies.

5.2.1 Galaxy Formation

In the very early Universe, quantum fluctuations of the scalar field drive inflation and generate density perturbations in the initial matter density field, sowing the seeds for galaxy formation (Guth and Pi, 1982; Hawking, 1982; Linde, 1982; Starobinsky, 1982; Bardeen et al., 1983). The small perturbations evolve under gravitational instability as regions of space with above-average density attract matter and become denser over time. Conversely, regions of space with below-average density lose matter and become rarefied over time. The outcome is the amplification of the initial density contrast.

Once a region reaches over-density ($\delta\rho/\rho \sim 1$), it breaks away from the cosmological expansion and collapses to form a dark matter halo (Mo et al., 2010). The primordial haloes are small as perturbations on the smallest scales collapse first (Benson, 2010). The mass and environment of the dark matter halo are a product of the evolution of the initial matter density field, or more specifically, the amplitude and pattern of the initial density perturbations, respectively. In the causal model, we loosely label this as "initial conditions": the 'cause' of the initial haloes and their environment (Figure 5.1–1). Given that galaxies form in dark matter haloes, we associate nature with halo mass, and nurture to environment.

The ordinary baryonic matter falls into the gravitational potential well of the dark matter halo and is shock-heated to the haloes' virial temperature to produce a hot gas halo that is supported against further collapse by the pressure of the gas. Thus, halo gas mass and temperature depend on halo mass (Figure 5.1–2,3). Subsequently, the hot gas can cool through various mechanisms (Kauffmann et al., 1993), which removes the pressure support and causes the gas to sink to the centre of the gravitational potential well (Silk, 1977; Rees and Ostriker, 1977; Binney, 1977; White and Frenk, 1991; Cole, 1991; Lacey and Silk, 1991). If the angular momentum is conserved during the cooling process, the gas spins up as it flows inwards and forms a rotationally supported disc (Fall and Efstathiou, 1980; Mo et al., 1998).

Primarily, two factors determine the mass of cold gas in the disc: (i) the cooling rate (i.e., the mass of gas cooled per unit time) and (ii) the free-fall time (i.e., the time taken for the cooled gas to transfer from the halo to the disc) (Figure 5.1–6). The cooling rate depends on the metallicity, temperature, and density of the halo gas (Figure 5.1–4). Specifically, the temperature and density determine the ionisation state and collision rate, respectively. The free-fall time depends on the halo mass and radius (Figure 5.1–5).

As the gas accumulates, its self-gravity dominates over that of the dark matter—and it collapses. The exact process of star formation from a self-gravitating gas cloud is unknown, but there are two theories. In the bottom-up theory, low-mass stellar cores acquire gas from the cloud in a competitive accretion process (Bonnell et al., 1997), while in the top-down theory, the gas cloud simply fragments and the sub-clouds collapse to form stars (Krumholz et al., 2005). Independent of the exact model, the star-formation rate (SFR) depends on the local density of cold gas (Schmidt, 1959; Kennicutt, 1998) (Figure 5.1–7,8). This is the standard paradigm of galaxy formation.

We remark that halo accretion also depends on environment, and generally, the halo and forming galaxy are subject to external processes (discussed in Section 5.2.2.2). Thus, galaxy formation depends not only on nature but also nurture.

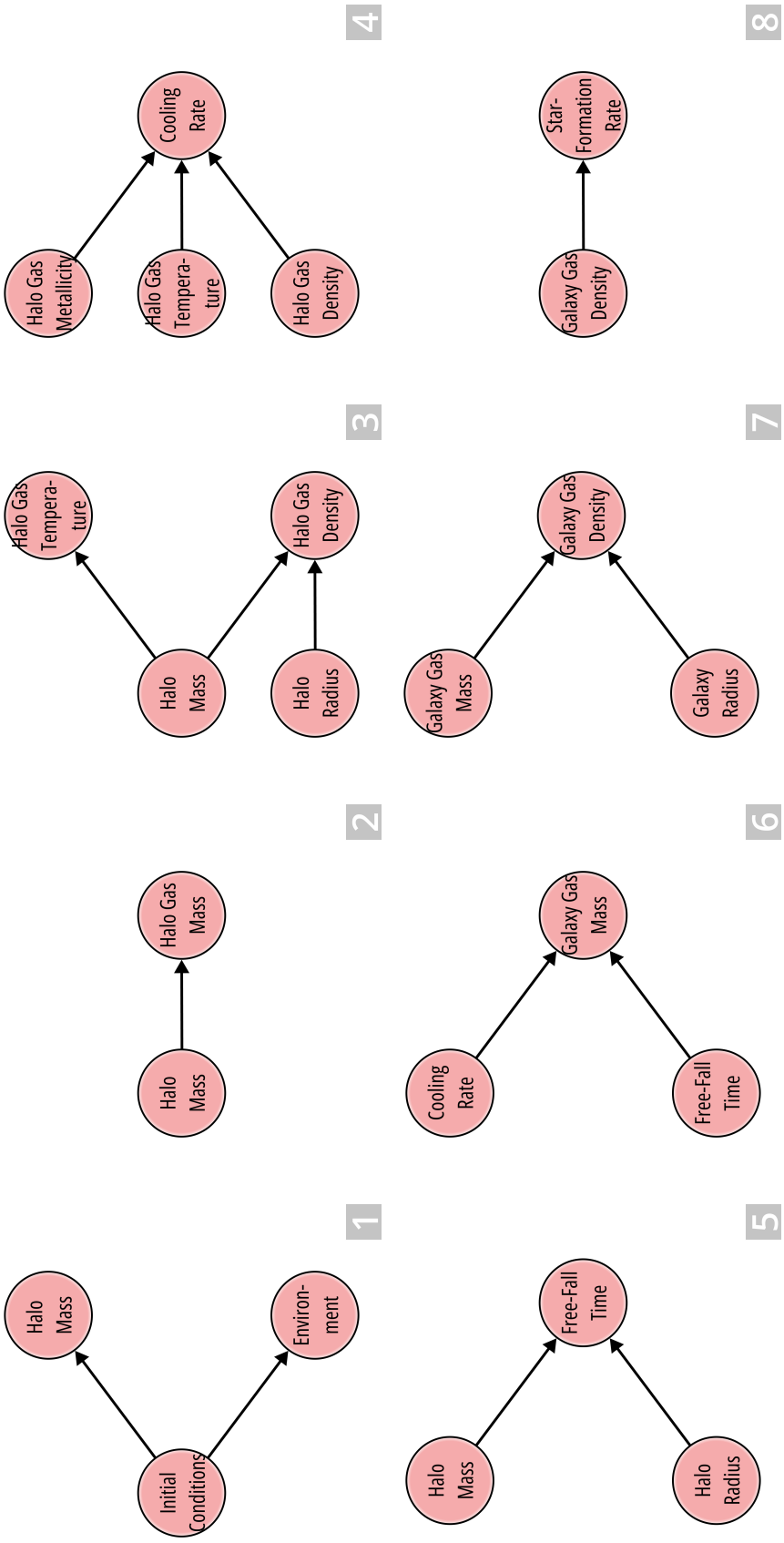

Figure 5.1: Mini causal models of different stages of galaxy formation and standard physical processes occurring in galaxies. For visual clarity, all the possible causal connections of a variable with others are not drawn.

5.2.2 Galaxy Evolution

In this section, we describe the internal and external processes that shape the evolution of galaxies. We do not attempt to model the different processes in detail or as accurately as possible because our goal is to estimate the overall causal effect of environment rather than of individual processes. Instead, we focus on conveying how the processes are related to halo mass and environment and their impact on galaxy properties, especially SFR. Figures 5.2 and 5.3 show the mini causal models of internal and external processes related to galaxy evolution, respectively.

5.2.2.1 Internal Processes

As stars form, the stellar mass of a galaxy increases, and the amount of cold gas available for future star formation decreases by construction (Figure 5.2–1). The consequence of the feedback loop between galaxy gas mass and SFR is that without further accretion of gas, a galaxy will eventually die as it exhausts its cold gas and star formation ceases.

Besides the natural evolution, feedback from massive stars can actively shape a galaxy's evolution and accelerate its demise. The most massive stars explode in a supernova at the end of their lives, and the resulting feedback (Larson, 1974; Dekel and Silk, 1986) can both positively and negatively affect SFR (see Hopkins et al., 2014, for an overview). For example, supernova-driven galactic winds heat the interstellar medium (ISM) and eject cold gas from the disc back to the halo, or in the extreme case, out of the halo altogether, thus suppressing star formation (Heckman et al., 1990; Martin, 1999; Scannapieco et al., 2008). Conversely, the blast waves may compress the cold gas to temporarily boost star formation. Supernovae (SNe) feedback also ejects material, which enriches the halo and galaxy gases. A more metal-rich halo gas increases the cooling rate (or shortens the cooling time), which may ultimately lead to increased star formation (Figure 5.2–3).

Supermassive black holes (SMBHs) are also important in the evolution of a galaxy because they are responsible for AGN feedback (Dekel and Silk, 1986). There are two main modes of AGN feedback: the quasar mode and the radio mode. In the quasar mode, a SMBH grows via accretion of cold gas and mergers with other SMBHs (in galaxy mergers). In the radio mode, SMBHs accrete gas directly from the halo and release a vast amount of energy, heating the halo gas and suppressing cooling

(Croton et al., 2006) (Figure 5.2–6,8). In both modes, AGN feedback negatively impacts star-formation activity by diminishing the cold gas. Nevertheless, like SNe feedback, there are mechanisms whereby AGN feedback can boost SFR (see Fabian, 2012; Heckman and Best, 2014, for recent reviews). In the causal model, AGN feedback represents only the 'output' processes.

SNe feedback depends on the initial mass function (IMF) and the SFR (Figure 5.2–2). The IMF dictates the overall fraction of stars that end up as supernovae, while the SFR determines the overall number. On the other hand, the picture for AGN feedback is far less clear as it depends on how, when, and where SMBHs form. Nevertheless, AGN feedback must scale with the mass of the SMBH (Soltan, 1982; Silk and Rees, 1998) (Figure 5.2–7), which depends on accretion and merger rates, but the reverse is true for the former as well, so there is a feedback loop (Figure 5.2–4). The accretion rate depends on halo and galaxy gas masses (Figure 5.2–6), while the merger rate is broadly determined by the number of galaxy mergers (Figure 5.2–5), which as will be discussed in detail in the following section, depends on halo mass and environment. In summary, there is believed to be a causal connection between AGN feedback and star-formation activity.

Overall, there are feedback cycles between halo and galaxy gases, SFR, and feedback. For example, an increase in cold galaxy gas from enhanced cooling of hot halo gas boosts star formation. A fraction of the stars born explode in a supernova, determined by the IMF, and the resulting feedback expels and/or heats the cold gas in the galaxy, transferring it back to the halo, which in turn reduces star formation. We emphasise that while the feedback theories discussed are likely to resemble reality, the fact is that the precise mechanisms are unknown. Furthermore, it is still unclear how SMBHs form in the first place.

In the following section, we describe the external environmental processes that shape a galaxy's evolution (see Boselli and Gavazzi, 2006, for a review). There are many definitions of environment, but ultimately one means the mass density field. Thus, we bear this in mind to derive the causal model.

Figure 5.2: Mini causal models of different internal processes of galaxy evolution. For visual clarity, all the possible causal connections of a variable with others are not drawn.

5.2.2.2 External Processes

Many processes associated with environment influence galaxies, but two of the most fundamental are accretion and mergers. The halo accretion and merger rates depend on halo mass and environment. For example, a massive halo is able to accrete more matter, but environment also plays a role since it determines the amount available for accretion. Also, a massive halo in a dense environment has to compete with neighbouring haloes to attract matter. Accretion changes halo mass and environment (assuming the local mass density field), so there is a feedback loop. Undoubtedly, a feedback loop also exists between halo mass, environment, and mergers. However, unlike accretion, mergers may not affect halo mass depending on the merger type (clarified below). In summary, halo mass (i.e., nature) and environment (i.e., nurture) influence each other via accretion and mergers in a feedback loop. In this context, we define the nature versus nurture debate in this thesis (Figure 5.3–1).

Mergers are broadly categorised into two types: major and minor. A major merger occurs when the progenitors are of similar masses, and in such a merger, the progenitor haloes and galaxies merge violently to form a more massive halo with a new galaxy residing at its centre. If the progenitors are disc galaxies with a mass ratio $1:1$, then the post-merger remnant resembles an elliptical (Toomre and Toomre, 1972; Toomre, 1977; Hernquist, 1992, 1993; Barnes, 1988, 2002; Cox et al., 2006). Later on, if the shock-heated and ejected gas from outflows cools with significant angular momentum, a disc forms, and then the post-merger remnant resembles an early-type spiral galaxy with a disc-bulge system (Hopkins et al., 2009; Sparre and Springel, 2016; Pontzen et al., 2017). A galaxy merger is a cause of morphological transformation (Figure 5.3–2).

A period of star formation activity follows a major merger if the progenitor galaxies contain large quantities of cold gas. In the short term, the influx of cold gas and/or an increase in the galaxy gas density due to interactions between galaxies trigger starbursts (Mihos and Hernquist, 1994, 1996; Hopkins et al., 2006, 2008b,a; Snyder et al., 2011; Hayward et al., 2014; Sparre and Springel, 2016). Also, the halo gas shock-heated during the merger has the opportunity to cool, leading to star formation in the long term. However, AGN feedback can prevent this from happening (Sanders et al., 1988; Di Matteo et al., 2005; Hopkins and Hernquist, 2009;

Treister et al., 2012). If the progenitor galaxies harbour SMBHs, they may merge in the process. Additionally, the same influx of gas that fuels star formation can feed the SMBH. The subsequent growth of the SMBH from the merger and accretion can consume any leftover halo and galaxy gases (in a feedback loop) and suppress the halo gas from cooling, resulting in a galaxy devoid of star formation (Figure 5.3–2).

A minor merger occurs when the progenitors are of dissimilar masses, and in such a merger, the smaller galaxy is 'absorbed' by the larger galaxy. In our causal model, we have defined two types of mergers: "halo mergers" and "galaxy mergers". As the names suggest, a halo merger refers to the merger of haloes, while a galaxy merger refers to the merger of galaxies. As such, major and minor mergers are halo mergers followed by galaxy mergers in our causal model (Figure 5.3–1). We distinguish minor mergers into "minor halo mergers" and "minor galaxy mergers". In a minor halo merger, the haloes 'merge' as the smaller halo orbits within the larger halo, but the galaxies may or may not. Accordingly, we refer to it as a halo merger, but not exclusively. As in simulations, we model the halo merger with the following perspective: the smaller and larger subhaloes occupy a common host halo that is a sum of its parts. In other words, the progenitor haloes retain their identity unless a galaxy merger follows a halo merger. Consequently, we continue referring to progenitor haloes (and the associated variables) post-merger as haloes rather than subhaloes of the host halo in the causal model.

Halo mergers are responsible for the formation of groups and clusters. In such environments, the central galaxy is the most massive and located near the centre, while the satellite galaxies orbit around it. Central galaxies reside deep in the gravitational potential well of the host halo, while satellite galaxies reside further out at different depths and distances. As a result, the environmental effect on these galaxies is asymmetrical as satellites experience most of the processes and not centrals. Satellite galaxies in these dense environments are subject to different processes that are either a consequence of, or scale with, the host halo mass.

A satellite galaxy experiences dynamical friction (Chandrasekhar, 1943a,b,c) as it orbits within its host halo. The drag slows down the satellite, which causes it to spiral inwards and eventually merge with the central galaxy in a process called galactic cannibalism. The magnitude of dynamical friction depends on the satellite's

halo mass and environment. For example, a satellite is subject to greater dynamical friction if it is more massive and occupies a larger host halo. Galactic cannibalism is the predominant environmental process that affects central galaxies (Figure 5.3–3).

Another critical process linked to environment is ram-pressure stripping (RPS; Gunn and Gott 1972). As a satellite travels through the hot intergalactic medium (IGM) of groups and clusters, its relatively cold halo and galaxy gases encounter a hydrodynamical drag force due to the relative motion of the two fluids. If the drag force exceeds the satellites' restoring force, its cold gas is ablated. Accordingly, while environment causes RPS (assuming the amount and temperature of hot gas correlates), its extent also depends on halo mass. Evidently, the depletion of gas (hot and cold) negatively impacts the SFR, and a decline in star formation affects the visual morphology of the galaxy. More specifically, a satellite galaxy that is initially spiral may resemble a lenticular (S0) galaxy. Nonetheless, there is doubt whether the effects of RPS are negative and/or permanent. For example, there is evidence that any gas not stripped may be compressed by RPS to cause an increase in star formation activity in the disc (Dressler and Gunn, 1983; Gavazzi et al., 1995). Additionally, the stripped gas may remain bound, to later fall back and induce starbursts (Vollmer et al., 2001). In retrospect, RPS is likely to be only partially responsible for the morphology–density and SFR–density relations (Abadi et al., 1999) (Figure 5.3–4).

Groups and clusters comprise tens and upwards of hundreds of galaxies respectively, so gravitational interactions are a common occurrence. In group environments, a satellite galaxy experiences tidal forces from other galaxies. The tidal interactions can remove its cold and hot gases, stars, and dark matter via tidal stripping (Moore et al., 1999). As was the case with RPS, the effectiveness of tidal stripping depends on environment (the number of interactions is related to the density) and halo mass. Note that there is a feedback loop between tidal stripping and halo mass, so the process becomes more effective over time (Kampakoglou and Benson, 2007) (Figure 5.3–5).

In cluster environments, satellite galaxies are typically not subject to tidal stripping and mergers (not resulting from dynamical friction) because strong gravitational interactions are infrequent due to their high velocities (Ghigna et al., 1998).

Instead, they are subject to multiple, weak interactions, and the cumulative effect of such interactions is called galaxy harassment (Farouki and Shapiro, 1981; Moore et al., 1996). The high-speed encounters can impulsively heat the disc of a satellite galaxy, which pushes its stars onto elliptical orbits, and the disc transforms into a spheroidal component, thus altering its morphology (Moore et al., 1998; Gnedin, 2003; Mastropietro et al., 2005; Aguerri and González-García, 2009). At its extreme, the stars can become completely unbound, which decreases the galaxy's stellar mass (Smith et al., 2010, 2015; Bialas et al., 2015). The heating of the disc naturally impacts the SFR as it affects the density of the cold gas (via a change in the galaxy gas mass and/or radius). Galaxy harassment scales with the number and strength of interactions, which depends on environment, and resistance to its effects depends on halo mass, like tidal stripping (Figure 5.3–6).

The hot halo surrounding a galaxy is in constant flux as the gas condenses to form stars, and the subsequent feedback returns the cold gas back to the halo. Simply put, the hot gas acts as a reservoir for future star formation. The combination of RPS and tidal stripping can annihilate this reservoir, and without further accretion in a dense environment, a satellite galaxy eventually stops forming stars as it exhausts its fuel. This process is called strangulation (Larson et al., 1980; Benson et al., 2000). We do not have a specific node for it in our causal model because it is not a process in and of itself and is already captured by the existing variables. Also, we do not have nodes for thermal evaporation (Cowie and Songaila, 1977) and viscous stripping (Nulsen, 1982) because they are variants of RPS. Furthermore, whilst important, variables such as colour, stellar metallicity, and luminosity are not included as they are not the subject of this study.

Finally, we have not precisely defined or modelled morphology and related processes because our target is the SFR–density relation. Nonetheless, internal dynamical effects can change the morphology of galaxies, a well-known example being the bar instability. A thin disc with high surface density is susceptible to a non-axisymmetric instability, which creates a bar-like structure. Bars can funnel gas to the central region of a galaxy (Athanassoula, 1992), which can fuel AGNs and star formation (Zurita et al., 2004; Sheth et al., 2005). The bar may also buckle to produce a "pseudobulge" (see Kormendy and Kennicutt, 2004, for a review),

which can prevent the disc from collapsing and forming stars (Fang et al., 2013). Additionally, there is a strong connection between bulges and SMBHs (Kormendy and Richstone 1995; Magorrian et al. 1998; Ferrarese and Merritt 2000; Gebhardt et al. 2000; Häring and Rix 2004; also see Kormendy and Ho 2013, for a review). Thus, morphology can directly and indirectly influence SFR (and vice versa). Still, detailed modelling of morphology is unnecessary to estimate the SFR–density relation because it is not a confounding factor given that it does not also impact environment. In fact, controlling for morphology may induce selection bias (Figure 3.3) since it is a common effect of environment and SFR.

The key findings are: (i) galaxy formation and evolution depends on nature and nurture, (ii) nature (i.e., halo mass) and nurture (i.e., environment) influence each other through accretion and mergers, and (iii) internal processes associated with nature also depend on nurture, and external processes associated with nurture also depend on nature, as both halo mass and environment determine their impact on galaxies. In conclusion, nature and nurture are heavily intertwined. In Section 5.4, we describe a causal inference method to disentangle the causal effects of nature and nurture. And to do so, we first unravel the feedback loops between them over time in the causal model.

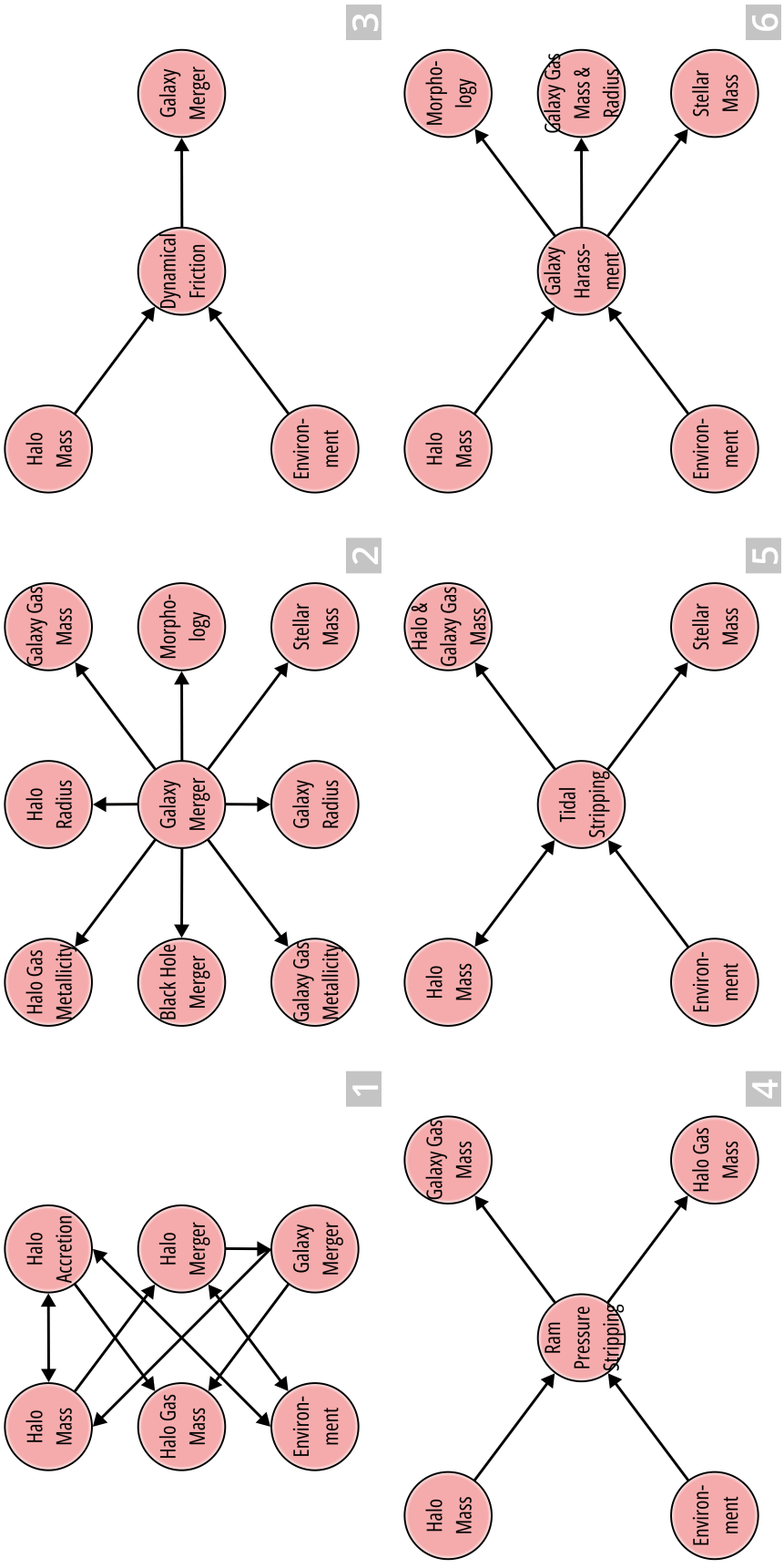

Figure 5.3: Mini causal models of different external processes of galaxy evolution. For visual clarity, all the possible causal connections of a variable with others are not drawn.

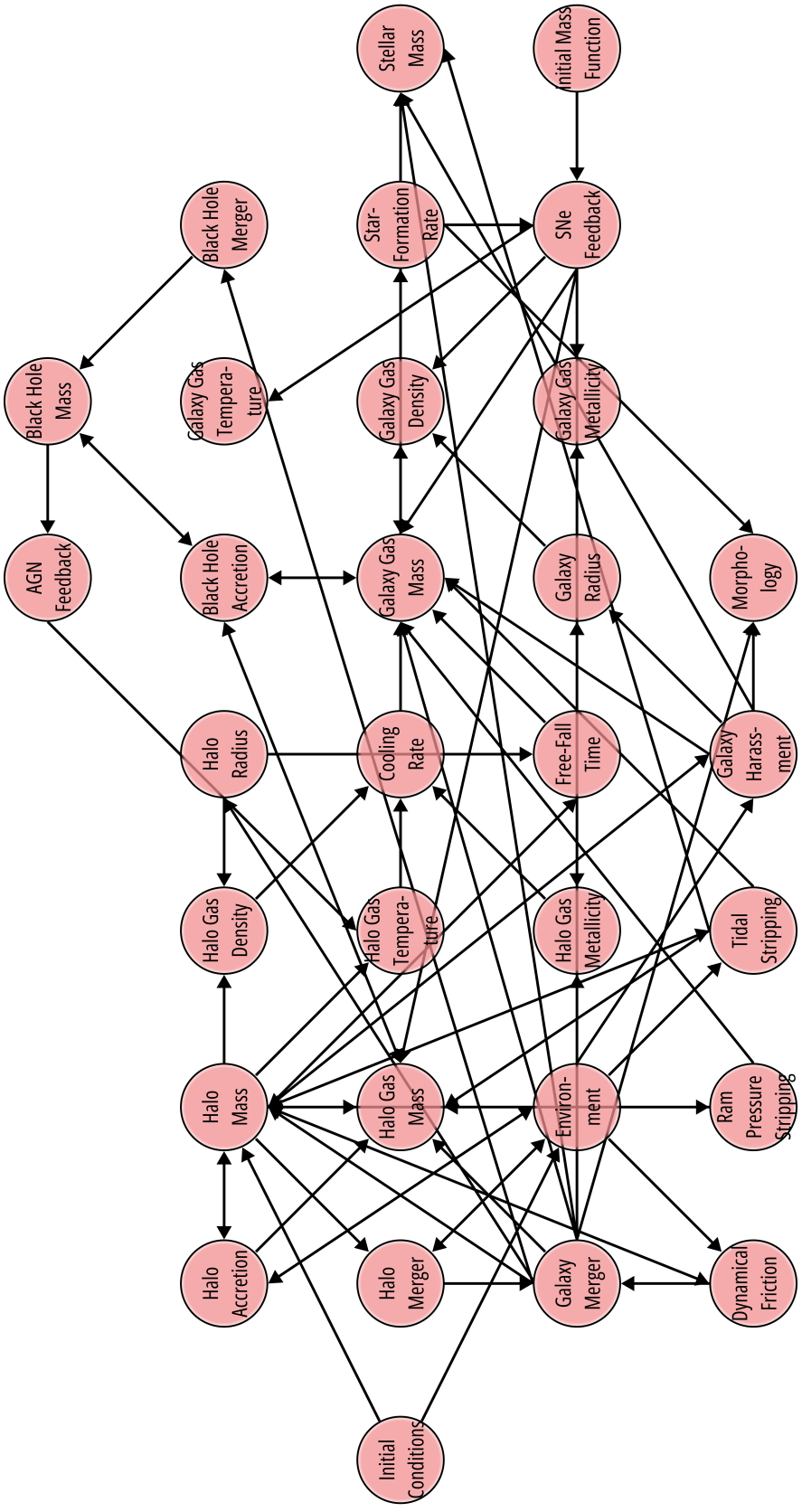

Figure 5.4: Causal model of galaxy formation and evolution, with all the mini causal models and variables connected.

5.2.3 Causal DAG and Effects

Figure 5.4 shows the causal model of galaxy formation and evolution in its entirety with all the mini causal models and variables connected. The causal model is complex and richly interconnected with multiple interactions and feedback loops between the variables. The presence of feedback loops blurs the notion of causality. If two variables cause each other in a cycle, then what is the causal effect of one thing on another? Alternatively, the flow of causal association is symmetric along bidirected edges, so the causal effect is undefined. Fundamentally, the fuzziness emerges due to a lack of a causal arrow of time, i.e., a cause precedes its effect. Technically, the causal graph is a directed cyclic graph (DCG) because it does not satisfy the "variable does not cause itself" criterion. We transform the DCG into a DAG by unravelling the feedback loops over time to make it easy to interpret and estimate causal effects.

5.2.3.1 Causal DAG

We aim to estimate the causal effect of environment on SFR. Assuming the causal model is representative of the DGP, we identify potential biases that may distort the causal effect. Upon careful inspection, we find that halo mass is the fundamental confounder as it causes the treatment (i.e., environment) and outcome (i.e., SFR) through various processes. We focus only on these quantities of interest and unravel the feedback loops between them to construct a DAG of the causal model, as shown in Figure 5.5. In the DAG, H, E, and SFR denote halo mass, environment, and SFR respectively, and the subscripts indicate time, increasing from left to right (with zero marking the present). The causal model refers to the DAG from hereon unless otherwise specified.

The initial haloes and their environments emerge from the initial conditions in the early Universe. Subsequently, they interact and co-evolve over time in a feedback loop, influencing galaxies in the process via various mechanisms. The structure of the causal model is as follows:

$E_k \rightarrow SFR_k$ Environment affects the SFR as: (i) tidal stripping and RPS deplete the fuel necessary for star formation by annihilating the cold galaxy and hot halo gases and (ii) galaxy harassment impacts the galaxy gas density by impulsively heating the cold gas.

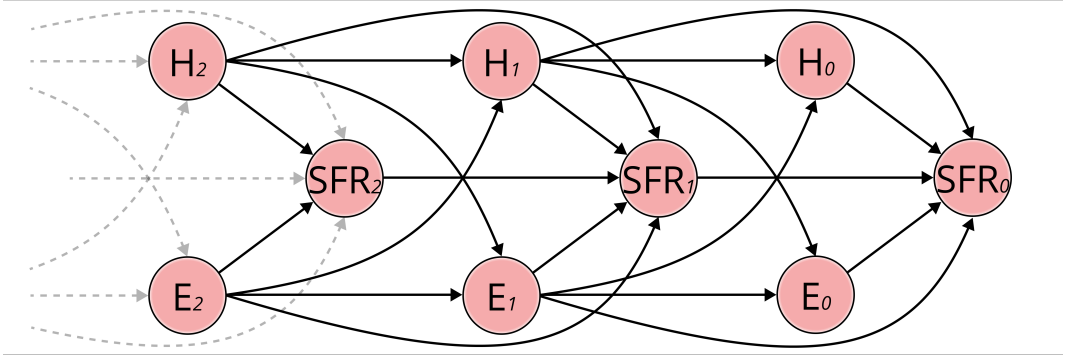

Figure 5.5: Directed acyclic graph (DAG) of the causal model of galaxy formation and evolution (Figure 5.4). It is constructed from carefully tracing the causal chains and unravelling the feedback loops between halo mass (H), environment (E), and star-formation rate (SFR). The subscripts indicate time, increasing from left to right (with zero marking the present). The DAG is the causal model unless otherwise specified.

$H_k \to SFR_k$ Halo mass dictates the amount and density of the cold gas for star formation as it indirectly influences the cooling rate and free-fall time via the halo gas temperature and density. Furthermore, it determines the susceptibility of a galaxy to environmental processes, which affects the SFR (see above).

$SFR_k \to SFR_{k+1}$ Intrinsically, the act of forming stars consumes gas, thus impacting the future SFR. Additionally, feedback as a consequence of star formation actively affects the SFR through the expulsion of hot halo and cold galaxy gases and suppression of the cooling process.

$H_{k-1}, E_{k-1} \to H_k, E_k$ Halo mass and environment are determined by the halo accretion and merger rates, which ultimately depend on the previous halo mass and environment. Also, environmental processes such as tidal stripping affect the halo mass.

$H_{k-1}, E_{k-1} \to SFR_k$ Accretion and mergers alter many halo and galaxy properties besides halo mass, which all converge on the SFR. In other words, there is a direct lagged effect of the previous halo mass and environment on the current SFR.

There are many causal effects in the causal model. Then, what is the causal effect of environment on SFR? We provide an explicit definition.

5.2.3.2 Causal Effects

Environment affects galaxies over a period of time, so it is a time-varying treatment rather than a time-fixed treatment. Concretely, a time-fixed treatment takes place at a single point in time, while a time-varying treatment occurs at multiple points in time. The causal effect of a time-varying treatment is not uniquely defined (Hernan and Robins, 2023). We define two types of causal effects:

1. The marginal causal effect is the effect of a single treatment T_k on outcome Y_k.

2. The joint causal effect is the effect of multiple treatments or treatment history $\bar{T}_k$ on outcome Y_k, where $\bar{T}_k = [T_0, T_1, ..., T_k]$.

The marginal and joint causal effects of environment on SFR provide different insights. The marginal effect of E_k represents the short-term impact of environment, while the joint effect of $\bar{E}_k$, captures the long-term impact on SFR. We estimate the joint effect as we are interested in the overall impact and refer to it as the causal effect. Although, we also determine the marginal effect for comparison. We define the environmental history,

$$\bar{E}_j = \frac{1}{N} \sum_{k=0}^{j} E_k, \tag{5.1}$$

where N is the number of treatments and $j = k$ (see Hagedoorn and Helbich, 2021, for more complex characterisations). Note that j is used instead of k for mathematical correctness in this equation and where necessary, but not in text for consistency. The joint effect of $\bar{E}_k$ represents the impact of average environment, which we de facto mean by the causal effect of environment.

We highlight that while our goal is simply to determine the causal effect of environment, there are many other causal questions one could investigate as there are at least 2^k possible treatment histories to contrast and thus 2^{k-1} causal effects to estimate at time point k (for a binary treatment). For example, what is the causal effect of occupying a moderately dense environment throughout time versus a late infall into a high-density environment? In practice, data is limited, and the number of histories observed is far less than the total, so specific questions require careful consideration of the causal assumptions. In Section 5.4, we explain the causal

inference method we apply to estimate both types of causal effects. Before that, we describe the data we use in the next section.

5.3 Data

According to the causal model and method (as will become apparent in the next section), we require the evolutionary history of galaxies to disentangle nature and nurture. Such data is not readily available observationally, so we rely on simulations, which enable the tracing of galaxies over time using merger trees. In particular, we utilise the IllustrisTNG simulations (Pillepich et al., 2018a; Springel et al., 2018; Nelson et al., 2018; Naiman et al., 2018; Marinacci et al., 2018; Nelson et al., 2019).

5.3.1 IllustrisTNG

IllustrisTNG (hereafter TNG) is a suite of cosmological, gravo-magnetohydrodynamical (MHD) simulations run with the moving-mesh code `AREPO` (Springel, 2010). TNG adopts a flat ΛCDM cosmology with Planck Collaboration et al. (2016) cosmological parameters ($\Omega_{\Lambda,0} = 0.6911, \Omega_{m,0} = 0.3089, \Omega_{b,0} = 0.0486, \sigma_8 = 0.8159, n_s = 0.9667$, and $h = 0.6774$). The simulations start at $z = 127$ from initial conditions created with the Zeldovich approximation (Zel'dovich, 1970) and the `N-GenIC` code (Springel, 2015). There are 100 snapshots of each simulation, approximately equally spaced in cosmic time from $z \sim 20$ to the present day $z = 0$.

TNG is the next-generation follow-up to the original Illustris simulation (Vogelsberger et al., 2014b,a; Genel et al., 2014) and improves upon its predecessor in many aspects. It incorporates a comprehensive physical model (Weinberger et al., 2017; Pillepich et al., 2018b) to simulate the formation and evolution of galaxies within the CDM paradigm, built upon the original model (Vogelsberger et al., 2013; Torrey et al., 2014). The model includes prescriptions of various astrophysical processes, such as star formation, stellar evolution, chemical enrichment, primordial and metal-line gas cooling, stellar feedback-driven galactic outflows, and SMBH formation, growth, and feedback (Pillepich et al., 2018a). Furthermore, the model has been tuned or calibrated to reproduce key observational results at $z = 0$, such as the galaxy stellar mass function and the stellar-to-halo mass relations, the total gas mass content within the virial radius of massive groups, and the stellar mass–stellar size and the BH–galaxy mass relations. Additionally, the overall shape of the cosmic SFR density

at $z \lesssim 10$ has also been preserved (Nelson et al., 2019).

Haloes and galaxies are identified in the simulations in a two-step process. A friends-of-friend (FoF) algorithm (Davis et al., 1985) connects dark matter particles separated by less than 0.2 times the mean interparticle distance to construct a FoF halo. The `SUBFIND` code (Springel et al., 2001; Dolag et al., 2009) detects subhaloes within each FoF halo by identifying gravitationally bound substructures using all the particle types. Subhaloes may be dark or contain a luminous galaxy. A FoF halo can contain zero, one, or more than one subhalo. A FoF halo with one subhalo is simply a halo, while one with two or more subhaloes is a host halo. The most massive subhalo in a host halo is the central subhalo; the rest are satellite subhaloes. In postprocessing, merger trees are generated by linking the FoF haloes and subhaloes over time using `LHALOTREE` (Springel et al., 2005) and `SUBLINK` (Rodriguez-Gomez et al., 2015).

There are three flagship simulations: TNG50, TNG100, and TNG300, corresponding to the rough side lengths of the simulation boxes in comoving Mpc. The different simulations enable the exploration of various aspects of galaxy formation. The largest volume simulation, TNG300, enables analyses of galaxy clustering, for example. At the other end of the spectrum, TNG50 allows examinations of the structural properties of galaxies in finer detail because the mass resolution is a few hundred times better than the TNG300 simulation (Nelson et al., 2019). We use the TNG100 simulation, which represents a good trade-off between volume and resolution, particularly for intermediate mass haloes. Specifically, we utilise the highest-resolution run of the simulation, TNG100-1. The simulation is initialised with 1820^3 dark matter and gas particles of mass resolutions $5.1 \times 10^5 \mathrm{M}_\odot$ and $9.4 \times 10^5 \mathrm{M}_\odot$, respectively.

5.3.2 The Galaxy Sample

We require the evolutionary history of galaxies for our analysis. First, we select a sample of galaxies to trace over time as follows. We start with the group catalogue at $z = 0$, which contains 6291349 FoF haloes and 4371211 subhaloes. We match each subhalo to its FoF halo using the `SubhaloGrNr` field, which results in 3430706 FoF haloes (i.e., more than half of FoF haloes do not have any subhaloes). There are some subhaloes of non-cosmological origin, which means they have not formed

due to the process of structure formation and collapse and are likely fragments or clumps rather than bonafide galaxies (Nelson et al., 2019). We discard these objects by setting `SubhaloFlag` = 1. Finally, we remove any subhaloes with no detectable dark matter and retain all galaxies with stellar mass $M_\star > 10^9 \mathrm{M}_\odot$, resulting in 20935 galaxies. We chose the relatively high stellar mass cut because it corresponds to well-resolved galaxies with at least 1000 star particles (Donnari et al., 2019), but more importantly, to trace galaxies further back in time.

There is a possibility that applying the stellar mass cut introduces selection bias since stellar mass may be a common effect of both environment and SFR. One can interpret this as survivor bias (a form of selection bias) since we are selecting galaxies that made it to the stellar mass at the 'end' of the galaxy formation and evolution process. In the model, there is a causal connection between SFR and stellar mass, as well as environment and stellar mass, but significantly only the former is direct, while the latter is indirect through SFR. There is a 'direct' connection via harassment and tidal stripping between environment and stellar mass, but it is likely to be weak in comparison and not universal. Consequently, we reason that selecting galaxies based on their stellar mass at $z = 0$ does not bias our analysis. Indeed, preliminary tests supported this, as different stellar mass cuts were applied, and it was found that while the amplitude of the SFR–density relation changed, the shape did not. In other words, the causal effect remained unmodified. Another potential source of bias is that haloes form earlier in denser environments (Gottlöber et al., 2001; Sheth and Tormen, 2004; Gao et al., 2005; Harker et al., 2006; Maulbetsch et al., 2007), and thus galaxies within them have had more time to evolve. This assembly bias can explain the observed phenomenon of "downsizing" (Cowie et al., 1996), i.e., massive galaxies form early and rapidly, while low-mass galaxies form later and over a more extended timescale (see Fontanot et al., 2009, for a detailed discussion). We assume that selecting galaxies above a relatively high stellar mass means the formation times are similar.

We track the selected galaxies back in time with `SUBLINK` merger trees. The merger tree of a subhalo can have many branches if its progenitors have undergone mergers. We follow the main progenitor branch (MPB), which traces the most massive progenitor at each point in time. For the analysis, we use 11 approximately

equally-spaced snapshots in cosmic time from $z \sim 6$ to $z = 0$ (i.e., snapshots $13, 25, 35, 43, 51, 59, 67, 75, 83, 91,$ and 99). We decided upon $z \sim 6$ as the baseline because it was the furthest we could trace most galaxies back in time. The average timespan between each snapshot is ~ 1.3 Gyr. After all the preprocessing steps, the galaxy sample contains 18629 galaxies.

5.3.2.1 Environment and Measurement Choices

There are different measures available of halo and galaxy properties. In our analysis, we use the quantities derived by summing all particles/cells bound to a subhalo associated with the particular property. The choice of measure does not impact our results because our questions are causal rather than statistical in nature. For the same reason, we stick with instantaneous SFRs measured in the simulations instead of using time-averaged SFRs that better match SFRs estimated observationally with various tracers. Due to the finite numerical resolution of the simulation, the instantaneous SFRs of galaxies are unresolvable if they are below the minimum value of $\log(SFR) \sim -4$ for TNG100 (Donnari et al., 2019). The SFRs of such galaxies are labelled zero, which could cause numerical issues when estimating the causal effect. Following Donnari et al. (2019), we resolve the problem by randomly assigning an SFR value between -4 and -5.

There are many definitions of environment in the literature (see Muldrew et al., 2012, for a review), but the most popular are nearest-neighbour-based and fixed-aperture-based measures. The former best probe the 'local environment', while the latter the 'large-scale environment'. Simply put, there is no universal definition of environment, and the most suitable method is scale dependent (Muldrew et al., 2012). As we are interested in the impact of the local environment, our environment proxy is the Nth nearest neighbour density,

$$\log(\Sigma_N) = \frac{N}{(4\pi/3)r_N^3}, \tag{5.2}$$

where r_N is the three-dimensional (3D) distance to the Nth nearest neighbour from the galaxy in question. Specifically, we compute densities at the 10th nearest neighbour, which is a popular choice in the literature (Lewis et al., 2002; Pimbblet et al., 2002; Cassata et al., 2007; Sobral et al., 2011). We note that a rough analysis was performed with a range of nearest neighbours from $N = 3 - 64$. Below $N \leq 7$,

the SFR–density relation was found to be noisy and flat, and thereafter, it became more stable and negative with increasing N. These preliminary results indicate that the causal effect of environment varies at different scales. Most subhaloes in the simulation are small and dark (i.e., do not possess any galaxies), so considering the entire population would result in a noisy density measure. For a more informative estimate, we remove such subhaloes by applying the same cuts as when selecting the galaxy sample, but we do not apply the stellar mass cut at $10^9 M_\odot$. Instead, we drop subhaloes with no detectable stars.

We considered using host halo mass as a proxy since many environmental processes are either a consequence of it or scale with it. Ultimately, we opted against it because it is not a fine-grained measure of environment and its effects. Galaxies in a group or cluster are not in the same environment because they reside at different depths in the gravitational potential well of the host halo. Consequently, they are subject to varying degrees of environmental effects, and the effects are asymmetrical, as satellites experience most of the environmental processes and not centrals (as explained in Section 5.2.2.2). Precisely, the treatment is not well defined with host halo mass and thus the consistency assumption is violated. Furthermore, there are conceptual and practical issues with using host halo mass as an environmental proxy. The host halo mass of a central galaxy is approximately equal to its subhalo mass, and they are equivalent for an isolated galaxy (i.e., a galaxy that is not part of a group or cluster). So, the environment would be undefined for isolated galaxies, and for both, the line between nature and nurture would be blurred.

Following our naming convention, FoF haloes and subhaloes are host haloes and haloes in our causal model respectively, so we refer to them and the associated properties accordingly from here onwards. Figure 5.6 shows the relationships between fundamental halo and galaxy properties such as host halo mass, halo mass, stellar mass, and SFR, as well as the average environmental density of the galaxy sample at $z = 0$. A clear positive correlation can be observed between host halo mass and the 10th nearest neighbour density, which suggests that the latter is a suitable measure of environment, at least to the first order (see Haas et al., 2012, for a comparison between different environment measures and host halo mass). As expected, the SFR overall decreases with increasing environmental density.

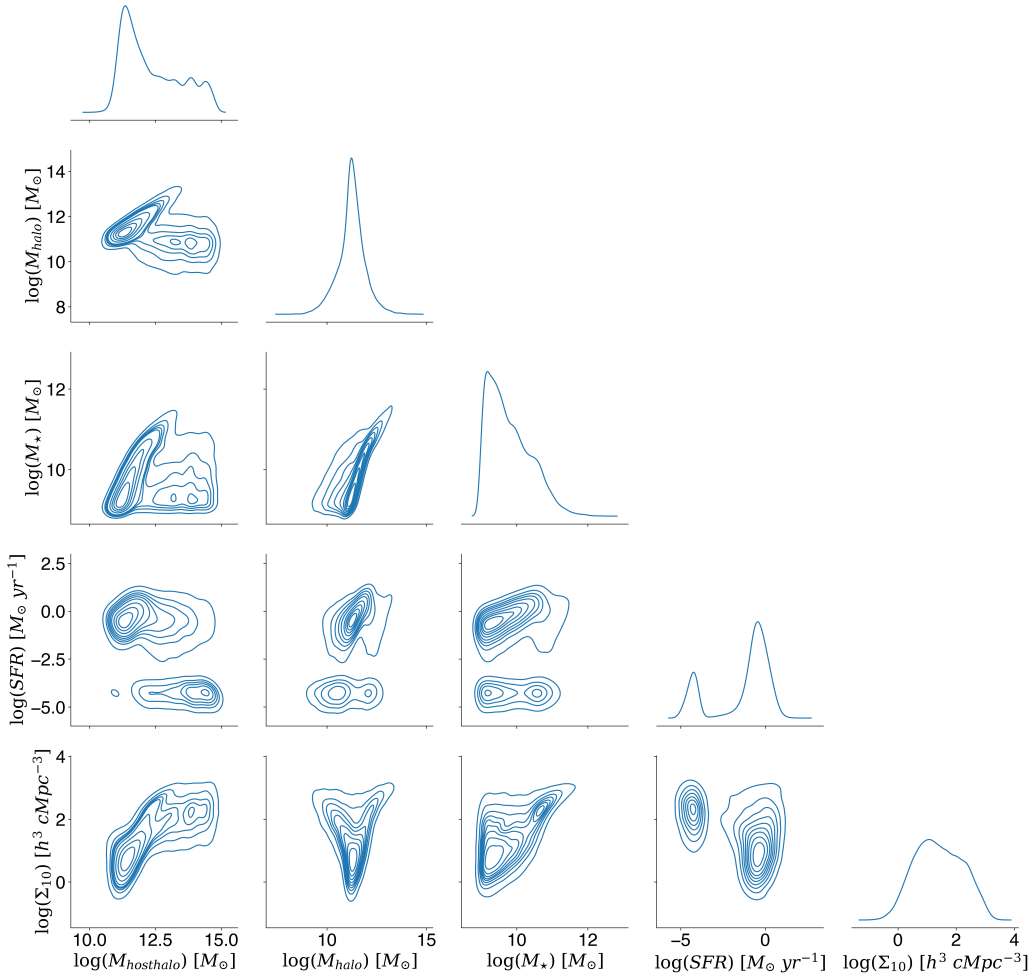

Figure 5.6: Distributions of fundamental halo and galaxy properties, such as host halo mass, halo mass, stellar mass, and star-formation rate (SFR), as well as the average environmental density (10th nearest neighbour density), of the galaxy sample at $z = 0$.

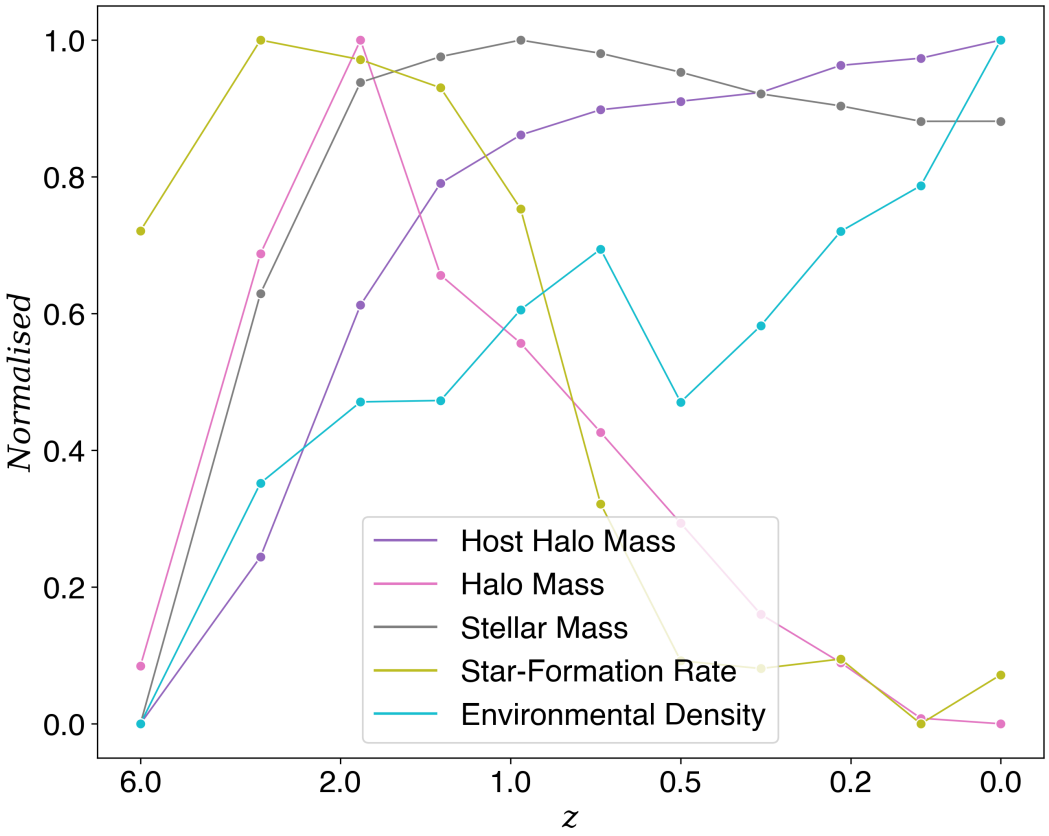

Figure 5.7: Evolutionary history of a galaxy (following the main progenitor branch) in terms of its host halo mass, halo mass, stellar mass, star-formation rate (SFR), and environmental density (10th nearest neighbour density), from $z \sim 6$ to $z = 0$. The various histories are min-max normalised to allow for comparison on the same scale.

Figure 5.7 shows the evolutionary history of a galaxy in terms of the aforementioned properties from $z \sim 6$ to $z = 0$. The various histories have been min-max normalised to allow for comparison on the same scale. Between $z \sim 6$ and $z \sim 2$, the galaxies' halo mass and stellar mass increase sharply, with a peak in the SFR at $z \sim 3$. Soon after, the halo mass and SFR start to decline rapidly, and the stellar mass plateaus. In other words, star formation is effectively shutdown. We believe the cause is a halo merger because there is a significant jump in the host halo mass. Specifically, the merger cuts off the supply of fresh fuel, and environmental processes possibly strip the remaining halo and galaxy gases.

5.4 Method

There are many causal inference methods to infer causal effects from observational data. Fundamentally, they exploit one of two approaches to adjust for biases, specifically confounding bias. The first approach is to block the backdoor path between the treatment and outcome by conditioning on the confounder (as described in Section 3.4.1). The act of conditioning stops the flow of non-causal confounding association via the confounder (Figure 3.2b), which means that all association is causal and the causal effect is unbiased. We refer to this as the conditional approach. The second approach is to remove the backdoor path entirely by making the treatment independent of the confounder, as achieved experimentally with RCTs. Visually, this translates to no direct edge (i.e., arrow) from the confounder to the treatment in the DAG. By removing the backdoor path, confounding bias is eliminated altogether. We refer to this as the marginal approach. For time-fixed treatments, both approaches produce unbiased causal effects. However, for time-varying treatments, only the marginal approach performs well. Specifically, the conditional approach cannot estimate valid joint causal effects, but the marginal approach can estimate both the marginal and joint causal effects of time-varying treatments.

Consider the marginal effect of E_0 on SFR_0 in the causal model in Figure 5.5. There are two confounders, H_1 and E_1, as they directly cause the treatment E_0, and directly and indirectly (via SFR_1 and H_0) cause the outcome SFR_0. To estimate the causal effect of the 'current' environment on the 'current' SFR, it is essential to adjust for the confounders, i.e., the 'previous' halo mass and environment. Intuitively, if the previous halo mass and environment affect the current SFR, then it is necessary to negate their roles to determine only the impact of the current environment. Both conditional and marginal approaches can appropriately adjust for the confounding bias to estimate the marginal effect.

Now consider the joint effect of E_0, E_1, and E_2 on SFR_0. Once again, H_1 is a confounder of the causal effect of E_0 on SFR_0. However, unlike before, H_1 is now also a mediator as it lies on the causal pathway of the causal effect of E_2 on SFR_0. This scenario is problematic for conditional approaches because conditioning on the confounder to eliminate confounding bias will block some of the causal effect of the previous environment on the current SFR and introduce over-adjustment bias.

Simply put, the causal effect of environment on the SFR would be underestimated. It is possible to either estimate the unbiased causal effect of the current environment or the previous environment on the current SFR, but not both simultaneously. On the other hand, marginal approaches do not suffer from the same conundrum and can estimate the joint effect.

Generally, conditional approaches fail in estimating unbiased joint causal effects of time-varying treatments when there is: (i) a time-varying confounder that causes the outcome and subsequent treatment and (ii) the time-varying confounder itself is affected by the previous treatment, i.e., there is treatment-confounder feedback. The causal model satisfies both conditions: H_k is a time-varying confounder since it causes outcome SFR_k and the subsequent treatment E_{k+1}, and there is treatment-confounder feedback as H_k is affected by the previous treatment E_{k-1}, i.e., the previous environment affects the current halo mass which then affects the subsequent environment in a cycle. Consequently, we adopt a marginal approach to infer the causal effect of environment.

In summary, estimating the causal effect of environment is difficult due to the interdependence of nature and nurture. The causal effects of nature and nurture are intertwined as the causal effect of environment partially flows through halo mass and vice versa. As a result, it is challenging to isolate the effect of one from the other without introducing bias. Conditional approaches cannot adequately separate the causal effects even if given all the necessary data. So, the challenge is not only of data but also methodological. In this section, we present a method for disentangling nature and nurture to estimate the causal effect of environment.

There are three different methods to estimate causal effects of time-varying treatments in the presence of time-varying confounding and treatment-confounder feedback: (i) the g-computation algorithm formula (g-formula; Robins 1986), (ii) g-estimation of structural nested models (SNMs; Robins 1994; see Vansteelandt and Joffe 2015, for an overview), and (iii) inverse probability weighting (IPW) of marginal structural models (MSMs; Robins et al. 2000). These are collectively referred to as Robins' generalised methods (g-methods; see Naimi et al., 2017, for an overview).

We utilise IPW of MSMs to estimate the marginal and joint causal effects of environment on SFR. The method has been applied to conceptually similar

problems in other fields, e.g., to study the effects of methotrexate on mortality among people with rheumatoid arthritis (Fewell et al., 2004), asthma rescue medication on pulmonary function (Mortimer et al., 2005), neighbourhood poverty on alcohol use (Cerdá et al., 2010), physical activity on knee pain in patients with osteoarthritis (Mansournia et al., 2012), adverse childhood social conditions on chronic diseases (Nandi et al., 2012), and religious service attendance on depression (Li et al., 2016). Before we describe the method, we introduce its key component—the propensity score.

5.4.1 Propensity Scores

The propensity score (PS; Rosenbaum and Rubin 1983) is the conditional probability of treatment given covariates X,

$$e(x) = p(t|x) = P(T = 1|X = x). \tag{5.3}$$

An extension of the propensity score to continuous treatments is the generalized propensity score (GPS; Hirano and Imbens 2004),

$$e(t, x) = f(t|x), \tag{5.4}$$

where $f(t|x)$ is the conditional probability density function (PDF). For conciseness, we refer to the GPS as simply the propensity score from hereon. Furthermore, we denote $p(t|x)$ as $f(t|x)$ in the equations even when the treatment is binary because the concept is the same. A propensity score close to zero or one means there is a low or high probability of receiving the specific treatment given covariates, respectively. Essentially, the propensity score represents the dependence of treatment on covariates. As treatment dependence correlates with confounding bias when the covariates are confounders, the propensity score can adjust for confounding to estimate causal effects. There are four known techniques to adjust using the propensity score (see D'Agostino Jr, 1998; Austin, 2011, for overviews):

1. *Matching* – units from the treatment group are matched to their counterparts in the control group based on their propensity scores. This process makes the treatment and control groups comparable in terms of their covariate distributions, which ultimately means they are exchangeable. As explained in more

detail in Section 3.3, exchangeability ensures no confounding.

2. *Stratification* – the population is divided into distinct strata or subgroups based on the propensity score. This negates any confounding effect because within each stratum the level of confounding is similar.

3. *Covariate adjustment* – the propensity score is included along with the treatment as a covariate in a model to predict the outcome.

4. *IPW* – units are weighted according to their propensity score. We discuss how this eliminates confounding bias in the following section.

Previous studies have employed matching, stratification, and covariate adjustment to eliminate confounding bias, but just not with the propensity score. For example, the common approach of binning galaxies according to their stellar mass is a form of stratification. Also, galaxies have been matched on redshift and stellar mass when creating treatment and control groups (Ellison et al., 2008; Smethurst et al., 2017; Garduño et al., 2021; Sotillo-Ramos et al., 2021), and stellar mass has been included as a variable in models (Teimoorinia et al., 2016; Bluck et al., 2019, 2020a,b, 2022; Brownson et al., 2022; Piotrowska et al., 2022). We use the IPW approach (see Chesnaye et al., 2022, for an overview) as the other techniques are either unable or unsuitable to estimate the causal effect of environment. Stratification and covariate adjustment are conditional approaches (Williamson and Ravani, 2017) and thus cannot estimate the joint effect, and there is no clear strategy with matching (Thoemmes and Ong, 2016).

5.4.2 Inverse Probability Weighting

In this section, we first describe the IPW method for time-fixed treatments and then extend it to time-varying treatments.

5.4.2.1 Time-fixed Treatments

IPW is a statistical technique that adjusts for confounding bias by weighting each unit with the inverse of their probability of receiving treatment, i.e., the propensity score.

$$w(t) = \frac{1}{f(t|x)}. \tag{5.5}$$

Intuitively, the propensity score quantifies the magnitude of confounding bias, so weighting each unit with its propensity score directly negates the influence of confounders. Specifically, the method works as follows: a unit with a high propensity score implies the treatment it received is likely given the confounders. In other words, the influence of the confounders is significant, so the unit is down-weighted to reduce its impact. Conversely, a unit with a low propensity score implies that the treatment it received is unlikely given the confounders. Crucially, such a unit is a counterfactual of units that received a different treatment, and thus it is up-weighted because it holds valuable information. In a sense, IPW is comparable to the technique of importance sampling (Kloek and Van Dijk, 1978). Overall, assigning weights to each unit creates a pseudo-population in which treatment is independent of confounders, and thus IPW is a marginal approach.

Units with specific characteristics that predispose them to a particular treatment, or from the alternative viewpoint, units subject to a treatment confined to a subpopulation, will have propensity scores close to zero or one because of the strong causal association between the covariates and treatment. Consequently, a disproportionately small fraction of units can dominate and drastically skew the causal effect. A simple solution is to truncate or trim the extreme weights from the analysis, typically at the 1st and 99th percentiles. Though this can introduce its own unknown bias (Cole and Hernán, 2008). A better approach is to stabilise the weights with the marginal probability of treatment $f(t)$ such that,

$$w(t) = \frac{f(t)}{f(t|x)}. \tag{5.6}$$

Besides counteracting the effect of extreme weights, stabilised weights generally reduce the variance of causal effect estimates (Robins et al., 2000). Furthermore, when the treatment is continuous, unstabilised weights are not an option as they have infinite variance (Robins et al., 2000). For binary or discrete treatments,

$$\mathbb{E}[Y(t)] = \mathbb{E}\left[\frac{\mathbb{1}(T=t)Y}{f(T=t|X)}\right], \tag{5.7}$$

where $\mathbb{1}$ is an indicator function that is 1 if $T = t$ and 0 otherwise. Thus, the ACE of a binary treatment,

$$\tau = \mathbb{E}[Y(1) - Y(0)] = \mathbb{E}\left[\frac{\mathbb{1}(T=1)Y}{f(T=1|X)}\right] - \mathbb{E}\left[\frac{\mathbb{1}(T=0)Y}{f(T=0|X)}\right]. \tag{5.8}$$

Using the Horvitz-Thompson estimator (Horvitz and Thompson, 1952),

$$\hat{\tau} = \frac{1}{N}\sum_{i=1}^{N}\left(\frac{\mathbb{1}(T_i=1)Y_i}{\hat{e}(X_i)} - \frac{\mathbb{1}(T_i=0)Y_i}{1-\hat{e}(X_i)}\right), \tag{5.9}$$

where N is the number of units. Therefore, ACEs of binary treatments can be directly estimated using the weights. However, this is not the case for continuous treatments as the estimand (Equation 5.7) is biased for $\mathbb{E}[Y(t)]$ and is not valid (Hernan and Robins, 2023). For continuous treatments, a model that describes the causal relationship between the treatment and outcome is necessary. One such class of causal models are MSMs. A MSM is a model for the potential outcome under treatment, for example,

$$\mathbb{E}[Y(t)] = \beta_0 + \beta_1 t. \tag{5.10}$$

Unlike 'regular' models, MSMs consider the expected outcome under different treatments, which is not observable due to the "fundamental problem of causal inference". Nonetheless, it is possible to reliably estimate MSMs with IPW adjustment because if the causal assumptions are met, the MSM is equal to:

$$\mathbb{E}[Y|T] = \beta_0 + \beta_1 T. \tag{5.11}$$

The parameters of MSMs have causal interpretations. For example, β_1 represents the ACE in the case of binary treatments. To summarise, weights are applied to fit a MSM to estimate ACEs of continuous treatments (and also binary treatments). As there are an infinite number of values when a variable is continuous, the goal with continuous treatments is to estimate the causal dose-response curve (CDRC), $\mu(t) = \mathbb{E}[Y(t)]$, rather than a single causal effect τ.

The weights in their current form are valid for causal effects of time-fixed treatments and marginal causal effects of time-varying treatments but may not sufficiently adjust to estimate joint causal effects of time-varying treatments. Thus, we describe the extension of the method to joint effects in the following section.

5.4.2.2 Time-varying Treatments

Time-varying treatments affected by time-varying confounders necessitate adjustments to eliminate confounding bias as before. However, unlike time-fixed treatments, simply adjusting for all the confounders together in the presence of treatment-confounder feedback fails when the goal is to estimate the joint effect. Suppose we adjust for halo masses H_k since it is the time-varying confounder in the causal model. Accordingly, there are no direct paths from H_k to time-varying treatments E_k, so there is no confounding bias. But, since the same paths constitute causal pathways of E_k to outcomes SFR_k, the joint effect now suffers from over-adjustment bias. This scenario is exactly the same as encountered with conditional approaches where the joint effect is biased whether one adjusts for confounders or not. The solution to the dilemma is simple: adjust for biases step-by-step rather than all at once.

With joint effects, the idea is to repeat the IPW process to adjust for biases at each time point. The exact method is as follows: estimate weights for each time point and then multiply them together to construct a final weight. This strategy eliminates confounding bias without introducing over-adjustment bias, so there is no overall bias. The method creates pseudo-populations at each time point, so the principle is the same as with time-fixed treatments. The general form of stabilised weights at time point $k(=j)$ (Robins et al., 2000),

$$w_j = \prod_{k=0}^{j} \frac{f(T_k|\bar{T}_{k-1})}{f(T_k|\bar{T}_{k-1}, \bar{X}_k)}, \tag{5.12}$$

where T_k is the treatment at time point k, $\bar{T}_{k-1}$ is the treatment history up until the time point, and $\bar{X}_k$ is the confounder history to the time point. The numerator is the conditional PDF of the current treatment given the previous treatment history, and the denominator is the conditional PDF of the current treatment given previous treatment and confounder histories. Compared to the weights for time-fixed treatments, the treatment history is conditioned on because time-varying treatments can be, and are, confounders if the previous treatments influence the current treatment and outcome from the perspective of a point in time. As before, the weights are applied to fit a MSM to estimate joint causal effects of interest. We apply the methodology to estimate the causal effect of environment. The key takeaway is that simply adjusting for the halo mass and environmental histories is insufficient to disentangle nature

and nurture.

In summary, IPW of MSMs consists of: (i) estimating weights to adjust for biases and (ii) fitting a MSM using the weights to estimate causal effects. Weights can be estimated directly from data if the treatment and confounders are binary or categorical variables and there are a limited number of them. In our case, environment and halo mass are inherently continuous variables, and we suffer from the curse of dimensionality with 11 total snapshots, so direct estimation is not feasible. Additionally, we cannot fit a parametric MSM to estimate causal effects since the causal relationship between environment and SFR is unknown. For both stages, we apply ML to estimate the marginal and joint causal effects of environment. We describe the ML algorithm we employ and the estimation process in the next section.

5.5 Estimation

Machine learning (ML) has revolutionised most fields, including astrophysics (see Baron, 2019; Fluke and Jacobs, 2020, for recent reviews). Significantly, in recent years, ML has been applied for causal insights into galaxy formation and evolution. Many studies have estimated the predictive power in an attempt to determine the primary factors in galaxy quenching (Teimoorinia et al., 2016; Bluck et al., 2019, 2020a,b, 2022; Brownson et al., 2022; Piotrowska et al., 2022). Moreover, McGibbon and Khochfar (2022) explored the importance of nature versus nurture. They incorporated the evolutionary histories of galaxies from the TNG simulations (similar to this analysis) and predicted galaxy properties with halo properties as inputs. Based on the feature importance being higher at later rather than earlier cosmic times, they concluded that nurture plays a more important role than nature. Nonetheless, predictive power does not necessarily imply causation due to the possibility of confounding factors, for example. If the confounders are input, ML can account for their influence by covariate adjustment to output predictive power with causal implications. At the same time, the predictive power can easily be biased if one is not careful and simply includes all variables assuming that ML will automatically make the necessary adjustments. For example, if a collider is present the predictive power would suffer from selection bias. In our case, if we input the halo mass and environmental histories and estimate the causal effect of environment, it would be biased because of the conditional approach. Overall, ML on its own cannot infer causality because it is correlation-based.

Causal machine learning (Causal ML) seeks to integrate causal reasoning into ML to move from correlations to causation (see Kaddour et al., 2022, for a review). The aim is to improve both causal inference with ML and ML with causal inference. The field is being pioneered but has already had successes, e.g., in improving the accuracy of medical diagnosis (Richens et al. 2020; also see Sanchez et al. 2022, for a review of causal ML for healthcare). We combine ML and causal inference to estimate the causal effect of environment on SFR. ML allows us to handle the high-dimensional data and model the potentially non-linear relationships between halo mass, environment, and SFR, and causal inference provides a theoretical framework to infer causality. Specifically, we follow the IPW method and utilise ML for estimation. In this regard, various ML algorithms have been applied to estimate propensity scores (see Setoguchi et al., 2008; Lee et al., 2010; Westreich et al., 2010; Cannas and Arpino, 2019, for comparisons), including a boosting algorithm based on decision trees (McCaffrey et al., 2004; Zhu et al., 2015). Furthermore, a recurrent neural network (RNN) architecture based on the method has been proposed that forecasts treatment responses over time (Lim, 2018). We employ the random forest (RF; Breiman 2001) as it has been shown to perform the best (out of the algorithms compared) in estimating propensity scores (Cannas and Arpino, 2019).

RF is an ML algorithm for regression, classification, and other tasks. It is an ensemble learning method as it leverages a multitude of decision trees to make predictions. Each decision tree is built by recursively dissecting the feature space to cluster data with similar target values until some predefined threshold. This process creates a mapping from input features to target variables, which enables predictions on new data after training. The algorithm is versatile and has been applied to solve a wide range of problems. In astrophysics, RFs have been utilised to predict photometric redshifts (photo-zs) and physical properties of galaxies (Carliles et al., 2008, 2010; Bonjean et al., 2019; Mucesh et al., 2021), classify supernovae (Lochner et al., 2016), and detect trans-Neptunian objects (Henghes et al., 2021), for example. Furthermore, the ML method has been used by most of the aforementioned galaxy quenching studies (Bluck et al., 2020a,b, 2022; Brownson et al., 2022; Piotrowska et al., 2022).

5.5.1 Overview

Estimation of causal effects using IPW of MSMs requires: (i) weights and (ii) a MSM. We utilise the RF algorithm for both tasks and define two types of models:

- *Weighting model* – the input features and target variable are the confounders and treatment, respectively. The model output is the expectation of treatment given confounders, $\mathbb{E}[T|X]$.
- *Outcome model* – the input feature and target variable are the treatment and outcome, respectively. The model output is the expectation of outcome given treatment, $\mathbb{E}[Y|T]$.

As the names suggest, the weighting and outcome models estimate weights and MSMs, respectively. We devise the following multi-step estimation process:

1. Train a weighting model.
2. Predict the treatment of each unit with the weighting model to estimate the propensity score.
3. Repeat the above steps, but now to estimate the numerator.
4. Construct weights.
5. Train an outcome model with each unit weighted.
6. Predict treatment outcomes with the outcome model to estimate causal effects.

5.5.2 Application

In the causal model, the previous halo mass H_{k-1} and environment E_{k-1} affect the current environment E_k and star-formation rate SFR_k. Therefore, it is necessary to adjust for them at each time point to eliminate confounding bias. We go a step beyond and adjust for the entire previous halo mass and environmental histories ($\bar{H}_{k-1}$ and $\bar{E}_{k-1}$) as a precautionary measure to account for any direct lagged effects of halo mass and environment that may hypothetically exist from further back in time. Taking everything into consideration leads us to the weights,

$$w_j = \prod_{k=0}^{j} \frac{f(E_k|\bar{E}_{k-1})}{f(E_k|\bar{E}_{k-1}, \bar{H}_{k-1})}. \tag{5.13}$$

The only difference compared to the general form (Equation 5.12) is in the denominator, where $\bar{X}_k$ ($\bar{H}_k$) is replaced with $\bar{X}_{k-1}$ ($\bar{H}_{k-1}$) because halo mass does not affect environment in the same time point. The numerator is the conditional PDF of the current environment given the previous environmental history, and the denominator is the conditional PDF of the current environment given the previous environmental and halo mass histories.

We estimate the propensity score (i.e., the denominator) as follows. We train a weighting model with the previous halo mass and environmental histories as the inputs and the current environment as the target. Once trained, we predict the current environment with the model, which is the $\mathbb{E}[E_k|\bar{E}_{k-1}, \bar{H}_{k-1}]$. Subsequently, we construct a normal distribution with the mean set to the prediction and the standard deviation equal to that of the residuals. Finally, we evaluate the density function at the true value.

We estimate the numerator following the same process. In the weighting model, we input the previous environmental history, with the target once again the current environment. The model output is the $\mathbb{E}[E_k|\bar{E}_{k-1}]$. We train separate weighting models to estimate the weights at each time point. The exception being $z \sim 6$ because there is no prior confounding by default as it is the baseline snapshot. The weights at the redshift are equal to one. We note that we have assumed the conditional PDFs follow the normal distribution to estimate the densities. Also, we trained and predicted on the same dataset because our goal is inference, not prediction.

Finally, we construct the weights as appropriate and incorporate them in outcome models to estimate the marginal and joint causal effects of environment. For the joint effect, we multiply the weights and use the final product weight. For the marginal effect, we simply apply the time-point weight. As our environment proxy, the 10th nearest neighbour density, is a continuous variable, we estimate CDRCs rather than single causal effects. For this, we define a grid of 21 treatment values between the 1st and 99th percentiles of the treatment distribution and predict with outcome models. As discussed in Section 5.2.3.2, the marginal effect of environment represents the short-term impact, while the joint effect represents the long-term impact. As per the defined environmental history $\bar{E}_k$ (Equation 5.1), the joint effect is the impact of the average environment, which we de facto mean by the causal effect of environment.

First, we focus on $z = 0$ to understand the final outcome of the galaxy formation and evolution process. We estimate the joint causal effect of environment on the SFR at $z = 0$ to determine the overall impact. We train an outcome model with the average environment $\bar{E}_0$ and the star-formation rate SFR_0 at $z = 0$ as the input and target, respectively. Once trained, we predict the final SFR at different average environments to estimate the CDRC. The weights applied are the product of weights at all redshifts, and the model prediction is the $\mathbb{E}[SFR_0|\bar{E}_0]$. Following the same process, we estimate the marginal causal effect of environment on the SFR at $z = 0$ to understand the most recent impact. In the outcome model, we input the final environment E_0, with the target once again the final star-formation rate SFR_0. The weights applied are simply the weights at $z = 0$, and the model prediction is the $\mathbb{E}[SFR_0|E_0]$.

Next, we extend our analysis to all the redshifts to determine how the role of environment has changed over time. We bootstrapped the entire estimation process to obtain confidence intervals around the CDRCs. This resulted in weighting models predicting a few extreme weights, probably due to the limited sample size. Given that they could drastically skew the causal effect, we trimmed the weights at the 1st and 99th percentiles. 1000 bootstrap samples were used.

We utilised the `scikit-learn` (Pedregosa et al., 2011) ML Python package to train the RF models, specifically the `RANDOMFORESTREGRESSOR` module. In regards to hyperparameter tuning, we kept the defaults and only coarsely tuned `min_samples_leaf`, which is the minimum number of samples in a leaf node. Our primary motivation was to best reduce the noise in the CDRCs due to: (i) the non-linear nature of RF and (ii) extrapolation beyond the training data. We found that the combination of 5 and 200 for the weighting and outcome models performed the best out of a limited parameter space, respectively. Consequently, we trained all the models with the aforementioned values. Before presenting and discussing the results in Section 5.7, we verify their validity in the next section by qualitatively and quantitatively checking whether the causal assumptions are met.

5.6 Validation

The validity of any causal inference depends on the satisfaction of the key causal assumptions described in Section 3.3, which are exchangeability, positivity, consistency, and no interference.

The exchangeability assumption states that potential outcomes must be independent of the treatment. In other words, it must be possible to swap treatment groups without changing their potential outcomes. To achieve exchangeability, it is necessary to adjust for any confounders, and thus we adjusted for halo mass, the time-varying confounder in the causal model. Whether or not the assumption is satisfied is untestable due to the possibility of unobserved confounders, which by definition are not known. Here, sensitivity analysis is invaluable because it allows one to determine the magnitude of impact on the results in the presence of unobserved confounding (Robins, 1999). However, we do not perform any such analysis as we have considered many known aspects of galaxy formation and evolution to construct the causal model, which shows no other confounders besides halo mass that causally affect both environment and SFR.

Positivity states that there must be a non-zero probability of receiving any treatment. In the context of this study, galaxies of all halo masses (or stellar masses, due to their correlation) must have some probability of occupying different environments to reliably estimate the causal effect of environment at any particular density. This is reasonably true according to the halo/stellar mass–environment distribution in Figure 5.6, which shows a relatively uniform halo/stellar mass coverage at different environmental densities. Though, in the lowest-density environments, there is a lack of the least and the most massive haloes. To alleviate this positivity violation, we have defined the treatment grid between the 1st and 99th percentiles of the environmental density distribution, so environments at both extremes are not considered.

Consistency states that the observed outcome must equal the potential outcome under treatment. In other words, the treatment must be well-defined. The treatment in our case is the environment, which has no universal definition, and this opens up the possibility of violating the assumption. We employ the 10th nearest neighbour density, and as long as the proxy consistently measures the environmental density in

varied environments and the effect of environment is similar at a particular density, we satisfy the consistency assumption.

Lastly, the no interference assumption states that the potential outcome of a unit must only depend on its treatment. This assumption is irrelevant in our case because galaxies in close proximity are roughly in the same environment, so they are subject to the same treatment. We are concerned about neighbourhood-level no interference (VanderWeele, 2008), which means that a galaxy's SFR must only depend on its environment and not the neighbouring environment. It is hard to imagine a physical mechanism that would result in the above being untrue, so we are reasonably confident that the no interference assumption holds. In summary, we believe the consistency and no interference assumptions hold. In the following section, we quantitatively verify exchangeability (assuming no unmeasured confounders) and positivity.

5.6.1 Diagnostic Tests

The critical component of our causal analysis is the weights, which we utilise to capture and adjust biases via the IPW method to estimate MSMs. Their validity directly translates to unbiased causal effects, which means they can provide clues on the satisfaction of the causal assumptions. As a result, we perform diagnostic tests on them to check exchangeability and positivity. We highlight that we conduct the tests on the weights estimated from the non-bootstrapped analysis.

The goal of IPW is to create a pseudo-population in which the treatment is independent, and this produces exchangeability as the treatment groups are comparable in terms of their covariate distributions when the treatment does not depend on anything. We assess the covariate balance using the correlation-based method of Zhu et al. (2015) to determine exchangeability. The basic premise is to determine the correlation between the confounders and treatment in the pseudo-population, and if it is minimal, then the treatment is independent, there is no confounding, and exchangeability is achieved. The exact procedure is as follows:

1. Sample data with replacement from the original dataset according to the weights w_i.

2. Compute the correlation coefficient ρ_m between confounder X_m and treatment T in the weighted sample.

3. Repeat the above steps N times and calculate the average correlation coefficient $\bar{\rho}_m$.

4. Finally, average the absolute values of all the average correlation coefficients to compute the average absolute correlation coefficient $AACC$.

We assess the covariate balance at each time point because, if achieved, the joint effects are valid along with the marginal effects. Accordingly, the data is sampled per the time-point weights, not the final product weights. For consistency, the correlation coefficients are computed with the previous environments $\bar{E}_{k-1}$ and halo masses $\bar{H}_{k-1}$ even though the confounders of the current environment E_k and star-formation rate SFR_k may only be the prior environment E_{k-1} and halo mass H_{k-1}. Specifically, Kendall's tau coefficient (Kendall, 1938) is estimated because the halo mass and environment distributions are not normal, and the relationship between them is non-linear (as can be observed in Figure 5.6). In total, 1000 bootstrap samples are generated to calculate the average correlation coefficients.

Figure 5.8 shows the $AACC$ at the different redshifts in the original population before weighting and in the pseudo-population after weighting. Zhu et al. (2015) claim that there is minimal confounding when $AACC < 0.1$, medium confounding when $0.1 < AACC < 0.3$, and large confounding when $AACC > 0.55$. However, these limits are based on heuristics, and there is no theoretical $AACC$ value for exchangeability. In this case, the relative change in the $AACC$ is more important than the absolute value. As observed, there is a clear decrease in the $AACC$ post weighting across all the redshifts, which indicates that IPW has reduced confounding and improved exchangeability.

The mean of the stabilised weights is expected to be one because the size of the pseudo-population equals that of the original population (Hernán and Robins, 2006). Crucially, significant deviations indicate misspecification of the weighting model, violation of positivity, or both (Cole and Hernán, 2008). However, as is the case with the $AACC$, there is no reference value. Figure 5.9 shows the weight distributions at the different redshifts. The means are close to one, so the causal model seems to be valid, and positivity is not violated. Based on the reasoning and diagnostics, the causal assumptions seem to have been met or at least not grossly violated (although it cannot be definitively proven). Thus, the results can be considered valid.

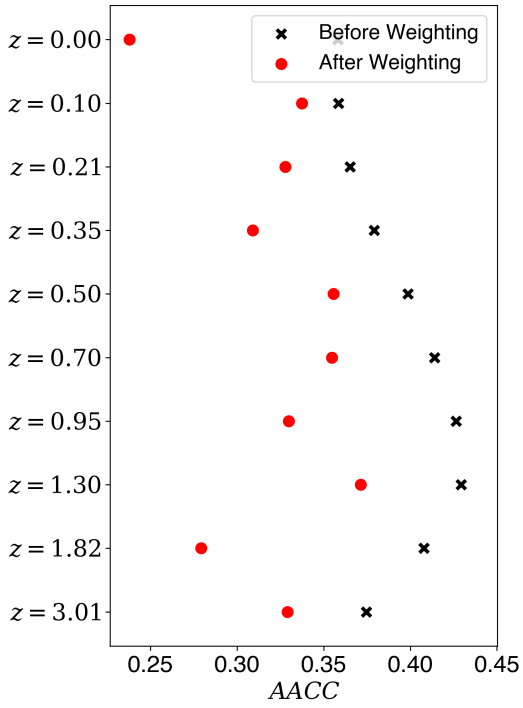

Figure 5.8: Average absolute correlation coefficients ($AACC$) at different redshifts in the original population before weighting and in the pseudo-population after weighting.

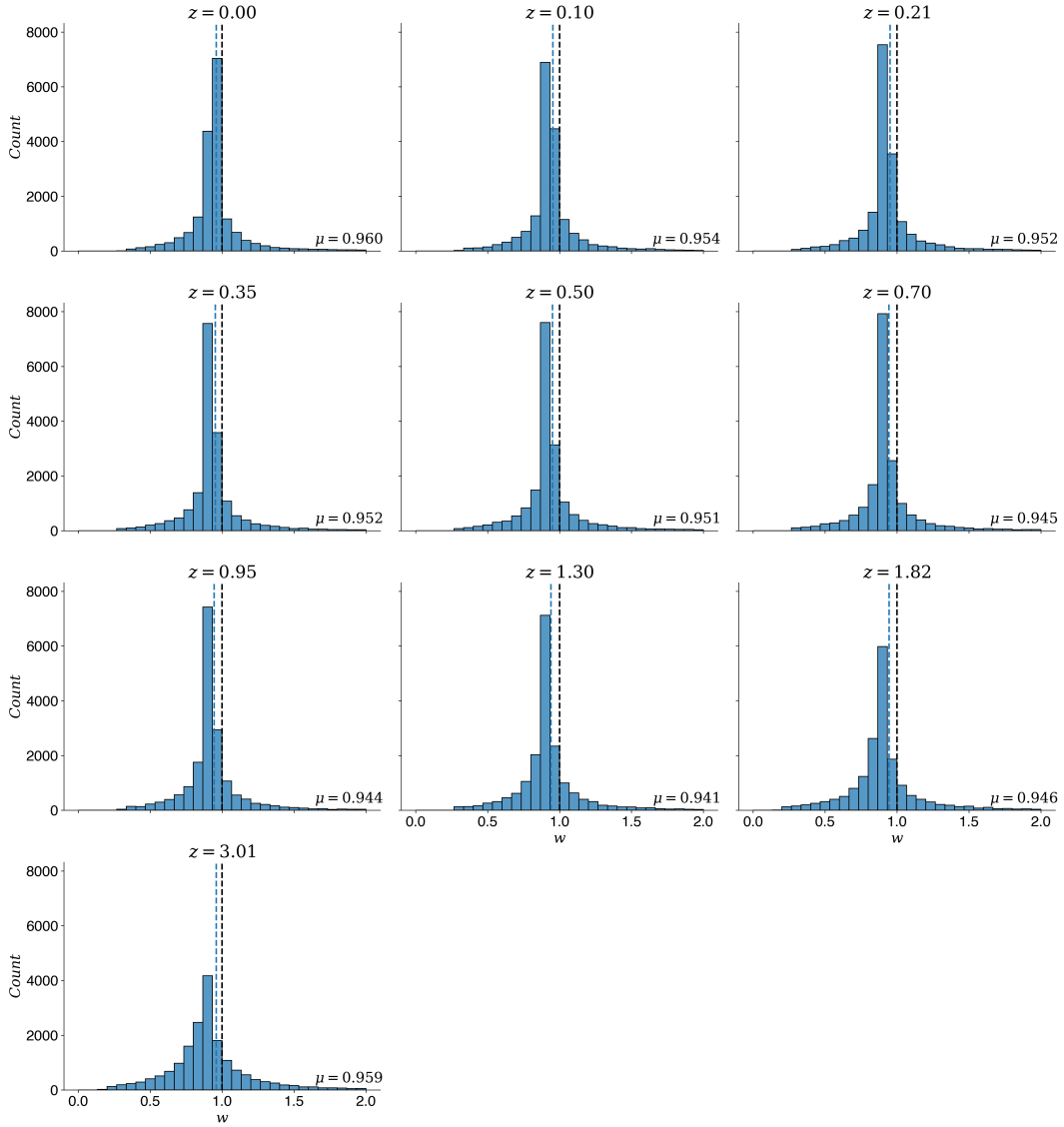

Figure 5.9: Weight distributions at different redshifts, assuming the causal model. The black and blue dashed lines indicate the reference mean (1) and the mean of the distribution (stated), respectively.

5.7 Results and Discussion

In this section, we first discuss the overall causal effect of environment, contrasting the marginal and joint causal effects. Next, we describe how the role of environment has changed over time. Finally, we compare different causal models to our causal model.

5.7.1 Overall Causal Effect of Environment

Figure 5.10 shows the CDRCs of the marginal and joint causal effects of environment on the SFR (i.e., causal SFR–density relations) at $z = 0$. The CDRC denotes the average response in the population if all units were subject to treatment $T = t$. By comparing any two points on the curve, one can determine the mean change in the outcome if all units received, for example, treatment $T = t_a$ instead of $T = t_b$. This difference in outcome is the ACE τ. The CDRC of the marginal effect represents the average SFR of galaxies if they inhabited the specific environment at $z = 0$, and the CDRC of the joint effect represents the average SFR of galaxies if they inhabited, on average, the specific environment over time. The bottom panel shows the ACEs of different density environments (comparing to the lowest-density environment).

Focusing on the joint effect (i.e., the causal effect), the CDRC is relatively flat and the causal effect of environment is negligible up to $\log(\Sigma_{10}) \sim 1$. Subsequently, the CDRC trends downwards and the causal effect of environment becomes negative as the average SFR decreases with increasing environmental density until $\log(\Sigma_{10}) \sim 2.5$, at which point there is a reversal as the average SFR rises overall. In summary, environment does not influence the SFR at low densities, but at intermediate-to-high densities, it has a negative effect. On the other hand, at the highest densities, the causal effect of environment is positive (explained in Section 5.7.3). Furthermore, there is a characteristic density ($\log(\Sigma_{10}) \sim 1$) beyond which environment starts playing a role. We believe this may be physical, as not only has it previously been evidenced by Lewis et al. (2002) and Gómez et al. (2003), but they also reported the same characteristic density (albeit projected 2D). The density probably marks a transition from the field to group environment. In short, the overall causal effect is negative and substantial, with environment maximally suppressing the average SFR by a factor of ~ 100.

Comparing the marginal and joint effects, the CDRCs are broadly similar in

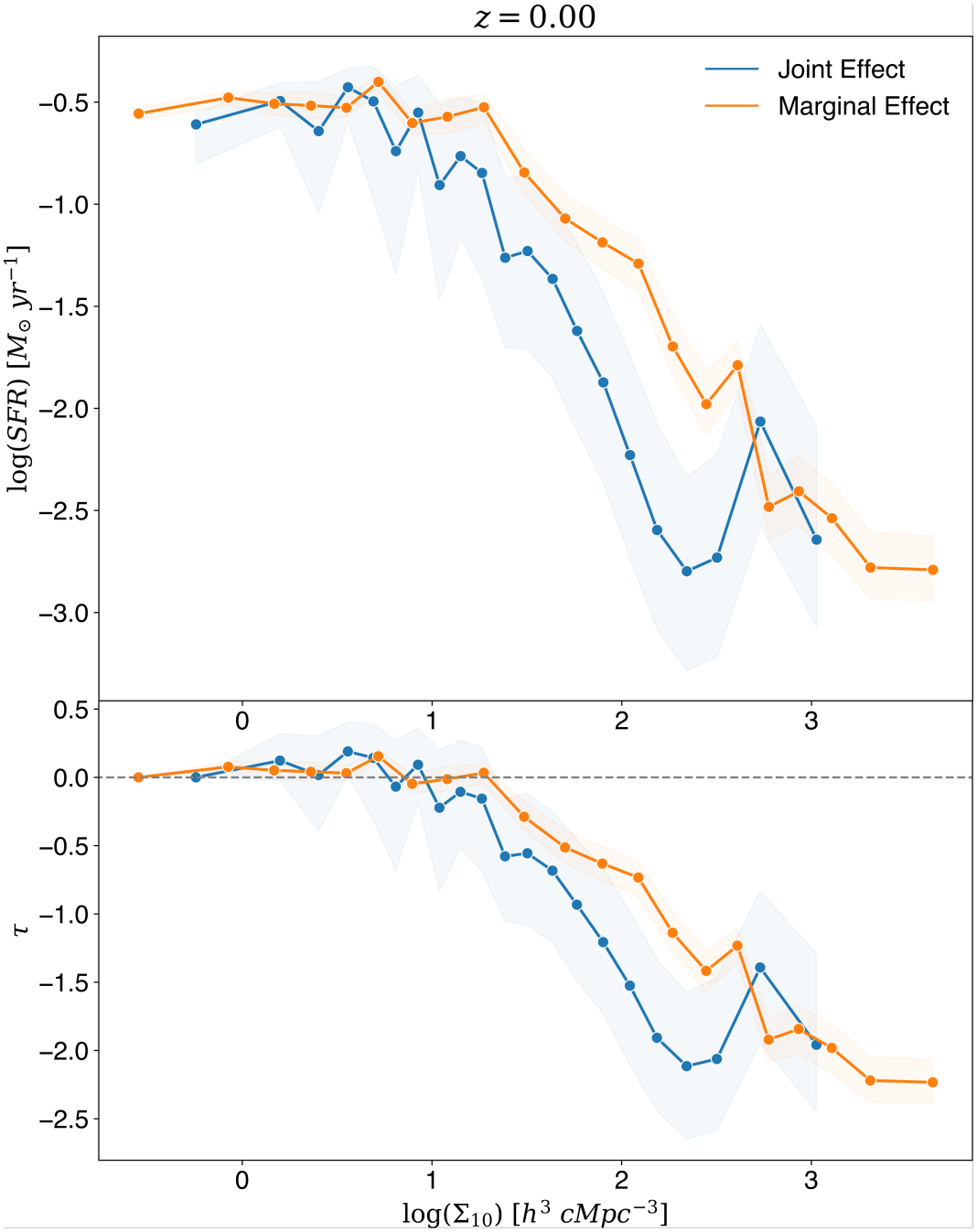

Figure 5.10: Causal dose-response curves (CDRCs) of the marginal and joint causal effects of environment on the SFR (i.e., causal SFR–density relations) at $z = 0$. The bottom panel shows the average causal effects τ of different density environments (comparing to the lowest-density environment). The shaded regions represent the 68% confidence interval, estimated with bootstrapping.

terms of the overall trend. However, they diverge in absolute values, especially after the characteristic density. Specifically, the marginal effect predicts a higher average SFR than the joint effect across most of the domain. There are two important implications given the above: (i) the SFR does not only depend on the current environment but also the previous environments, i.e., there is a long-term effect of environment, and thus (ii) the marginal effect is a biased estimator of the overall causal effect of environment. Neighbourhood effect studies (Do, 2009; Do et al., 2013; Clarke et al., 2014; Yang and South, 2018) have also evidenced the same in their context (see Jivraj et al., 2019, for a recent review). In conclusion, snapshot studies are insufficient to estimate the causal effect of environment. And longitudinal studies that employ snapshot environment as a measure rather than the environmental history (in some form) will estimate a biased causal effect. Consequently, we focus on the joint effect from hereon, referring to it as the causal effect.

5.7.2 Role of Environment over Time

Figure 5.11 shows the CDRCs of the causal effects of environment on the SFR at $z = 0$ and at different redshifts going back to $z \sim 3$. The causal effect is the most substantial at $z = 0$ and weaker in the recent past, implying that the impact of environment accumulates over time. The negative trend largely flatlines at $z = 0.7$—and surprisingly—reverses at $z = 0.95$. At and beyond this redshift, the average SFR increases with increasing environmental density, so the causal effect of environment on the SFR is positive. Furthermore, the effect is significant and becomes stronger with redshift, from a factor of ~ 10 to over 100.

The downtrend observed at low redshifts is consistent with previous studies, but the uptrend at high redshifts is unexpected given the consensus: environment negatively affects star formation. Despite this, studies have been inconsistent in their findings, and there is an active debate on whether the SFR–density relation, as observed in the local Universe, exists at intermediate ($z \sim 1$) to high redshifts ($z > 1$). Some studies have found that the relation persists in the early Universe (Patel et al., 2009; Muzzin et al., 2012; Quadri et al., 2012; Chartab et al., 2020), others have evidenced a flattening (Feruglio et al., 2010; Grützbauch et al., 2011; Scoville et al., 2013; Ziparo et al., 2014; Darvish et al., 2016), while others yet have noted a reversal (Elbaz et al., 2007; Cooper et al., 2008; Tran et al., 2010; Popesso et al., 2011; Santos

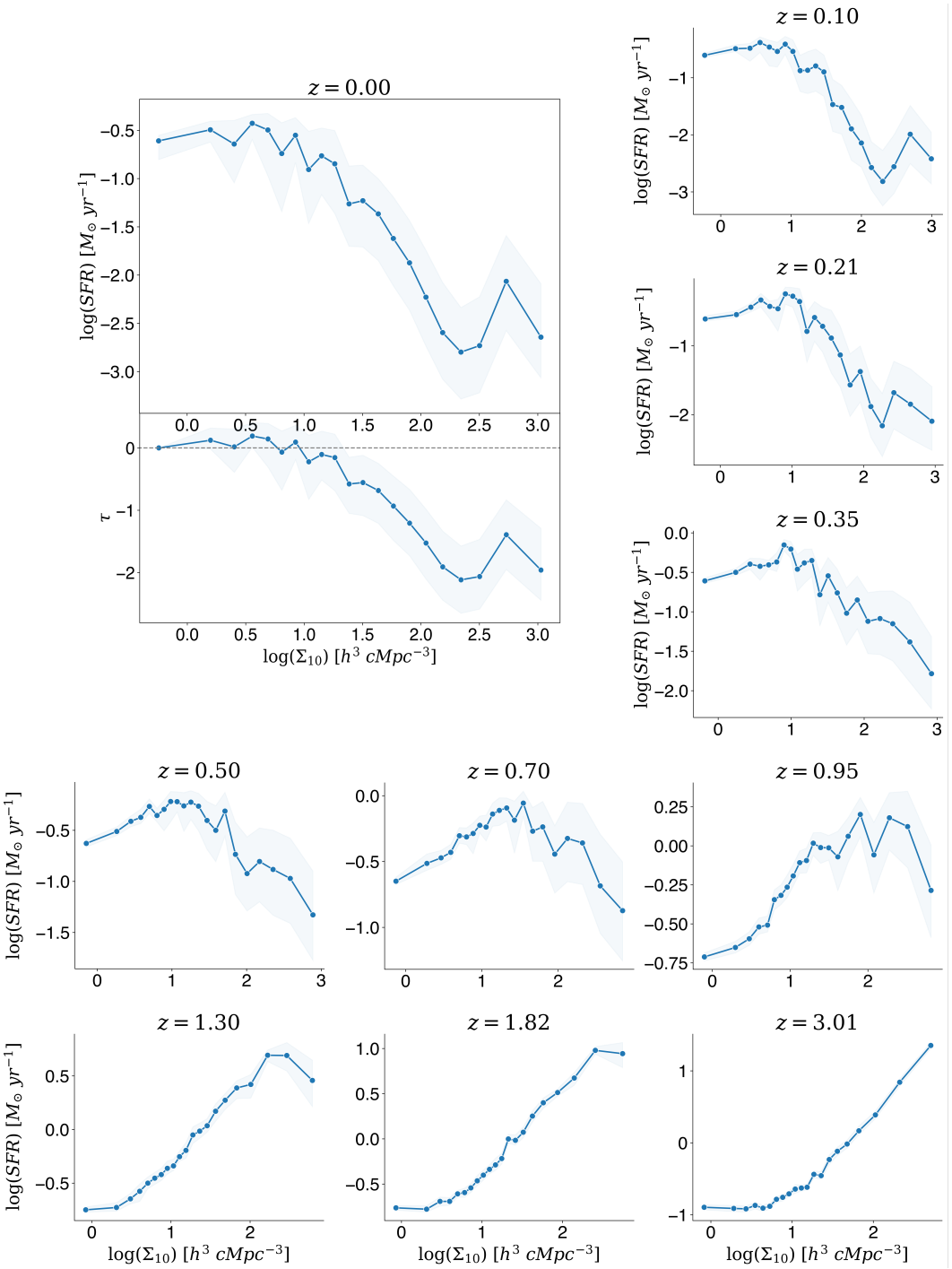

Figure 5.11: Causal dose-response curves (CDRCs) of the causal effects of environment on the SFR (i.e., causal SFR–density relations) at $z = 0$ and at different redshifts going back to $z \sim 3$. The bottom panel of $z = 0$ shows the average causal effects τ of different density environments (comparing to the lowest-density environment). The shaded regions represent the 68% confidence interval, estimated with bootstrapping.

et al., 2015; Lemaux et al., 2022). The lack of consistency between the studies is due to a multitude of reasons, beginning with the ambiguity around the SFR–density relation itself. The term is loosely used in the literature and is polysemous, as studies have analysed the specific star-formation rate (sSFR)–density, colour–density, and star-forming/quiescent fraction–density relations under the SFR–density relation moniker. These quantities, while related, are fundamentally different and cannot be compared. Another point for contention is the data or lack thereof. Deep surveys observe a small patch of the sky, so the studies are susceptible to cosmic variance. Lastly, since there is no universal definition of environment (Muldrew et al., 2012), the choice of measure is possibly responsible for part of the disagreements.

It is difficult to draw parallels to the literature for all the aforementioned reasons, but the most critical aspect is that the analyses have been largely statistical in nature. In summary, studies have attempted to adjust for confounding by investigating sSFR instead of SFR and/or binning the relation into fixed bins of stellar mass, which is only correct if stellar mass is a true confounder. Furthermore, they have focused on snapshots of galaxies with no knowledge of their evolutionary histories due to the restrictions of observational data. As a result, they have been unable to disentangle the causal effects of nature and nurture by unravelling the feedback loops present in the causal model. Regardless, both observational (Elbaz et al., 2007; Lemaux et al., 2022) and simulation studies (Tonnesen and Cen, 2014; Hwang et al., 2019) have found SFR–density reversals (albeit at a weaker level) independent of the stellar mass correlation, thus supporting a positive impact of environment. Additionally, Hwang et al. (2019) and Lemaux et al. (2022) observed the uptrend strengthening with redshift, as we do here. The consistency of our results, with Hwang et al. (2019) in particular, given that they also used the TNG simulations (though the larger volume TNG300 instead of TNG100), is strong evidence for the reliability of our study.

Assuming our results are genuine, a possible explanation for the positive causal effect of environment in the early Universe is that denser environments have a larger reservoir of material. As a result, galaxies in such environments are able to accrete more matter, which assuming gas cooling translates to enhanced star formation. While this is true for high-density environments in the late Universe as well, the

difference is that in the early Universe there is limited competition between haloes and thus accretion is more unrestricted because the density is not too high. The lower density also means that the negative environmental processes have yet to affect galaxies, which in addition to the above, can explain the positive causal effect.

Another potential cause is major mergers, which are more likely at high redshifts (Le Fèvre et al., 2000; Kampczyk et al., 2007; Kartaltepe et al., 2007; Lotz et al., 2011) in dense regions when the velocities are not too large. An influx of cold gas in a gas-rich galaxy merger can trigger starbursts. It is a different fact that such mergers can accelerate the evolution of a galaxy and quench it altogether, so the causal effect of environment in the long term is still negative, as observed at $z = 0$. We iterate that the positive trend is not just a consequence of massive galaxies in denser environments. Given that haloes form earlier in denser regions (i.e., assembly bias), a significant positive causal effect of environment on SFR in the early Universe followed by a downturn later on, is consistent with and explains galaxy downsizing. That is, massive galaxies form earlier and at an accelerated rate, while low-mass galaxies form later and more slowly (Cowie et al., 1996; Heavens et al., 2004; Kodama et al., 2004; Jimenez et al., 2005; Juneau et al., 2005; Thomas et al., 2005; Bauer et al., 2005; Bell et al., 2005; Nelan et al., 2005; Feulner et al., 2005; Bundy et al., 2006; Drory and Alvarez, 2008; Vergani et al., 2008; Mortlock et al., 2011).

In the following section, we place our results into a wider context by comparing our causal model to others. We answer the following critical questions: (i) is nature important in the nature versus nurture debate? Specifically, is galaxy formation and evolution top-down dominated by environment with no reverse influence of halo mass? (ii) is controlling for the stellar mass at a snapshot in time sufficient to estimate the causal effect of environment? and (iii) is stellar mass an adequate proxy of nature? In other words, can stellar mass be substituted for halo mass in the causal model to estimate the causal effect?

5.7.3 Model Comparison

We first consider the possibility of no confounders. In our causal model, halo mass is the sole confounder as it causes environment and SFR. However, this may be time-dependent and scale-dependent as it is likely that in the late Universe and on the largest scales, environment completely dominates the evolution of a galaxy and halo mass has no reverse influence on environment, so it ceases to be a confounder. In this scenario, the raw correlation between environment and SFR is the unbiased causal effect of environment. Consequently, the first step of the estimation process is skipped as no bias adjustment is necessary and unweighted outcome models are directly trained to learn the SFR–density relation. As before, an outcome model is trained for each time point with environment $\bar{E}_k$ and star-formation rate SFR_k as the input and target, respectively. We refer to the model as the naïve model.

Next, we mimic previous studies—that is—we adjust for stellar mass at a snapshot in time to estimate the causal effect of environment. The method supposes the causal model illustrated in Figure 5.12, in which stellar mass ($M_\star$) is the confounder. Obviously, stellar mass does not cause environment and SFR, and hence the model is implicit in the literature. Furthermore, the model fails to capture dynamic systems with feedback loops that galaxies ultimately are. Nonetheless, the model/approach is still adopted, in part because of the shortcomings of observational data where the halo mass information and evolutionary history of galaxies are not readily available. Controlling for the stellar mass at a snapshot in time represents the only practical option (given that it correlates with halo mass) to disentangle nature from nurture, even though it has been demonstrated by De Lucia et al. (2012) that this is not sufficient. We refer to the model as the traditional model.

We implement the model following the same estimation process. In the weighting models, the input is the stellar mass, and the target is the current environment. We highlight that we only input the current stellar mass and not the stellar mass history into the models, unlike in the causal model case, where we had input both the halo mass and environmental histories. The weighting models are then used to estimate the conditional densities $f(E|M_\star)$. The marginal densities $f(E)$ are determined via kernel density estimation (KDE), and no further models are trained. Finally, the weights are constructed with both densities and incorporated into outcome models.

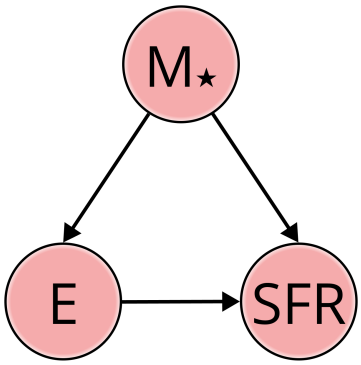

Figure 5.12: The causal model assumed implicitly in the literature to estimate the effect of environment. We refer to it as the traditional model.

The time-point weights are not multiplied together to form the final product weights, but rather they are applied separately to replicate the previous analyses. We train two outcome models, one with the snapshot environment and the other with the average environment, for a like-to-like comparison with the previous studies and consistency with our results, respectively. For brevity, we refer to the causal effect estimated with the former as the marginal and the latter as the joint effect, even though it is technically neither.

Finally, we redo the analysis assuming our causal model, but on this occasion, we input stellar mass as the time-varying confounder instead of halo mass in the weighting models (labelled as "causal model (stellar mass)"). Our goal is to answer the question: is stellar mass a suitable proxy of nature (halo mass) given a valid causal model and method to disentangle nature and nurture. This is important because halo mass (not host halo mass) is challenging to infer observationally. Figure 5.13 shows the CDRCs of the causal effects of environment on the SFR at $z = 0$ and at different redshifts going back to $z \sim 3$, of the different causal models. The bottom panel of $z = 0$ shows the difference in the average SFRs between the different causal models and the causal model (labelled as "causal model (halo mass)").

5.7.3.1 Causal versus Naïve Model

At $z \sim 3$, the CDRCs of the naïve and causal models are largely similar, which implies halo mass has minimal influence on environment (assuming it impacts the SFR).

This is not surprising because at this redshift, haloes are mostly isolated and yet to majorly influence the environment a galaxy inhabits. There is a slight deviation after $\log(\Sigma_{10}) \sim 2$, so halo mass does have an impact in the denser regions, essentially supporting the former. Over time, the curves diverge further as the impact of halo mass accumulates. At $z = 0$, there is a factor of ~ 6 difference in the average SFR in the densest environment between the two models.

Up to $\log(\Sigma_{10}) \sim 2$ at $z = 0$, the CDRC of the naïve model is above the causal model's, which signifies that halo mass has a positive effect on the SFR because, post adjustment, the average SFR is lower. The probable explanation is that at low-to-intermediate densities, a larger halo is able to accrete more gas from its surroundings, which up to a certain extent, translates to enhanced star formation if the hot gas can effectively cool. Between $\log(\Sigma_{10}) \sim 2 - 2.5$, there is no discernible difference between the two models, so halo mass has no effect on environment. In the host halo mass–environment distribution in Figure 5.6, $\log(\Sigma_{10}) \gtrsim 2$ in average density probably corresponds to large group and cluster host haloes, where environment is indeed believed to dictate galaxy evolution. Ultimately, the causal effect of environment is the largest in this density regime.

Beyond $\log(\Sigma_{10}) \sim 2.5$, there is no consistent pattern. To begin with, the CDRC of the naïve model is below the causal model's, so halo mass has a negative impact on the SFR. However, just before $\log(\Sigma_{10}) \sim 3$, the curves flip, and halo mass resumes its positive effect. We do not think this is physical and believe the fluctuation is just a manifestation of galaxies switching from centrals to satellites when a smaller group merges with a larger group. Halo mass is considered to influence centrals more than satellites, so when galaxies switch from the former to the latter, its effect also changes. And since the causal effect is of the average environment over time, the effect of halo mass is observed to be inconsistent. Surprisingly, the causal effect of environment is less negative as the average SFR, on the whole, increases with environmental density. However, we do not think galaxies are actually less affected in the highest-density environments. We argue that the result is because of the asymmetry of the environmental effects on centrals versus satellites, whereby the former is not subject to most of the environmental processes. As for the uptick itself, the cause is likely galactic cannibalism since it is one of the few known processes that

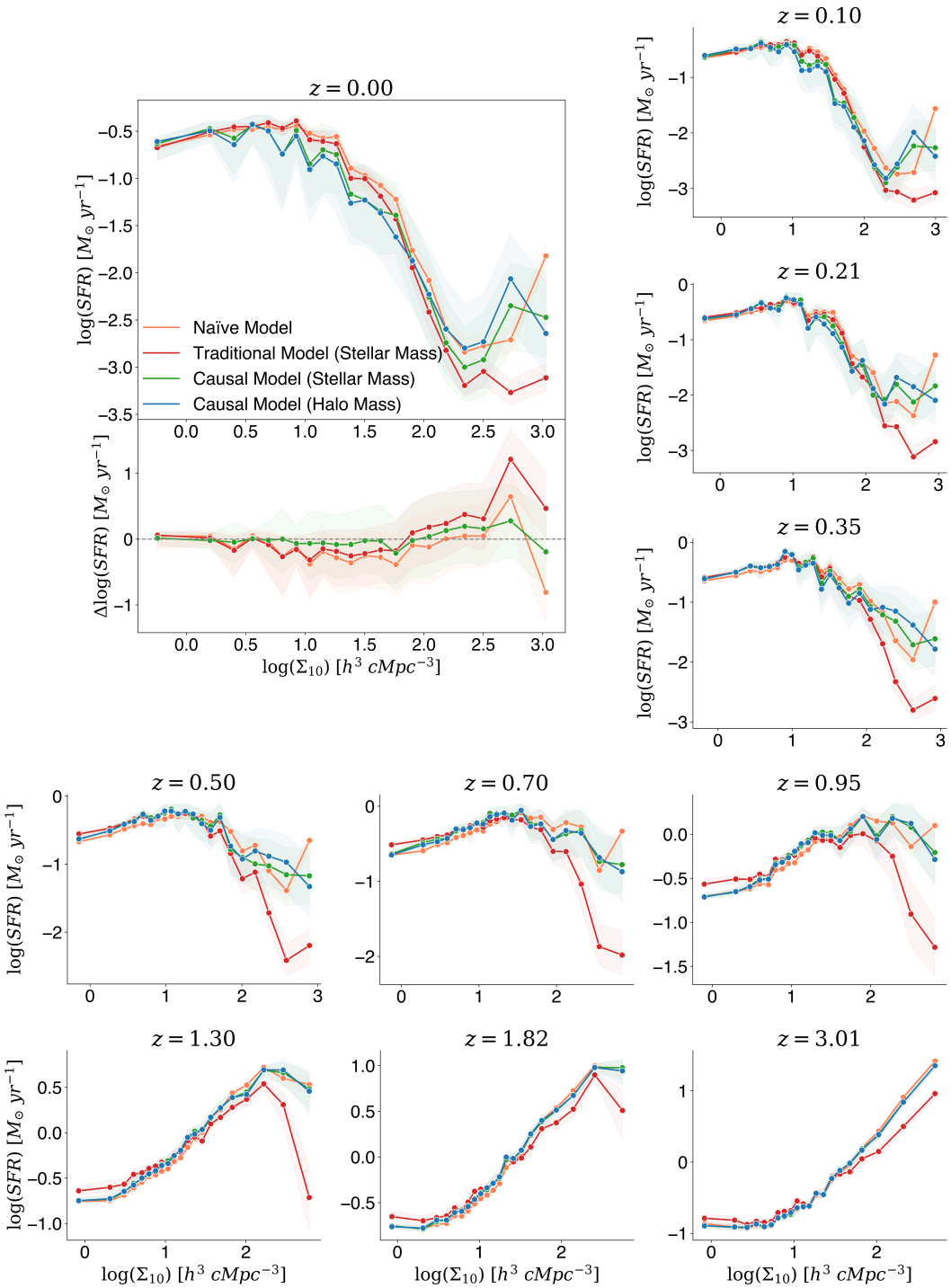

Figure 5.13: Causal dose-response curves (CDRCs) of the causal effects of environment on the SFR (i.e., causal SFR–density relations) at $z = 0$ and at different redshifts going back to $z \sim 3$, of the naïve, traditional, and causal models (with stellar mass and halo mass as the confounder, respectively). The bottom panel of $z = 0$ shows the difference in the average SFRs between the different causal models and the causal model (i.e., causal model (halo mass)). The shaded regions represent the 68% confidence interval, estimated with bootstrapping.

is understood to affect central galaxies in dense cluster environments and one that can boost the SFR. All things considered, the next step is to split the causal effect of environment on centrals and satellites. When the causal effect of a treatment is modified by a variable V (central or satellite), it is referred to as effect modification, and IPW of MSMs can be adapted to estimate the separate effects. We do not explore this in this thesis and leave it for future work.

In conclusion, nature is important and galaxy formation and evolution is not top-down determined by environment. The environment affects halo mass, but halo mass influences the environment of a galaxy as well. Ignoring the role of nature by not adjusting for halo mass leads to the causal effect in the densest environment being underestimated by a factor of ~ 6. The next step is to estimate the causal effect of halo mass on SFR to answer the long-outstanding question: which is more important, nature or nurture? This can be achieved by repeating the analysis but now with halo mass as the treatment and environment as the confounder.

5.7.3.2 Causal versus Traditional Model

As expected, the traditional model predicts a negative causal effect of environment at low-to-intermediate redshifts. However, unlike many previous studies, the negative trend does not flatten at high redshifts. Instead, it reverses analogous to the causal model, and the causal effect of environment becomes positive. For a like-to-like comparison, Figure 5.14 shows the marginal causal effects. While the uptrend is certainly weaker than the joint causal effect, it is still present nonetheless, especially at $z = 1.82$ and $z \sim 3$. The results further confirm that the positive trend observed with the causal model is not simply due to massive galaxies in denser environments that form more stars because we adjust for this fact by controlling for stellar mass with the traditional model. As explained in the previous section, the positive causal effect at high redshifts may be a consequence of the early Universe not being dense enough for the negative environmental processes whilst simultaneously being conducive to the positive processes such as halo accretion and (major) mergers. For a definitive answer, the causal effect of individual environmental processes must be estimated. The critical work has been done with the construction of a comprehensive causal model (Figure 5.4). Using this model, we can extend our analysis to estimate the causal effects of different processes (see Smethurst et al., 2017, for work in this

direction).

Comparing the traditional to causal model, the former overestimates the negative causal effect of environment at low-to-intermediate redshifts and underestimates the positive causal effect at high redshifts by up to a factor $\gtrsim 10$ at specific densities. At $z = 0$, the CDRC of the traditional model is largely identical to the naïve model's except in the high-density regime, so adjusting for the stellar mass at the redshift has mostly had no effect. It has not eliminated the confounding bias and is therefore insufficient to estimate the causal effect of environment. In fact, the traditional model deviates further from the assumed truth (i.e., the causal model) than the naïve model, so adjusting for the stellar mass at a snapshot in time actually has an adverse effect. The failure of the traditional model is hinted by the skewed weight distributions in Figure 5.15, with means farther from one compared to the causal model's (Figure 5.9).

5.7.3.3 Causal Model: Halo versus Stellar Mass

While there are differences at specific densities, the CDRCs of causal model (halo mass) and causal model (stellar mass) are similar overall. Consequently, stellar mass is an adequate proxy of halo mass and thus nature. This finding is highly significant because unlike halo mass (not host halo mass), stellar mass can be readily inferred observationally, and the ultimate goal of this study is to estimate the causal effect of environment on galaxies in the real Universe. Evidently, the lack of evolutionary histories of galaxies, or more specifically, the halo/stellar mass and environmental histories is a major hurdle. On this front, star-formation histories (and thus stellar mass histories) can be recovered by modelling and fitting spectral energy distributions (see Conroy, 2013, for a recent review), both in parametric (Maraston et al., 2010; Papovich et al., 2011; Ciesla et al., 2016; Lee et al., 2018; Carnall et al., 2018) and non-parametric forms (Heavens et al., 2000; Cid Fernandes et al., 2005; Ocvirk et al., 2006; Tojeiro et al., 2007; Koleva et al., 2009; MacArthur et al., 2009; Pacifici et al., 2016; Leja et al., 2017; Belli et al., 2019; Iyer et al., 2019; Johnson et al., 2021; Ji and Giavalisco, 2022, 2023). And recently, Sarpa et al. (2022) employed the extended Fast Action Minimization (eFAM) method to reconstruct the environmental history of galaxies. Consequently, it is feasible to estimate the real causal effect (on star formation at least).

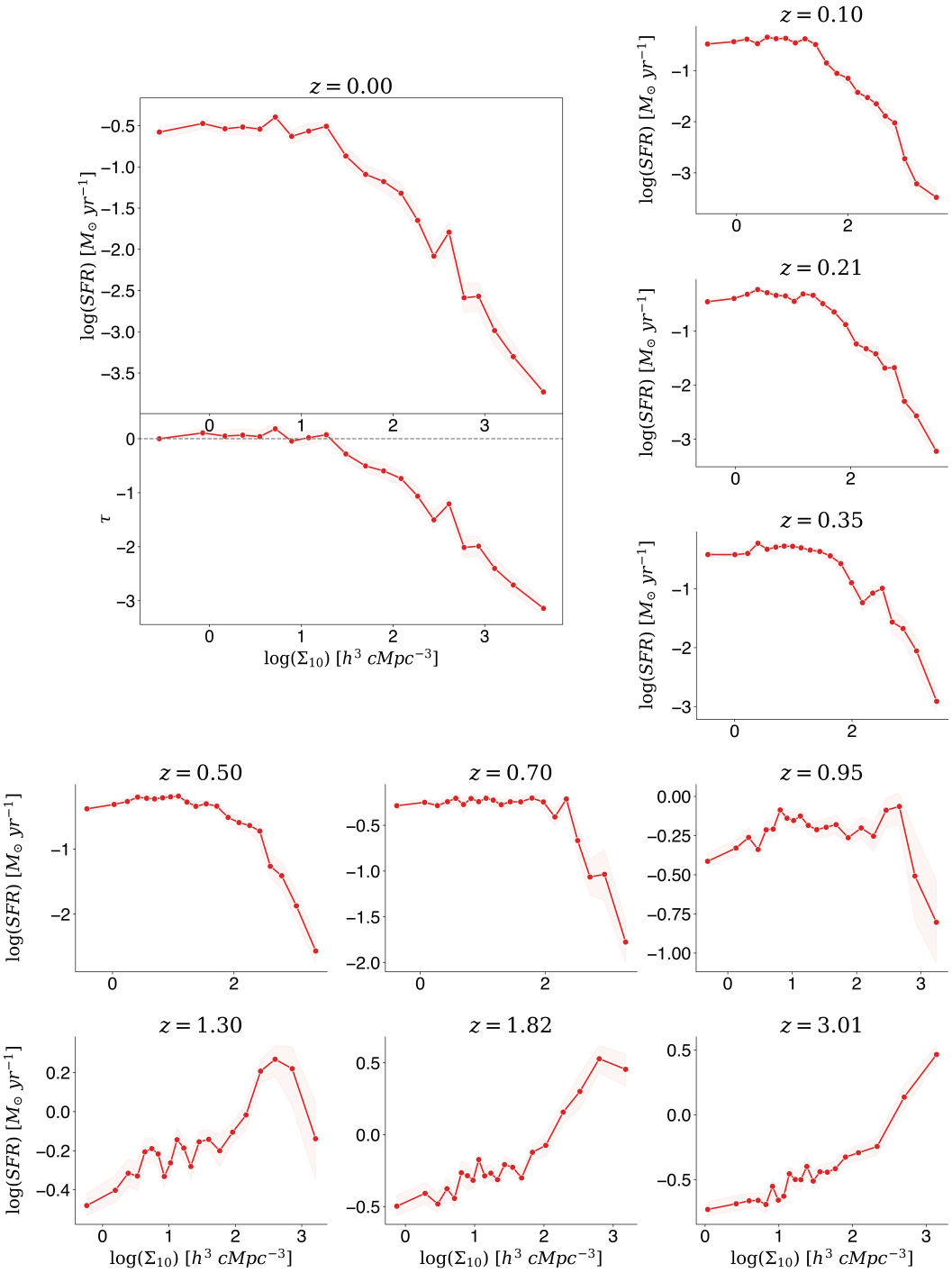

Figure 5.14: Causal dose-response curves (CDRCs) of the marginal causal effects of environment on the SFR (i.e., causal SFR–density relations) at $z = 0$ and at different redshifts going back to $z \sim 3$, assuming the traditional model. The bottom panel of $z = 0$ shows the average causal effects τ of different density environments (comparing to the lowest-density environment). The shaded regions represent the 68% confidence interval, estimated with bootstrapping.

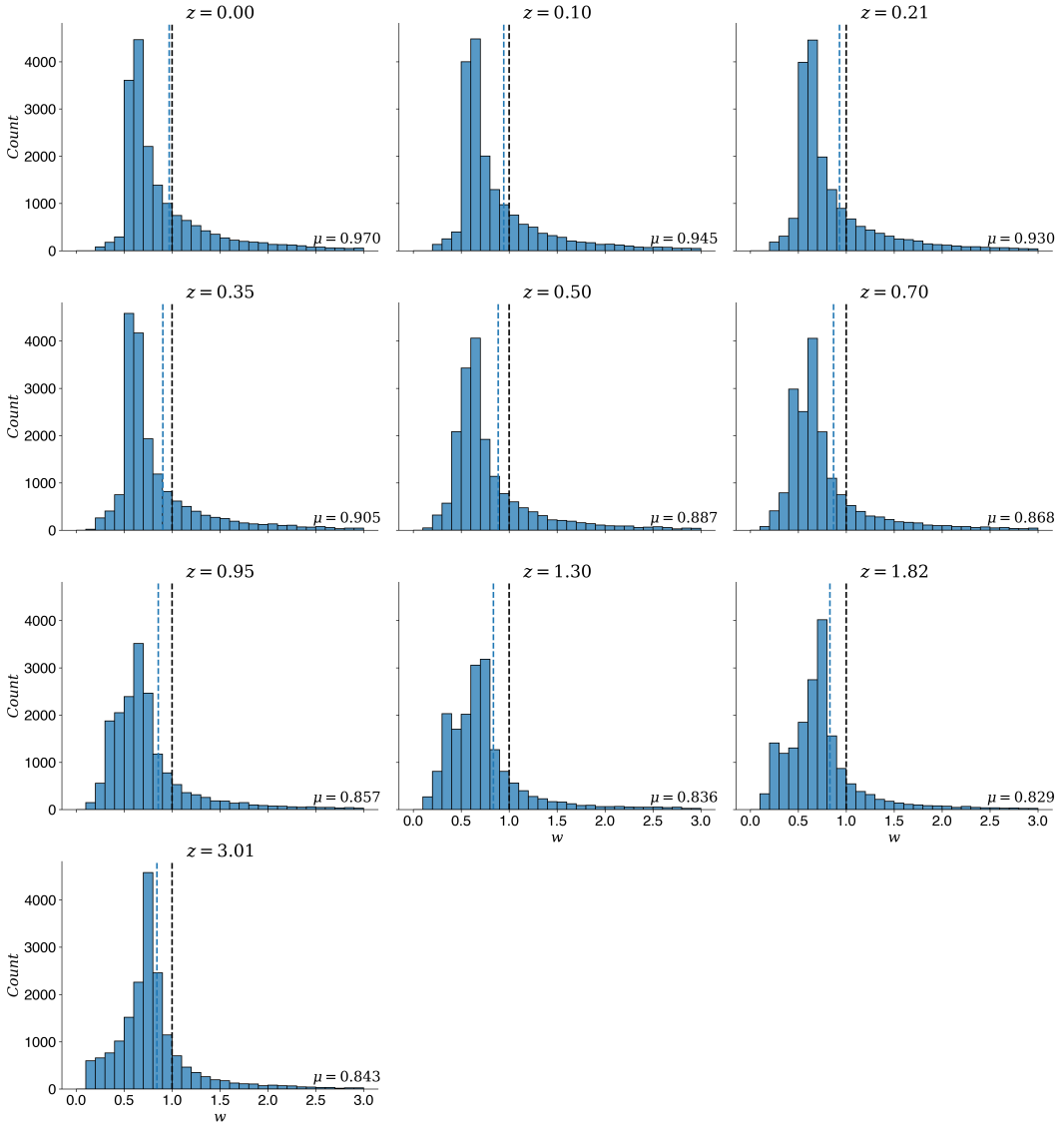

Figure 5.15: Weight distributions at different redshifts, assuming the traditional model. The black and blue dashed lines indicate the reference mean (1) and the mean of the distribution (stated), respectively.

5.8 Conclusions

In this chapter, we tackle the challenging problem of disentangling nature and nurture to estimate the causal effect of environment on star-formation rate (SFR). We develop a comprehensive causal model of galaxy formation and evolution and apply causal machine learning (causal ML) by combining the causal inference framework with ML. Specifically, we employ the g-method, inverse probability weighting (IPW) of marginal structural models (MSMs), and the random forest (RF) algorithm. We devise and implement an overall two-step estimation process on the IllustrisTNG simulations, specifically the TNG100-1 run. The dataset consists of 18629 galaxies traced over cosmic time with merger trees from $z \sim 6$ to the present day $z = 0$, and our environment proxy is the 3D 10th nearest neighbour density. We estimate the causal effect at $z = 0$ to determine the overall impact and at different redshifts going back to $z \sim 3$ to understand the role of environment over time. Also, we compare our causal model to others to place our results into a wider context and answer some fundamental questions.

The causal effect is found to be negative and substantial, with environment suppressing the SFR by a factor of ~ 100. Furthermore, we discover that:

1. There is a characteristic density, $\log(\Sigma_{10}) \sim 1$, at which environment starts playing a role. This 'break' in the SFR–density relation has been previously evidenced by Lewis et al. (2002) and Gómez et al. (2003), who in fact reported the same value (albeit in projected 2D density). We believe the density marks a transition from the field to group environment.

2. The causal effect is not the strongest in the densest environments ($\log(\Sigma_{10}) \gtrsim 2.5$) as the average SFR, overall, increases with environmental density. We argue the reason is the asymmetry of the environmental effects on centrals and satellites (with the former not subject to most of the environmental processes) rather than galaxies being inherently less affected at the highest densities. Specifically, the density regime primarily probes cluster environments where central galaxies are likely cannibalising their satellites, and hence the SFR is mildly boosted and the causal effect appears to be weaker. All things considered, the separate causal effects of environment on centrals and satellites must be estimated. We note this is feasible with the causal inference method we have

utilised, IPW of MSMs.

3. While the environment negatively affects the SFR at low-to-intermediate redshifts ($z \lesssim 1$), at high redshifts ($z \gtrsim 1$), it has a positive impact as the average SFR increases with environmental density. Furthermore, the causal is significant, with environment boosting star formation by a factor of ~ 10 at $z \sim 1$ and by even greater amounts at higher redshifts. The result goes against the general consensus, but some recent studies, both observational (Lemaux et al., 2022) and simulation (Hwang et al., 2019), have hinted towards a positive environmental effect at high redshifts (albeit at a weaker level), as the SFR–density relation has been found to reverse even after adjusting for stellar mass. Moreover, they also observed the SFR enhancement increasing with redshift. The fact that our findings are consistent with Hwang et al. (2019), who also employed the IllustrisTNG simulations (though the larger volume TNG300 instead of TNG100), instils confidence in the reliability of our study. The simplest explanation for the positive causal effect is that the early Universe is not sufficiently dense for the negative environmental processes whilst being favourable to the positive processes. Specifically, we think halo accretion and major mergers are responsible for the boosted SFR in denser environments, with the former being the primary cause. Nonetheless, for a definitive answer, the causal effect of individual environmental processes must be estimated. Our work can be extended to achieve this. We iterate that the positive trend is not just due to massive galaxies in denser environments that form more stars.

4. Nature (associated with halo mass) is important in the nature–nurture debate. Specifically, galaxy formation and evolution is not top-down determined by environment as the environment affects halo mass, but halo mass also influences the environment of a galaxy as well. Ignoring the role of nature leads to the causal effect in the densest environment being underestimated by a factor of ~ 6. At low-to-intermediate densities ($\log(\Sigma_{10}) \lesssim 2$), halo mass has a positive impact on the SFR. But at high densities ($\log(\Sigma_{10}) \gtrsim 2 - 2.5$), it has negligible influence as the environment dominates galaxy evolution, which aligns with the general belief. Although at the highest densities ($\log(\Sigma_{10}) \gtrsim 2.5$), the role of halo mass is inconclusive. We attribute this to central galaxies becoming

satellites as part of mergers. As before, the solution is to distinguish between the two in the analysis and estimate the separate causal effects on both.

5. Controlling for the stellar mass at a snapshot in time, as is common in the literature, does not disentangle nature and nurture (in agreement with De Lucia et al. 2012). Not only is it insufficient to estimate the causal effect of environment, but it actually has an adverse effect. The causal effect is biased as it is overestimated at low-to-intermediate redshifts and underestimated at high redshifts, by up to a factor $\gtrsim 10$ at specific densities. We remark the causal effect at high redshifts is still positive, though reduced in magnitude. Overall, snapshot studies are inadequate, and the evolutionary history of galaxies is required.

6. Nevertheless, stellar mass is a sufficient proxy of the effects of nature (i.e., halo mass), assuming our causal model is valid and given stellar mass history and method to disentangle nature and nurture.

Our results can be relied upon because the diagnostic tests we perform suggest that the causal assumptions are met (or at least not outright violated) and our causal model is valid—the basis of causal inference.

By moving beyond correlations to causal effects, this work represents a significant leap towards truly understanding how galaxies form and evolve. We have laid the foundations in this thesis by estimating the causal effect of environment on SFR, and now one can expand further to answer fundamental questions, such as what drives galaxy quenching, are environmental processes responsible for the morphological transformations of galaxies, what is the impact of supermassive black holes (SMBHs) on their host galaxies, and above all, which is more important: nature or nurture? The stumbling block, observationally, is the lack of evolutionary histories of galaxies, which are critical to disentangling nature and nurture. Here, spectral energy distribution (SED) fitting can recover the star-formation history (SFH), and recently, a back-in-time reconstruction technique was shown to reconstruct the environmental history of galaxies (Sarpa et al., 2022). Thus, with additional effort and further advancements, our work can be applied to the real Universe. Alternatively, our work can be viewed as an approach to interpret and tune simulations, which are an indispensable tool for

testing our theories of galaxy formation and evolution. The timing is opportune as the James Webb Space Telescope (JSWT; Gardner et al. 2006), Euclid (Laureijs et al., 2011), the Rubin Observatory Legacy Survey of Space and Time (LSST; LSST Science Collaboration et al. 2009), and the Nancy Grace Roman Space Telescope (Roman; Spergel et al. 2015) are set to revolutionise our understanding (see Robertson et al., 2019; Robertson, 2022, for reviews). For example, the discovery of candidate massive galaxies at high redshifts (Castellano et al., 2022; Naidu et al., 2022; Finkelstein et al., 2022; Adams et al., 2023; Rodighiero et al., 2023; Atek et al., 2023; Donnan et al., 2023; Harikane et al., 2023; Labbé et al., 2023), if confirmed, may have ramifications for galaxy formation models and/or cosmology (Lovell et al., 2023; Boylan-Kolchin, 2023).

Chapter 6

Conclusions

How galaxies have formed and evolved is one of the biggest mysteries in modern astronomy. In the last few decades, tremendous progress has been made as the overall picture has been pieced together. Having said that, the importance of the physical processes responsible for the observed phenomena are not fully known, as establishing causality has been challenging. The primary approach has been through simulations: by developing and simulating physical models and then comparing the outcome to observations, causal insights have been made. Nonetheless, the causal effect itself is intractable in a simulation of any meaningful complexity. In this thesis, the causal inference framework has been applied to move beyond correlations to causation, in an effort to truly understand the galaxy formation and evolution process.

6.1 Summary

Before inference (i.e., the why), the task of prediction (i.e., the what) is tackled because to understand galaxy formation and evolution, galaxy properties are required first. In this thesis, a novel machine learning (ML) approach is developed based on the random forest (RF) algorithm to generate joint probability distribution functions (PDFs) of galaxy properties. As an example, the method is applied to estimate highly important joint redshift–stellar mass PDFs, which showed unprecedented levels of calibration in diagnostic tests. Benchmarked against a traditional SED-fitting approach, the ML-based method demonstrates superior performance in terms of both accuracy (based on predefined metrics) and speed (by ~ 5 orders of magnitude).

This work culminated in `GALPRO`—a Python package capable of estimating multivariate PDFs of galaxy properties (Appendix A). `GALPRO` generates PDFs quickly and efficiently, for example, it estimated joint redshift–stellar mass PDFs of a million galaxies in just under 6 minutes on consumer computer hardware. Furthermore, it can generate PDFs on the fly. The speed combined with the on-the-fly ability means `GALPRO` will facilitate galaxy formation and evolution and cosmological studies in the era of "Big Data". The package has already been employed to estimate joint redshift–luminosity and redshift–stellar mass PDFs to determine the Hubble constant from gravitational waves (Palmese et al., 2023) and constrain the stellar-to-halo mass relation (SHMR) with galaxy clustering and weak lensing (Zacharegkas et al., in prep), respectively.

Next, the causal inference framework is combined with ML, and causal ML is applied to infer the causal effect of environment on star-formation rate (SFR). To achieve this, a comprehensive causal model of galaxy formation and evolution is constructed from established theories, and using the g-method, inverse probability weighting (IPW) of marginal structural models (MSMs), the long-outstanding problem of disentangling nature (i.e., internal processes) and nurture (i.e., external processes) is tackled. Utilising the RF in an overall two-step estimation process, the causal effect at $z \sim 0$ is estimated to determine the overall impact and at different redshifts going back to $z \sim 3$ (with a baseline at $z \sim 6$) to understand how the role of environment has evolved over time.

The causal effect is found to be negative and substantial, with environment suppressing the SFR by a factor of ~ 100. However, while the overall effect is negative, it is discovered that in the early Universe ($z \gtrsim 1$), environment had a positive impact. Furthermore, the causal effect is significant, with environment boosting the SFR by a factor of ~ 10 at $z \sim 1$ and by even greater amounts at higher redshifts. Again, this is independent of the fact of massive galaxies inhabiting denser environments that form more stars. The causes are likely halo accretion and major mergers, with the former being the primary. Given haloes forming earlier in denser regions (i.e., assembly bias), a substantial positive causal effect of environment on SFR in the early Universe, followed by a negative impact in the late Universe, is consistent with and explains the observed galaxy "downsizing". Other key results include:

1. Nature (associated with halo mass) is important in the nature–nurture debate, and galaxy formation and evolution is not top-down determined by environment. Specifically, the environment affects halo mass, but halo mass also influences the environment of a galaxy as well. Ignoring the role of nature leads to the causal effect in the densest environment being underestimated by a factor of ~ 6.

2. Controlling for the stellar mass at a snapshot in time, as is common in the literature, does not disentangle nature and nurture. Overall, snapshot studies are inadequate, and the evolutionary history of galaxies is required.

3. However, stellar mass is an adequate proxy of the effects of nature, assuming the causal model is valid and given stellar mass history and method to disentangle nature and nurture.

With the introduction of a theoretical framework (to the field) to infer causality and a potential solution to the challenging nature–nurture problem, this work paves the way towards potentially unravelling some of the biggest mysteries in galaxy formation and evolution, such as: why do galaxies quench, what is responsible for morphological transformations of galaxies, what is the impact of supermassive black holes (SMBHs) on their host galaxies, and the age-old question, which is more important: nature or nurture?

6.2 Future Prospects

Galaxy Properties from Images

In this thesis, magnitudes and colours (along with errors) are input into ML to predict galaxy properties (i.e., redshift and stellar mass). A natural extension of this work would be to train a deep learning (DL) algorithm directly on photometric images to estimate the properties. Images contain information that is simply not captured by integrated quantities, such as morphology, size, surface brightness, disk inclination and, if present, colour gradients and companions. This additional information, if important, can improve the prediction accuracy. Furthermore, with images as inputs, no prior belief is imposed through feature selection. On the other hand, compared to 'traditional' ML, DL methods are generally less interpretable, explainable, and more computationally expensive.

Research has already been conducted in this direction as studies have estimated redshifts (Hoyle, 2016; Schuldt et al., 2021; Henghes et al., 2022), physical properties (Dobbels et al., 2019; Wu and Boada, 2019; Wu, 2020), and both (Euclid Collaboration et al., 2023). Furthermore, PDFs of redshift have also been estimated (D'Isanto and Polsterer, 2018; Pasquet et al., 2019). The proposed work would push beyond by estimating multivariate PDFs of redshift and physical properties.

Temporal-based Causal Inference

In order to estimate the causal effect of environment on SFR, a causal model was constructed from established galaxy formation and evolution theories and assumed. As such, the validity of the effect depends on the model being accurate, which does appear to be the case according to diagnostic tests. Regardless, a 'model-free' approach would be incredibly valuable. Besides a causal effect free from potential biases due to gaps in our knowledge, by imposing no prior beliefs, the door is left open to new discoveries. Here, it is feasible to not only estimate the causal effect but also learn the causal model itself from time series data (see Moraffah et al., 2021; Runge et al., 2023, for reviews), based on temporal order as a constraint, i.e., a cause precedes its effect in time.

1. Model-Free Causal Effects

Galaxies form and evolve over a vast period of time. However, the impact of environment may occur in a relatively short timescale (Darvish et al., 2016), possibly in a "once-only" process (Peng et al., 2010), e.g., when a galaxy falls into a group or cluster. In this instance, the treatment is time-invariant, and a method called Difference-in-Differences (DiD) can be applied to estimate the causal effect of environment. The basic idea would be to create treatment and control groups of galaxies, define a treatment point (e.g., an average point in time at which galaxies in the treatment group enter a 'dense' environment), and then compare the outcome of interest (e.g., SFR) of the two groups before and after to estimate the causal effect. A generalisation of DiD is Bayesian Structural Time Series (BSTS; Scott and Varian 2014, 2015), which can explicitly model the counterfactual (Brodersen et al., 2015).

2. Causal Discovery of Galaxy Formation and Evolution

As mentioned, although very difficult, it is possible to learn the causal structure—a task called causal discovery (see Glymour et al., 2019; Zanga et al., 2022, for reviews). In other words, one may be able to infer the causal model of galaxy formation and evolution. Causal discovery is still in development but has already been successfully applied in many fields, such as Earth system science (see Runge et al., 2019, for a review). For example, causal discovery algorithms correctly identified the causal relationship between greenhouse gases and global warming (Stips et al., 2016) and discovered that sea surface temperature is a common driver of both sardine and anchovy abundances (Sugihara et al., 2012). To begin with, one could attempt to recover the physical models in simulations.

Appendix A

GALPRO

`GALPRO`[1] is a novel Python machine learning (ML) code based on the random forest (RF) algorithm for estimating multivariate posterior probability distribution functions (PDFs) of galaxy properties (e.g., redshift, stellar mass, star-formation rate, metallicity).

It is hosted on PyPI and can be installed using:

```
pip install galpro
```

`GALPRO` is built on top of other excellent Python packages such as:

- `scikit-learn`: for implementing the random forest algorithm.
- `joblib`: for saving and loading a trained random forest model.
- `h5py`: for reading and writing PDFs to disk.

To become familiar with the package, we recommend going through the example Ipython notebooks. For ease of use, `GALPRO` is built around a single core class Model.

[1] https://github.com/smucesh/galpro

A.1 Training Model

To train a random forest model, the training and testing datasets are required. The model must be given a unique name using `model_name`. Besides this, there are other optional parameters, such as `target_features` and `save_model`, for passing in a list of all the target features and saving the model, respectively:

```
import galpro as gp

target_features = [‘$z$’, ‘$\log(M_{\star} / M_{\odot})$’]

model = gp.Model(model_name=‘model’,
                 x_train=x_train,
                 y_train=y_train,
                 x_test=x_test,
                 y_test=y_test,
                 target_features=target_features,
                 save_model=True)
```

If the model is saved, it will be located in the directory `/galpro/model_name/` as a `.sav` file. The `Model` class can also be used to load a previously trained model by specifying its name via `model_name`. Once a new model has been trained or a previously trained model has been loaded, it can be utilised.

A.2 Testing Model

The trained model can be used to generate point predictions and posterior PDFs using:

```
point_estimates = model.point_estimate(save_estimate=True,
                                       make_plots=True)

posteriors = model.posterior(save_posteriors=True,
                             make_plots=True,
                             on_the_fly=False)
```

The `point_estimate` function will return an array of point estimates. The `posterior` function will return an `h5` file object containing posteriors, which can be

accessed using test object numbers as keys. If the point predictions and PDFs are saved, they will be stored as `.h5` (Hierarchical Data Format) files in the subdirectories `/galpro/model_name/point_estimates/` and `/galpro/model_name/posteriors/`, respectively. The plots will be saved in the `/plots/` folder.

A.3 On-the-fly PDFs

`GALPRO` has the ability to generate PDFs on the fly, thus eliminating the problem of storage. It can be easily incorporated into research codes with the following:

```
posterior = model.posterior(save_posteriors=False,
                            make_plots=False,
                            on_the_fly=True)

for sample in range(no_samples):
    sample_posterior = next(posterior)
```

In this instance, the `on_the_fly` parameter is set to `True`. By calling `next(posterior)`, the function will return posterior PDFs of test objects one at a time. Naturally, the other parameters are set to `False`, and the following functionalities are not available if generating PDFs in this mode.

A.4 Validating Model

The posterior PDFs generated by the trained model can be validated using:

```
validation = model.validate(save_validation=True,
                            make_plots=True)
```

Marginal PDFs are validated using the framework developed by Gneiting et al. (2007), and multivariate PDFs are validated using the multivariate extension of the framework developed by Ziegel and Gneiting. (2014). A brief introduction to the methods can be found in our paper (Mucesh et al. 2021). The function will return a `.h5` file object, and the different modes of validation can be accessed using the keys: `pits`, `coppits`, `marginal_calibration`, and `kendall_calibration`. The validation is stored in the subdirectory `/galpro/model_name/validation/`.

A.5 Plotting

GALPRO can generate various plots:

```
model.plot.scatter() # Creates scatter plots of point predictions.
model.plot.marginal() # Creates marginal PDF plots.
model.plot.joint_pdf() # Creates joint PDF plots.
model.plot.corner() # Creates a corner style plot for multivariate PDFs.
model.plot.pit() # Plots the probability integral transform (PIT) distribution.
model.plot.coppit() # Plots the copula probability integral transform (copPIT) distri
model.marginal_calibration() # Plots the marginal calibration.
model.kendall_calibration() # Plots the kendall calibration.
```

These plotting functions can take in two optional parameters, which are `show` and `save`. By default, these are set to `False` and `True`, respectively. All plots are saved in the `/plots/` folder in the respective subdirectories. The same plots can also be created by setting `make_plots=True`, when running `model.point_estimate`, `model.posterior`, or `model.validate`. Additionally, these functions can also be used to recreate the different plots, given that the model and the necessary `.h5` files have been saved in the previous run.

A.6 Configuration

The hyperparameters associated with the random forest algorithm are defined in the `conf.py` file. We expect the default hyperparameters to work well in most situations. However, if the user wishes to tune the hyperparameter to their liking, they can do so by modifying their values in the configuration file before loading the package. The plotting aesthetics are also defined in the same configuration file. The user can tweak them to their preference by stating the `matplotlib` or `seaborn` settings accordingly.

Bibliography

Abadi, M. G., Moore, B., and Bower, R. G. (1999). Ram pressure stripping of spiral galaxies in clusters. *MNRAS*, 308(4):947–954.

Abell, G. O. (1958). The Distribution of Rich Clusters of Galaxies. *ApJS*, 3:211.

Abell, G. O. (1965). Clustering of Galaxies. *ARA&A*, 3:1.

Abrahamse, A., Knox, L., Schmidt, S., Thorman, P., Tyson, J. A., and Zhan, H. (2011). Characterizing and Propagating Modeling Uncertainties in Photometrically Derived Redshift Distributions. *ApJ*, 734(1):36.

Acquaviva, V. (2016). How to measure metallicity from five-band photometry with supervised machine learning algorithms. *MNRAS*, 456(2):1618–1626.

Acquaviva, V., Gawiser, E., and Guaita, L. (2011). Spectral Energy Distribution Fitting with Markov Chain Monte Carlo: Methodology and Application to z = 3.1 Lyα-emitting Galaxies. *ApJ*, 737(2):47.

Acquaviva, V., Gawiser, E., and Guaita, L. (2012). SED fitting with MCMC: methodology and application to large galaxy surveys. In Tuffs, R. J. and Popescu, C. C., editors, *The Spectral Energy Distribution of Galaxies - SED 2011*, volume 284, pages 42–45.

Adams, N. J., Conselice, C. J., Ferreira, L., Austin, D., Trussler, J. A. A., Juodžbalis, I., Wilkins, S. M., Caruana, J., Dayal, P., Verma, A., and Vijayan, A. P. (2023). Discovery and properties of ultra-high redshift galaxies (9 ¡ z ¡ 12) in the JWST ERO SMACS 0723 Field. *MNRAS*, 518(3):4755–4766.

Aguerri, J. A. L. and González-García, A. C. (2009). On the origin of dwarf elliptical galaxies: the fundamental plane. *A&A*, 494(3):891–904.

Ahmed, O., Träuble, F., Goyal, A., Neitz, A., Bengio, Y., Schölkopf, B., Wüthrich, M., and Bauer, S. (2020). CausalWorld: A Robotic Manipulation Benchmark for Causal Structure and Transfer Learning. *arXiv e-prints*, page arXiv:2010.04296.

Almaini, O., Wild, V., Maltby, D. T., Hartley, W. G., Simpson, C., Hatch, N. A., McLure, R. J., Dunlop, J. S., and Rowlands, K. (2017). Massive post-starburst galaxies at z ¿ 1 are compact proto-spheroids. *MNRAS*, 472(2):1401–1412.

Almosallam, I. A., Lindsay, S. N., Jarvis, M. J., and Roberts, S. J. (2016). A sparse Gaussian process framework for photometric redshift estimation. *MNRAS*, 455(3):2387–2401.

Angrist, J. D. and Krueger, A. B. (1991). Does compulsory school attendance affect schooling and earnings? *The Quarterly Journal of Economics*, 106(4):979–1014.

Angrist, J. D. and Lavy, V. (1999). Using maimonides' rule to estimate the effect of class size on scholastic achievement. *The Quarterly journal of economics*, 114(2):533–575.

Aragon-Salamanca, A., Ellis, R. S., Couch, W. J., and Carter, D. (1993). Evidence for systematic evolution in the properties of galaxies in distant clusters. *MNRAS*, 262:764–794.

Arnouts, S., Cristiani, S., Moscardini, L., Matarrese, S., Lucchin, F., Fontana, A., and Giallongo, E. (1999). Measuring and modelling the redshift evolution of clustering: the Hubble Deep Field North. *MNRAS*, 310(2):540–556.

Assef, R. J., Kochanek, C. S., Brodwin, M., Cool, R., Forman, W., Gonzalez, A. H., Hickox, R. C., Jones, C., Le Floc'h, E., Moustakas, J., Murray, S. S., and Stern, D. (2010). Low-Resolution Spectral Templates for Active Galactic Nuclei and Galaxies from 0.03 to 30 μm. *ApJ*, 713(2):970–985.

Atek, H., Shuntov, M., Furtak, L. J., Richard, J., Kneib, J.-P., Mahler, G., Zitrin, A., McCracken, H. J., Charlot, S., Chevallard, J., and Chemerynska, I. (2023). Revealing galaxy candidates out to z 16 with JWST observations of the lensing cluster SMACS0723. *MNRAS*, 519(1):1201–1220.

Athanassoula, E. (1992). The existence and shapes of dust lanes in galactic bars. *MNRAS*, 259:345–364.

Athey, S., Tibshirani, J., and Wager, S. (2016). Generalized Random Forests. *arXiv e-prints*, page arXiv:1610.01271.

Austin, P. C. (2011). An introduction to propensity score methods for reducing the effects of confounding in observational studies. *Multivariate behavioral research*, 46(3):399–424.

Baldry, I. K., Balogh, M. L., Bower, R., Glazebrook, K., and Nichol, R. C. (2004a). Color bimodality: Implications for galaxy evolution. In Allen, R. E., Nanopoulos, D. V., and Pope, C. N., editors, *The New Cosmology: Conference on Strings and Cosmology*, volume 743 of *American Institute of Physics Conference Series*, pages 106–119.

Baldry, I. K., Balogh, M. L., Bower, R. G., Glazebrook, K., Nichol, R. C., Bamford, S. P., and Budavari, T. (2006). Galaxy bimodality versus stellar mass and environment. *MNRAS*, 373(2):469–483.

Baldry, I. K., Glazebrook, K., Brinkmann, J., Ivezić, Ž., Lupton, R. H., Nichol, R. C., and Szalay, A. S. (2004b). Quantifying the Bimodal Color-Magnitude Distribution of Galaxies. *ApJ*, 600(2):681–694.

Ball, N. M., Brunner, R. J., Myers, A. D., Strand, N. E., Alberts, S. L., Tcheng, D., and Llorà, X. (2007). Robust Machine Learning Applied to Astronomical Data Sets. II. Quantifying Photometric Redshifts for Quasars Using Instance-based Learning. *ApJ*, 663(2):774–780.

Balogh, M., Eke, V., Miller, C., Lewis, I., Bower, R., Couch, W., Nichol, R., Bland-Hawthorn, J., Baldry, I. K., Baugh, C., Bridges, T., Cannon, R., Cole, S., Colless, M., Collins, C., Cross, N., Dalton, G., de Propris, R., Driver, S. P., Efstathiou, G., Ellis, R. S., Frenk, C. S., Glazebrook, K., Gomez, P., Gray, A., Hawkins, E., Jackson, C., Lahav, O., Lumsden, S., Maddox, S., Madgwick, D., Norberg, P., Peacock, J. A., Percival, W., Peterson, B. A., Sutherland, W., and Taylor, K. (2004a). Galaxy ecology: groups and low-density environments in the SDSS and 2dFGRS. *MNRAS*, 348(4):1355–1372.

Balogh, M. L., Baldry, I. K., Nichol, R., Miller, C., Bower, R., and Glazebrook, K. (2004b). The Bimodal Galaxy Color Distribution: Dependence on Luminosity and Environment. *ApJ*, 615(2):L101–L104.

Balogh, M. L., Christlein, D., Zabludoff, A. I., and Zaritsky, D. (2001). The Environmental Dependence of the Infrared Luminosity and Stellar Mass Functions. *ApJ*, 557(1):117–125.

Balogh, M. L., Morris, S. L., Yee, H. K. C., Carlberg, R. G., and Ellingson, E. (1997). Star Formation in Cluster Galaxies at 0.2 ¡ Z ¡ 0.55. *ApJ*, 488(2):L75–L78.

Balogh, M. L., Navarro, J. F., and Morris, S. L. (2000). The Origin of Star Formation Gradients in Rich Galaxy Clusters. *ApJ*, 540(1):113–121.

Balogh, M. L., Schade, D., Morris, S. L., Yee, H. K. C., Carlberg, R. G., and Ellingson, E. (1998). The Dependence of Cluster Galaxy Star Formation Rates on the Global Environment. *ApJ*, 504(2):L75–L78.

Bamford, S. P., Nichol, R. C., Baldry, I. K., Land, K., Lintott, C. J., Schawinski, K., Slosar, A., Szalay, A. S., Thomas, D., Torki, M., Andreescu, D., Edmondson, E. M., Miller, C. J., Murray, P., Raddick, M. J., and Vandenberg, J. (2009). Galaxy Zoo: the dependence of morphology and colour on environment*. *MNRAS*, 393(4):1324–1352.

Bardeen, J. M., Steinhardt, P. J., and Turner, M. S. (1983). Spontaneous creation of almost scale-free density perturbations in an inflationary universe. *Phys. Rev. D*, 28(4):679–693.

Barnes, J. E. (1988). Encounters of Disk/Halo Galaxies. *ApJ*, 331:699.

Barnes, J. E. (2002). Formation of gas discs in merging galaxies. *MNRAS*, 333(3):481–494.

Baron, D. (2019). Machine Learning in Astronomy: a practical overview. *arXiv e-prints*, page arXiv:1904.07248.

Bauer, A. E., Drory, N., Hill, G. J., and Feulner, G. (2005). Specific Star Formation Rates to Redshift 1.5. *ApJ*, 621(2):L89–L92.

Baugh, C. M. (2006). A primer on hierarchical galaxy formation: the semi-analytical approach. *Reports on Progress in Physics*, 69(12):3101–3156.

Baum, W. A. (1962). Photoelectric Magnitudes and Red-Shifts. In McVittie, G. C., editor, *Problems of Extra-Galactic Research*, volume 15, page 390.

Bell, E. F., Papovich, C., Wolf, C., Le Floc'h, E., Caldwell, J. A. R., Barden, M., Egami, E., McIntosh, D. H., Meisenheimer, K., Pérez-González, P. G., Rieke, G. H., Rieke, M. J., Rigby, J. R., and Rix, H.-W. (2005). Toward an Understanding of the Rapid Decline of the Cosmic Star Formation Rate. *ApJ*, 625(1):23–36.

Bell, E. F., Wolf, C., Meisenheimer, K., Rix, H.-W., Borch, A., Dye, S., Kleinheinrich, M., Wisotzki, L., and McIntosh, D. H. (2004). Nearly 5000 Distant Early-Type Galaxies in COMBO-17: A Red Sequence and Its Evolution since z˜1. *ApJ*, 608(2):752–767.

Belli, S., Newman, A. B., and Ellis, R. S. (2019). MOSFIRE Spectroscopy of Quiescent Galaxies at 1.5 ¡ z ¡ 2.5. II. Star Formation Histories and Galaxy Quenching. *ApJ*, 874(1):17.

Benítez, N. (2000). Bayesian Photometric Redshift Estimation. *ApJ*, 536(2):571–583.

Benson, A. J. (2010). Galaxy formation theory. *Phys. Rep.*, 495(2-3):33–86.

Benson, A. J. (2012). G ALACTICUS: A semi-analytic model of galaxy formation. *New A*, 17(2):175–197.

Benson, A. J., Bower, R. G., Frenk, C. S., and White, S. D. M. (2000). Diffuse X-ray emission from late-type galaxy haloes. *MNRAS*, 314(3):557–565.

Bertelli, G., Bressan, A., Chiosi, C., Fagotto, F., and Nasi, E. (1994). Theoretical isochrones from models with new radiative opacities. *A&AS*, 106:275–302.

Bertin, E. and Arnouts, S. (1996). SExtractor: Software for source extraction. *A&AS*, 117:393–404.

Bialas, D., Lisker, T., Olczak, C., Spurzem, R., and Kotulla, R. (2015). On the occurrence of galaxy harassment. *A&A*, 576:A103.

Binney, J. (1977). The physics of dissipational galaxy formation. *ApJ*, 215:483–491.

Blanton, M. R., Eisenstein, D., Hogg, D. W., Schlegel, D. J., and Brinkmann, J. (2005). Relationship between Environment and the Broadband Optical Properties of Galaxies in the Sloan Digital Sky Survey. *ApJ*, 629(1):143–157.

Blanton, M. R., Hogg, D. W., Bahcall, N. A., Baldry, I. K., Brinkmann, J., Csabai, I., Eisenstein, D., Fukugita, M., Gunn, J. E., Ivezić, Ž., Lamb, D. Q., Lupton, R. H., Loveday, J., Munn, J. A., Nichol, R. C., Okamura, S., Schlegel, D. J., Shimasaku, K., Strauss, M. A., Vogeley, M. S., and Weinberg, D. H. (2003). The Broadband Optical Properties of Galaxies with Redshifts 0.02¡z¡0.22. *ApJ*, 594(1):186–207.

Bluck, A. F. L., Bottrell, C., Teimoorinia, H., Henriques, B. M. B., Mendel, J. T., Ellison, S. L., Thanjavur, K., Simard, L., Patton, D. R., Conselice, C. J., Moreno, J., and Woo, J. (2019). What shapes a galaxy? - unraveling the role of mass, environment, and star formation in forming galactic structure. *MNRAS*, 485(1):666–696.

Bluck, A. F. L., Maiolino, R., Brownson, S., Conselice, C. J., Ellison, S. L., Piotrowska, J. M., and Thorp, M. D. (2022). The quenching of galaxies, bulges, and disks since cosmic noon. A machine learning approach for identifying causality in astronomical data. *A&A*, 659:A160.

Bluck, A. F. L., Maiolino, R., Piotrowska, J. M., Trussler, J., Ellison, S. L., Sánchez, S. F., Thorp, M. D., Teimoorinia, H., Moreno, J., and Conselice, C. J. (2020a). How do central and satellite galaxies quench? - Insights from spatially resolved spectroscopy in the MaNGA survey. *MNRAS*, 499(1):230–268.

Bluck, A. F. L., Maiolino, R., Sánchez, S. F., Ellison, S. L., Thorp, M. D., Piotrowska, J. M., Teimoorinia, H., and Bundy, K. A. (2020b). Are galactic star formation and quenching governed by local, global, or environmental phenomena? *MNRAS*, 492(1):96–139.

Blumenthal, G. R., Faber, S. M., Primack, J. R., and Rees, M. J. (1984). Formation of galaxies and large-scale structure with cold dark matter. *Nature*, 311:517–525.

Bolzonella, M., Kovač, K., Pozzetti, L., Zucca, E., Cucciati, O., Lilly, S. J., Peng, Y., Iovino, A., Zamorani, G., Vergani, D., Tasca, L. A. M., Lamareille, F., Oesch, P., Caputi, K., Kampczyk, P., Bardelli, S., Maier, C., Abbas, U., Knobel, C.,

Scodeggio, M., Carollo, C. M., Contini, T., Kneib, J. P., Le Fèvre, O., Mainieri, V., Renzini, A., Bongiorno, A., Coppa, G., de la Torre, S., de Ravel, L., Franzetti, P., Garilli, B., Le Borgne, J. F., Le Brun, V., Mignoli, M., Pelló, R., Perez-Montero, E., Ricciardelli, E., Silverman, J. D., Tanaka, M., Tresse, L., Bottini, D., Cappi, A., Cassata, P., Cimatti, A., Guzzo, L., Koekemoer, A. M., Leauthaud, A., Maccagni, D., Marinoni, C., McCracken, H. J., Memeo, P., Meneux, B., Porciani, C., Scaramella, R., Aussel, H., Capak, P., Halliday, C., Ilbert, O., Kartaltepe, J., Salvato, M., Sanders, D., Scarlata, C., Scoville, N., Taniguchi, Y., and Thompson, D. (2010). Tracking the impact of environment on the galaxy stellar mass function up to z ~1 in the 10 k zCOSMOS sample. *A&A*, 524:A76.

Bolzonella, M., Miralles, J. M., and Pelló, R. (2000). Photometric redshifts based on standard SED fitting procedures. *A&A*, 363:476–492.

Bond, J. R., Kofman, L., and Pogosyan, D. (1996). How filaments of galaxies are woven into the cosmic web. *Nature*, 380(6575):603–606.

Bonjean, V., Aghanim, N., Salomé, P., Beelen, A., Douspis, M., and Soubrié, E. (2019). Star formation rates and stellar masses from machine learning. *A&A*, 622:A137.

Bonnell, I. A., Bate, M. R., Clarke, C. J., and Pringle, J. E. (1997). Accretion and the stellar mass spectrum in small clusters. *MNRAS*, 285(1):201–208.

Bonnett, C. (2015). Using neural networks to estimate redshift distributions. An application to CFHTLenS. *MNRAS*, 449(1):1043–1056.

Bonnett, C., Troxel, M. A., Hartley, W., Amara, A., Leistedt, B., Becker, M. R., Bernstein, G. M., Bridle, S. L., Bruderer, C., Busha, M. T., Carrasco Kind, M., Childress, M. J., Castander, F. J., Chang, C., Crocce, M., Davis, T. M., Eifler, T. F., Frieman, J., Gangkofner, C., Gaztanaga, E., Glazebrook, K., Gruen, D., Kacprzak, T., King, A., Kwan, J., Lahav, O., Lewis, G., Lidman, C., Lin, H., MacCrann, N., Miquel, R., O'Neill, C. R., Palmese, A., Peiris, H. V., Refregier, A., Rozo, E., Rykoff, E. S., Sadeh, I., Sánchez, C., Sheldon, E., Uddin, S., Wechsler, R. H., Zuntz, J., Abbott, T., Abdalla, F. B., Allam, S., Armstrong, R., Banerji, M., Bauer, A. H., Benoit-Lévy, A., Bertin, E., Brooks, D., Buckley-Geer, E., Burke,

D. L., Capozzi, D., Carnero Rosell, A., Carretero, J., Cunha, C. E., D'Andrea, C. B., da Costa, L. N., DePoy, D. L., Desai, S., Diehl, H. T., Dietrich, J. P., Doel, P., Fausti Neto, A., Fernandez, E., Flaugher, B., Fosalba, P., Gerdes, D. W., Gruendl, R. A., Honscheid, K., Jain, B., James, D. J., Jarvis, M., Kim, A. G., Kuehn, K., Kuropatkin, N., Li, T. S., Lima, M., Maia, M. A. G., March, M., Marshall, J. L., Martini, P., Melchior, P., Miller, C. J., Neilsen, E., Nichol, R. C., Nord, B., Ogando, R., Plazas, A. A., Reil, K., Romer, A. K., Roodman, A., Sako, M., Sanchez, E., Santiago, B., Smith, R. C., Soares-Santos, M., Sobreira, F., Suchyta, E., Swanson, M. E. C., Tarle, G., Thaler, J., Thomas, D., Vikram, V., Walker, A. R., and Dark Energy Survey Collaboration (2016). Redshift distributions of galaxies in the Dark Energy Survey Science Verification shear catalogue and implications for weak lensing. *Phys. Rev. D*, 94(4):042005.

Boquien, M., Burgarella, D., Roehlly, Y., Buat, V., Ciesla, L., Corre, D., Inoue, A. K., and Salas, H. (2019). CIGALE: a python Code Investigating GALaxy Emission. *A&A*, 622:A103.

Bordoloi, R., Lilly, S. J., and Amara, A. (2010). Photo-z performance for precision cosmology. *MNRAS*, 406(2):881–895.

Boselli, A. and Gavazzi, G. (2006). Environmental Effects on Late-Type Galaxies in Nearby Clusters. *PASP*, 118(842):517–559.

Boylan-Kolchin, M. (2023). Stress testing ΛCDM with high-redshift galaxy candidates. *Nature Astronomy*, 7:731–735.

Brammer, G. B., van Dokkum, P. G., and Coppi, P. (2008). EAZY: A Fast, Public Photometric Redshift Code. *ApJ*, 686(2):1503–1513.

Brammer, G. B., Whitaker, K. E., van Dokkum, P. G., Marchesini, D., Labbé, I., Franx, M., Kriek, M., Quadri, R. F., Illingworth, G., Lee, K. S., Muzzin, A., and Rudnick, G. (2009). The Dead Sequence: A Clear Bimodality in Galaxy Colors from z = 0 to z = 2.5. *ApJ*, 706(1):L173–L177.

Breiman, L. (2001). Random forests. *Mach. Learn.*, 45(1):5–32.

Breiman, L., Friedman, J., Stone, C., and Olshen, R. (1984). *Classification and Regression Trees*. Taylor & Francis.

Breskvar, M., Kocev, D., and Džeroski, S. (2018). Ensembles for multi-target regression with random output selections. *Mach. Learn.*, 107:1673–1709.

Brinchmann, J., Charlot, S., White, S. D. M., Tremonti, C., Kauffmann, G., Heckman, T., and Brinkmann, J. (2004). The physical properties of star-forming galaxies in the low-redshift Universe. *MNRAS*, 351(4):1151–1179.

Brodersen, K. H., Gallusser, F., Koehler, J., Remy, N., and Scott, S. L. (2015). Inferring causal impact using Bayesian structural time-series models. *arXiv e-prints*, page arXiv:1506.00356.

Brown, M. J. I., Webster, R. L., and Boyle, B. J. (2000). The clustering of colour-selected galaxies. *MNRAS*, 317(4):782–794.

Brownson, S., Bluck, A. F. L., Maiolino, R., and Jones, G. C. (2022). What drives galaxy quenching? A deep connection between galaxy kinematics and quenching in the local Universe. *MNRAS*, 511(2):1913–1941.

Bruzual, G. and Charlot, S. (2003). Stellar population synthesis at the resolution of 2003. *MNRAS*, 344(4):1000–1028.

Bruzual A., G. (1983). Spectral evolution of galaxies. I. Early-type systems. *ApJ*, 273:105–127.

Buchner, J., Georgakakis, A., Nandra, K., Hsu, L., Rangel, C., Brightman, M., Merloni, A., Salvato, M., Donley, J., and Kocevski, D. (2014). X-ray spectral modelling of the AGN obscuring region in the CDFS: Bayesian model selection and catalogue. *A&A*, 564:A125.

Bundy, K., Ellis, R. S., Conselice, C. J., Taylor, J. E., Cooper, M. C., Willmer, C. N. A., Weiner, B. J., Coil, A. L., Noeske, K. G., and Eisenhardt, P. R. M. (2006). The Mass Assembly History of Field Galaxies: Detection of an Evolving Mass Limit for Star-Forming Galaxies. *ApJ*, 651(1):120–141.

Burgarella, D., Buat, V., and Iglesias-Páramo, J. (2005). Star formation and dust attenuation properties in galaxies from a statistical ultraviolet-to-far-infrared analysis. *MNRAS*, 360(4):1413–1425.

Burkart, N. and Huber, M. F. (2020). A Survey on the Explainability of Supervised Machine Learning. *arXiv e-prints*, page arXiv:2011.07876.

Butcher, H. and Oemler, A., J. (1978). The evolution of galaxies in clusters. I. ISIT photometry of Cl 0024+1654 and 3C 295. *ApJ*, 219:18–30.

Butcher, H. and Oemler, A., J. (1984). The evolution of galaxies in clusters. V. A study of populations since Z 0.5. *ApJ*, 285:426–438.

Buzzoni, A. (1989). Evolutionary Population Synthesis in Stellar Systems. I. A Global Approach. *ApJS*, 71:817.

Cadiou, C., Pontzen, A., Peiris, H. V., and Lucie-Smith, L. (2021). The causal effect of environment on halo mass and concentration. *MNRAS*, 508(1):1189–1194.

Caldwell, N., Rose, J. A., Franx, M., and Leonardi, A. J. (1996). Spatial Distribution of the Starbursts in Post-Starburst Coma Cluster Galaxies. *AJ*, 111:78.

Calzetti, D., Armus, L., Bohlin, R. C., Kinney, A. L., Koornneef, J., and Storchi-Bergmann, T. (2000). The Dust Content and Opacity of Actively Star-forming Galaxies. *ApJ*, 533(2):682–695.

Cannas, M. and Arpino, B. (2019). A comparison of machine learning algorithms and covariate balance measures for propensity score matching and weighting. *Biometrical Journal*, 61(4):1049–1072.

Capak, P., Abraham, R. G., Ellis, R. S., Mobasher, B., Scoville, N., Sheth, K., and Koekemoer, A. (2007). The Effects of Environment on Morphological Evolution at 0¡z¡1.2 in the COSMOS Survey. *ApJS*, 172(1):284–294.

Capozzi, D., Etherington, J., Thomas, D., Maraston, C., Rykoff, E. S., Sevilla-Noarbe, I., Bechtol, K., Carrasco Kind, M., Drlica-Wagner, A., Pforr, J., Gschwend, J., Carnero Rosell, A., Pellegrini, P., Maia, M. A. G., da Costa, L. N., Benoit-Lévy, A., Swanson, M. E. C., Wechsler, R. H., Banerji, M., Papovich, C., Morice-Atkinson, X., Abdalla, F., Brooks, D., Carretero, J., Cunha, C., D'Andrea, C., Desai, S., Diehl, T. H., Evrards, A., Flaugher, B., Fosalba, P., Frieman, J., García-Bellido, J., Gaztanaga, E., Gerdes, D. W., Gruen, D., Gruendl, R. A., Gutierrez, G., Hartley, W. G., James, D., Jeltema, T., Kuehn, K., Kuhlmann, S., Kuropatkin,

N., Lahav, O., Lima, M., Marshall, J. L., Martini, P., Menanteau, F., Miquel, R., Nord, B., Ogando, R. L. C., Plazas Malagòn, A. A., Romer, A. K., Sanchez, E., Scarpine, V., Schindler, R., Schubnell, M., Smith, M., Soares-Santos, M., Sobreira, F., Suchyta, E., and Tarle, G. (2017). Evolution of Galaxy Luminosity and Stellar-Mass Functions since $z = 1$ with the Dark Energy Survey Science Verification Data. *arXiv e-prints*, page arXiv:1707.09066.

Card, D. and Krueger, A. (1993). Minimum wages and employment: A case study of the fast food industry in new jersey and pennsylvania. *American Economic Review*, 84.

Carliles, S., Budavári, T., Heinis, S., Priebe, C., and Szalay, A. (2008). Photometric Redshift Estimation on SDSS Data Using Random Forests. In Argyle, R. W., Bunclark, P. S., and Lewis, J. R., editors, *Astronomical Data Analysis Software and Systems XVII*, volume 394 of *Astronomical Society of the Pacific Conference Series*, page 521.

Carliles, S., Budavári, T., Heinis, S., Priebe, C., and Szalay, A. S. (2010). Random Forests for Photometric Redshifts. *ApJ*, 712(1):511–515.

Carlsson, M., Dahl, G. B., Öckert, B., and Rooth, D.-O. (2015). The effect of schooling on cognitive skills. *Review of Economics and Statistics*, 97(3):533–547.

Carnall, A. C., McLure, R. J., Dunlop, J. S., and Davé, R. (2018). Inferring the star formation histories of massive quiescent galaxies with BAGPIPES: evidence for multiple quenching mechanisms. *MNRAS*, 480(4):4379–4401.

Carnero, A., Sánchez, E., Crocce, M., Cabré, A., and Gaztañaga, E. (2012). Clustering of photometric luminous red galaxies - II. Cosmological implications from the baryon acoustic scale. *MNRAS*, 419(2):1689–1694.

Carrasco Kind, M. and Brunner, R. J. (2013). TPZ: photometric redshift PDFs and ancillary information by using prediction trees and random forests. *MNRAS*, 432(2):1483–1501.

Carrasco Kind, M. and Brunner, R. J. (2014). SOMz: photometric redshift PDFs with self-organizing maps and random atlas. *MNRAS*, 438(4):3409–3421.

Carter, B. J., Fabricant, D. G., Geller, M. J., Kurtz, M. J., and McLean, B. (2001). Star Formation in a Complete Spectroscopic Survey of Galaxies. *ApJ*, 559(2):606–619.

Cassata, P., Guzzo, L., Franceschini, A., Scoville, N., Capak, P., Ellis, R. S., Koekemoer, A., McCracken, H. J., Mobasher, B., Renzini, A., Ricciardelli, E., Scodeggio, M., Taniguchi, Y., and Thompson, D. (2007). The Cosmic Evolution Survey (COSMOS): The Morphological Content and Environmental Dependence of the Galaxy Color-Magnitude Relation at z ~0.7. *ApJS*, 172(1):270–283.

Castellano, M., Fontana, A., Treu, T., Santini, P., Merlin, E., Leethochawalit, N., Trenti, M., Vanzella, E., Mestric, U., Bonchi, A., Belfiori, D., Nonino, M., Paris, D., Polenta, G., Roberts-Borsani, G., Boyett, K., Bradač, M., Calabrò, A., Glazebrook, K., Grillo, C., Mascia, S., Mason, C., Mercurio, A., Morishita, T., Nanayakkara, T., Pentericci, L., Rosati, P., Vulcani, B., Wang, X., and Yang, L. (2022). Early Results from GLASS-JWST. III. Galaxy Candidates at z 9-15. *ApJ*, 938(2):L15.

Cavanagh, M. K., Bekki, K., and Groves, B. A. (2023). The redshift evolution of the S0 fraction for z ¡ 1 in COSMOS. *MNRAS*, 520(4):5885–5902.

Cenarro, A. J., Peletier, R. F., Sánchez-Blázquez, P., Selam, S. O., Toloba, E., Cardiel, N., Falcón-Barroso, J., Gorgas, J., Jiménez-Vicente, J., and Vazdekis, A. (2007). Medium-resolution Isaac Newton Telescope library of empirical spectra - II. The stellar atmospheric parameters. *MNRAS*, 374(2):664–690.

Cengiz, D., Dube, A., Lindner, A., and Zipperer, B. (2019). The effect of minimum wages on low-wage jobs. *The Quarterly Journal of Economics*, 134(3):1405–1454.

Cerdá, M., Diez-Roux, A. V., Tchetgen, E. T., Gordon-Larsen, P., and Kiefe, C. (2010). The relationship between neighborhood poverty and alcohol use: estimation by marginal structural models. *Epidemiology (Cambridge, Mass.)*, 21(4):482.

Chabrier, G. (2003). Galactic Stellar and Substellar Initial Mass Function. *PASP*, 115(809):763–795.

Chalmers, T. C., Smith Jr, H., Blackburn, B., Silverman, B., Schroeder, B., Reitman, D., and Ambroz, A. (1981). A method for assessing the quality of a randomized control trial. *Controlled clinical trials*, 2(1):31–49.

Chandrasekhar, S. (1943a). Dynamical Friction. I. General Considerations: the Coefficient of Dynamical Friction. *ApJ*, 97:255.

Chandrasekhar, S. (1943b). Dynamical Friction. II. The Rate of Escape of Stars from Clusters and the Evidence for the Operation of Dynamical Friction. *ApJ*, 97:263.

Chandrasekhar, S. (1943c). Dynamical Friction. III. a More Exact Theory of the Rate of Escape of Stars from Clusters. *ApJ*, 98:54.

Charlot, S. and Bruzual A, G. (1991). Stellar Population Synthesis Revisited. *ApJ*, 367:126.

Charlot, S. and Fall, S. M. (2000). A Simple Model for the Absorption of Starlight by Dust in Galaxies. *ApJ*, 539(2):718–731.

Chartab, N., Mobasher, B., Darvish, B., Finkelstein, S., Guo, Y., Kodra, D., Lee, K.-S., Newman, J. A., Pacifici, C., Papovich, C., Sattari, Z., Shahidi, A., Dickinson, M. E., Faber, S. M., Ferguson, H. C., Giavalisco, M., and Jafariyazani, M. (2020). Large-scale Structures in the CANDELS Fields: The Role of the Environment in Star Formation Activity. *ApJ*, 890(1):7.

Chay, K. Y. and Greenstone, M. (2003). The impact of air pollution on infant mortality: evidence from geographic variation in pollution shocks induced by a recession. *The quarterly journal of economics*, 118(3):1121–1167.

Chesnaye, N. C., Stel, V. S., Tripepi, G., Dekker, F. W., Fu, E. L., Zoccali, C., and Jager, K. J. (2022). An introduction to inverse probability of treatment weighting in observational research. *Clinical Kidney Journal*, 15(1):14–20.

Chevallard, J. and Charlot, S. (2016). Modelling and interpreting spectral energy distributions of galaxies with BEAGLE. *MNRAS*, 462(2):1415–1443.

Chiosi, C., Bertelli, G., and Bressan, A. (1988). Integrated colours and ages of LMC clusters : the nature of the bimodal distribution of the (B-V) colours. *A&A*, 196:84–108.

Cid Fernandes, R., Mateus, A., Sodré, L., Stasińska, G., and Gomes, J. M. (2005). Semi-empirical analysis of Sloan Digital Sky Survey galaxies - I. Spectral synthesis method. *MNRAS*, 358(2):363–378.

Ciesla, L., Boselli, A., Elbaz, D., Boissier, S., Buat, V., Charmandaris, V., Schreiber, C., Béthermin, M., Baes, M., Boquien, M., De Looze, I., Fernández-Ontiveros, J. A., Pappalardo, C., Spinoglio, L., and Viaene, S. (2016). The imprint of rapid star formation quenching on the spectral energy distributions of galaxies. *A&A*, 585:A43.

Clark, D. and Royer, H. (2013). The effect of education on adult mortality and health: Evidence from britain. *American Economic Review*, 103(6):2087–2120.

Clarke, P., Morenoff, J., Debbink, M., Golberstein, E., Elliott, M. R., and Lantz, P. M. (2014). Cumulative exposure to neighborhood context: consequences for health transitions over the adult life course. *Research on aging*, 36(1):115–142.

Cole, S. (1991). Modeling Galaxy Formation in Evolving Dark Matter Halos. *ApJ*, 367:45.

Cole, S., Aragon-Salamanca, A., Frenk, C. S., Navarro, J. F., and Zepf, S. E. (1994). A recipe for galaxy formation. *MNRAS*, 271:781–806.

Cole, S. R. and Hernán, M. A. (2008). Constructing Inverse Probability Weights for Marginal Structural Models. *American Journal of Epidemiology*, 168(6):656–664.

Coleman, G. D., Wu, C. C., and Weedman, D. W. (1980). Colors and magnitudes predicted for high redshift galaxies. *ApJS*, 43:393–416.

Colless, M., Dalton, G., Maddox, S., Sutherland, W., Norberg, P., Cole, S., Bland-Hawthorn, J., Bridges, T., Cannon, R., Collins, C., Couch, W., Cross, N., Deeley, K., De Propris, R., Driver, S. P., Efstathiou, G., Ellis, R. S., Frenk, C. S., Glazebrook, K., Jackson, C., Lahav, O., Lewis, I., Lumsden, S., Madgwick, D., Peacock, J. A., Peterson, B. A., Price, I., Seaborne, M., and Taylor, K. (2001). The 2dF Galaxy Redshift Survey: spectra and redshifts. *MNRAS*, 328(4):1039–1063.

Collister, A. A. and Lahav, O. (2004). ANNz: Estimating Photometric Redshifts Using Artificial Neural Networks. *PASP*, 116(818):345–351.

Connolly, A. J., Csabai, I., Szalay, A. S., Koo, D. C., Kron, R. G., and Munn, J. A. (1995). Slicing Through Multicolor Space: Galaxy Redshifts from Broadband Photometry. *AJ*, 110:2655.

Conroy, C. (2013). Modeling the Panchromatic Spectral Energy Distributions of Galaxies. *ARA&A*, 51(1):393–455.

Conroy, C. and Gunn, J. E. (2010). The Propagation of Uncertainties in Stellar Population Synthesis Modeling. III. Model Calibration, Comparison, and Evaluation. *ApJ*, 712(2):833–857.

Conroy, C., Gunn, J. E., and White, M. (2009). The Propagation of Uncertainties in Stellar Population Synthesis Modeling. I. The Relevance of Uncertain Aspects of Stellar Evolution and the Initial Mass Function to the Derived Physical Properties of Galaxies. *ApJ*, 699(1):486–506.

Cooper, M. C., Newman, J. A., Coil, A. L., Croton, D. J., Gerke, B. F., Yan, R., Davis, M., Faber, S. M., Guhathakurta, P., Koo, D. C., Weiner, B. J., and Willmer, C. N. A. (2007). The DEEP2 galaxy redshift survey: evolution of the colour-density relation at 0.4 ¡ z ¡ 1.35. *MNRAS*, 376(4):1445–1459.

Cooper, M. C., Newman, J. A., Weiner, B. J., Yan, R., Willmer, C. N. A., Bundy, K., Coil, A. L., Conselice, C. J., Davis, M., Faber, S. M., Gerke, B. F., Guhathakurta, P., Koo, D. C., and Noeske, K. G. (2008). The DEEP2 Galaxy Redshift Survey: the role of galaxy environment in the cosmic star formation history. *MNRAS*, 383(3):1058–1078.

Cordier, D., Pietrinferni, A., Cassisi, S., and Salaris, M. (2007). A Large Stellar Evolution Database for Population Synthesis Studies. III. Inclusion of the Full Asymptotic Giant Branch Phase and Web Tools for Stellar Population Analyses. *AJ*, 133(2):468–478.

Couch, W. J., Balogh, M. L., Bower, R. G., Smail, I., Glazebrook, K., and Taylor, M. (2001). A Low Global Star Formation Rate in the Rich Galaxy Cluster AC 114 at z=0.32. *ApJ*, 549(2):820–831.

Couch, W. J., Barger, A. J., Smail, I., Ellis, R. S., and Sharples, R. M. (1998). Morphological Studies of the Galaxy Populations in Distant "Butcher-Oemler" Clusters with the Hubble Space Telescope. II. AC 103, AC 118, and AC 114 at Z = 0.31. *ApJ*, 497(1):188–211.

Couch, W. J., Ellis, R. S., Sharples, R. M., and Smail, I. (1994). Morphological Studies of the Galaxy Populations in Distant "Butcher-Oemler" Clusters with HST. I. AC 114 at Z = 0.31 and Abell 370 at Z = 0.37. *ApJ*, 430:121.

Couch, W. J. and Newell, E. B. (1984). Distant clusters of galaxies. I. Uniform photometry of 14 rich clusters. *ApJS*, 56:143–192.

Couch, W. J. and Sharples, R. M. (1987). A spectroscopic study of three rich galaxy clusters at zeta=0.31. *MNRAS*, 229:423–456.

Cowie, L. L. and Songaila, A. (1977). Thermal evaporation of gas within galaxies by a hot intergalactic medium. *Nature*, 266:501–503.

Cowie, L. L., Songaila, A., Hu, E. M., and Cohen, J. G. (1996). New Insight on Galaxy Formation and Evolution From Keck Spectroscopy of the Hawaii Deep Fields. *AJ*, 112:839.

Cox, D. (1958). *Planning of Experiments*. Wiley Series in Probability and Statistics - Applied Probability and Statistics Section. Wiley.

Cox, T. J., Dutta, S. N., Di Matteo, T., Hernquist, L., Hopkins, P. F., Robertson, B., and Springel, V. (2006). The Kinematic Structure of Merger Remnants. *ApJ*, 650(2):791–811.

Cramér, H. (1928). On the composition of elementary errors. *Scand. Actuarial J.*, 1928(1):13–74.

Croton, D. J., Farrar, G. R., Norberg, P., Colless, M., Peacock, J. A., Baldry, I. K., Baugh, C. M., Bland-Hawthorn, J., Bridges, T., Cannon, R., Cole, S., Collins, C., Couch, W., Dalton, G., De Propris, R., Driver, S. P., Efstathiou, G., Ellis, R. S., Frenk, C. S., Glazebrook, K., Jackson, C., Lahav, O., Lewis, I., Lumsden, S., Maddox, S., Madgwick, D., Peterson, B. A., Sutherland, W., and Taylor, K. (2005). The 2dF Galaxy Redshift Survey: luminosity functions by density environment and galaxy type. *MNRAS*, 356(3):1155–1167.

Croton, D. J., Springel, V., White, S. D. M., De Lucia, G., Frenk, C. S., Gao, L., Jenkins, A., Kauffmann, G., Navarro, J. F., and Yoshida, N. (2006). The many

lives of active galactic nuclei: cooling flows, black holes and the luminosities and colours of galaxies. *MNRAS*, 365(1):11–28.

Cucciati, O., Iovino, A., Marinoni, C., Ilbert, O., Bardelli, S., Franzetti, P., Le Fèvre, O., Pollo, A., Zamorani, G., Cappi, A., Guzzo, L., McCracken, H. J., Meneux, B., Scaramella, R., Scodeggio, M., Tresse, L., Zucca, E., Bottini, D., Garilli, B., Le Brun, V., Maccagni, D., Picat, J. P., Vettolani, G., Zanichelli, A., Adami, C., Arnaboldi, M., Arnouts, S., Bolzonella, M., Charlot, S., Ciliegi, P., Contini, T., Foucaud, S., Gavignaud, I., Marano, B., Mazure, A., Merighi, R., Paltani, S., Pellò, R., Pozzetti, L., Radovich, M., Bondi, M., Bongiorno, A., Busarello, G., de la Torre, S., Gregorini, L., Lamareille, F., Mathez, G., Mellier, Y., Merluzzi, P., Ripepi, V., Rizzo, D., Temporin, S., and Vergani, D. (2006). The VIMOS VLT Deep Survey: the build-up of the colour-density relation. *A&A*, 458(1):39–52.

da Cunha, E., Charlot, S., Dunne, L., Smith, D., and Rowlands, K. (2011). Magphys: a publicly available tool to interpret observed galaxy seds. *Proceedings of the International Astronomical Union*, 7(S284):292–296.

Daddi, E., Dickinson, M., Morrison, G., Chary, R., Cimatti, A., Elbaz, D., Frayer, D., Renzini, A., Pope, A., Alexander, D. M., Bauer, F. E., Giavalisco, M., Huynh, M., Kurk, J., and Mignoli, M. (2007). Multiwavelength Study of Massive Galaxies at z~2. I. Star Formation and Galaxy Growth. *ApJ*, 670(1):156–172.

D'Agostino Jr, R. B. (1998). Propensity score methods for bias reduction in the comparison of a treatment to a non-randomized control group. *Statistics in medicine*, 17(19):2265–2281.

Darvish, B., Mobasher, B., Sobral, D., Rettura, A., Scoville, N., Faisst, A., and Capak, P. (2016). The Effects of the Local Environment and Stellar Mass on Galaxy Quenching to z $\sim$ 3. *ApJ*, 825(2):113.

Darvish, B., Mobasher, B., Sobral, D., Scoville, N., and Aragon-Calvo, M. (2015). A Comparative Study of Density Field Estimation for Galaxies: New Insights into the Evolution of Galaxies with Environment in COSMOS out to z$\sim$3. *ApJ*, 805(2):121.

Davidzon, I., Cucciati, O., Bolzonella, M., De Lucia, G., Zamorani, G., Arnouts, S., Moutard, T., Ilbert, O., Garilli, B., Scodeggio, M., Guzzo, L., Abbas, U., Adami, C., Bel, J., Bottini, D., Branchini, E., Cappi, A., Coupon, J., de la Torre, S., Di Porto, C., Fritz, A., Franzetti, P., Fumana, M., Granett, B. R., Guennou, L., Iovino, A., Krywult, J., Le Brun, V., Le Fèvre, O., Maccagni, D., Małek, K., Marulli, F., McCracken, H. J., Mellier, Y., Moscardini, L., Polletta, M., Pollo, A., Tasca, L. A. M., Tojeiro, R., Vergani, D., and Zanichelli, A. (2016). The VIMOS Public Extragalactic Redshift Survey (VIPERS). Environmental effects shaping the galaxy stellar mass function. *A&A*, 586:A23.

Davis, M., Efstathiou, G., Frenk, C. S., and White, S. D. M. (1985). The evolution of large-scale structure in a universe dominated by cold dark matter. *ApJ*, 292:371–394.

Davis, M., Faber, S. M., Newman, J., Phillips, A. C., Ellis, R. S., Steidel, C. C., Conselice, C., Coil, A. L., Finkbeiner, D. P., Koo, D. C., Guhathakurta, P., Weiner, B., Schiavon, R., Willmer, C., Kaiser, N., Luppino, G. A., Wirth, G., Connolly, A., Eisenhardt, P., Cooper, M., and Gerke, B. (2003). Science Objectives and Early Results of the DEEP2 Redshift Survey. In Guhathakurta, P., editor, *Discoveries and Research Prospects from 6- to 10-Meter-Class Telescopes II*, volume 4834 of *Society of Photo-Optical Instrumentation Engineers (SPIE) Conference Series*, pages 161–172.

Davis, M. and Geller, M. J. (1976). Galaxy Correlations as a Function of Morphological Type. *ApJ*, 208:13–19.

Dawid, A. P. (1984). Present position and potential developments: Some personal views: Statistical theory: The prequential approach. *J. R. Stat. Soc. A*, 147(2):278–292.

De Lucia, G., Weinmann, S., Poggianti, B. M., Aragón-Salamanca, A., and Zaritsky, D. (2012). The environmental history of group and cluster galaxies in a Λ cold dark matter universe. *MNRAS*, 423(2):1277–1292.

de Vaucouleurs, G. (1961). Integrated Colors of Bright Galaxies in the u, b, V System. *ApJS*, 5:233.

Dekel, A. and Silk, J. (1986). The Origin of Dwarf Galaxies, Cold Dark Matter, and Biased Galaxy Formation. *ApJ*, 303:39.

Delli Veneri, M., Cavuoti, S., Brescia, M., Longo, G., and Riccio, G. (2019). Star formation rates for photometric samples of galaxies using machine learning methods. *MNRAS*, 486(1):1377–1391.

Desai, V., Dalcanton, J. J., Aragón-Salamanca, A., Jablonka, P., Poggianti, B., Gogarten, S. M., Simard, L., Milvang-Jensen, B., Rudnick, G., Zaritsky, D., Clowe, D., Halliday, C., Pelló, R., Saglia, R., and White, S. (2007). The Morphological Content of 10 EDisCS Clusters at 0.5 ¡ z ¡ 0.8. *ApJ*, 660(2):1151–1164.

DESI Collaboration, Aghamousa, A., Aguilar, J., Ahlen, S., Alam, S., Allen, L. E., Allende Prieto, C., Annis, J., Bailey, S., Balland, C., Ballester, O., Baltay, C., Beaufore, L., Bebek, C., Beers, T. C., Bell, E. F., Bernal, J. L., Besuner, R., Beutler, F., Blake, C., Bleuler, H., Blomqvist, M., Blum, R., Bolton, A. S., Briceno, C., Brooks, D., Brownstein, J. R., Buckley-Geer, E., Burden, A., Burtin, E., Busca, N. G., Cahn, R. N., Cai, Y.-C., Cardiel-Sas, L., Carlberg, R. G., Carton, P.-H., Casas, R., Castander, F. J., Cervantes-Cota, J. L., Claybaugh, T. M., Close, M., Coker, C. T., Cole, S., Comparat, J., Cooper, A. P., Cousinou, M. C., Crocce, M., Cuby, J.-G., Cunningham, D. P., Davis, T. M., Dawson, K. S., de la Macorra, A., De Vicente, J., Delubac, T., Derwent, M., Dey, A., Dhungana, G., Ding, Z., Doel, P., Duan, Y. T., Ealet, A., Edelstein, J., Eftekharzadeh, S., Eisenstein, D. J., Elliott, A., Escoffier, S., Evatt, M., Fagrelius, P., Fan, X., Fanning, K., Farahi, A., Farihi, J., Favole, G., Feng, Y., Fernandez, E., Findlay, J. R., Finkbeiner, D. P., Fitzpatrick, M. J., Flaugher, B., Flender, S., Font-Ribera, A., Forero-Romero, J. E., Fosalba, P., Frenk, C. S., Fumagalli, M., Gaensicke, B. T., Gallo, G., Garcia-Bellido, J., Gaztanaga, E., Pietro Gentile Fusillo, N., Gerard, T., Gershkovich, I., Giannantonio, T., Gillet, D., Gonzalez-de-Rivera, G., Gonzalez-Perez, V., Gott, S., Graur, O., Gutierrez, G., Guy, J., Habib, S., Heetderks, H., Heetderks, I., Heitmann, K., Hellwing, W. A., Herrera, D. A., Ho, S., Holland, S., Honscheid, K., Huff, E., Hutchinson, T. A., Huterer, D., Hwang, H. S., Illa Laguna, J. M., Ishikawa, Y., Jacobs, D., Jeffrey, N., Jelinsky, P., Jennings, E., Jiang, L., Jimenez, J., Johnson, J., Joyce, R., Jullo, E., Juneau, S., Kama, S., Karcher, A., Karkar, S.,

Kehoe, R., Kennamer, N., Kent, S., Kilbinger, M., Kim, A. G., Kirkby, D., Kisner, T., Kitanidis, E., Kneib, J.-P., Koposov, S., Kovacs, E., Koyama, K., Kremin, A., Kron, R., Kronig, L., Kueter-Young, A., Lacey, C. G., Lafever, R., Lahav, O., Lambert, A., Lampton, M., Landriau, M., Lang, D., Lauer, T. R., Le Goff, J.-M., Le Guillou, L., Le Van Suu, A., Lee, J. H., Lee, S.-J., Leitner, D., Lesser, M., Levi, M. E., L'Huillier, B., Li, B., Liang, M., Lin, H., Linder, E., Loebman, S. R., Lukić, Z., Ma, J., MacCrann, N., Magneville, C., Makarem, L., Manera, M., Manser, C. J., Marshall, R., Martini, P., Massey, R., Matheson, T., McCauley, J., McDonald, P., McGreer, I. D., Meisner, A., Metcalfe, N., Miller, T. N., Miquel, R., Moustakas, J., Myers, A., Naik, M., Newman, J. A., Nichol, R. C., Nicola, A., Nicolati da Costa, L., Nie, J., Niz, G., Norberg, P., Nord, B., Norman, D., Nugent, P., O'Brien, T., Oh, M., Olsen, K. A. G., Padilla, C., Padmanabhan, H., Padmanabhan, N., Palanque-Delabrouille, N., Palmese, A., Pappalardo, D., Pâris, I., Park, C., Patej, A., Peacock, J. A., Peiris, H. V., Peng, X., Percival, W. J., Perruchot, S., Pieri, M. M., Pogge, R., Pollack, J. E., Poppett, C., Prada, F., Prakash, A., Probst, R. G., Rabinowitz, D., Raichoor, A., Ree, C. H., Refregier, A., Regal, X., Reid, B., Reil, K., Rezaie, M., Rockosi, C. M., Roe, N., Ronayette, S., Roodman, A., Ross, A. J., Ross, N. P., Rossi, G., Rozo, E., Ruhlmann-Kleider, V., Rykoff, E. S., Sabiu, C., Samushia, L., Sanchez, E., Sanchez, J., Schlegel, D. J., Schneider, M., Schubnell, M., Secroun, A., Seljak, U., Seo, H.-J., Serrano, S., Shafieloo, A., Shan, H., Sharples, R., Sholl, M. J., Shourt, W. V., Silber, J. H., Silva, D. R., Sirk, M. M., Slosar, A., Smith, A., Smoot, G. F., Som, D., Song, Y.-S., Sprayberry, D., Staten, R., Stefanik, A., Tarle, G., Sien Tie, S., Tinker, J. L., Tojeiro, R., Valdes, F., Valenzuela, O., Valluri, M., Vargas-Magana, M., Verde, L., Walker, A. R., Wang, J., Wang, Y., Weaver, B. A., Weaverdyck, C., Wechsler, R. H., Weinberg, D. H., White, M., Yang, Q., Yeche, C., Zhang, T., Zhao, G.-B., Zheng, Y., Zhou, X., Zhou, Z., Zhu, Y., Zou, H., and Zu, Y. (2016). The DESI Experiment Part I: Science,Targeting, and Survey Design. *arXiv e-prints*, page arXiv:1611.00036.

Desouza, P. N., Dey, S., Mwenda, K. M., Kim, R., Subramanian, S., and Kinney, P. L. (2022). Robust relationship between ambient air pollution and infant mortality in india. *Science of The Total Environment*, 815:152755.

Di Matteo, T., Springel, V., and Hernquist, L. (2005). Energy input from quasars regulates the growth and activity of black holes and their host galaxies. *Nature*, 433(7026):604–607.

D'Isanto, A. and Polsterer, K. L. (2018). Photometric redshift estimation via deep learning. Generalized and pre-classification-less, image based, fully probabilistic redshifts. *A&A*, 609:A111.

Do, D. P. (2009). The dynamics of income and neighborhood context for population health: do long-term measures of socioeconomic status explain more of the black/white health disparity than single-point-in-time measures? *Social science & medicine*, 68(8):1368–1375.

Do, D. P., Wang, L., and Elliott, M. R. (2013). Investigating the relationship between neighborhood poverty and mortality risk: a marginal structural modeling approach. *Social Science & Medicine*, 91:58–66.

Dobbels, W., Krier, S., Pirson, S., Viaene, S., De Geyter, G., Salim, S., and Baes, M. (2019). Morphology-assisted galaxy mass-to-light predictions using deep learning. *A&A*, 624:A102.

Dolag, K., Borgani, S., Murante, G., and Springel, V. (2009). Substructures in hydrodynamical cluster simulations. *MNRAS*, 399(2):497–514.

Doll, R. and Hill, A. B. (1950). Smoking and carcinoma of the lung. *British medical journal*, 2(4682):739.

Domínguez, M., Muriel, H., and Lambas, D. G. (2001). Galaxy Morphological Segregation in Clusters: Local versus Global Conditions. *AJ*, 121(3):1266–1274.

Donnan, C. T., McLeod, D. J., Dunlop, J. S., McLure, R. J., Carnall, A. C., Begley, R., Cullen, F., Hamadouche, M. L., Bowler, R. A. A., Magee, D., McCracken, H. J., Milvang-Jensen, B., Moneti, A., and Targett, T. (2023). The evolution of the galaxy UV luminosity function at redshifts $z \simeq 8 - 15$ from deep JWST and ground-based near-infrared imaging. *MNRAS*, 518(4):6011–6040.

Donnari, M., Pillepich, A., Nelson, D., Vogelsberger, M., Genel, S., Weinberger, R., Marinacci, F., Springel, V., and Hernquist, L. (2019). The star formation activity

of IllustrisTNG galaxies: main sequence, UVJ diagram, quenched fractions, and systematics. *MNRAS*, 485(4):4817–4840.

Došilović, F. K., Brčić, M., and Hlupić, N. (2018). Explainable artificial intelligence: A survey. In *2018 41st International Convention on Information and Communication Technology, Electronics and Microelectronics (MIPRO)*, pages 0210–0215.

Dressler, A. (1980). Galaxy morphology in rich clusters: implications for the formation and evolution of galaxies. *ApJ*, 236:351–365.

Dressler, A. and Gunn, J. E. (1983). Spectroscopy of galaxies in distant clusters. II. The population of the 3C 295 cluster. *ApJ*, 270:7–19.

Dressler, A., Oemler, Augustus, J., Couch, W. J., Smail, I., Ellis, R. S., Barger, A., Butcher, H., Poggianti, B. M., and Sharples, R. M. (1997). Evolution since z = 0.5 of the Morphology-Density Relation for Clusters of Galaxies. *ApJ*, 490(2):577–591.

Dressler, A., Oemler, Augustus, J., Sparks, W. B., and Lucas, R. A. (1994). New Images of the Distant, Rich Cluster CL 0939+4713 with WFPC2. *ApJ*, 435:L23.

Dressler, A., Smail, I., Poggianti, B. M., Butcher, H., Couch, W. J., Ellis, R. S., and Oemler, Augustus, J. (1999). A Spectroscopic Catalog of 10 Distant Rich Clusters of Galaxies. *ApJS*, 122(1):51–80.

Drlica-Wagner, A., Sevilla-Noarbe, I., Rykoff, E. S., Gruendl, R. A., Yanny, B., Tucker, D. L., Hoyle, B., Carnero Rosell, A., Bernstein, G. M., Bechtol, K., Becker, M. R., Benoit-Lévy, A., Bertin, E., Carrasco Kind, M., Davis, C., de Vicente, J., Diehl, H. T., Gruen, D., Hartley, W. G., Leistedt, B., Li, T. S., Marshall, J. L., Neilsen, E., Rau, M. M., Sheldon, E., Smith, J., Troxel, M. A., Wyatt, S., Zhang, Y., Abbott, T. M. C., Abdalla, F. B., Allam, S., Banerji, M., Brooks, D., Buckley-Geer, E., Burke, D. L., Capozzi, D., Carretero, J., Cunha, C. E., D'Andrea, C. B., da Costa, L. N., DePoy, D. L., Desai, S., Dietrich, J. P., Doel, P., Evrard, A. E., Fausti Neto, A., Flaugher, B., Fosalba, P., Frieman, J., García-Bellido, J., Gerdes, D. W., Giannantonio, T., Gschwend, J., Gutierrez, G., Honscheid, K., James, D. J., Jeltema, T., Kuehn, K., Kuhlmann, S., Kuropatkin, N., Lahav, O., Lima, M., Lin, H., Maia, M. A. G., Martini, P., McMahon, R. G., Melchior, P., Menanteau, F., Miquel, R., Nichol, R. C., Ogand o, R. L. C., Plazas, A. A., Romer, A. K.,

Roodman, A., Sanchez, E., Scarpine, V., Schindler, R., Schubnell, M., Smith, M., Smith, R. C., Soares-Santos, M., Sobreira, F., Suchyta, E., Tarle, G., Vikram, V., Walker, A. R., Wechsler, R. H., Zuntz, J., and DES Collaboration (2018). Dark Energy Survey Year 1 Results: The Photometric Data Set for Cosmology. *ApJS*, 235(2):33.

Drory, N. and Alvarez, M. (2008). The Contribution of Star Formation and Merging to Stellar Mass Buildup in Galaxies. *ApJ*, 680(1):41–53.

Dunlop, J. S. (2013). Observing the First Galaxies. In Wiklind, T., Mobasher, B., and Bromm, V., editors, *The First Galaxies*, volume 396 of *Astrophysics and Space Science Library*, page 223.

Eales, S., de Vis, P., Smith, M. W. L., Appah, K., Ciesla, L., Duffield, C., and Schofield, S. (2017). The Galaxy End Sequence. *MNRAS*, 465(3):3125–3133.

Efstathiou, G. and Silk, J. (1983). The Formation of Galaxies. *Fund. Cosmic Phys.*, 9:1–138.

Einstein, A. (1916). Die Grundlage der allgemeinen Relativitätstheorie. *Annalen der Physik*, 354(7):769–822.

Eisenstein, D. J. (2005). Dark Energy and Cosmic Sound. In Wolff, S. C. and Lauer, T. R., editors, *Observing Dark Energy*, volume 339 of *Astronomical Society of the Pacific Conference Series*, page 187.

Elbaz, D., Daddi, E., Le Borgne, D., Dickinson, M., Alexander, D. M., Chary, R. R., Starck, J. L., Brandt, W. N., Kitzbichler, M., MacDonald, E., Nonino, M., Popesso, P., Stern, D., and Vanzella, E. (2007). The reversal of the star formation-density relation in the distant universe. *A&A*, 468(1):33–48.

Ellingson, E., Lin, H., Yee, H. K. C., and Carlberg, R. G. (2001). The Evolution of Population Gradients in Galaxy Clusters: The Butcher-Oemler Effect and Cluster Infall. *ApJ*, 547(2):609–622.

Ellison, S. L., Patton, D. R., Simard, L., and McConnachie, A. W. (2008). Galaxy Pairs in the Sloan Digital Sky Survey. I. Star Formation, Active Galactic Nucleus Fraction, and the Mass-Metallicity Relation. *AJ*, 135(5):1877–1899.

Eriksen, M., Alarcon, A., Gaztanaga, E., Amara, A., Cabayol, L., Carretero, J., Castander, F. J., Crocce, M., Delfino, M., De Vicente, J., Fernand ez, E., Fosalba, P., Garcia-Bellido, J., Hildebrand t, H., Hoekstra, H., Joachimi, B., Norberg, P., Miquel, R., Padilla, C., Refregier, A., Sanchez, E., Serrano, S., Sevilla-Noarbe, I., Tallada, P., Tonello, N., and Tortorelli, L. (2019). The PAU Survey: early demonstration of photometric redshift performance in the COSMOS field. *MNRAS*, 484(3):4200–4215.

Euclid Collaboration, Bisigello, L., Conselice, C. J., Baes, M., Bolzonella, M., Brescia, M., Cavuoti, S., Cucciati, O., Humphrey, A., Hunt, L. K., Maraston, C., Pozzetti, L., Tortora, C., van Mierlo, S. E., Aghanim, N., Auricchio, N., Baldi, M., Bender, R., Bodendorf, C., Bonino, D., Branchini, E., Brinchmann, J., Camera, S., Capobianco, V., Carbone, C., Carretero, J., Castander, F. J., Castellano, M., Cimatti, A., Congedo, G., Conversi, L., Copin, Y., Corcione, L., Courbin, F., Cropper, M., Da Silva, A., Degaudenzi, H., Douspis, M., Dubath, F., Duncan, C. A. J., Dupac, X., Dusini, S., Farrens, S., Ferriol, S., Frailis, M., Franceschi, E., Franzetti, P., Fumana, M., Garilli, B., Gillard, W., Gillis, B., Giocoli, C., Grazian, A., Grupp, F., Guzzo, L., Haugan, S. V. H., Holmes, W., Hormuth, F., Hornstrup, A., Jahnke, K., Kümmel, M., Kermiche, S., Kiessling, A., Kilbinger, M., Kohley, R., Kunz, M., Kurki-Suonio, H., Ligori, S., Lilje, P. B., Lloro, I., Maiorano, E., Mansutti, O., Marggraf, O., Markovic, K., Marulli, F., Massey, R., Maurogordato, S., Medinaceli, E., Meneghetti, M., Merlin, E., Meylan, G., Moresco, M., Moscardini, L., Munari, E., Niemi, S. M., Padilla, C., Paltani, S., Pasian, F., Pedersen, K., Pettorino, V., Polenta, G., Poncet, M., Popa, L., Raison, F., Renzi, A., Rhodes, J., Riccio, G., Rix, H. W., Romelli, E., Roncarelli, M., Rosset, C., Rossetti, E., Saglia, R., Sapone, D., Sartoris, B., Schneider, P., Scodeggio, M., Secroun, A., Seidel, G., Sirignano, C., Sirri, G., Stanco, L., Tallada-Crespí, P., Tavagnacco, D., Taylor, A. N., Tereno, I., Toledo-Moreo, R., Torradeflot, F., Tutusaus, I., Valentijn, E. A., Valenziano, L., Vassallo, T., Wang, Y., Zacchei, A., Zamorani, G., Zoubian, J., Andreon, S., Bardelli, S., Boucaud, A., Colodro-Conde, C., Di Ferdinando, D., Graciá-Carpio, J., Lindholm, V., Maino, D., Mei, S., Scottez, V., Sureau, F., Tenti, M., Zucca, E., Borlaff, A. S., Ballardini, M., Biviano, A., Bozzo, E., Burigana, C., Cabanac, R., Cappi, A., Carvalho, C. S.,

Casas, S., Castignani, G., Cooray, A., Coupon, J., Courtois, H. M., Cuby, J., Davini, S., De Lucia, G., Desprez, G., Dole, H., Escartin, J. A., Escoffier, S., Farina, M., Fotopoulou, S., Ganga, K., Garcia-Bellido, J., George, K., Giacomini, F., Gozaliasl, G., Hildebrandt, H., Hook, I., Huertas-Company, M., Kansal, V., Keihanen, E., Kirkpatrick, C. C., Loureiro, A., Macías-Pérez, J. F., Magliocchetti, M., Mainetti, G., Marcin, S., Martinelli, M., Martinet, N., Metcalf, R. B., Monaco, P., Morgante, G., Nadathur, S., Nucita, A. A., Patrizii, L., Peel, A., Potter, D., Pourtsidou, A., Pöntinen, M., Reimberg, P., Sánchez, A. G., Sakr, Z., Schirmer, M., Sefusatti, E., Sereno, M., Stadel, J., Teyssier, R., Valieri, C., Valiviita, J., and Viel, M. (2023). Euclid preparation - XXIII. Derivation of galaxy physical properties with deep machine learning using mock fluxes and H-band images. *MNRAS*, 520(3):3529–3548.

Euclid Collaboration: Desprez, Desprez, G., Paltani, S., Coupon, J., Almosallam, I., Alvarez-Ayllon, A., Amaro, V., Brescia, M., Brodwin, M., Cavuoti, S., De Vicente-Albendea, J., Fotopoulou, S., Hatfield, P. W., Hartley, W. G., Ilbert, O., Jarvis, M. J., Longo, G., Rau, M. M., Saha, R., Speagle, J. S., Tramacere, A., Castellano, M., Dubath, F., Galametz, A., Kuemmel, M., Laigle, C., Merlin, E., Mohr, J. J., Pilo, S., Salvato, M., Andreon, S., Auricchio, N., Baccigalupi, C., Balaguera-Antolínez, A., Baldi, M., Bardelli, S., Bender, R., Biviano, A., Bodendorf, C., Bonino, D., Bozzo, E., Branchini, E., Brinchmann, J., Burigana, C., Cabanac, R., Camera, S., Capobianco, V., Cappi, A., Carbone, C., Carretero, J., Carvalho, C. S., Casas, R., Casas, S., Castander, F. J., Castignani, G., Cimatti, A., Cledassou, R., Colodro-Conde, C., Congedo, G., Conselice, C. J., Conversi, L., Copin, Y., Corcione, L., Courtois, H. M., Cuby, J. G., Da Silva, A., de la Torre, S., Degaudenzi, H., Di Ferdinando, D., Douspis, M., Duncan, C. A. J., Dupac, X., Ealet, A., Fabbian, G., Fabricius, M., Farrens, S., Ferreira, P. G., Finelli, F., Fosalba, P., Fourmanoit, N., Frailis, M., Franceschi, E., Fumana, M., Galeotta, S., Garilli, B., Gillard, W., Gillis, B., Giocoli, C., Gozaliasl, G., Graciá-Carpio, J., Grupp, F., Guzzo, L., Hailey, M., Haugan, S. V. H., Holmes, W., Hormuth, F., Humphrey, A., Jahnke, K., Keihanen, E., Kermiche, S., Kilbinger, M., Kirkpatrick, C. C., Kitching, T. D., Kohley, R., Kubik, B., Kunz, M., Kurki-Suonio, H., Ligori, S., Lilje, P. B., Lloro, I., Maino, D., Maiorano, E., Marggraf, O., Markovic, K.,

Martinet, N., Marulli, F., Massey, R., Maturi, M., Mauri, N., Maurogordato, S., Medinaceli, E., Mei, S., Meneghetti, M., Benton Metcalf, R., Meylan, G., Moresco, M., Moscardini, L., Munari, E., Niemi, S., Padilla, C., Pasian, F., Patrizii, L., Pettorino, V., Pires, S., Polenta, G., Poncet, M., Popa, L., Potter, D., Pozzetti, L., Raison, F., Renzi, A., Rhodes, J., Riccio, G., Rossetti, E., Saglia, R., Sapone, D., Schneider, P., Scottez, V., Secroun, A., Serrano, S., Sirignano, C., Sirri, G., Stanco, L., Stern, D., Sureau, F., Tallada Crespí, P., Tavagnacco, D., Taylor, A. N., Tenti, M., Tereno, I., Toledo-Moreo, R., Torradeflot, F., Valenziano, L., Valiviita, J., Vassallo, T., Viel, M., Wang, Y., Welikala, N., Whittaker, L., Zacchei, A., Zamorani, G., Zoubian, J., and Zucca, E. (2020). Euclid preparation. X. The Euclid photometric-redshift challenge. *A&A*, 644:A31.

Everett, S., Yanny, B., Kuropatkin, N., Huff, E. M., Zhang, Y., Myles, J., Masegian, A., Elvin-Poole, J., Allam, S., Bernstein, G. M., Sevilla-Noarbe, I., Splettstoesser, M., Sheldon, E., Jarvis, M., Amon, A., Harrison, I., Choi, A., Hartley, W. G., Alarcon, A., Sánchez, C., Gruen, D., Eckert, K., Prat, J., Tabbutt, M., Busti, V., Becker, M. R., MacCrann, N., Diehl, H. T., Tucker, D. L., Bertin, E., Jeltema, T., Drlica-Wagner, A., Gruendl, R. A., Bechtol, K., Carnero Rosell, A., Abbott, T. M. C., Aguena, M., Annis, J., Bacon, D., Bhargava, S., Brooks, D., Burke, D. L., Carrasco Kind, M., Carretero, J., Castander, F. J., Conselice, C., Costanzi, M., da Costa, L. N., Pereira, M. E. S., De Vicente, J., DeRose, J., Desai, S., Eifler, T. F., Evrard, A. E., Ferrero, I., Fosalba, P., Frieman, J., García-Bellido, J., Gaztanaga, E., Gerdes, D. W., Gutierrez, G., Hinton, S. R., Hollowood, D. L., Honscheid, K., Huterer, D., James, D. J., Kent, S., Krause, E., Kuehn, K., Lahav, O., Lima, M., Lin, H., Maia, M. A. G., Marshall, J. L., Melchior, P., Menanteau, F., Miquel, R., Mohr, J. J., Morgan, R., Muir, J., Ogando, R. L. C., Palmese, A., Paz-Chinchón, F., Plazas, A. A., Rodriguez-Monroy, M., Romer, A. K., Roodman, A., Sanchez, E., Scarpine, V., Serrano, S., Smith, M., Soares-Santos, M., Suchyta, E., Swanson, M. E. C., Tarle, G., To, C., Troxel, M. A., Varga, T. N., Weller, J., and Wilkinson, R. D. (2020). Dark Energy Survey Year 3 Results: Measuring the Survey Transfer Function with Balrog. *arXiv e-prints*, page arXiv:2012.12825.

Fabian, A. C. (2012). Observational Evidence of Active Galactic Nuclei Feedback. *ARA&A*, 50:455–489.

Fabricant, D. G., McClintock, J. E., and Bautz, M. W. (1991). Galaxy Evolution in Distant, X-Ray–Selected Clusters of Galaxies. I. CL 1358+6245. *ApJ*, 381:33.

Fall, S. M. and Efstathiou, G. (1980). Formation and rotation of disc galaxies with haloes. *MNRAS*, 193:189–206.

Fang, J. J., Faber, S. M., Koo, D. C., and Dekel, A. (2013). A Link between Star Formation Quenching and Inner Stellar Mass Density in Sloan Digital Sky Survey Central Galaxies. *ApJ*, 776(1):63.

Farouki, R. and Shapiro, S. L. (1981). Computer simulations of environmental influences on galaxy evolution in dense clusters. II - Rapid tidal encounters. *ApJ*, 243:32–41.

Fasano, G., Poggianti, B. M., Couch, W. J., Bettoni, D., Kjærgaard, P., and Moles, M. (2000). The Evolution of the Galactic Morphological Types in Clusters. *ApJ*, 542(2):673–683.

Feldmann, R. (2017). Are star formation rates of galaxies bimodal? *MNRAS*, 470(1):L59–L63.

Feldmann, R., Carollo, C. M., Porciani, C., Lilly, S. J., Capak, P., Taniguchi, Y., Le Fèvre, O., Renzini, A., Scoville, N., Ajiki, M., Aussel, H., Contini, T., McCracken, H., Mobasher, B., Murayama, T., Sanders, D., Sasaki, S., Scarlata, C., Scodeggio, M., Shioya, Y., Silverman, J., Takahashi, M., Thompson, D., and Zamorani, G. (2006). The Zurich Extragalactic Bayesian Redshift Analyzer and its first application: COSMOS. *MNRAS*, 372(2):565–577.

Ferland, G. J., Korista, K. T., Verner, D. A., Ferguson, J. W., Kingdon, J. B., and Verner, E. M. (1998). CLOUDY 90: Numerical Simulation of Plasmas and Their Spectra. *PASP*, 110(749):761–778.

Feroz, F., Hobson, M., Cameron, E., and Pettitt, A. (2019). Importance Nested Sampling and the MultiNest Algorithm. *Open J. Astrophys.*, 2(1):10.

Feroz, F. and Hobson, M. P. (2008). Multimodal nested sampling: an efficient and robust alternative to Markov Chain Monte Carlo methods for astronomical data analyses. *MNRAS*, 384(2):449–463.

Feroz, F., Hobson, M. P., and Bridges, M. (2009). MultiNest: an efficient and robust Bayesian inference tool for cosmology and particle physics. *MNRAS*, 398(4):1601–1614.

Ferrarese, L. and Merritt, D. (2000). A Fundamental Relation between Supermassive Black Holes and Their Host Galaxies. *ApJ*, 539(1):L9–L12.

Feruglio, C., Aussel, H., Le Floc'h, E., Ilbert, O., Salvato, M., Capak, P., Fiore, F., Kartaltepe, J., Sanders, D., Scoville, N., Koekemoer, A. M., and Ideue, Y. (2010). Obscured Star Formation and Environment in the COSMOS Field. *ApJ*, 721(1):607–614.

Feulner, G., Gabasch, A., Salvato, M., Drory, N., Hopp, U., and Bender, R. (2005). Specific Star Formation Rates to Redshift 5 from the FORS Deep Field and the GOODS-S Field. *ApJ*, 633(1):L9–L12.

Fewell, Z., Hernán, M. A., Wolfe, F., Tilling, K., Choi, H., and Sterne, J. A. (2004). Controlling for time-dependent confounding using marginal structural models. *The Stata Journal*, 4(4):402–420.

Finkelstein, S. L., Bagley, M. B., Arrabal Haro, P., Dickinson, M., Ferguson, H. C., Kartaltepe, J. S., Papovich, C., Burgarella, D., Kocevski, D. D., Huertas-Company, M., Iyer, K. G., Koekemoer, A. M., Larson, R. L., Pérez-González, P. G., Rose, C., Tacchella, S., Wilkins, S. M., Chworowsky, K., Medrano, A., Morales, A. M., Somerville, R. S., Yung, L. Y. A., Fontana, A., Giavalisco, M., Grazian, A., Grogin, N. A., Kewley, L. J., Kirkpatrick, A., Kurczynski, P., Lotz, J. M., Pentericci, L., Pirzkal, N., Ravindranath, S., Ryan, R. E., Trump, J. R., Yang, G., Almaini, O., Amorín, R. O., Annunziatella, M., Backhaus, B. E., Barro, G., Behroozi, P., Bell, E. F., Bhatawdekar, R., Bisigello, L., Bromm, V., Buat, V., Buitrago, F., Calabrò, A., Casey, C. M., Castellano, M., Chávez Ortiz, Ó. A., Ciesla, L., Cleri, N. J., Cohen, S. H., Cole, J. W., Cooke, K. C., Cooper, M. C., Cooray, A. R., Costantin, L., Cox, I. G., Croton, D., Daddi, E., Davé, R., de La Vega, A., Dekel, A., Elbaz, D., Estrada-Carpenter, V., Faber, S. M., Fernández, V., Finkelstein, K. D., Freundlich, J., Fujimoto, S., García-Argumánez, Á., Gardner, J. P., Gawiser, E., Gómez-Guijarro, C., Guo, Y., Hamblin, K., Hamilton, T. S., Hathi, N. P.,

Holwerda, B. W., Hirschmann, M., Hutchison, T. A., Jaskot, A. E., Jha, S. W., Jogee, S., Juneau, S., Jung, I., Kassin, S. A., Bail, A. L., Leung, G. C. K., Lucas, R. A., Magnelli, B., Mantha, K. B., Matharu, J., McGrath, E. J., McIntosh, D. H., Merlin, E., Mobasher, B., Newman, J. A., Nicholls, D. C., Pandya, V., Rafelski, M., Ronayne, K., Santini, P., Seillé, L.-M., Shah, E. A., Shen, L., Simons, R. C., Snyder, G. F., Stanway, E. R., Straughn, A. N., Teplitz, H. I., Vanderhoof, B. N., Vega-Ferrero, J., Wang, W., Weiner, B. J., Willmer, C. N. A., Wuyts, S., Zavala, J. A., and Ceers Team (2022). A Long Time Ago in a Galaxy Far, Far Away: A Candidate z $\sim$ 12 Galaxy in Early JWST CEERS Imaging. *ApJ*, 940(2):L55.

Fioc, M. and Rocca-Volmerange, B. (1997). PEGASE: a UV to NIR spectral evolution model of galaxies. Application to the calibration of bright galaxy counts. *A&A*, 326:950–962.

Firth, A. E., Lahav, O., and Somerville, R. S. (2003). Estimating photometric redshifts with artificial neural networks. *MNRAS*, 339(4):1195–1202.

Flaugher, B., Diehl, H. T., Honscheid, K., Abbott, T. M. C., Alvarez, O., Angstadt, R., Annis, J. T., Antonik, M., Ballester, O., Beaufore, L., Bernstein, G. M., Bernstein, R. A., Bigelow, B., Bonati, M., Boprie, D., Brooks, D., Buckley-Geer, E. J., Campa, J., Cardiel-Sas, L., Castand er, F. J., Castilla, J., Cease, H., Cela-Ruiz, J. M., Chappa, S., Chi, E., Cooper, C., da Costa, L. N., Dede, E., Derylo, G., DePoy, D. L., de Vicente, J., Doel, P., Drlica-Wagner, A., Eiting, J., Elliott, A. E., Emes, J., Estrada, J., Fausti Neto, A., Finley, D. A., Flores, R., Frieman, J., Gerdes, D., Gladders, M. D., Gregory, B., Gutierrez, G. R., Hao, J., Holland, S. E., Holm, S., Huffman, D., Jackson, C., James, D. J., Jonas, M., Karcher, A., Karliner, I., Kent, S., Kessler, R., Kozlovsky, M., Kron, R. G., Kubik, D., Kuehn, K., Kuhlmann, S., Kuk, K., Lahav, O., Lathrop, A., Lee, J., Levi, M. E., Lewis, P., Li, T. S., Mand richenko, I., Marshall, J. L., Martinez, G., Merritt, K. W., Miquel, R., Muñoz, F., Neilsen, E. H., Nichol, R. C., Nord, B., Ogando, R., Olsen, J., Palaio, N., Patton, K., Peoples, J., Plazas, A. A., Rauch, J., Reil, K., Rheault, J. P., Roe, N. A., Rogers, H., Roodman, A., Sanchez, E., Scarpine, V., Schindler, R. H., Schmidt, R., Schmitt, R., Schubnell, M., Schultz, K., Schurter, P., Scott, L., Serrano, S., Shaw, T. M., Smith, R. C., Soares-Santos, M., Stefanik, A., Stuermer,

W., Suchyta, E., Sypniewski, A., Tarle, G., Thaler, J., Tighe, R., Tran, C., Tucker, D., Walker, A. R., Wang, G., Watson, M., Weaverdyck, C., Wester, W., Woods, R., Yanny, B., and DES Collaboration (2015). The Dark Energy Camera. *AJ*, 150(5):150.

Fluke, C. J. and Jacobs, C. (2020). Surveying the reach and maturity of machine learning and artificial intelligence in astronomy. *WIREs Data Mining and Knowledge Discovery*, 10(2):e1349.

Fontana, A., Santini, P., Grazian, A., Pentericci, L., Fiore, F., Castellano, M., Giallongo, E., Menci, N., Salimbeni, S., Cristiani, S., Nonino, M., and Vanzella, E. (2009). The fraction of quiescent massive galaxies in the early Universe. *A&A*, 501(1):15–20.

Fontanot, F., De Lucia, G., Monaco, P., Somerville, R. S., and Santini, P. (2009). The many manifestations of downsizing: hierarchical galaxy formation models confront observations. *MNRAS*, 397(4):1776–1790.

Foreman-Mackey, D., Hogg, D. W., Lang, D., and Goodman, J. (2013). emcee: The MCMC Hammer. *PASP*, 125(925):306.

Freeman, K. C. (1970). On the Disks of Spiral and S0 Galaxies. *ApJ*, 160:811.

French, K. D. (2021). Evolution Through the Post-starburst Phase: Using Post-starburst Galaxies as Laboratories for Understanding the Processes that Drive Galaxy Evolution. *PASP*, 133(1025):072001.

Friedmann, A. (1922). Über die Krümmung des Raumes. *Zeitschrift fur Physik*, 10:377–386.

Gao, L., Springel, V., and White, S. D. M. (2005). The age dependence of halo clustering. *MNRAS*, 363(1):L66–L70.

Gardner, J. P., Mather, J. C., Clampin, M., Doyon, R., Greenhouse, M. A., Hammel, H. B., Hutchings, J. B., Jakobsen, P., Lilly, S. J., Long, K. S., Lunine, J. I., McCaughrean, M. J., Mountain, M., Nella, J., Rieke, G. H., Rieke, M. J., Rix, H.-W., Smith, E. P., Sonneborn, G., Stiavelli, M., Stockman, H. S., Windhorst,

R. A., and Wright, G. S. (2006). The James Webb Space Telescope. *Space Sci. Rev.*, 123(4):485–606.

Garduño, L. E., Lara-López, M. A., López-Cruz, O., Hopkins, A. M., Owers, M. S., Pimbblet, K. A., and Holwerda, B. W. (2021). Galaxy And Mass Assembly (GAMA): the interplay between galaxy mass, SFR, and heavy element abundance in paired galaxy sets. *MNRAS*, 501(2):2969–2982.

Gareth, J., Daniela, W., Trevor, H., and Robert, T. (2013). *An introduction to statistical learning: with applications in R*. Spinger.

Gavazzi, G., Contursi, A., Carrasco, L., Boselli, A., Kennicutt, R., Scodeggio, M., and Jaffe, W. (1995). The radio and optical structure of three peculiar galaxies in A 1367. *A&A*, 304:325.

Geach, J. E. (2012). Unsupervised self-organized mapping: a versatile empirical tool for object selection, classification and redshift estimation in large surveys. *MNRAS*, 419(3):2633–2645.

Gebhardt, K., Bender, R., Bower, G., Dressler, A., Faber, S. M., Filippenko, A. V., Green, R., Grillmair, C., Ho, L. C., Kormendy, J., Lauer, T. R., Magorrian, J., Pinkney, J., Richstone, D., and Tremaine, S. (2000). A Relationship between Nuclear Black Hole Mass and Galaxy Velocity Dispersion. *ApJ*, 539(1):L13–L16.

Genel, S., Vogelsberger, M., Springel, V., Sijacki, D., Nelson, D., Snyder, G., Rodriguez-Gomez, V., Torrey, P., and Hernquist, L. (2014). Introducing the Illustris project: the evolution of galaxy populations across cosmic time. *MNRAS*, 445(1):175–200.

Gerdes, D. W., Sypniewski, A. J., McKay, T. A., Hao, J., Weis, M. R., Wechsler, R. H., and Busha, M. T. (2010). ArborZ: Photometric Redshifts Using Boosted Decision Trees. *ApJ*, 715(2):823–832.

Ghigna, S., Moore, B., Governato, F., Lake, G., Quinn, T., and Stadel, J. (1998). Dark matter haloes within clusters. *MNRAS*, 300(1):146–162.

Ghosh, A., Simon, K., and Sommers, B. (2018). The effect of health insurance on

prescription drug use among low-income adults:evidence from recent medicaid expansions. *Journal of Health Economics*, 63.

Giallongo, E., Salimbeni, S., Menci, N., Zamorani, G., Fontana, A., Dickinson, M., Cristiani, S., and Pozzetti, L. (2005). The B-Band Luminosity Function of Red and Blue Galaxies up to z = 3.5. *ApJ*, 622(1):116–128.

Giavalisco, M., Ferguson, H. C., Koekemoer, A. M., Dickinson, M., Alexander, D. M., Bauer, F. E., Bergeron, J., Biagetti, C., Brandt, W. N., Casertano, S., Cesarsky, C., Chatzichristou, E., Conselice, C., Cristiani, S., Da Costa, L., Dahlen, T., de Mello, D., Eisenhardt, P., Erben, T., Fall, S. M., Fassnacht, C., Fosbury, R., Fruchter, A., Gardner, J. P., Grogin, N., Hook, R. N., Hornschemeier, A. E., Idzi, R., Jogee, S., Kretchmer, C., Laidler, V., Lee, K. S., Livio, M., Lucas, R., Madau, P., Mobasher, B., Moustakas, L. A., Nonino, M., Padovani, P., Papovich, C., Park, Y., Ravindranath, S., Renzini, A., Richardson, M., Riess, A., Rosati, P., Schirmer, M., Schreier, E., Somerville, R. S., Spinrad, H., Stern, D., Stiavelli, M., Strolger, L., Urry, C. M., Vandame, B., Williams, R., and Wolf, C. (2004). The Great Observatories Origins Deep Survey: Initial Results from Optical and Near-Infrared Imaging. *ApJ*, 600(2):L93–L98.

Gini, C. (1912). *Variabilità e mutabilità: contributo allo studio delle distribuzioni e delle relazioni statistiche.[Fasc. I.]*. Tipogr. di P. Cuppini.

Girardi, L., Bressan, A., Bertelli, G., and Chiosi, C. (2000). Evolutionary tracks and isochrones for low- and intermediate-mass stars: From 0.15 to 7 M_{sun}, and from Z=0.0004 to 0.03. *A&AS*, 141:371–383.

Girardi, M., Biviano, A., Giuricin, G., Mardirossian, F., and Mezzetti, M. (1993). Velocity Dispersions in Galaxy Clusters. *ApJ*, 404:38.

Giuricin, G., Samurović, S., Girardi, M., Mezzetti, M., and Marinoni, C. (2001). The Redshift-Space Two-Point Correlation Functions of Galaxies and Groups in the Nearby Optical Galaxy Sample. *ApJ*, 554(2):857–872.

Glymour, C., Zhang, K., and Spirtes, P. (2019). Review of causal discovery methods based on graphical models. *Frontiers in genetics*, 10:524.

Gnedin, O. Y. (2003). Tidal Effects in Clusters of Galaxies. *ApJ*, 582(1):141–161.

Gneiting, T., Balabdaoui, F., and Raftery, A. (2007). Probabilistic forecasts, calibration and sharpness. *J. R. Stat. Soc. B*, 69:243 – 268.

Gómez, P. L., Nichol, R. C., Miller, C. J., Balogh, M. L., Goto, T., Zabludoff, A. I., Romer, A. K., Bernardi, M., Sheth, R., Hopkins, A. M., Castander, F. J., Connolly, A. J., Schneider, D. P., Brinkmann, J., Lamb, D. Q., SubbaRao, M., and York, D. G. (2003). Galaxy Star Formation as a Function of Environment in the Early Data Release of the Sloan Digital Sky Survey. *ApJ*, 584(1):210–227.

Goodman, J. and Weare, J. (2010). Ensemble samplers with affine invariance. *Commun. Appl. Math. Comput. Sci.*, 5(1):65–80.

Goto, T., Yamauchi, C., Fujita, Y., Okamura, S., Sekiguchi, M., Smail, I., Bernardi, M., and Gomez, P. L. (2003). The morphology-density relation in the Sloan Digital Sky Survey. *MNRAS*, 346(2):601–614.

Gottlöber, S., Klypin, A., and Kravtsov, A. V. (2001). Merging History as a Function of Halo Environment. *ApJ*, 546(1):223–233.

Goyal, A. and Bengio, Y. (2020). Inductive Biases for Deep Learning of Higher-Level Cognition. *arXiv e-prints*, page arXiv:2011.15091.

Groves, B. A., Dopita, M. A., and Sutherland, R. S. (2004a). Dusty, Radiation Pressure-Dominated Photoionization. I. Model Description, Structure, and Grids. *ApJS*, 153(1):9–73.

Groves, B. A., Dopita, M. A., and Sutherland, R. S. (2004b). Dusty, Radiation Pressure-Dominated Photoionization. II. Multiwavelength Emission Line Diagnostics for Narrow-Line Regions. *ApJS*, 153(1):75–91.

Grützbauch, R., Conselice, C. J., Varela, J., Bundy, K., Cooper, M. C., Skibba, R., and Willmer, C. N. A. (2011). How does galaxy environment matter? The relationship between galaxy environments, colour and stellar mass at 0.4 ¡ z ¡ 1 in the Palomar/DEEP2 survey. *MNRAS*, 411(2):929–946.

Gunn, J. E. and Gott, J. Richard, I. (1972). On the Infall of Matter Into Clusters of Galaxies and Some Effects on Their Evolution. *ApJ*, 176:1.

Guth, A. H. and Pi, S. Y. (1982). Fluctuations in the New Inflationary Universe. *Phys. Rev. Lett.*, 49(15):1110–1113.

Guzzo, L., Cassata, P., Finoguenov, A., Massey, R., Scoville, N. Z., Capak, P., Ellis, R. S., Mobasher, B., Taniguchi, Y., Thompson, D., Ajiki, M., Aussel, H., Böhringer, H., Brusa, M., Calzetti, D., Comastri, A., Franceschini, A., Hasinger, G., Kasliwal, M. M., Kitzbichler, M. G., Kneib, J. P., Koekemoer, A., Leauthaud, A., McCracken, H. J., Murayama, T., Nagao, T., Rhodes, J., Sanders, D. B., Sasaki, S., Shioya, Y., Tasca, L., and Taylor, J. E. (2007). The Cosmic Evolution Survey (COSMOS): A Large-Scale Structure at z=0.73 and the Relation of Galaxy Morphologies to Local Environment. *ApJS*, 172(1):254–269.

Guzzo, L., Strauss, M. A., Fisher, K. B., Giovanelli, R., and Haynes, M. P. (1997). Redshift-Space Distortions and the Real-Space Clustering of Different Galaxy Types. *ApJ*, 489(1):37–48.

Haas, M. R., Schaye, J., and Jeeson-Daniel, A. (2012). Disentangling galaxy environment and host halo mass. *MNRAS*, 419(3):2133–2146.

Hagedoorn, P. and Helbich, M. (2021). Longitudinal exposure assessments of neighbourhood effects in health research: What can be learned from people's residential histories? *Health & Place*, 68:102543.

Haiman, Z., Mohr, J. J., and Holder, G. P. (2001). Constraints on Cosmological Parameters from Future Galaxy Cluster Surveys. *ApJ*, 553(2):545–561.

Hamill, T. (2000). Interpretation of rank histograms for verifying ensemble forecasts. *Monthly Weather Review*, 129:550–560.

Hamilton, D. (1985). The spectral evolution of galaxies. I. an observational approach. *ApJ*, 297:371–389.

Han, Y. and Han, Z. (2012). Decoding Spectral Energy Distributions of Dust-obscured Starburst-Active Galactic Nucleus. *ApJ*, 749(2):123.

Han, Y. and Han, Z. (2014). BayeSED: A General Approach to Fitting the Spectral Energy Distribution of Galaxies. *ApJS*, 215(1):2.

Han, Y. and Han, Z. (2019). A Comprehensive Bayesian Discrimination of the Simple Stellar Population Model, Star Formation History, and Dust Attenuation Law in the Spectral Energy Distribution Modeling of Galaxies. *ApJS*, 240(1):3.

Harikane, Y., Ouchi, M., Oguri, M., Ono, Y., Nakajima, K., Isobe, Y., Umeda, H., Mawatari, K., and Zhang, Y. (2023). A Comprehensive Study of Galaxies at z 9-16 Found in the Early JWST Data: Ultraviolet Luminosity Functions and Cosmic Star Formation History at the Pre-reionization Epoch. *ApJS*, 265(1):5.

Häring, N. and Rix, H.-W. (2004). On the Black Hole Mass-Bulge Mass Relation. *ApJ*, 604(2):L89–L92.

Harker, G., Cole, S., Helly, J., Frenk, C., and Jenkins, A. (2006). A marked correlation function analysis of halo formation times in the Millennium Simulation. *MNRAS*, 367(3):1039–1049.

Hartley, W. G., Choi, A., Amon, A., Gruendl, R. A., Sheldon, E., Harrison, I., Bernstein, G. M., Sevilla-Noarbe, I., Yanny, B., Eckert, K., Diehl, H. T., Alarcon, A., Banerji, M., Bechtol, K., Buchs, R., Cantu, S., Conselice, C., Cordero, J., Davis, C., Davis, T. M., Dodelson, S., Drlica-Wagner, A., Everett, S., Ferté, A., Gruen, D., Honscheid, K., Jarvis, M., Johnson, M. D., Kokron, N., MacCrann, N., Myles, J., Pace, A. B., Palmese, A., Paz-Chinchón, F., Pereira, M. E. S., Plazas, A. A., Prat, J., Rodriguez-Monroy, M., Rykoff, E. S., Samuroff, S., Sánchez, C., Secco, L. F., Tarsitano, F., Tong, A., Troxel, M. A., Vasquez, Z., Wang, K., Zhou, C., Abbott, T. M. C., Aguena, M., Allam, S., Annis, J., Bacon, D., Bertin, E., Bhargava, S., Brooks, D., Burke, D. L., Carnero Rosell, A., Carrasco Kind, M., Carretero, J., Castander, F. J., Costanzi, M., Crocce, M., da Costa, L. N., De Vicente, J., DeRose, J., Desai, S., Dietrich, J. P., Eifler, T. F., Elvin-Poole, J., Ferrero, I., Flaugher, B., Fosalba, P., García-Bellido, J., Gaztanaga, E., Gerdes, D. W., Gschwend, J., Gutierrez, G., Hinton, S. R., Hollowood, D. L., Huterer, D., James, D. J., Kent, S., Krause, E., Kuehn, K., Kuropatkin, N., Lahav, O., Lin, H., Maia, M. A. G., March, M., Marshall, J. L., Martini, P., Melchior, P., Menanteau, F., Miquel, R., Mohr, J. J., Morgan, R., Neilsen, E., Ogando, R. L. C., Pandey, S., Romer, A. K., Roodman, A., Sako, M., Sanchez, E., Scarpine, V., Serrano, S., Smith, M., Soares-Santos, M., Suchyta, E., Swanson, M. E. C., Tarle, G., Thomas,

D., To, C., Varga, T. N., Walker, A. R., Wester, W., Wilkinson, R. D., and Zuntz, J. (2020). Dark Energy Survey Year 3 Results: Deep Field Optical + Near-Infrared Images and Catalogue. *arXiv e-prints*, page arXiv:2012.12824.

Hashimoto, Y., Oemler, Augustus, J., Lin, H., and Tucker, D. L. (1998). The Influence of Environment on the Star Formation Rates of Galaxies. *ApJ*, 499(2):589–599.

Hatton, S., Devriendt, J. E. G., Ninin, S., Bouchet, F. R., Guiderdoni, B., and Vibert, D. (2003). GALICS- I. A hybrid N-body/semi-analytic model of hierarchical galaxy formation. *MNRAS*, 343(1):75–106.

Hawking, S. W. (1982). The development of irregularities in a single bubble inflationary universe. *Physics Letters B*, 115(4):295–297.

Hayward, C. C., Torrey, P., Springel, V., Hernquist, L., and Vogelsberger, M. (2014). Galaxy mergers on a moving mesh: a comparison with smoothed particle hydrodynamics. *MNRAS*, 442(3):1992–2016.

Heavens, A., Panter, B., Jimenez, R., and Dunlop, J. (2004). The star-formation history of the Universe from the stellar populations of nearby galaxies. *Nature*, 428(6983):625–627.

Heavens, A. F., Jimenez, R., and Lahav, O. (2000). Massive lossless data compression and multiple parameter estimation from galaxy spectra. *MNRAS*, 317(4):965–972.

Heckman, T. M., Armus, L., and Miley, G. K. (1990). On the Nature and Implications of Starburst-driven Galactic Superwinds. *ApJS*, 74:833.

Heckman, T. M. and Best, P. N. (2014). The Coevolution of Galaxies and Supermassive Black Holes: Insights from Surveys of the Contemporary Universe. *ARA&A*, 52:589–660.

Henghes, B., Lahav, O., Gerdes, D. W., Lin, H. W., Morgan, R., Abbott, T. M. C., Aguena, M., Allam, S., Annis, J., Avila, S., Bertin, E., Brooks, D., Burke, D. L., Carnero Rosell, A., Carrasco Kind, M., Carretero, J., Conselice, C., Costanzi, M., da Costa, L. N., De Vicente, J., Desai, S., Diehl, H. T., Doel, P., Everett, S., Ferrero, I., Frieman, J., García-Bellido, J., Gaztanaga, E., Gruen, D., Gruendl, R. A., Gschwend, J., Gutierrez, G., Hartley, W. G., Hinton, S. R., Honscheid, K.,

Hoyle, B., James, D. J., Kuehn, K., Kuropatkin, N., Marshall, J. L., Melchior, P., Menanteau, F., Miquel, R., Ogando, R. L. C., Palmese, A., Paz-Chinchón, F., Plazas, A. A., Romer, A. K., Sánchez, C., Sanchez, E., Scarpine, V., Schubnell, M., Serrano, S., Smith, M., Soares-Santos, M., Suchyta, E., Tarle, G., To, C., Wilkinson, R. D., and DES Collaboration (2021). Machine Learning for Searching the Dark Energy Survey for Trans-Neptunian Objects. *PASP*, 133(1019):014501.

Henghes, B., Thiyagalingam, J., Pettitt, C., Hey, T., and Lahav, O. (2022). Deep learning methods for obtaining photometric redshift estimations from images. *MNRAS*, 512(2):1696–1709.

Henriques, B. M. B., White, S. D. M., Thomas, P. A., Angulo, R., Guo, Q., Lemson, G., Springel, V., and Overzier, R. (2015). Galaxy formation in the Planck cosmology - I. Matching the observed evolution of star formation rates, colours and stellar masses. *MNRAS*, 451(3):2663–2680.

Henry, J. P. and Lavery, R. J. (1987). Multiaperture Spectroscopy of Galaxies in Abell 370. *ApJ*, 323:473.

Hermit, S., Santiago, B. X., Lahav, O., Strauss, M. A., Davis, M., Dressler, A., and Huchra, J. P. (1996). The two-point correlation function and morphological segregation in the Optical Redshift Survey. *MNRAS*, 283(2):709–720.

Hernan, M. and Robins, J. (2023). *Causal Inference*. Chapman & Hall/CRC Monographs on Statistics & Applied Probab. Taylor & Francis.

Hernán, M. A. and Robins, J. M. (2006). Estimating causal effects from epidemiological data. *Journal of Epidemiology & Community Health*, 60(7):578–586.

Hernquist, L. (1992). Structure of Merger Remnants. I. Bulgeless Progenitors. *ApJ*, 400:460.

Hernquist, L. (1993). Structure of Merger Remnants. II. Progenitors with Rotating Bulges. *ApJ*, 409:548.

Hirano, K. and Imbens, G. W. (2004). The propensity score with continuous treatments. *Applied Bayesian modeling and causal inference from incomplete-data perspectives*, 226164:73–84.

Ho, T. K. (1995). Random decision forests. In *Proceedings of 3rd international conference on document analysis and recognition*, volume 1, pages 278–282. IEEE.

Hoaglin, D. C. and Mosteller, F. (2000). *Understanding Robust and Exploratory Data Analysis*. Wiley, New York, 1 edition.

Hogan, R., Fairbairn, M., and Seeburn, N. (2015). GAz: a genetic algorithm for photometric redshift estimation. *MNRAS*, 449(2):2040–2046.

Hogg, D. W., Blanton, M., Strateva, I., Bahcall, N. A., Brinkmann, J., Csabai, I., Doi, M., Fukugita, M., Hennessy, G., Ivezić, Ž., Knapp, G. R., Lamb, D. Q., Lupton, R., Munn, J. A., Nichol, R., Schlegel, D. J., Schneider, D. P., and York, D. G. (2002). The Luminosity Density of Red Galaxies. *AJ*, 124(2):646–651.

Hogg, D. W., Blanton, M. R., Brinchmann, J., Eisenstein, D. J., Schlegel, D. J., Gunn, J. E., McKay, T. A., Rix, H.-W., Bahcall, N. A., Brinkmann, J., and Meiksin, A. (2004). The Dependence on Environment of the Color-Magnitude Relation of Galaxies. *ApJ*, 601(1):L29–L32.

Hogg, D. W., Blanton, M. R., Eisenstein, D. J., Gunn, J. E., Schlegel, D. J., Zehavi, I., Bahcall, N. A., Brinkmann, J., Csabai, I., Schneider, D. P., et al. (2003). The overdensities of galaxy environments as a function of luminosity and color. *The Astrophysical Journal*, 585(1):L5.

Holland, P. W. (1986). Statistics and causal inference. *Journal of the American statistical Association*, 81(396):945–960.

Hollenbach, D. J. and Tielens, A. G. G. M. (1997). Dense Photodissociation Regions (PDRs). *ARA&A*, 35:179–216.

Holmberg, E. (1958). A photographic photometry of extragalactic nebulae. *Meddelanden fran Lunds Astronomiska Observatorium Serie II*, 136:1.

Hopkins, A. M., Connolly, A. J., Haarsma, D. B., and Cram, L. E. (2001). Toward a Resolution of the Discrepancy between Different Estimators of Star Formation Rate. *AJ*, 122(1):288–296.

Hopkins, P. F., Cox, T. J., Kereš, D., and Hernquist, L. (2008a). A Cosmological Framework for the Co-Evolution of Quasars, Supermassive Black Holes, and Elliptical Galaxies. II. Formation of Red Ellipticals. *ApJS*, 175(2):390–422.

Hopkins, P. F., Cox, T. J., Younger, J. D., and Hernquist, L. (2009). How do Disks Survive Mergers? *ApJ*, 691(2):1168–1201.

Hopkins, P. F. and Hernquist, L. (2009). A Characteristic Division Between the Fueling of Quasars and Seyferts: Five Simple Tests. *ApJ*, 694(1):599–609.

Hopkins, P. F., Hernquist, L., Cox, T. J., Di Matteo, T., Robertson, B., and Springel, V. (2006). A Unified, Merger-driven Model of the Origin of Starbursts, Quasars, the Cosmic X-Ray Background, Supermassive Black Holes, and Galaxy Spheroids. *ApJS*, 163(1):1–49.

Hopkins, P. F., Hernquist, L., Cox, T. J., and Kereš, D. (2008b). A Cosmological Framework for the Co-Evolution of Quasars, Supermassive Black Holes, and Elliptical Galaxies. I. Galaxy Mergers and Quasar Activity. *ApJS*, 175(2):356–389.

Hopkins, P. F., Kereš, D., Oñorbe, J., Faucher-Giguère, C.-A., Quataert, E., Murray, N., and Bullock, J. S. (2014). Galaxies on FIRE (Feedback In Realistic Environments): stellar feedback explains cosmologically inefficient star formation. *MNRAS*, 445(1):581–603.

Horvitz, D. G. and Thompson, D. J. (1952). A generalization of sampling without replacement from a finite universe. *Journal of the American statistical Association*, 47(260):663–685.

Hoyle, B. (2016). Measuring photometric redshifts using galaxy images and Deep Neural Networks. *Astron. Comput.*, 16:34–40.

Hoyle, F., Rojas, R. R., Vogeley, M. S., and Brinkmann, J. (2005). The Luminosity Function of Void Galaxies in the Sloan Digital Sky Survey. *ApJ*, 620(2):618–628.

Hu, W. (1999). Power Spectrum Tomography with Weak Lensing. *ApJ*, 522(1):L21–L24.

Hubble, E. (1929). A Relation between Distance and Radial Velocity among Extra-Galactic Nebulae. *Proceedings of the National Academy of Science*, 15(3):168–173.

Hubble, E. (1936). *The Realm of the Nebulæ*. Memorial lectures. Yale University Press.

Hubble, E. and Humason, M. L. (1931). The Velocity-Distance Relation among Extra-Galactic Nebulae. *ApJ*, 74:43.

Humason, M. L. (1936). The Apparent Radial Velocities of 100 Extra-Galactic Nebulae. *ApJ*, 83:10.

Hwang, H. S., Shin, J., and Song, H. (2019). Evolution of star formation rate-density relation over cosmic time in a simulated universe: the observed reversal reproduced. *MNRAS*, 489(1):339–348.

Irwin, J. A. (1995). Galaxies and Their Environments. *PASP*, 107:715.

Iyer, K. G., Gawiser, E., Faber, S. M., Ferguson, H. C., Kartaltepe, J., Koekemoer, A. M., Pacifici, C., and Somerville, R. S. (2019). Nonparametric Star Formation History Reconstruction with Gaussian Processes. I. Counting Major Episodes of Star Formation. *ApJ*, 879(2):116.

Jee, M. J., Tyson, J. A., Schneider, M. D., Wittman, D., Schmidt, S., and Hilbert, S. (2013). Cosmic Shear Results from the Deep Lens Survey. I. Joint Constraints on Ω_M and σ_8 with a Two-dimensional Analysis. *ApJ*, 765(1):74.

Ji, Z. and Giavalisco, M. (2022). Reconstructing the Assembly of Massive Galaxies. I. The Importance of the Progenitor Effect in the Observed Properties of Quiescent Galaxies at z $\approx$ 2. *ApJ*, 935(2):120.

Ji, Z. and Giavalisco, M. (2023). Reconstructing the Assembly of Massive Galaxies. II. Galaxies Develop Massive and Dense Stellar Cores as They Evolve and Head toward Quiescence at Cosmic Noon. *ApJ*, 943(1):54.

Jimenez, R., Panter, B., Heavens, A. F., and Verde, L. (2005). Baryonic conversion tree: the global assembly of stars and dark matter in galaxies from the Sloan Digital Sky Survey. *MNRAS*, 356(2):495–501.

Jivraj, S., Murray, E. T., Norman, P., and Nicholas, O. (2019). The impact of life course exposures to neighbourhood deprivation on health and well-being: a review

of the long-term neighbourhood effects literature. *European Journal of Public Health*, 30(5):922–928.

Johnson, B. D., Leja, J., Conroy, C., and Speagle, J. S. (2021). Stellar Population Inference with Prospector. *ApJS*, 254(2):22.

Jones, L. R., Ponman, T. J., and Forbes, D. A. (2000). Multiwavelength observations of an evolved galaxy group: an end-point of galaxy merging? *MNRAS*, 312(1):139–150.

Jones, L. R., Ponman, T. J., Horton, A., Babul, A., Ebeling, H., and Burke, D. J. (2003). The nature and space density of fossil groups of galaxies. *MNRAS*, 343(2):627–638.

Juneau, S., Glazebrook, K., Crampton, D., McCarthy, P. J., Savaglio, S., Abraham, R., Carlberg, R. G., Chen, H.-W., Le Borgne, D., Marzke, R. O., Roth, K., Jørgensen, I., Hook, I., and Murowinski, R. (2005). Cosmic Star Formation History and Its Dependence on Galaxy Stellar Mass. *ApJ*, 619(2):L135–L138.

Just, D. W., Zaritsky, D., Sand, D. J., Desai, V., and Rudnick, G. (2010). The Environmental Dependence of the Evolving S0 Fraction. *ApJ*, 711(1):192–200.

Kaddour, J., Lynch, A., Liu, Q., Kusner, M. J., and Silva, R. (2022). Causal Machine Learning: A Survey and Open Problems. *arXiv e-prints*, page arXiv:2206.15475.

Kam, C. D. and Palmer, C. L. (2008). Reconsidering the effects of education on political participation. *The Journal of Politics*, 70(3):612–631.

Kampakoglou, M. and Benson, A. J. (2007). Tidal mass loss from collisionless systems. *MNRAS*, 374(3):775–786.

Kampczyk, P., Lilly, S. J., Carollo, C. M., Scarlata, C., Feldmann, R., Koekemoer, A., Leauthaud, A., Sargent, M. T., Taniguchi, Y., and Capak, P. (2007). Simulating the Cosmos: The Fraction of Merging Galaxies at High Redshift. *ApJS*, 172(1):329–340.

Kang, X., Jing, Y. P., Mo, H. J., and Börner, G. (2005). Semianalytical Model of Galaxy Formation with High-Resolution N-Body Simulations. *ApJ*, 631(1):21–40.

Karimi, A.-H., Barthe, G., Schölkopf, B., and Valera, I. (2020). A survey of algorithmic recourse: definitions, formulations, solutions, and prospects. *arXiv e-prints*, page arXiv:2010.04050.

Kartaltepe, J. S., Sanders, D. B., Scoville, N. Z., Calzetti, D., Capak, P., Koekemoer, A., Mobasher, B., Murayama, T., Salvato, M., Sasaki, S. S., and Taniguchi, Y. (2007). Evolution of the Frequency of Luminous (¿=L^*_V) Close Galaxy Pairs at z ¡ 1.2 in the COSMOS Field. *ApJS*, 172(1):320–328.

Kauffmann, G., Colberg, J. M., Diaferio, A., and White, S. D. M. (1999). Clustering of galaxies in a hierarchical universe - I. Methods and results at z=0. *MNRAS*, 303(1):188–206.

Kauffmann, G., Heckman, T. M., Tremonti, C., Brinchmann, J., Charlot, S., White, S. D. M., Ridgway, S. E., Brinkmann, J., Fukugita, M., Hall, P. B., Ivezić, Ž., Richards, G. T., and Schneider, D. P. (2003a). The host galaxies of active galactic nuclei. *MNRAS*, 346(4):1055–1077.

Kauffmann, G., Heckman, T. M., White, S. D. M., Charlot, S., Tremonti, C., Peng, E. W., Seibert, M., Brinkmann, J., Nichol, R. C., SubbaRao, M., and York, D. (2003b). The dependence of star formation history and internal structure on stellar mass for 10^5 low-redshift galaxies. *MNRAS*, 341(1):54–69.

Kauffmann, G., White, S. D. M., and Guiderdoni, B. (1993). The formation and evolution of galaxies within merging dark matter haloes. *MNRAS*, 264:201–218.

Kauffmann, G., White, S. D. M., Heckman, T. M., Ménard, B., Brinchmann, J., Charlot, S., Tremonti, C., and Brinkmann, J. (2004). The environmental dependence of the relations between stellar mass, structure, star formation and nuclear activity in galaxies. *MNRAS*, 353(3):713–731.

Kawinwanichakij, L., Papovich, C., Quadri, R. F., Glazebrook, K., Kacprzak, G. G., Allen, R. J., Bell, E. F., Croton, D. J., Dekel, A., Ferguson, H. C., Forrest, B., Grogin, N. A., Guo, Y., Kocevski, D. D., Koekemoer, A. M., Labbé, I., Lucas, R. A., Nanayakkara, T., Spitler, L. R., Straatman, C. M. S., Tran, K.-V. H., Tomczak, A., and van Dokkum, P. (2017). Effect of Local Environment and Stellar Mass on Galaxy Quenching and Morphology at 0.5 ¡ z ¡ 2.0. *ApJ*, 847(2):134.

Kendall, M. G. (1938). A NEW MEASURE OF RANK CORRELATION. *Biometrika*, 30(1-2):81–93.

Kennicutt, Robert C., J. (1998). Star Formation in Galaxies Along the Hubble Sequence. *ARA&A*, 36:189–232.

Kennicutt, R. C. and Evans, N. J. (2012). Star Formation in the Milky Way and Nearby Galaxies. *ARA&A*, 50:531–608.

Kinney, A. L., Calzetti, D., Bohlin, R. C., McQuade, K., Storchi-Bergmann, T., and Schmitt, H. R. (1996). Template Ultraviolet to Near-Infrared Spectra of Star-forming Galaxies and Their Application to K-Corrections. *ApJ*, 467:38.

Kloek, T. and Van Dijk, H. K. (1978). Bayesian estimates of equation system parameters: an application of integration by monte carlo. *Econometrica: Journal of the Econometric Society*, pages 1–19.

Knobel, C., Lilly, S. J., Woo, J., and Kovač, K. (2015). Quenching of Star Formation in Sloan Digital Sky Survey Groups: Centrals, Satellites, and Galactic Conformity. *ApJ*, 800(1):24.

Kodama, T. and Bower, R. G. (2001). Reconstructing the history of star formation in rich cluster cores. *MNRAS*, 321(1):18–36.

Kodama, T., Smail, I., Nakata, F., Okamura, S., and Bower, R. G. (2001). The Transformation of Galaxies within the Large-Scale Structure around a z=0.41 Cluster. *ApJ*, 562(1):L9–L13.

Kodama, T., Yamada, T., Akiyama, M., Aoki, K., Doi, M., Furusawa, H., Fuse, T., Imanishi, M., Ishida, C., Iye, M., Kajisawa, M., Karoji, H., Kobayashi, N., Komiyama, Y., Kosugi, G., Maeda, Y., Miyazaki, S., Mizumoto, Y., Morokuma, T., Nakata, F., Noumaru, J., Ogasawara, R., Ouchi, M., Sasaki, T., Sekiguchi, K., Shimasaku, K., Simpson, C., Takata, T., Tanaka, I., Ueda, Y., Yasuda, N., and Yoshida, M. (2004). Down-sizing in galaxy formation at z~1 in the Subaru/XMM-Newton Deep Survey (SXDS). *MNRAS*, 350(3):1005–1014.

Koleva, M., Prugniel, P., Bouchard, A., and Wu, Y. (2009). ULySS: a full spectrum fitting package. *A&A*, 501(3):1269–1279.

Koo, D. C. (1985). Optical multicolors : a poor person's Z machine for galaxies. *AJ*, 90:418–440.

Kormendy, J. and Bender, R. (1996). A Proposed Revision of the Hubble Sequence for Elliptical Galaxies. *ApJ*, 464:L119.

Kormendy, J. and Ho, L. C. (2013). Coevolution (Or Not) of Supermassive Black Holes and Host Galaxies. *ARA&A*, 51(1):511–653.

Kormendy, J. and Kennicutt, Robert C., J. (2004). Secular Evolution and the Formation of Pseudobulges in Disk Galaxies. *ARA&A*, 42(1):603–683.

Kormendy, J. and Richstone, D. (1995). Inward Bound—The Search For Supermassive Black Holes In Galactic Nuclei. *ARA&A*, 33:581.

Kovač, K., Lilly, S. J., Knobel, C., Bschorr, T. J., Peng, Y., Carollo, C. M., Contini, T., Kneib, J. P., Le Févre, O., Mainieri, V., Renzini, A., Scodeggio, M., Zamorani, G., Bardelli, S., Bolzonella, M., Bongiorno, A., Caputi, K., Cucciati, O., de la Torre, S., de Ravel, L., Franzetti, P., Garilli, B., Iovino, A., Kampczyk, P., Lamareille, F., Le Borgne, J. F., Le Brun, V., Maier, C., Mignoli, M., Oesch, P., Pello, R., Montero, E. P., Presotto, V., Silverman, J., Tanaka, M., Tasca, L., Tresse, L., Vergani, D., Zucca, E., Aussel, H., Koekemoer, A. M., Le Floc'h, E., Moresco, M., and Pozzetti, L. (2014). zCOSMOS 20k: satellite galaxies are the main drivers of environmental effects in the galaxy population at least to z $\sim$ 0.7. *MNRAS*, 438(1):717–738.

Kriek, M., van Dokkum, P. G., Labbé, I., Franx, M., Illingworth, G. D., Marchesini, D., and Quadri, R. F. (2009). An Ultra-Deep Near-Infrared Spectrum of a Compact Quiescent Galaxy at z = 2.2. *ApJ*, 700(1):221–231.

Kroupa, P. (2001). On the variation of the initial mass function. *MNRAS*, 322(2):231–246.

Kroupa, P. and Boily, C. M. (2002). On the mass function of star clusters. *MNRAS*, 336(4):1188–1194.

Krumholz, M. R., McKee, C. F., and Klein, R. I. (2005). Stars Form By Gravitational Collapse, Not Competitive Accretion. *arXiv e-prints*, pages astro–ph/0510412.

Kuhn, M., Johnson, K., et al. (2013). *Applied predictive modeling*, volume 26. Springer.

Kullback, S. and Leibler, R. A. (1951). On information and sufficiency. *Ann. Math. Stat.*, 22(1):79–86.

Labbé, I., van Dokkum, P., Nelson, E., Bezanson, R., Suess, K. A., Leja, J., Brammer, G., Whitaker, K., Mathews, E., Stefanon, M., and Wang, B. (2023). A population of red candidate massive galaxies 600 Myr after the Big Bang. *Nature*, 616(7956):266–269.

Lacey, C. and Silk, J. (1991). Tidally Triggered Galaxy Formation. I. Evolution of the Galaxy Luminosity Function. *ApJ*, 381:14.

Lahav, O., Calder, L., Mayers, J., and Frieman, J. (2020). *The Dark Energy Survey: The Story of a Cosmological Experiment*. World Scientific Press, Singapore.

Lahav, O., Naim, A., Buta, R. J., Corwin, H. G., de Vaucouleurs, G., Dressler, A., Huchra, J. P., van den Bergh, S., Raychaudhury, S., Sodre, L., J., and Storrie-Lombardi, M. C. (1995). Galaxies, Human Eyes, and Artificial Neural Networks. *Science*, 267(5199):859–862.

Laigle, C., McCracken, H. J., Ilbert, O., Hsieh, B. C., Davidzon, I., Capak, P., Hasinger, G., Silverman, J. D., Pichon, C., Coupon, J., Aussel, H., Le Borgne, D., Caputi, K., Cassata, P., Chang, Y. Y., Civano, F., Dunlop, J., Fynbo, J., Kartaltepe, J. S., Koekemoer, A., Le Fèvre, O., Le Floc'h, E., Leauthaud, A., Lilly, S., Lin, L., Marchesi, S., Milvang-Jensen, B., Salvato, M., Sanders, D. B., Scoville, N., Smolcic, V., Stockmann, M., Taniguchi, Y., Tasca, L., Toft, S., Vaccari, M., and Zabl, J. (2016). The COSMOS2015 Catalog: Exploring the 1 < z < 6 Universe with Half a Million Galaxies. *ApJS*, 224(2):24.

Larson, R. B. (1974). Effects of supernovae on the early evolution of galaxies. *MNRAS*, 169:229–246.

Larson, R. B. and Tinsley, B. M. (1978). Star formation rates in normal and peculiar galaxies. *ApJ*, 219:46–59.

Larson, R. B., Tinsley, B. M., and Caldwell, C. N. (1980). The evolution of disk galaxies and the origin of S0 galaxies. *ApJ*, 237:692–707.

Laureijs, R., Amiaux, J., Arduini, S., Augueres, J. L., Brinchmann, J., Cole, R., Cropper, M., Dabin, C., Duvet, L., Ealet, A., Garilli, B., Gondoin, P., Guzzo, L., Hoar, J., Hoekstra, H., Holmes, R., Kitching, T., Maciaszek, T., Mellier, Y., Pasian, F., Percival, W., Rhodes, J., Saavedra Criado, G., Sauvage, M., Scaramella, R., Valenziano, L., Warren, S., Bender, R., Castander, F., Cimatti, A., Le Fèvre, O., Kurki-Suonio, H., Levi, M., Lilje, P., Meylan, G., Nichol, R., Pedersen, K., Popa, V., Rebolo Lopez, R., Rix, H. W., Rottgering, H., Zeilinger, W., Grupp, F., Hudelot, P., Massey, R., Meneghetti, M., Miller, L., Paltani, S., Paulin-Henriksson, S., Pires, S., Saxton, C., Schrabback, T., Seidel, G., Walsh, J., Aghanim, N., Amendola, L., Bartlett, J., Baccigalupi, C., Beaulieu, J. P., Benabed, K., Cuby, J. G., Elbaz, D., Fosalba, P., Gavazzi, G., Helmi, A., Hook, I., Irwin, M., Kneib, J. P., Kunz, M., Mannucci, F., Moscardini, L., Tao, C., Teyssier, R., Weller, J., Zamorani, G., Zapatero Osorio, M. R., Boulade, O., Foumond, J. J., Di Giorgio, A., Guttridge, P., James, A., Kemp, M., Martignac, J., Spencer, A., Walton, D., Blümchen, T., Bonoli, C., Bortoletto, F., Cerna, C., Corcione, L., Fabron, C., Jahnke, K., Ligori, S., Madrid, F., Martin, L., Morgante, G., Pamplona, T., Prieto, E., Riva, M., Toledo, R., Trifoglio, M., Zerbi, F., Abdalla, F., Douspis, M., Grenet, C., Borgani, S., Bouwens, R., Courbin, F., Delouis, J. M., Dubath, P., Fontana, A., Frailis, M., Grazian, A., Koppenhöfer, J., Mansutti, O., Melchior, M., Mignoli, M., Mohr, J., Neissner, C., Noddle, K., Poncet, M., Scodeggio, M., Serrano, S., Shane, N., Starck, J. L., Surace, C., Taylor, A., Verdoes-Kleijn, G., Vuerli, C., Williams, O. R., Zacchei, A., Altieri, B., Escudero Sanz, I., Kohley, R., Oosterbroek, T., Astier, P., Bacon, D., Bardelli, S., Baugh, C., Bellagamba, F., Benoist, C., Bianchi, D., Biviano, A., Branchini, E., Carbone, C., Cardone, V., Clements, D., Colombi, S., Conselice, C., Cresci, G., Deacon, N., Dunlop, J., Fedeli, C., Fontanot, F., Franzetti, P., Giocoli, C., Garcia-Bellido, J., Gow, J., Heavens, A., Hewett, P., Heymans, C., Holland, A., Huang, Z., Ilbert, O., Joachimi, B., Jennins, E., Kerins, E., Kiessling, A., Kirk, D., Kotak, R., Krause, O., Lahav, O., van Leeuwen, F., Lesgourgues, J., Lombardi, M., Magliocchetti, M., Maguire, K., Majerotto, E., Maoli, R., Marulli, F., Maurogordato, S., McCracken, H., McLure, R., Melchiorri,

A., Merson, A., Moresco, M., Nonino, M., Norberg, P., Peacock, J., Pello, R., Penny, M., Pettorino, V., Di Porto, C., Pozzetti, L., Quercellini, C., Radovich, M., Rassat, A., Roche, N., Ronayette, S., Rossetti, E., Sartoris, B., Schneider, P., Semboloni, E., Serjeant, S., Simpson, F., Skordis, C., Smadja, G., Smartt, S., Spano, P., Spiro, S., Sullivan, M., Tilquin, A., Trotta, R., Verde, L., Wang, Y., Williger, G., Zhao, G., Zoubian, J., and Zucca, E. (2011). Euclid Definition Study Report. *arXiv e-prints*, page arXiv:1110.3193.

Le Borgne, D., Rocca-Volmerange, B., Prugniel, P., Lançon, A., Fioc, M., and Soubiran, C. (2004). Evolutionary synthesis of galaxies at high spectral resolution with the code PEGASE-HR. Metallicity and age tracers. *A&A*, 425:881–897.

Le Borgne, J. F., Bruzual, G., Pelló, R., Lançon, A., Rocca-Volmerange, B., Sanahuja, B., Schaerer, D., Soubiran, C., and Vílchez-Gómez, R. (2003). STELIB: A library of stellar spectra at R ~2000. *A&A*, 402:433–442.

Le Fèvre, O., Abraham, R., Lilly, S. J., Ellis, R. S., Brinchmann, J., Schade, D., Tresse, L., Colless, M., Crampton, D., Glazebrook, K., Hammer, F., and Broadhurst, T. (2000). Hubble Space Telescope imaging of the CFRS and LDSS redshift surveys - IV. Influence of mergers in the evolution of faint field galaxies from z~1. *MNRAS*, 311(3):565–575.

Lee, B., Giavalisco, M., Whitaker, K., Williams, C. C., Ferguson, H. C., Acquaviva, V., Koekemoer, A. M., Straughn, A. N., Guo, Y., Kartaltepe, J. S., Lotz, J., Pacifici, C., Croton, D. J., Somerville, R. S., and Lu, Y. (2018). The Intrinsic Characteristics of Galaxies on the SFR-M $_*$ Plane at 1.2 ¡ z ¡ 4: I. The Correlation between Stellar Age, Central Density, and Position Relative to the Main Sequence. *ApJ*, 853(2):131.

Lee, B. K., Lessler, J., and Stuart, E. A. (2010). Improving propensity score weighting using machine learning. *Statistics in medicine*, 29(3):337–346.

Lee, N., Sanders, D. B., Casey, C. M., Toft, S., Scoville, N. Z., Hung, C.-L., Le Floc'h, E., Ilbert, O., Zahid, H. J., Aussel, H., Capak, P., Kartaltepe, J. S., Kewley, L. J., Li, Y., Schawinski, K., Sheth, K., and Xiao, Q. (2015). A Turnover in the Galaxy

Main Sequence of Star Formation at M $_*$ ~10^{10} M $_\odot$ for Redshifts z ¡ 1.3. *ApJ*, 801(2):80.

Lee, S.-K., Idzi, R., Ferguson, H. C., Somerville, R. S., Wiklind, T., and Giavalisco, M. (2009). Biases and Uncertainties in Physical Parameter Estimates of Lyman Break Galaxies from Broadband Photometry. *ApJS*, 184(1):100–132.

Leitherer, C., Schaerer, D., Goldader, J. D., Delgado, R. M. G., Robert, C., Kune, D. F., de Mello, D. F., Devost, D., and Heckman, T. M. (1999). Starburst99: Synthesis Models for Galaxies with Active Star Formation. *ApJS*, 123(1):3–40.

Leja, J., Johnson, B. D., Conroy, C., van Dokkum, P. G., and Byler, N. (2017). Deriving Physical Properties from Broadband Photometry with Prospector: Description of the Model and a Demonstration of its Accuracy Using 129 Galaxies in the Local Universe. *ApJ*, 837(2):170.

Lejeune, T., Cuisinier, F., and Buser, R. (1997). Standard stellar library for evolutionary synthesis. I. Calibration of theoretical spectra. *A&AS*, 125:229–246.

Lejeune, T., Cuisinier, F., and Buser, R. (1998). A standard stellar library for evolutionary synthesis. II. The M dwarf extension. *A&AS*, 130:65–75.

Lejeune, T. and Schaerer, D. (2001). Database of Geneva stellar evolution tracks and isochrones for $(UBV)_J(RI)_C$ JHKLL'M, HST-WFPC2, Geneva and Washington photometric systems. *A&A*, 366:538–546.

Lemaître, G. (1927). Un Univers homogène de masse constante et de rayon croissant rendant compte de la vitesse radiale des nébuleuses extra-galactiques. *Annales de la Société Scientifique de Bruxelles*, 47:49–59.

Lemaux, B. C., Cucciati, O., Le Fèvre, O., Zamorani, G., Lubin, L. M., Hathi, N., Ilbert, O., Pelliccia, D., Amorín, R., Bardelli, S., Cassata, P., Gal, R. R., Garilli, B., Guaita, L., Giavalisco, M., Hung, D., Koekemoer, A., Maccagni, D., Pentericci, L., Ribeiro, B., Schaerer, D., Shah, E., Shen, L., Staab, P., Talia, M., Thomas, R., Tomczak, A. R., Tresse, L., Vanzella, E., Vergani, D., and Zucca, E. (2022). The VIMOS Ultra Deep Survey: The reversal of the star-formation rate − density relation at 2 ¡ z ¡ 5. *A&A*, 662:A33.

Lewis, I., Balogh, M., De Propris, R., Couch, W., Bower, R., Offer, A., Bland-Hawthorn, J., Baldry, I. K., Baugh, C., Bridges, T., Cannon, R., Cole, S., Colless, M., Collins, C., Cross, N., Dalton, G., Driver, S. P., Efstathiou, G., Ellis, R. S., Frenk, C. S., Glazebrook, K., Hawkins, E., Jackson, C., Lahav, O., Lumsden, S., Maddox, S., Madgwick, D., Norberg, P., Peacock, J. A., Percival, W., Peterson, B. A., Sutherland, W., and Taylor, K. (2002). The 2dF Galaxy Redshift Survey: the environmental dependence of galaxy star formation rates near clusters. *MNRAS*, 334(3):673–683.

Li, S., Okereke, O. I., Chang, S.-C., Kawachi, I., and VanderWeele, T. J. (2016). Religious service attendance and lower depression among women—a prospective cohort study. *Annals of Behavioral Medicine*, 50(6):876–884.

Lilly, S. J., Le Fèvre, O., Renzini, A., Zamorani, G., Scodeggio, M., Contini, T., Carollo, C. M., Hasinger, G., Kneib, J. P., Iovino, A., Le Brun, V., Maier, C., Mainieri, V., Mignoli, M., Silverman, J., Tasca, L. A. M., Bolzonella, M., Bongiorno, A., Bottini, D., Capak, P., Caputi, K., Cimatti, A., Cucciati, O., Daddi, E., Feldmann, R., Franzetti, P., Garilli, B., Guzzo, L., Ilbert, O., Kampczyk, P., Kovac, K., Lamareille, F., Leauthaud, A., Le Borgne, J. F., McCracken, H. J., Marinoni, C., Pello, R., Ricciardelli, E., Scarlata, C., Vergani, D., Sanders, D. B., Schinnerer, E., Scoville, N., Taniguchi, Y., Arnouts, S., Aussel, H., Bardelli, S., Brusa, M., Cappi, A., Ciliegi, P., Finoguenov, A., Foucaud, S., Franceschini, A., Halliday, C., Impey, C., Knobel, C., Koekemoer, A., Kurk, J., Maccagni, D., Maddox, S., Marano, B., Marconi, G., Meneux, B., Mobasher, B., Moreau, C., Peacock, J. A., Porciani, C., Pozzetti, L., Scaramella, R., Schiminovich, D., Shopbell, P., Smail, I., Thompson, D., Tresse, L., Vettolani, G., Zanichelli, A., and Zucca, E. (2007). zCOSMOS: A Large VLT/VIMOS Redshift Survey Covering 0 ¡ z ¡ 3 in the COSMOS Field. *ApJS*, 172(1):70–85.

Lim, B. (2018). Forecasting treatment responses over time using recurrent marginal structural networks. *Advances in neural information processing systems*, 31.

Lin, L., Jian, H.-Y., Foucaud, S., Norberg, P., Bower, R. G., Cole, S., Arnalte-Mur, P., Chen, C.-W., Coupon, J., Hsieh, B.-C., Heinis, S., Phleps, S., Chen, W.-P., Lee, C.-H., Burgett, W., Chambers, K. C., Denneau, L., Draper, P., Flewelling,

H., Hodapp, K. W., Huber, M. E., Kaiser, N., Kudritzki, R. P., Magnier, E. A., Metcalfe, N., Price, P. A., Tonry, J. L., Wainscoat, R. J., and Waters, C. (2014). The Pan-STARRS1 Medium-Deep Survey: The Role of Galaxy Group Environment in the Star Formation Rate versus Stellar Mass Relation and Quiescent Fraction out to z ~0.8. *ApJ*, 782(1):33.

Linde, A. D. (1982). A new inflationary universe scenario: A possible solution of the horizon, flatness, homogeneity, isotropy and primordial monopole problems. *Physics Letters B*, 108(6):389–393.

Lipton, Z. C. (2016). The Mythos of Model Interpretability. *arXiv e-prints*, page arXiv:1606.03490.

Lochner, M., McEwen, J. D., Peiris, H. V., Lahav, O., and Winter, M. K. (2016). Photometric Supernova Classification with Machine Learning. *ApJS*, 225(2):31.

Loh, E. D. and Spillar, E. J. (1986). Photometric Redshifts of Galaxies. *ApJ*, 303:154.

Lotz, J. M., Jonsson, P., Cox, T. J., Croton, D., Primack, J. R., Somerville, R. S., and Stewart, K. (2011). The Major and Minor Galaxy Merger Rates at z ¡ 1.5. *ApJ*, 742(2):103.

Lovell, C. C., Harrison, I., Harikane, Y., Tacchella, S., and Wilkins, S. M. (2023). Extreme value statistics of the halo and stellar mass distributions at high redshift: are JWST results in tension with ΛCDM? *MNRAS*, 518(2):2511–2520.

LSST Science Collaboration, Abell, P. A., Allison, J., Anderson, S. F., Andrew, J. R., Angel, J. R. P., Armus, L., Arnett, D., Asztalos, S. J., Axelrod, T. S., Bailey, S., Ballantyne, D. R., Bankert, J. R., Barkhouse, W. A., Barr, J. D., Barrientos, L. F., Barth, A. J., Bartlett, J. G., Becker, A. C., Becla, J., Beers, T. C., Bernstein, J. P., Biswas, R., Blanton, M. R., Bloom, J. S., Bochanski, J. J., Boeshaar, P., Borne, K. D., Bradac, M., Brandt, W. N., Bridge, C. R., Brown, M. E., Brunner, R. J., Bullock, J. S., Burgasser, A. J., Burge, J. H., Burke, D. L., Cargile, P. A., Chand rasekharan, S., Chartas, G., Chesley, S. R., Chu, Y.-H., Cinabro, D., Claire, M. W., Claver, C. F., Clowe, D., Connolly, A. J., Cook, K. H., Cooke, J., Cooray, A., Covey, K. R., Culliton, C. S., de Jong, R., de Vries, W. H., Debattista, V. P., Delgado, F., Dell'Antonio, I. P., Dhital, S., Di Stefano, R., Dickinson, M., Dilday,

B., Djorgovski, S. G., Dobler, G., Donalek, C., Dubois-Felsmann, G., Durech, J., Eliasdottir, A., Eracleous, M., Eyer, L., Falco, E. E., Fan, X., Fassnacht, C. D., Ferguson, H. C., Fernandez, Y. R., Fields, B. D., Finkbeiner, D., Figueroa, E. E., Fox, D. B., Francke, H., Frank, J. S., Frieman, J., Fromenteau, S., Furqan, M., Galaz, G., Gal-Yam, A., Garnavich, P., Gawiser, E., Geary, J., Gee, P., Gibson, R. R., Gilmore, K., Grace, E. A., Green, R. F., Gressler, W. J., Grillmair, C. J., Habib, S., Haggerty, J. S., Hamuy, M., Harris, A. W., Hawley, S. L., Heavens, A. F., Hebb, L., Henry, T. J., Hileman, E., Hilton, E. J., Hoadley, K., Holberg, J. B., Holman, M. J., Howell, S. B., Infante, L., Ivezic, Z., Jacoby, S. H., Jain, B., R, Jedicke, Jee, M. J., Garrett Jernigan, J., Jha, S. W., Johnston, K. V., Jones, R. L., Juric, M., Kaasalainen, M., Styliani, Kafka, Kahn, S. M., Kaib, N. A., Kalirai, J., Kantor, J., Kasliwal, M. M., Keeton, C. R., Kessler, R., Knezevic, Z., Kowalski, A., Krabbendam, V. L., Krughoff, K. S., Kulkarni, S., Kuhlman, S., Lacy, M., Lepine, S., Liang, M., Lien, A., Lira, P., Long, K. S., Lorenz, S., Lotz, J. M., Lupton, R. H., Lutz, J., Macri, L. M., Mahabal, A. A., Mandelbaum, R., Marshall, P., May, M., McGehee, P. M., Meadows, B. T., Meert, A., Milani, A., Miller, C. J., Miller, M., Mills, D., Minniti, D., Monet, D., Mukadam, A. S., Nakar, E., Neill, D. R., Newman, J. A., Nikolaev, S., Nordby, M., O'Connor, P., Oguri, M., Oliver, J., Olivier, S. S., Olsen, J. K., Olsen, K., Olszewski, E. W., Oluseyi, H., Padilla, N. D., Parker, A., Pepper, J., Peterson, J. R., Petry, C., Pinto, P. A., Pizagno, J. L., Popescu, B., Prsa, A., Radcka, V., Raddick, M. J., Rasmussen, A., Rau, A., Rho, J., Rhoads, J. E., Richards, G. T., Ridgway, S. T., Robertson, B. E., Roskar, R., Saha, A., Sarajedini, A., Scannapieco, E., Schalk, T., Schindler, R., Schmidt, S., Schmidt, S., Schneider, D. P., Schumacher, G., Scranton, R., Sebag, J., Seppala, L. G., Shemmer, O., Simon, J. D., Sivertz, M., Smith, H. A., Allyn Smith, J., Smith, N., Spitz, A. H., Stanford, A., Stassun, K. G., Strader, J., Strauss, M. A., Stubbs, C. W., Sweeney, D. W., Szalay, A., Szkody, P., Takada, M., Thorman, P., Trilling, D. E., Trimble, V., Tyson, A., Van Berg, R., Vand en Berk, D., VanderPlas, J., Verde, L., Vrsnak, B., Walkowicz, L. M., Wand elt, B. D., Wang, S., Wang, Y., Warner, M., Wechsler, R. H., West, A. A., Wiecha, O., Williams, B. F., Willman, B., Wittman, D., Wolff, S. C., Wood-Vasey, W. M., Wozniak, P., Young, P., Zentner, A., and Zhan, H. (2009). LSST Science Book,

Version 2.0. *arXiv e-prints*, page arXiv:0912.0201.

Lu, Y., Mo, H. J., Weinberg, M. D., and Katz, N. (2011). A Bayesian approach to the semi-analytic model of galaxy formation: methodology. *MNRAS*, 416(3):1949–1964.

Lubin, L. M. (1996). The Palomar Distant Cluster Survey. III. The Colors of the Cluster Galaxy. *AJ*, 112:23.

Lupton, R. H., Gunn, J. E., and Szalay, A. S. (1999). A Modified Magnitude System that Produces Well-Behaved Magnitudes, Colors, and Errors Even for Low Signal-to-Noise Ratio Measurements. *AJ*, 118(3):1406–1410.

MacArthur, L. A., González, J. J., and Courteau, S. (2009). Stellar population and kinematic profiles in spiral bulges and discs: population synthesis of integrated spectra. *MNRAS*, 395(1):28–63.

Maeder, A. and Meynet, G. (1988). Tables of evolutionary star modles from 0.85 to 120 solar mass with overshooting and mass loss. *A&AS*, 76:411–425.

Magorrian, J., Tremaine, S., Richstone, D., Bender, R., Bower, G., Dressler, A., Faber, S. M., Gebhardt, K., Green, R., Grillmair, C., Kormendy, J., and Lauer, T. (1998). The Demography of Massive Dark Objects in Galaxy Centers. *AJ*, 115(6):2285–2305.

Maltby, D. T., Almaini, O., Wild, V., Hatch, N. A., Hartley, W. G., Simpson, C., Rowlands, K., and Socolovsky, M. (2018). The structure of post-starburst galaxies at 0.5 ¡ z ¡ 2: evidence for two distinct quenching routes at different epochs. *MNRAS*, 480(1):381–401.

Mandelbaum, R., Seljak, U., Hirata, C. M., Bardelli, S., Bolzonella, M., Bongiorno, A., Carollo, M., Contini, T., Cunha, C. E., Garilli, B., Iovino, A., Kampczyk, P., Kneib, J. P., Knobel, C., Koo, D. C., Lamareille, F., Le Fèvre, O., Le Borgne, J. F., Lilly, S. J., Maier, C., Mainieri, V., Mignoli, M., Newman, J. A., Oesch, P. A., Perez-Montero, E., Ricciardelli, E., Scodeggio, M., Silverman, J., and Tasca, L. (2008). Precision photometric redshift calibration for galaxy-galaxy weak lensing. *MNRAS*, 386(2):781–806.

Mannucci, F., Basile, F., Poggianti, B. M., Cimatti, A., Daddi, E., Pozzetti, L., and Vanzi, L. (2001). Near-infrared template spectra of normal galaxies: k-corrections, galaxy models and stellar populations. *MNRAS*, 326(2):745–758.

Mansournia, M. A., Danaei, G., Forouzanfar, M. H., Mahmoodi, M., Jamali, M., Mansournia, N., and Mohammad, K. (2012). Effect of physical activity on functional performance and knee pain in patients with osteoarthritis: analysis with marginal structural models. *Epidemiology*, pages 631–640.

Maraston, C. (1998). Evolutionary synthesis of stellar populations: a modular tool. *MNRAS*, 300(3):872–892.

Maraston, C. (2005). Evolutionary population synthesis: models, analysis of the ingredients and application to high-z galaxies. *MNRAS*, 362(3):799–825.

Maraston, C., Pforr, J., Renzini, A., Daddi, E., Dickinson, M., Cimatti, A., and Tonini, C. (2010). Star formation rates and masses of z ~2 galaxies from multicolour photometry. *MNRAS*, 407(2):830–845.

Margoniner, V. E. and de Carvalho, R. R. (2000). Photometric Properties of 48 Clusters of Galaxies. I. The Butcher-Oemler Effect. *AJ*, 119(4):1562–1578.

Margoniner, V. E., de Carvalho, R. R., Gal, R. R., and Djorgovski, S. G. (2001). The Butcher-Oemler Effect in 295 Clusters: Strong Redshift Evolution and Cluster Richness Dependence. *ApJ*, 548(2):L143–L146.

Marigo, P. and Girardi, L. (2007). Evolution of asymptotic giant branch stars. I. Updated synthetic TP-AGB models and their basic calibration. *A&A*, 469(1):239–263.

Marigo, P., Girardi, L., Bressan, A., Groenewegen, M. A. T., Silva, L., and Granato, G. L. (2008). Evolution of asymptotic giant branch stars. II. Optical to far-infrared isochrones with improved TP-AGB models. *A&A*, 482(3):883–905.

Marinacci, F., Vogelsberger, M., Pakmor, R., Torrey, P., Springel, V., Hernquist, L., Nelson, D., Weinberger, R., Pillepich, A., Naiman, J., and Genel, S. (2018). First results from the IllustrisTNG simulations: radio haloes and magnetic fields. *MNRAS*, 480(4):5113–5139.

Martin, C. L. (1999). Properties of Galactic Outflows: Measurements of the Feedback from Star Formation. *ApJ*, 513(1):156–160.

Martin, D. C., Wyder, T. K., Schiminovich, D., Barlow, T. A., Forster, K., Friedman, P. G., Morrissey, P., Neff, S. G., Seibert, M., Small, T., Welsh, B. Y., Bianchi, L., Donas, J., Heckman, T. M., Lee, Y.-W., Madore, B. F., Milliard, B., Rich, R. M., Szalay, A. S., and Yi, S. K. (2007). The UV-Optical Galaxy Color-Magnitude Diagram. III. Constraints on Evolution from the Blue to the Red Sequence. *ApJS*, 173(2):342–356.

Martínez, H. J. and Muriel, H. (2006). Groups of galaxies: relationship between environment and galaxy properties. *MNRAS*, 370(2):1003–1007.

Massey, R., Kitching, T., and Richard, J. (2010). The dark matter of gravitational lensing. *Reports on Progress in Physics*, 73(8):086901.

Masters, K. L., Mosleh, M., Romer, A. K., Nichol, R. C., Bamford, S. P., Schawinski, K., Lintott, C. J., Andreescu, D., Campbell, H. C., Crowcroft, B., Doyle, I., Edmondson, E. M., Murray, P., Raddick, M. J., Slosar, A., Szalay, A. S., and Vandenberg, J. (2010). Galaxy Zoo: passive red spirals. *MNRAS*, 405(2):783–799.

Mastropietro, C., Moore, B., Mayer, L., Debattista, V. P., Piffaretti, R., and Stadel, J. (2005). Morphological evolution of discs in clusters. *MNRAS*, 364(2):607–619.

Maulbetsch, C., Avila-Reese, V., Colín, P., Gottlöber, S., Khalatyan, A., and Steinmetz, M. (2007). The Dependence of the Mass Assembly History of Cold Dark Matter Halos on Environment. *ApJ*, 654(1):53–65.

McCaffrey, D. F., Ridgeway, G., and Morral, A. R. (2004). Propensity score estimation with boosted regression for evaluating causal effects in observational studies. *Psychological methods*, 9(4):403.

McGaugh, S. S. and de Blok, W. J. G. (1997). Gas Mass Fractions and the Evolution of Spiral Galaxies. *ApJ*, 481(2):689–702.

McGee, S. L., Balogh, M. L., Wilman, D. J., Bower, R. G., Mulchaey, J. S., Parker, L. C., and Oemler, A. (2011). The Dawn of the Red: star formation histories of group galaxies over the past 5 billion years. *MNRAS*, 413(2):996–1012.

McGibbon, R. J. and Khochfar, S. (2022). Multi-epoch machine learning 1: Unravelling nature versus nurture for galaxy formation. *MNRAS*, 513(4):5423–5437.

Mehrabi, N., Morstatter, F., Saxena, N., Lerman, K., and Galstyan, A. (2019). A Survey on Bias and Fairness in Machine Learning. *arXiv e-prints*, page arXiv:1908.09635.

Mihos, J. C. and Hernquist, L. (1994). Ultraluminous Starbursts in Major Mergers. *ApJ*, 431:L9.

Mihos, J. C. and Hernquist, L. (1996). Gasdynamics and Starbursts in Major Mergers. *ApJ*, 464:641.

Miller, T. (2017). Explanation in Artificial Intelligence: Insights from the Social Sciences. *arXiv e-prints*, page arXiv:1706.07269.

Mo, H., van den Bosch, F., and White, S. (2010). *Galaxy Formation and Evolution*. Galaxy Formation and Evolution. Cambridge University Press.

Mo, H. J., Mao, S., and White, S. D. M. (1998). The formation of galactic discs. *MNRAS*, 295(2):319–336.

Mo, H. J., Yang, X., van den Bosch, F. C., and Jing, Y. P. (2004). The dependence of the galaxy luminosity function on large-scale environment. *MNRAS*, 349(1):205–212.

Moore, B., Katz, N., Lake, G., Dressler, A., and Oemler, A. (1996). Galaxy harassment and the evolution of clusters of galaxies. *Nature*, 379(6566):613–616.

Moore, B., Lake, G., and Katz, N. (1998). Morphological Transformation from Galaxy Harassment. *ApJ*, 495(1):139–151.

Moore, B., Lake, G., Quinn, T., and Stadel, J. (1999). On the survival and destruction of spiral galaxies in clusters. *MNRAS*, 304(3):465–474.

Moraffah, R., Sheth, P., Karami, M., Bhattacharya, A., Wang, Q., Tahir, A., Raglin, A., and Liu, H. (2021). Causal Inference for Time series Analysis: Problems, Methods and Evaluation. *arXiv e-prints*, page arXiv:2102.05829.

Morgan, W. W. (1961). The classification of clusters of galaxies. *Proceedings of the National Academy of Sciences*, 47(7):905–906.

Mortimer, K. M., Neugebauer, R., Van Der Laan, M., and Tager, I. B. (2005). An application of model-fitting procedures for marginal structural models. *American Journal of Epidemiology*, 162(4):382–388.

Mortlock, A., Conselice, C. J., Bluck, A. F. L., Bauer, A. E., Grützbauch, R., Buitrago, F., and Ownsworth, J. (2011). A deep probe of the galaxy stellar mass functions at z$\sim$ 1-3 with the GOODS NICMOS Survey. *MNRAS*, 413(4):2845–2859.

Mortlock, A., Conselice, C. J., Hartley, W. G., Duncan, K., Lani, C., Ownsworth, J. R., Almaini, O., Wel, A. v. d., Huang, K.-H., Ashby, M. L. N., Willner, S. P., Fontana, A., Dekel, A., Koekemoer, A. M., Ferguson, H. C., Faber, S. M., Grogin, N. A., and Kocevski, D. D. (2015). Deconstructing the galaxy stellar mass function with UKIDSS and CANDELS: the impact of colour, structure and environment. *MNRAS*, 447(1):2–24.

Mucesh, S., Hartley, W. G., Palmese, A., Lahav, O., Whiteway, L., Bluck, A. F. L., Alarcon, A., Amon, A., Bechtol, K., Bernstein, G. M., Carnero Rosell, A., Carrasco Kind, M., Choi, A., Eckert, K., Everett, S., Gruen, D., Gruendl, R. A., Harrison, I., Huff, E. M., Kuropatkin, N., Sevilla-Noarbe, I., Sheldon, E., Yanny, B., Aguena, M., Allam, S., Bacon, D., Bertin, E., Bhargava, S., Brooks, D., Carretero, J., Castander, F. J., Conselice, C., Costanzi, M., Crocce, M., da Costa, L. N., Pereira, M. E. S., De Vicente, J., Desai, S., Diehl, H. T., Drlica-Wagner, A., Evrard, A. E., Ferrero, I., Flaugher, B., Fosalba, P., Frieman, J., García-Bellido, J., Gaztanaga, E., Gerdes, D. W., Gschwend, J., Gutierrez, G., Hinton, S. R., Hollowood, D. L., Honscheid, K., James, D. J., Kuehn, K., Lima, M., Lin, H., Maia, M. A. G., Melchior, P., Menanteau, F., Miquel, R., Morgan, R., Paz-Chinchón, F., Plazas, A. A., Sanchez, E., Scarpine, V., Schubnell, M., Serrano, S., Smith, M., Suchyta, E., Tarle, G., Thomas, D., To, C., Varga, T. N., Wilkinson, R. D., and DES Collaboration (2021). A machine learning approach to galaxy properties: joint redshift-stellar mass probability distributions with Random Forest. *MNRAS*, 502(2):2770–2786.

Muldrew, S. I., Croton, D. J., Skibba, R. A., Pearce, F. R., Ann, H. B., Baldry, I. K., Brough, S., Choi, Y.-Y., Conselice, C. J., Cowan, N. B., Gallazzi, A., Gray, M. E., Grützbauch, R., Li, I. H., Park, C., Pilipenko, S. V., Podgorzec, B. J., Robotham, A. S. G., Wilman, D. J., Yang, X., Zhang, Y., and Zibetti, S. (2012). Measures of galaxy environment - I. What is 'environment'? *MNRAS*, 419(3):2670–2682.

Muzzin, A., Marchesini, D., van Dokkum, P. G., Labbé, I., Kriek, M., and Franx, M. (2009). A Near-Infrared Spectroscopic Survey of K-Selected Galaxies at z˜2.3: Comparison of Stellar Population Synthesis Codes and Constraints from the Rest-Frame NIR. *ApJ*, 701(2):1839–1864.

Muzzin, A., Wilson, G., Yee, H. K. C., Gilbank, D., Hoekstra, H., Demarco, R., Balogh, M., van Dokkum, P., Franx, M., Ellingson, E., Hicks, A., Nantais, J., Noble, A., Lacy, M., Lidman, C., Rettura, A., Surace, J., and Webb, T. (2012). The Gemini Cluster Astrophysics Spectroscopic Survey (GCLASS): The Role of Environment and Self-regulation in Galaxy Evolution at z ˜1. *ApJ*, 746(2):188.

Myers, A. D., White, M., and Ball, N. M. (2009). Incorporating photometric redshift probability density information into real-space clustering measurements. *MNRAS*, 399(4):2279–2287.

Naidu, R. P., Oesch, P. A., van Dokkum, P., Nelson, E. J., Suess, K. A., Brammer, G., Whitaker, K. E., Illingworth, G., Bouwens, R., Tacchella, S., Matthee, J., Allen, N., Bezanson, R., Conroy, C., Labbe, I., Leja, J., Leonova, E., Magee, D., Price, S. H., Setton, D. J., Strait, V., Stefanon, M., Toft, S., Weaver, J. R., and Weibel, A. (2022). Two Remarkably Luminous Galaxy Candidates at z $\approx$ 10-12 Revealed by JWST. *ApJ*, 940(1):L14.

Naiman, J. P., Pillepich, A., Springel, V., Ramirez-Ruiz, E., Torrey, P., Vogelsberger, M., Pakmor, R., Nelson, D., Marinacci, F., Hernquist, L., Weinberger, R., and Genel, S. (2018). First results from the IllustrisTNG simulations: a tale of two elements - chemical evolution of magnesium and europium. *MNRAS*, 477(1):1206–1224.

Naimi, A. I., Cole, S. R., and Kennedy, E. H. (2017). An introduction to g methods. *International journal of epidemiology*, 46(2):756–762.

Nandi, A., Glymour, M., Kawachi, I., and VanderWeele, T. (2012). Using marginal structural models to estimate the direct effect of fadverse childhood social conditions on onset of heart disease, diabetes, and stroke. *Epidemiology (Cambridge, Mass.)*, 23:223–32.

Nayyeri, H., Mobasher, B., Hemmati, S., De Barros, S., Ferguson, H. C., Wiklind, T., Dahlen, T., Dickinson, M., Giavalisco, M., Fontana, A., Ashby, M., Barro, G., Guo, Y., Hathi, N. P., Kassin, S., Koekemoer, A., Willner, S., Dunlop, J. S., Paris, D., and Targett, T. A. (2014). A Study of Massive and Evolved Galaxies at High Redshift. *ApJ*, 794(1):68.

Neilsen, Eric H., J., Annis, J. T., Diehl, H. T., Swanson, M. E. C., D'Andrea, C., Kent, S., and Drlica-Wagner, A. (2019). Dark Energy Survey's Observation Strategy, Tactics, and Exposure Scheduler. *arXiv e-prints*, page arXiv:1912.06254.

Nelan, J. E., Smith, R. J., Hudson, M. J., Wegner, G. A., Lucey, J. R., Moore, S. A. W., Quinney, S. J., and Suntzeff, N. B. (2005). NOAO Fundamental Plane Survey. II. Age and Metallicity along the Red Sequence from Line-Strength Data. *ApJ*, 632(1):137–156.

Nelson, D., Pillepich, A., Springel, V., Weinberger, R., Hernquist, L., Pakmor, R., Genel, S., Torrey, P., Vogelsberger, M., Kauffmann, G., Marinacci, F., and Naiman, J. (2018). First results from the IllustrisTNG simulations: the galaxy colour bimodality. *MNRAS*, 475(1):624–647.

Nelson, D., Springel, V., Pillepich, A., Rodriguez-Gomez, V., Torrey, P., Genel, S., Vogelsberger, M., Pakmor, R., Marinacci, F., Weinberger, R., Kelley, L., Lovell, M., Diemer, B., and Hernquist, L. (2019). The IllustrisTNG simulations: public data release. *Computational Astrophysics and Cosmology*, 6(1):2.

Newman, J. A., Cooper, M. C., Davis, M., Faber, S. M., Coil, A. L., Guhathakurta, P., Koo, D. C., Phillips, A. C., Conroy, C., Dutton, A. A., Finkbeiner, D. P., Gerke, B. F., Rosario, D. J., Weiner, B. J., Willmer, C. N. A., Yan, R., Harker, J. J., Kassin, S. A., Konidaris, N. P., Lai, K., Madgwick, D. S., Noeske, K. G., Wirth, G. D., Connolly, A. J., Kaiser, N., Kirby, E. N., Lemaux, B. C., Lin, L., Lotz, J. M., Luppino, G. A., Marinoni, C., Matthews, D. J., Metevier, A., and Schiavon,

R. P. (2013). The DEEP2 Galaxy Redshift Survey: Design, Observations, Data Reduction, and Redshifts. *ApJS*, 208(1):5.

Noeske, K. G., Weiner, B. J., Faber, S. M., Papovich, C., Koo, D. C., Somerville, R. S., Bundy, K., Conselice, C. J., Newman, J. A., Schiminovich, D., Le Floc'h, E., Coil, A. L., Rieke, G. H., Lotz, J. M., Primack, J. R., Barmby, P., Cooper, M. C., Davis, M., Ellis, R. S., Fazio, G. G., Guhathakurta, P., Huang, J., Kassin, S. A., Martin, D. C., Phillips, A. C., Rich, R. M., Small, T. A., Willmer, C. N. A., and Wilson, G. (2007). Star Formation in AEGIS Field Galaxies since z=1.1: The Dominance of Gradually Declining Star Formation, and the Main Sequence of Star-forming Galaxies. *ApJ*, 660(1):L43–L46.

Noll, S., Burgarella, D., Giovannoli, E., Buat, V., Marcillac, D., and Muñoz-Mateos, J. C. (2009). Analysis of galaxy spectral energy distributions from far-UV to far-IR with CIGALE: studying a SINGS test sample. *A&A*, 507(3):1793–1813.

Norton, S. A., Gebhardt, K., Zabludoff, A. I., and Zaritsky, D. (2001). The Spatial Distribution and Kinematics of Stellar Populations in E+A Galaxies. *ApJ*, 557(1):150–164.

Nulsen, P. E. J. (1982). Transport processes and the stripping of cluster galaxies. *MNRAS*, 198:1007–1016.

Ocvirk, P., Pichon, C., Lançon, A., and Thiébaut, E. (2006). STECMAP: STEllar Content from high-resolution galactic spectra via Maximum A Posteriori. *MNRAS*, 365(1):46–73.

Odewahn, S. C., Stockwell, E. B., Pennington, R. L., Humphreys, R. M., and Zumach, W. A. (1992). Automated Star/Galaxy Discrimination With Neural Networks. *AJ*, 103:318.

Oemler, Augustus, J. (1974). The Systematic Properties of Clusters of Galaxies. Photometry of 15 Clusters. *ApJ*, 194:1–20.

Oemler, Augustus, J., Dressler, A., and Butcher, H. R. (1997). The Morphology of Distant Cluster Galaxies. II. HST Observations of Four Rich Clusters at z ˜= 0.4. *ApJ*, 474(2):561–575.

Oort, J. H. (1932). The force exerted by the stellar system in the direction perpendicular to the galactic plane and some related problems. *Bull. Astron. Inst. Netherlands*, 6:249.

Paccagnella, A., Vulcani, B., Poggianti, B. M., Moretti, A., Fritz, J., Gullieuszik, M., and Fasano, G. (2019). The strong correlation between post-starburst fraction and environment. *MNRAS*, 482(1):881–894.

Pacifici, C., Kassin, S. A., Weiner, B. J., Holden, B., Gardner, J. P., Faber, S. M., Ferguson, H. C., Koo, D. C., Primack, J. R., Bell, E. F., Dekel, A., Gawiser, E., Giavalisco, M., Rafelski, M., Simons, R. C., Barro, G., Croton, D. J., Davé, R., Fontana, A., Grogin, N. A., Koekemoer, A. M., Lee, S.-K., Salmon, B., Somerville, R., and Behroozi, P. (2016). The Evolution of Star Formation Histories of Quiescent Galaxies. *ApJ*, 832(1):79.

Palmese, A. (2018). *Unveiling the unseen with the Dark Energy Survey: gravitational waves and dark matter*. PhD thesis, UCL (University College London).

Palmese, A., Annis, J., Burgad, J., Farahi, A., Soares-Santos, M., Welch, B., da Silva Pereira, M., Lin, H., Bhargava, S., Hollowood, D. L., Wilkinson, R., Giles, P., Jeltema, T., Romer, A. K., Evrard, A. E., Hilton, M., Vergara Cervantes, C., Bermeo, A., Mayers, J., DeRose, J., Gruen, D., Hartley, W. G., Lahav, O., Leistedt, B., McClintock, T., Rozo, E., Rykoff, E. S., Varga, T. N., Wechsler, R. H., Zhang, Y., Avila, S., Brooks, D., Buckley-Geer, E., Burke, D. L., Carnero Rosell, A., Carrasco Kind, M., Carretero, J., Castander, F. J., Collins, C., da Costa, L. N., Desai, S., De Vicente, J., Diehl, H. T., Dietrich, J. P., Doel, P., Flaugher, B., Fosalba, P., Frieman, J., García-Bellido, J., Gerdes, D. W., Gruendl, R. A., Gschwend, J., Gutierrez, G., Honscheid, K., James, D. J., Krause, E., Kuehn, K., Kuropatkin, N., Liddle, A., Lima, M., Maia, M. A. G., Mann, R. G., Marshall, J. L., Menanteau, F., Miquel, R., Ogand o, R. L. C., Plazas, A. A., Roodman, A., Rooney, P., Sahlen, M., Sanchez, E., Scarpine, V., Schubnell, M., Serrano, S., Sevilla-Noarbe, I., Sobreira, F., Stott, J., Suchyta, E., Swanson, M. E. C., Tarle, G., Thomas, D., Tucker, D. L., Viana, P. T. P., Vikram, V., Walker, A. R., and DES Collaboration (2020a). Stellar mass as a galaxy cluster mass proxy: application to the Dark Energy Survey redMaPPer clusters. *MNRAS*, 493(4):4591–4606.

Palmese, A., Bom, C. R., Mucesh, S., and Hartley, W. G. (2023). A Standard Siren Measurement of the Hubble Constant Using Gravitational-wave Events from the First Three LIGO/Virgo Observing Runs and the DESI Legacy Survey. *ApJ*, 943(1):56.

Palmese, A., deVicente, J., Pereira, M. E. S., Annis, J., Hartley, W., Herner, K., Soares-Santos, M., et al. (2020b). A Statistical Standard Siren Measurement of the Hubble Constant from the LIGO/Virgo Gravitational Wave Compact Object Merger GW190814 and Dark Energy Survey Galaxies. *ApJ*, 900(2):L33.

Palmese, A., Graur, O., Annis, J. T., BenZvi, S., Di Valentino, E., Garcia-Bellido, J., Gontcho, S. G. A., Keeley, R., Kim, A., Lahav, O., Nissanke, S., Paterson, K., Sako, M., Shafieloo, A., and Tsai, Y.-D. (2019). Gravitational wave cosmology and astrophysics with large spectroscopic galaxy surveys. *BAAS*, 51(3):310.

Palmese, A., Lahav, O., Banerji, M., Gruen, D., Jouvel, S., Melchior, P., Aleksić, J., Annis, J., Diehl, H. T., Hartley, W. G., Jeltema, T., Romer, A. K., Rozo, E., Rykoff, E. S., Seitz, S., Suchyta, E., Zhang, Y., Abbott, T. M. C., Abdalla, F. B., Allam, S., Benoit-Lévy, A., Bertin, E., Brooks, D., Buckley-Geer, E., Burke, D. L., Capozzi, D., Carnero Rosell, A., Carrasco Kind, M., Carretero, J., Crocce, M., Cunha, C. E., D'Andrea, C. B., da Costa, L. N., Desai, S., Dietrich, J. P., Doel, P., Estrada, J., Evrard, A. E., Flaugher, B., Frieman, J., Gerdes, D. W., Goldstein, D. A., Gruendl, R. A., Gutierrez, G., Honscheid, K., James, D. J., Kuehn, K., Kuropatkin, N., Li, T. S., Lima, M., Maia, M. A. G., Marshall, J. L., Miller, C. J., Miquel, R., Nord, B., Ogando, R., Plazas, A. A., Roodman, A., Sanchez, E., Scarpine, V., Sevilla-Noarbe, I., Smith, R. C., Soares-Santos, M., Sobreira, F., Swanson, M. E. C., Tarle, G., Thomas, D., Tucker, D., and Vikram, V. (2016). Comparing Dark Energy Survey and HST-CLASH observations of the galaxy cluster RXC J2248.7-4431: implications for stellar mass versus dark matter. *MNRAS*, 463(2):1486–1499.

Papovich, C., Dickinson, M., and Ferguson, H. C. (2001). The Stellar Populations and Evolution of Lyman Break Galaxies. *ApJ*, 559(2):620–653.

Papovich, C., Dickinson, M., and Ferguson, H. C. (2003). Stellar Masses of High-

Redshift Galaxies. In Bender, R. and Renzini, A., editors, *The Mass of Galaxies at Low and High Redshift*, page 296. Springer Berlin, Heidelberg.

Papovich, C., Finkelstein, S. L., Ferguson, H. C., Lotz, J. M., and Giavalisco, M. (2011). The rising star formation histories of distant galaxies and implications for gas accretion with time. *MNRAS*, 412(2):1123–1136.

Pasquali, A., van den Bosch, F. C., Mo, H. J., Yang, X., and Somerville, R. (2009). The rise and fall of galaxy activity in dark matter haloes. *MNRAS*, 394(1):38–50.

Pasquet, J., Bertin, E., Treyer, M., Arnouts, S., and Fouchez, D. (2019). Photometric redshifts from SDSS images using a convolutional neural network. *A&A*, 621:A26.

Patel, S. G., Holden, B. P., Kelson, D. D., Illingworth, G. D., and Franx, M. (2009). The Dependence of Star Formation Rates on Stellar Mass and Environment at z ~0.8. *ApJ*, 705(1):L67–L70.

Pattarakijwanich, P., Strauss, M. A., Ho, S., and Ross, N. P. (2016). The Evolution of Post-starburst Galaxies from z ~1 to the Present. *ApJ*, 833(1):19.

Peacock, J. A., 2dF Galaxy Redshift Survey Team, Colless, M., Baldry, I., Baugh, C., Bland-Hawthorn, J., Bridges, T., Cannon, R., Cole, S., Collins, C., Couch, W., Dalton, G., De Propris, R., Driver, S., Efstathiou, G., Ellis, R., Frenk, C., Glazebrook, K., Jackson, C., sLahav, O., Lewis, I., Lumsden, S., Maddox, S., Madgwick, D., Norberg, P., Percival, W., Peterson, B., Sutherland, W., and Taylor, K. (2002). Studying Large-scale Structure with the 2dF Galaxy Redshift Survey. In Metcalfe, N. and Shanks, T., editors, *A New Era in Cosmology*, volume 283 of *Astronomical Society of the Pacific Conference Series*, page 19.

Pearl, J. (2009a). Causal inference in statistics: An overview. *Statistics Surveys*, 3(none):96 – 146.

Pearl, J. (2009b). *Causality*. Cambridge university press.

Pearl, J. (2010). The foundations of causal inference. *Sociological Methodology*, 40(1):75–149.

Pearl, J. (2019). The seven tools of causal inference, with reflections on machine learning. *Communications of the ACM*, 62(3):54–60.

Pedregosa, F., Varoquaux, G., Gramfort, A., Michel, V., Thirion, B., Grisel, O., Blondel, M., Prettenhofer, P., Weiss, R., Dubourg, V., Vanderplas, J., Passos, A., Cournapeau, D., Brucher, M., Perrot, M., and Duchesnay, E. (2011). Scikit-learn: Machine learning in Python. *Journal of Machine Learning Research*, 12:2825–2830.

Pello, R., Miralles, J. M., Le Borgne, J. F., Picat, J. P., Soucail, G., and Bruzual, G. (1996). Identification of a high redshift cluster. in the field of Q2345+007 through deep BRIJK' photometry. *A&A*, 314:73–86.

Peng, Y.-j., Lilly, S. J., Kovač, K., Bolzonella, M., Pozzetti, L., Renzini, A., Zamorani, G., Ilbert, O., Knobel, C., Iovino, A., Maier, C., Cucciati, O., Tasca, L., Carollo, C. M., Silverman, J., Kampczyk, P., de Ravel, L., Sanders, D., Scoville, N., Contini, T., Mainieri, V., Scodeggio, M., Kneib, J.-P., Le Fèvre, O., Bardelli, S., Bongiorno, A., Caputi, K., Coppa, G., de la Torre, S., Franzetti, P., Garilli, B., Lamareille, F., Le Borgne, J.-F., Le Brun, V., Mignoli, M., Perez Montero, E., Pello, R., Ricciardelli, E., Tanaka, M., Tresse, L., Vergani, D., Welikala, N., Zucca, E., Oesch, P., Abbas, U., Barnes, L., Bordoloi, R., Bottini, D., Cappi, A., Cassata, P., Cimatti, A., Fumana, M., Hasinger, G., Koekemoer, A., Leauthaud, A., Maccagni, D., Marinoni, C., McCracken, H., Memeo, P., Meneux, B., Nair, P., Porciani, C., Presotto, V., and Scaramella, R. (2010). Mass and Environment as Drivers of Galaxy Evolution in SDSS and zCOSMOS and the Origin of the Schechter Function. *ApJ*, 721(1):193–221.

Perlmutter, S., Aldering, G., Goldhaber, G., Knop, R. A., Nugent, P., Castro, P. G., Deustua, S., Fabbro, S., Goobar, A., Groom, D. E., Hook, I. M., Kim, A. G., Kim, M. Y., Lee, J. C., Nunes, N. J., Pain, R., Pennypacker, C. R., Quimby, R., Lidman, C., Ellis, R. S., Irwin, M., McMahon, R. G., Ruiz-Lapuente, P., Walton, N., Schaefer, B., Boyle, B. J., Filippenko, A. V., Matheson, T., Fruchter, A. S., Panagia, N., Newberg, H. J. M., Couch, W. J., and Project, T. S. C. (1999). Measurements of Ω and Λ from 42 High-Redshift Supernovae. *ApJ*, 517(2):565–586.

Pietrinferni, A., Cassisi, S., Salaris, M., and Castelli, F. (2004). A Large Stellar Evolution Database for Population Synthesis Studies. I. Scaled Solar Models and Isochrones. *ApJ*, 612(1):168–190.

Pietrinferni, A., Cassisi, S., Salaris, M., and Castelli, F. (2006). A Large Stellar Evolution Database for Population Synthesis Studies. II. Stellar Models and Isochrones for an α-enhanced Metal Distribution. *ApJ*, 642(2):797–812.

Pillepich, A., Nelson, D., Hernquist, L., Springel, V., Pakmor, R., Torrey, P., Weinberger, R., Genel, S., Naiman, J. P., Marinacci, F., and Vogelsberger, M. (2018a). First results from the IllustrisTNG simulations: the stellar mass content of groups and clusters of galaxies. *MNRAS*, 475(1):648–675.

Pillepich, A., Springel, V., Nelson, D., Genel, S., Naiman, J., Pakmor, R., Hernquist, L., Torrey, P., Vogelsberger, M., Weinberger, R., and Marinacci, F. (2018b). Simulating galaxy formation with the IllustrisTNG model. *MNRAS*, 473(3):4077–4106.

Pimbblet, K. A., Smail, I., Kodama, T., Couch, W. J., Edge, A. C., Zabludoff, A. I., and O'Hely, E. (2002). The Las Campanas/AAT Rich Cluster Survey - II. The environmental dependence of galaxy colours in clusters at z~0.1. *MNRAS*, 331(2):333–350.

Piotrowska, J. M., Bluck, A. F. L., Maiolino, R., and Peng, Y. (2022). On the quenching of star formation in observed and simulated central galaxies: evidence for the role of integrated AGN feedback. *MNRAS*, 512(1):1052–1090.

Planck Collaboration, Ade, P. A. R., Aghanim, N., Arnaud, M., Ashdown, M., Aumont, J., Baccigalupi, C., Banday, A. J., Barreiro, R. B., Bartlett, J. G., Bartolo, N., Battaner, E., Battye, R., Benabed, K., Benoît, A., Benoit-Lévy, A., Bernard, J. P., Bersanelli, M., Bielewicz, P., Bock, J. J., Bonaldi, A., Bonavera, L., Bond, J. R., Borrill, J., Bouchet, F. R., Boulanger, F., Bucher, M., Burigana, C., Butler, R. C., Calabrese, E., Cardoso, J. F., Catalano, A., Challinor, A., Chamballu, A., Chary, R. R., Chiang, H. C., Chluba, J., Christensen, P. R., Church, S., Clements, D. L., Colombi, S., Colombo, L. P. L., Combet, C., Coulais, A., Crill, B. P., Curto, A., Cuttaia, F., Danese, L., Davies, R. D., Davis, R. J., de Bernardis, P., de Rosa, A., de Zotti, G., Delabrouille, J., Désert, F. X., Di Valentino, E., Dickinson, C., Diego, J. M., Dolag, K., Dole, H., Donzelli, S., Doré, O., Douspis, M., Ducout, A., Dunkley, J., Dupac, X., Efstathiou, G., Elsner, F., Enßlin, T. A.,

Eriksen, H. K., Farhang, M., Fergusson, J., Finelli, F., Forni, O., Frailis, M., Fraisse, A. A., Franceschi, E., Frejsel, A., Galeotta, S., Galli, S., Ganga, K., Gauthier, C., Gerbino, M., Ghosh, T., Giard, M., Giraud-Héraud, Y., Giusarma, E., Gjerløw, E., González-Nuevo, J., Górski, K. M., Gratton, S., Gregorio, A., Gruppuso, A., Gudmundsson, J. E., Hamann, J., Hansen, F. K., Hanson, D., Harrison, D. L., Helou, G., Henrot-Versillé, S., Hernández-Monteagudo, C., Herranz, D., Hildebrandt, S. R., Hivon, E., Hobson, M., Holmes, W. A., Hornstrup, A., Hovest, W., Huang, Z., Huffenberger, K. M., Hurier, G., Jaffe, A. H., Jaffe, T. R., Jones, W. C., Juvela, M., Keihänen, E., Keskitalo, R., Kisner, T. S., Kneissl, R., Knoche, J., Knox, L., Kunz, M., Kurki-Suonio, H., Lagache, G., Lähteenmäki, A., Lamarre, J. M., Lasenby, A., Lattanzi, M., Lawrence, C. R., Leahy, J. P., Leonardi, R., Lesgourgues, J., Levrier, F., Lewis, A., Liguori, M., Lilje, P. B., Linden-Vørnle, M., López-Caniego, M., Lubin, P. M., Macías-Pérez, J. F., Maggio, G., Maino, D., Mandolesi, N., Mangilli, A., Marchini, A., Maris, M., Martin, P. G., Martinelli, M., Martínez-González, E., Masi, S., Matarrese, S., McGehee, P., Meinhold, P. R., Melchiorri, A., Melin, J. B., Mendes, L., Mennella, A., Migliaccio, M., Millea, M., Mitra, S., Miville-Deschênes, M. A., Moneti, A., Montier, L., Morgante, G., Mortlock, D., Moss, A., Munshi, D., Murphy, J. A., Naselsky, P., Nati, F., Natoli, P., Netterfield, C. B., Nørgaard-Nielsen, H. U., Noviello, F., Novikov, D., Novikov, I., Oxborrow, C. A., Paci, F., Pagano, L., Pajot, F., Paladini, R., Paoletti, D., Partridge, B., Pasian, F., Patanchon, G., Pearson, T. J., Perdereau, O., Perotto, L., Perrotta, F., Pettorino, V., Piacentini, F., Piat, M., Pierpaoli, E., Pietrobon, D., Plaszczynski, S., Pointecouteau, E., Polenta, G., Popa, L., Pratt, G. W., Prézeau, G., Prunet, S., Puget, J. L., Rachen, J. P., Reach, W. T., Rebolo, R., Reinecke, M., Remazeilles, M., Renault, C., Renzi, A., Ristorcelli, I., Rocha, G., Rosset, C., Rossetti, M., Roudier, G., Rouillé d'Orfeuil, B., Rowan-Robinson, M., Rubiño-Martín, J. A., Rusholme, B., Said, N., Salvatelli, V., Salvati, L., Sandri, M., Santos, D., Savelainen, M., Savini, G., Scott, D., Seiffert, M. D., Serra, P., Shellard, E. P. S., Spencer, L. D., Spinelli, M., Stolyarov, V., Stompor, R., Sudiwala, R., Sunyaev, R., Sutton, D., Suur-Uski, A. S., Sygnet, J. F., Tauber, J. A., Terenzi, L., Toffolatti, L., Tomasi, M., Tristram, M., Trombetti, T., Tucci, M., Tuovinen, J., Türler, M., Umana, G., Valenziano, L., Valiviita, J., Van Tent, F., Vielva, P.,

Villa, F., Wade, L. A., Wandelt, B. D., Wehus, I. K., White, M., White, S. D. M., Wilkinson, A., Yvon, D., Zacchei, A., and Zonca, A. (2016). Planck 2015 results. XIII. Cosmological parameters. *A&A*, 594:A13.

Planck Collaboration, Aghanim, N., Akrami, Y., Ashdown, M., Aumont, J., Baccigalupi, C., Ballardini, M., Banday, A. J., Barreiro, R. B., Bartolo, N., Basak, S., Battye, R., Benabed, K., Bernard, J. P., Bersanelli, M., Bielewicz, P., Bock, J. J., Bond, J. R., Borrill, J., Bouchet, F. R., Boulanger, F., Bucher, M., Burigana, C., Butler, R. C., Calabrese, E., Cardoso, J. F., Carron, J., Challinor, A., Chiang, H. C., Chluba, J., Colombo, L. P. L., Combet, C., Contreras, D., Crill, B. P., Cuttaia, F., de Bernardis, P., de Zotti, G., Delabrouille, J., Delouis, J. M., Di Valentino, E., Diego, J. M., Doré, O., Douspis, M., Ducout, A., Dupac, X., Dusini, S., Efstathiou, G., Elsner, F., Enßlin, T. A., Eriksen, H. K., Fantaye, Y., Farhang, M., Fergusson, J., Fernandez-Cobos, R., Finelli, F., Forastieri, F., Frailis, M., Fraisse, A. A., Franceschi, E., Frolov, A., Galeotta, S., Galli, S., Ganga, K., Génova-Santos, R. T., Gerbino, M., Ghosh, T., González-Nuevo, J., Górski, K. M., Gratton, S., Gruppuso, A., Gudmundsson, J. E., Hamann, J., Handley, W., Hansen, F. K., Herranz, D., Hildebrandt, S. R., Hivon, E., Huang, Z., Jaffe, A. H., Jones, W. C., Karakci, A., Keihänen, E., Keskitalo, R., Kiiveri, K., Kim, J., Kisner, T. S., Knox, L., Krachmalnicoff, N., Kunz, M., Kurki-Suonio, H., Lagache, G., Lamarre, J. M., Lasenby, A., Lattanzi, M., Lawrence, C. R., Le Jeune, M., Lemos, P., Lesgourgues, J., Levrier, F., Lewis, A., Liguori, M., Lilje, P. B., Lilley, M., Lindholm, V., López-Caniego, M., Lubin, P. M., Ma, Y. Z., Macías-Pérez, J. F., Maggio, G., Maino, D., Mandolesi, N., Mangilli, A., Marcos-Caballero, A., Maris, M., Martin, P. G., Martinelli, M., Martínez-González, E., Matarrese, S., Mauri, N., McEwen, J. D., Meinhold, P. R., Melchiorri, A., Mennella, A., Migliaccio, M., Millea, M., Mitra, S., Miville-Deschênes, M. A., Molinari, D., Montier, L., Morgante, G., Moss, A., Natoli, P., Nørgaard-Nielsen, H. U., Pagano, L., Paoletti, D., Partridge, B., Patanchon, G., Peiris, H. V., Perrotta, F., Pettorino, V., Piacentini, F., Polastri, L., Polenta, G., Puget, J. L., Rachen, J. P., Reinecke, M., Remazeilles, M., Renzi, A., Rocha, G., Rosset, C., Roudier, G., Rubiño-Martín, J. A., Ruiz-Granados, B., Salvati, L., Sandri, M., Savelainen, M., Scott, D., Shellard, E. P. S., Sirignano, C., Sirri, G., Spencer, L. D., Sunyaev, R., Suur-Uski, A. S., Tauber, J. A., Tavagnacco,

D., Tenti, M., Toffolatti, L., Tomasi, M., Trombetti, T., Valenziano, L., Valiviita, J., Van Tent, B., Vibert, L., Vielva, P., Villa, F., Vittorio, N., Wandelt, B. D., Wehus, I. K., White, M., White, S. D. M., Zacchei, A., and Zonca, A. (2020). Planck 2018 results. VI. Cosmological parameters. *A&A*, 641:A6.

Poggianti, B. M., Aragón-Salamanca, A., Zaritsky, D., De Lucia, G., Milvang-Jensen, B., Desai, V., Jablonka, P., Halliday, C., Rudnick, G., Varela, J., Bamford, S., Best, P., Clowe, D., Noll, S., Saglia, R., Pelló, R., Simard, L., von der Linden, A., and White, S. (2009). The Environments of Starburst and Post-Starburst Galaxies at z = 0.4-0.8. *ApJ*, 693(1):112–131.

Poggianti, B. M., Smail, I., Dressler, A., Couch, W. J., Barger, A. J., Butcher, H., Ellis, R. S., and Oemler, Augustus, J. (1999). The Star Formation Histories of Galaxies in Distant Clusters. *ApJ*, 518(2):576–593.

Poggianti, B. M., von der Linden, A., De Lucia, G., Desai, V., Simard, L., Halliday, C., Aragón-Salamanca, A., Bower, R., Varela, J., Best, P., Clowe, D. I., Dalcanton, J., Jablonka, P., Milvang-Jensen, B., Pello, R., Rudnick, G., Saglia, R., White, S. D. M., and Zaritsky, D. (2006). The Evolution of the Star Formation Activity in Galaxies and Its Dependence on Environment. *ApJ*, 642(1):188–215.

Polsterer, K. L., D'Isanto, A., and Gieseke, F. (2016). Uncertain Photometric Redshifts. *arXiv e-prints*, page arXiv:1608.08016.

Ponman, T. J., Allan, D. J., Jones, L. R., Merrifield, M., McHardy, I. M., Lehto, H. J., and Luppino, G. A. (1994). A possible fossil galaxy group. *Nature*, 369(6480):462–464.

Pontzen, A., Tremmel, M., Roth, N., Peiris, H. V., Saintonge, A., Volonteri, M., Quinn, T., and Governato, F. (2017). How to quench a galaxy. *MNRAS*, 465(1):547–558.

Popesso, P., Concas, A., Morselli, L., Schreiber, C., Rodighiero, G., Cresci, G., Belli, S., Erfanianfar, G., Mancini, C., Inami, H., Dickinson, M., Ilbert, O., Pannella, M., and Elbaz, D. (2019). The main sequence of star-forming galaxies - I. The local relation and its bending. *MNRAS*, 483(3):3213–3226.

Popesso, P., Rodighiero, G., Saintonge, A., Santini, P., Grazian, A., Lutz, D., Brusa, M., Altieri, B., Andreani, P., Aussel, H., Berta, S., Bongiovanni, A., Cava, A., Cepa, J., Cimatti, A., Daddi, E., Dominguez, H., Elbaz, D., Förster Schreiber, N., Genzel, R., Gruppioni, C., Magdis, G., Maiolino, R., Magnelli, B., Nordon, R., Pérez García, A. M., Poglitsch, A., Pozzi, F., Riguccini, L., Sanchez-Portal, M., Shao, L., Sturm, E., Tacconi, L., Valtchanov, I., Wieprecht, E., and Wetzstein, M. (2011). The effect of environment on star forming galaxies at redshift. I. First insight from PACS. *A&A*, 532:A145.

Postman, M., Franx, M., Cross, N. J. G., Holden, B., Ford, H. C., Illingworth, G. D., Goto, T., Demarco, R., Rosati, P., Blakeslee, J. P., Tran, K. V., Benítez, N., Clampin, M., Hartig, G. F., Homeier, N., Ardila, D. R., Bartko, F., Bouwens, R. J., Bradley, L. D., Broadhurst, T. J., Brown, R. A., Burrows, C. J., Cheng, E. S., Feldman, P. D., Golimowski, D. A., Gronwall, C., Infante, L., Kimble, R. A., Krist, J. E., Lesser, M. P., Martel, A. R., Mei, S., Menanteau, F., Meurer, G. R., Miley, G. K., Motta, V., Sirianni, M., Sparks, W. B., Tran, H. D., Tsvetanov, Z. I., White, R. L., and Zheng, W. (2005). The Morphology-Density Relation in z ~1 Clusters. *ApJ*, 623(2):721–741.

Postman, M. and Geller, M. J. (1984). The morphology-density relation - The group connection. *ApJ*, 281:95–99.

Postman, M., Lubin, L. M., and Oke, J. B. (2001). A Study of Nine High-Redshift Clusters of Galaxies. IV. Photometry and Spectra of Clusters 1324+3011 and 1604+4321. *AJ*, 122(3):1125–1150.

Pracy, M. B., Kuntschner, H., Couch, W. J., Blake, C., Bekki, K., and Briggs, F. (2009). The kinematics and spatial distribution of stellar populations in E+A galaxies. *MNRAS*, 396(3):1349–1369.

Puschell, J. J., Owen, F. N., and Laing, R. A. (1982). Near-infrared photometry of distant radio galaxies - Spectral flux distributions and redshift estimates. *ApJ*, 257:L57–L61.

Quadri, R. F., Williams, R. J., Franx, M., and Hildebrandt, H. (2012). Tracing the Star-formation-Density Relation to z ~2. *ApJ*, 744(2):88.

Quinlan, J. R. (1986). Induction of decision trees. *Machine learning*, 1:81–106.

Quinlan, J. R. (1993). *C4. 5: Programs for Machine Learning*. Morgan Kaufmann.

Rakos, K. and Schombert, J. (1996). Color Evolution from z=0 to z=1. *arXiv e-prints*, pages astro–ph/9603058.

Rau, M. M., Seitz, S., Brimioulle, F., Frank, E., Friedrich, O., Gruen, D., and Hoyle, B. (2015). Accurate photometric redshift probability density estimation - method comparison and application. *MNRAS*, 452(4):3710–3725.

Rees, M. J. and Ostriker, J. P. (1977). Cooling, dynamics and fragmentation of massive gas clouds: clues to the masses and radii of galaxies and clusters. *MNRAS*, 179:541–559.

Reichenbach, H. (1956). *The Direction of Time*. Mineola, N.Y.: Dover Publications.

Renzini, A. (2006). Stellar Population Diagnostics of Elliptical Galaxy Formation. *ARA&A*, 44(1):141–192.

Renzini, A. and Buzzoni, A. (1986). Global properties of stellar populations and the spectral evolution of galaxies. In Chiosi, C. and Renzini, A., editors, *Spectral Evolution of Galaxies*, volume 122 of *Astrophysics and Space Science Library*, pages 195–231.

Renzini, A. and Peng, Y.-j. (2015). An Objective Definition for the Main Sequence of Star-forming Galaxies. *ApJ*, 801(2):L29.

Richens, J. G., Lee, C. M., and Johri, S. (2020). Improving the accuracy of medical diagnosis with causal machine learning. *Nature communications*, 11(1):1–9.

Riess, A. G., Filippenko, A. V., Challis, P., Clocchiatti, A., Diercks, A., Garnavich, P. M., Gilliland, R. L., Hogan, C. J., Jha, S., Kirshner, R. P., Leibundgut, B., Phillips, M. M., Reiss, D., Schmidt, B. P., Schommer, R. A., Smith, R. C., Spyromilio, J., Stubbs, C., Suntzeff, N. B., and Tonry, J. (1998). Observational Evidence from Supernovae for an Accelerating Universe and a Cosmological Constant. *AJ*, 116(3):1009–1038.

Rines, K., Geller, M. J., Kurtz, M. J., and Diaferio, A. (2005). CAIRNS: The Cluster and Infall Region Nearby Survey. III. Environmental Dependence of Hα Properties of Galaxies. *AJ*, 130(4):1482–1501.

Roberts, M. S. and Haynes, M. P. (1994). Physical Parameters along the Hubble Sequence. *ARA&A*, 32:115–152.

Robertson, B. E. (2022). Galaxy Formation and Reionization: Key Unknowns and Expected Breakthroughs by the James Webb Space Telescope. *ARA&A*, 60:121–158.

Robertson, B. E., Banerji, M., Brough, S., Davies, R. L., Ferguson, H. C., Hausen, R., Kaviraj, S., Newman, J. A., Schmidt, S. J., Tyson, J. A., and Wechsler, R. H. (2019). Galaxy formation and evolution science in the era of the Large Synoptic Survey Telescope. *Nature Reviews Physics*, 1(7):450–462.

Robins, J. (1986). A new approach to causal inference in mortality studies with a sustained exposure period—application to control of the healthy worker survivor effect. *Mathematical modelling*, 7(9-12):1393–1512.

Robins, J. M. (1994). Correcting for non-compliance in randomized trials using structural nested mean models. *Communications in Statistics-Theory and methods*, 23(8):2379–2412.

Robins, J. M. (1999). Association, causation, and marginal structural models. *Synthese*, 121(1/2):151–179.

Robins, J. M., Hernan, M. A., and Brumback, B. (2000). Marginal structural models and causal inference in epidemiology.

Rodighiero, G., Bisigello, L., Iani, E., Marasco, A., Grazian, A., Sinigaglia, F., Cassata, P., and Gruppioni, C. (2023). JWST unveils heavily obscured (active and passive) sources up to z 13. *MNRAS*, 518(1):L19–L24.

Rodriguez-Gomez, V., Genel, S., Vogelsberger, M., Sijacki, D., Pillepich, A., Sales, L. V., Torrey, P., Snyder, G., Nelson, D., Springel, V., Ma, C.-P., and Hernquist, L. (2015). The merger rate of galaxies in the Illustris simulation: a comparison with observations and semi-empirical models. *MNRAS*, 449(1):49–64.

Rosenbaum, P. R. and Rubin, D. B. (1983). The central role of the propensity score in observational studies for causal effects. *Biometrika*, 70(1):41–55.

Rosenblatt, M. (1952). Remarks on a multivariate transformation. *Ann. Math. Statist.*, 23(3):470–472.

Roth, N., Pontzen, A., and Peiris, H. V. (2016). Genetically modified haloes: towards controlled experiments in ΛCDM galaxy formation. *MNRAS*, 455(1):974–986.

Rowe, B. T. P., Jarvis, M., Mandelbaum, R., Bernstein, G. M., Bosch, J., Simet, M., Meyers, J. E., Kacprzak, T., Nakajima, R., Zuntz, J., Miyatake, H., Dietrich, J. P., Armstrong, R., Melchior, P., and Gill, M. S. S. (2015). GALSIM: The modular galaxy image simulation toolkit. *Astron. Comput.*, 10:121–150.

Rubin, D. B. (1974). Estimating causal effects of treatments in randomized and nonrandomized studies. *Journal of educational Psychology*, 66(5):688.

Rubin, D. B. (1980). Randomization analysis of experimental data: The fisher randomization test comment. *Journal of the American statistical association*, 75(371):591–593.

Rubin, V. C. and Ford, W. Kent, J. (1970). Rotation of the Andromeda Nebula from a Spectroscopic Survey of Emission Regions. *ApJ*, 159:379.

Runge, J., Bathiany, S., Bollt, E., Camps-Valls, G., Coumou, D., Deyle, E., Glymour, C., Kretschmer, M., Mahecha, M. D., Muñoz-Marí, J., van Nes, E. H., Peters, J., Quax, R., Reichstein, M., Scheffer, M., Schölkopf, B., Spirtes, P., Sugihara, G., Sun, J., Zhang, K., and Zscheischler, J. (2019). Inferring causation from time series in Earth system sciences. *Nature Communications*, 10:2553.

Runge, J., Gerhardus, A., Varando, G., Eyring, V., and Camps-Valls, G. (2023). Causal inference for time series. *Nature Reviews Earth & Environment*, 4(7):487–505.

Sadeh, I., Abdalla, F. B., and Lahav, O. (2016). ANNz2: Photometric Redshift and Probability Distribution Function Estimation using Machine Learning. *PASP*, 128(968):104502.

Salim, S., Rich, R. M., Charlot, S., Brinchmann, J., Johnson, B. D., Schiminovich, D., Seibert, M., Mallery, R., Heckman, T. M., Forster, K., Friedman, P. G., Martin, D. C., Morrissey, P., Neff, S. G., Small, T., Wyder, T. K., Bianchi, L., Donas, J., Lee, Y.-W., Madore, B. F., Milliard, B., Szalay, A. S., Welsh, B. Y., and Yi, S. K. (2007). UV Star Formation Rates in the Local Universe. *ApJS*, 173(2):267–292.

Salpeter, E. E. (1955). The Luminosity Function and Stellar Evolution. *ApJ*, 121:161.

Salvato, M., Ilbert, O., and Hoyle, B. (2019). The many flavours of photometric redshifts. *Nat. Astron.*, 3:212–222.

Samuel, A. L. (1959). Some studies in machine learning using the game of checkers. *IBM Journal of Research and Development*, 3(3):210–229.

Sanchez, P., Voisey, J. P., Xia, T., Watson, H. I., O'Neil, A. Q., and Tsaftaris, S. A. (2022). Causal machine learning for healthcare and precision medicine. *Royal Society Open Science*, 9(8):220638.

Sánchez-Blázquez, P., Peletier, R. F., Jiménez-Vicente, J., Cardiel, N., Cenarro, A. J., Falcón-Barroso, J., Gorgas, J., Selam, S., and Vazdekis, A. (2006). Medium-resolution Isaac Newton Telescope library of empirical spectra. *MNRAS*, 371(2):703–718.

Sanders, D. B., Soifer, B. T., Elias, J. H., Madore, B. F., Matthews, K., Neugebauer, G., and Scoville, N. Z. (1988). Ultraluminous Infrared Galaxies and the Origin of Quasars. *ApJ*, 325:74.

Santiago, B. X. and Strauss, M. A. (1992). Large-Scale Morphological Segregation in the Center for Astrophysics Redshift Survey. *ApJ*, 387:9.

Santos, J. S., Altieri, B., Valtchanov, I., Nastasi, A., Bohringer, H., Cresci, G., Elbaz, D., Fassbender, R., Rosati, P., Tozzi, P., and Verdugo, M. (2015). The reversal of the SF-density relation in a massive, X-ray-selected galaxy cluster at z = 1.58: results from Herschel. *MNRAS*, 447:L65–L69.

Sarpa, E., Longobardi, A., Kraljic, K., Veropalumbo, A., and Schimd, C. (2022). Tracing the environmental history of observed galaxies via extended fast action minimization method. *MNRAS*, 516(1):231–244.

Scannapieco, C., Tissera, P. B., White, S. D. M., and Springel, V. (2008). Effects of supernova feedback on the formation of galaxy discs. *MNRAS*, 389(3):1137–1149.

Schaller, G., Schaerer, D., Meynet, G., and Maeder, A. (1992). New Grids of Stellar Models from 0.8-SOLAR-MASS to 120-SOLAR-MASSES at Z=0.020 and Z=0.001. *A&AS*, 96:269.

Schawinski, K., Virani, S., Simmons, B., Urry, C. M., Treister, E., Kaviraj, S., and Kushkuley, B. (2009). Do Moderate-Luminosity Active Galactic Nuclei Suppress Star Formation? *ApJ*, 692(1):L19–L23.

Schiminovich, D., Wyder, T. K., Martin, D. C., Johnson, B. D., Salim, S., Seibert, M., Treyer, M. A., Budavári, T., Hoopes, C., Zamojski, M., Barlow, T. A., Forster, K. G., Friedman, P. G., Morrissey, P., Neff, S. G., Small, T. A., Bianchi, L., Donas, J., Heckman, T. M., Lee, Y.-W., Madore, B. F., Milliard, B., Rich, R. M., Szalay, A. S., Welsh, B. Y., and Yi, S. (2007). The UV-Optical Color Magnitude Diagram. II. Physical Properties and Morphological Evolution On and Off of a Star-forming Sequence. *ApJS*, 173(2):315–341.

Schmidt, M. (1959). The Rate of Star Formation. *ApJ*, 129:243.

Schmidt, S. J., Malz, A. I., Soo, J. Y. H., Almosallam, I. A., Brescia, M., Cavuoti, S., Cohen-Tanugi, J., Connolly, A. J., DeRose, J., Freeman, P. E., Graham, M. L., Iyer, K. G., Jarvis, M. J., Kalmbach, J. B., Kovacs, E., Lee, A. B., Longo, G., Morrison, C. B., Newman, J. A., Nourbakhsh, E., Nuss, E., Pospisil, T., Tranin, H., Wechsler, R. H., Zhou, R., Izbicki, R., and (The LSST Dark Energy Science Collaboration) (2020). Evaluation of probabilistic photometric redshift estimation approaches for The Rubin Observatory Legacy Survey of Space and Time (LSST). *MNRAS*, 499(2):1587–1606.

Schölkopf, B., Hogg, D. W., Wang, D., Foreman-Mackey, D., Janzing, D., Simon-Gabriel, C.-J., and Peters, J. (2015). Removing systematic errors for exoplanet search via latent causes. *arXiv e-prints*, page arXiv:1505.03036.

Schölkopf, B., Locatello, F., Bauer, S., Ke, N. R., Kalchbrenner, N., Goyal, A., and Bengio, Y. (2021). Towards Causal Representation Learning. *arXiv e-prints*, page arXiv:2102.11107.

Schreiber, C., Pannella, M., Elbaz, D., Béthermin, M., Inami, H., Dickinson, M., Magnelli, B., Wang, T., Aussel, H., Daddi, E., Juneau, S., Shu, X., Sargent, M. T., Buat, V., Faber, S. M., Ferguson, H. C., Giavalisco, M., Koekemoer, A. M., Magdis, G., Morrison, G. E., Papovich, C., Santini, P., and Scott, D. (2015). The Herschel view of the dominant mode of galaxy growth from z = 4 to the present day. *A&A*, 575:A74.

Schuldt, S., Suyu, S. H., Cañameras, R., Taubenberger, S., Meinhardt, T., Leal-Taixé, L., and Hsieh, B. C. (2021). Photometric redshift estimation with a convolutional neural network: NetZ. *A&A*, 651:A55.

Schutz, B. F. (1986). Determining the Hubble constant from gravitational wave observations. *Nature*, 323:310.

Scott, S. L. and Varian, H. R. (2014). Predicting the present with bayesian structural time series. *International Journal of Mathematical Modelling and Numerical Optimisation*, 5(1-2):4–23.

Scott, S. L. and Varian, H. R. (2015). Bayesian variable selection for nowcasting economic time series. In *Economic analysis of the digital economy*, pages 119–135. University of Chicago Press.

Scoville, N., Arnouts, S., Aussel, H., Benson, A., Bongiorno, A., Bundy, K., Calvo, M. A. A., Capak, P., Carollo, M., Civano, F., Dunlop, J., Elvis, M., Faisst, A., Finoguenov, A., Fu, H., Giavalisco, M., Guo, Q., Ilbert, O., Iovino, A., Kajisawa, M., Kartaltepe, J., Leauthaud, A., Le Fèvre, O., LeFloch, E., Lilly, S. J., Liu, C. T. C., Manohar, S., Massey, R., Masters, D., McCracken, H. J., Mobasher, B., Peng, Y. J., Renzini, A., Rhodes, J., Salvato, M., Sanders, D. B., Sarvestani, B. D., Scarlata, C., Schinnerer, E., Sheth, K., Shopbell, P. L., Smolčić, V., Taniguchi, Y., Taylor, J. E., White, S. D. M., and Yan, L. (2013). Evolution of Galaxies and Their Environments at z = 0.1-3 in COSMOS. *ApJS*, 206(1):3.

Scoville, N., Aussel, H., Brusa, M., Capak, P., Carollo, C. M., Elvis, M., Giavalisco, M., Guzzo, L., Hasinger, G., Impey, C., Kneib, J. P., LeFevre, O., Lilly, S. J., Mobasher, B., Renzini, A., Rich, R. M., Sanders, D. B., Schinnerer, E., Schminovich,

D., Shopbell, P., Taniguchi, Y., and Tyson, N. D. (2007). The Cosmic Evolution Survey (COSMOS): Overview. *ApJS*, 172(1):1–8.

Searle, L., Sargent, W. L. W., and Bagnuolo, W. G. (1973). The History of Star Formation and the Colors of Late-Type Galaxies. *ApJ*, 179:427–438.

Setoguchi, S., Schneeweiss, S., Brookhart, M. A., Glynn, R. J., and Cook, E. F. (2008). Evaluating uses of data mining techniques in propensity score estimation: a simulation study. *Pharmacoepidemiology and drug safety*, 17(6):546–555.

Sevilla-Noarbe, I., Bechtol, K., Carrasco Kind, M., Carnero Rosell, A., Becker, M. R., Drlica-Wagner, A., Gruendl, R. A., Rykoff, E. S., Sheldon, E., Yanny, B., Alarcon, A., Allam, S., Amon, A., Benoit-Lévy, A., Bernstein, G. M., Bertin, E., Burke, D. L., Carretero, J., Choi, A., Diehl, H. T., Everett, S., Flaugher, B., Gaztanaga, E., Gschwend, J., Harrison, I., Hartley, W. G., Hoyle, B., Jarvis, M., Johnson, M. D., Kessler, R., Kron, R., Kuropatkin, N., Leistedt, B., Li, T. S., Menanteau, F., Morganson, E., Ogando, R. L. C., Palmese, A., Paz-Chinchón, F., Pieres, A., Pond, C., Rodriguez-Monroy, M., Allyn-Smith, J., Stringer, K. M., Troxel, M. A., Tucker, D. L., de Vicente, J., Wester, W., Zhang, Y., Abbott, T. M. C., Aguena, M., Annis, J., Avila, S., Bhargava, S., Bridle, S. L., Brooks, D., Brout, D., Castander, F. J., Cawthon, R., Chang, C., Conselice, C., Costanzi, M., Crocce, M., da Costa, L. N., Pereira, M. E. E., Davis, T. M., Desai, S., Dietrich, J. P., Doel, P., Eckert, K., Evrard, A. E., Ferrero, I., Fosalba, P., García-Bellido, J., Gerdes, D. W., Giannantonio, T., Gruen, D., Gutierrez, G., Hinton, S. R., Hollowood, D. L., Honscheid, K., Huff, E. M., Huterer, D., James, D. J., Jeltema, T., Kuehn, K., Lahav, O., Lidman, C., Lima, M., Lin, H., Maia, M. A. G., Marshall, J. L., Martini, P., Melchior, P., Miquel, R., Mohr, J. J., Morgan, R., Neilsen, E., Plazas, A. A., Romer, A. K., Roodman, A., Sanchez, E., Scarpine, V., Schubnell, M., Serrano, S., Smith, M., Suchyta, E., Tarle, G., Thomas, D., To, C., Varga, T. N., Wechsler, R. H., Weller, J., and Wilkinson, R. D. (2020). Dark Energy Survey Year 3 Results: Photometric Data Set for Cosmology. *arXiv e-prints*, page arXiv:2011.03407.

Shannon, C. E. (1948). A mathematical theory of communication. *The Bell System Technical Journal*, 27(3):379–423.

Shapley, A. E., Steidel, C. C., Adelberger, K. L., Dickinson, M., Giavalisco, M., and Pettini, M. (2001). The Rest-Frame Optical Properties of z˜=3 Galaxies. *ApJ*, 562(1):95–123.

Shapley, H. (1933). Luminosity Distribution and Average Density of Matter in Twenty-Five Groups of Galaxies. *Proceedings of the National Academy of Science*, 19(6):591–596.

Sheldon, E. S., Cunha, C. E., Mandelbaum, R., Brinkmann, J., and Weaver, B. A. (2012). Photometric Redshift Probability Distributions for Galaxies in the SDSS DR8. *ApJS*, 201(2):32.

Shen, Z., Liu, J., He, Y., Zhang, X., Xu, R., Yu, H., and Cui, P. (2021). Towards Out-Of-Distribution Generalization: A Survey. *arXiv e-prints*, page arXiv:2108.13624.

Sheth, K., Vogel, S. N., Regan, M. W., Thornley, M. D., and Teuben, P. J. (2005). Secular Evolution via Bar-driven Gas Inflow: Results from BIMA SONG. *ApJ*, 632(1):217–226.

Sheth, R. K. and Tormen, G. (2004). On the environmental dependence of halo formation. *MNRAS*, 350(4):1385–1390.

Shi, C., Blei, D. M., and Veitch, V. (2019). Adapting Neural Networks for the Estimation of Treatment Effects. *arXiv e-prints*, page arXiv:1906.02120.

Shiryayev, A. N. (1992). *15. On The Empirical Determination of A Distribution Law*, pages 139–146. Springer, Dordrecht.

Silk, J. (1977). On the fragmentation of cosmic gas clouds. I. The formation of galaxies and the first generation of stars. *ApJ*, 211:638–648.

Silk, J. and Rees, M. J. (1998). Quasars and galaxy formation. *A&A*, 331:L1–L4.

Silva, L., Granato, G. L., Bressan, A., and Danese, L. (1998). Modeling the Effects of Dust on Galactic Spectral Energy Distributions from the Ultraviolet to the Millimeter Band. *ApJ*, 509(1):103–117.

Skibba, R. A., Bamford, S. P., Nichol, R. C., Lintott, C. J., Andreescu, D., Edmondson, E. M., Murray, P., Raddick, M. J., Schawinski, K., Slosar, A., Szalay,

A. S., Thomas, D., and Vandenberg, J. (2009). Galaxy Zoo: disentangling the environmental dependence of morphology and colour. *MNRAS*, 399(2):966–982.

Skilling, J. (2006). Nested sampling for general bayesian computation. *Bayesian Anal.*, 1(4):833–859.

Smethurst, R. J., Lintott, C. J., Bamford, S. P., Hart, R. E., Kruk, S. J., Masters, K. L., Nichol, R. C., and Simmons, B. D. (2017). Galaxy Zoo: the interplay of quenching mechanisms in the group environment★. *MNRAS*, 469(3):3670–3687.

Smith, G. P., Treu, T., Ellis, R. S., Moran, S. M., and Dressler, A. (2005). Evolution since z = 1 of the Morphology-Density Relation for Galaxies. *ApJ*, 620(1):78–87.

Smith, R., Davies, J. I., and Nelson, A. H. (2010). How effective is harassment on infalling late-type dwarfs? *MNRAS*, 405(3):1723–1735.

Smith, R., Sánchez-Janssen, R., Beasley, M. A., Candlish, G. N., Gibson, B. K., Puzia, T. H., Janz, J., Knebe, A., Aguerri, J. A. L., Lisker, T., Hensler, G., Fellhauer, M., Ferrarese, L., and Yi, S. K. (2015). The sensitivity of harassment to orbit: mass loss from early-type dwarfs in galaxy clusters. *MNRAS*, 454(3):2502–2516.

Snyder, G. F., Cox, T. J., Hayward, C. C., Hernquist, L., and Jonsson, P. (2011). K+A Galaxies as the Aftermath of Gas-rich Mergers: Simulating the Evolution of Galaxies as Seen by Spectroscopic Surveys. *ApJ*, 741(2):77.

Soares-Santos, M., Palmese, A., Hartley, W., Annis, J., Garcia-Bellido, J., Lahav, O., Doctor, Z., Fishbach, M., Holz, D. E., Lin, H., Pereira, M. E. S., Garcia, A., Herner, K., Kessler, R., Peiris, H. V., Sako, M., Allam, S., Brout, D., Carnero Rosell, A., Chen, H. Y., Conselice, C., deRose, J., deVicente, J., Diehl, H. T., Gill, M. S. S., Gschwend, J., Sevilla-Noarbe, I., Tucker, D. L., Wechsler, R., Berger, E., Cowperthwaite, P. S., Metzger, B. D., Williams, P. K. G., Abbott, T. M. C., Abdalla, F. B., Avila, S., Bechtol, K., Bertin, E., Brooks, D., Buckley-Geer, E., Burke, D. L., Carrasco Kind, M., Carretero, J., Castander, F. J., Crocce, M., Cunha, C. E., D'Andrea, C. B., da Costa, L. N., Davis, C., Desai, S., Doel, P., Drlica-Wagner, A., Eifler, T. F., Evrard, A. E., Flaugher, B., Fosalba, P., Frieman, J., Gaztanaga, E., Gerdes, D. W., Gruen, D., Gruendl, R. A., Gutierrez, G., Hollowood, D. L., Hoyle, B., James, D. J., Jeltema, T., Kuehn, K., Kuropatkin, N.,

Li, T. S., Lima, M., Maia, M. A. G., Marshall, J. L., Menanteau, F., Miquel, R., Neilsen, E., Ogando, R. L. C., Plazas, A. A., Romer, A. K., Roodman, A., Sanchez, E., Scarpine, V., Schindler, R., Schubnell, M., Serrano, S., Smith, M., Smith, R. C., Sobreira, F., Suchyta, E., Swanson, M. E. C., Tarle, G., Thomas, R. C., Walker, A. R., Wester, W., Zuntz, J., DES Collaboration, Abbott, B. P., Abbott, R., Abbott, T. D., Abraham, S., Acernese, F., Ackley, K., Adams, C., Adhikari, R. X., Adya, V. B., Affeldt, C., Agathos, M., Agatsuma, K., Aggarwal, N., Aguiar, O. D., Aiello, L., Ain, A., Ajith, P., Allen, G., Allocca, A., Aloy, M. A., Altin, P. A., Amato, A., Ananyeva, A., Anderson, S. B., Anderson, W. G., Angelova, S. V., Appert, S., Arai, K., Araya, M. C., Areeda, J. S., Arène, M., Ascenzi, S., Ashton, G., Aston, S. M., Astone, P., Aubin, F., Aufmuth, P., AultONeal, K., Austin, C., Avendano, V., Avila-Alvarez, A., Babak, S., Bacon, P., Badaracco, F., Bader, M. K. M., Bae, S., Baker, P. T., Baldaccini, F., Ballardin, G., Ballmer, S. W., Banagiri, S., Barayoga, J. C., Barclay, S. E., Barish, B. C., Barker, D., Barkett, K., Barnum, S., Barone, F., Barr, B., Barsotti, L., Barsuglia, M., Barta, D., Bartlett, J., Bartos, I., Bassiri, R., Basti, A., Bawaj, M., Bayley, J. C., Bazzan, M., Bécsy, B., Bejger, M., Bell, A. S., Beniwal, D., Bergmann, G., Bernuzzi, S., Bero, J. J., Berry, C. P. L., Bersanetti, D., Bertolini, A., Betzwieser, J., Bhandare, R., Bidler, J., Bilenko, I. A., Bilgili, S. A., Billingsley, G., Birch, J., Birney, R., Birnholtz, O., Biscans, S., Biscoveanu, S., Bisht, A., Bitossi, M., Blackburn, J. K., Blair, C. D., Blair, D. G., Blair, R. M., Bloemen, S., Bode, N., Boer, M., Boetzel, Y., Bogaert, G., Bondu, F., Bonilla, E., Bonnand, R., Booker, P., Boom, B. A., Booth, C. D., Bork, R., Boschi, V., Bose, S., Bossie, K., Bossilkov, V., Bosveld, J., Bouffanais, Y., Bozzi, A., Bradaschia, C., Brady, P. R., Bramley, A., Branchesi, M., Brau, J. E., Briant, T., Briggs, J. H., Brighenti, F., Brillet, A., Brinkmann, M., Brockill, P., Brooks, A. F., Brown, D. D., Brunett, S., Buikema, A., Bulik, T., Bulten, H. J., Buonanno, A., Buskulic, D., Buy, C., Byer, R. L., Cabero, M., Cadonati, L., Cagnoli, G., Cahillane, C., Calderón Bustillo, J., Callister, T. A., Calloni, E., Camp, J. B., Campbell, W. A., Cannon, K. C., Cao, H., Cao, J., Capocasa, E., Carbognani, F., Caride, S., Carney, M. F., Carullo, G., Casanueva Diaz, J., Casentini, C., Caudill, S., Cavaglià, M., Cavalieri, R., Cella, G., Cerdá-Durán, P., Cerretani, G., Cesarini, E., Chaibi, O., Chakravarti, K., Chamberlin, S. J.,

Chan, M., Chao, S., Charlton, P., Chase, E. A., Chassande-Mottin, E., Chatterjee, D., Chaturvedi, M., Chatziioannou, K., Cheeseboro, B. D., Chen, X., Chen, Y., Cheng, H. P., Cheong, C. K., Chia, H. Y., Chincarini, A., Chiummo, A., Cho, G., Cho, H. S., Cho, M., Christensen, N., Chu, Q., Chua, S., Chung, K. W., Chung, S., Ciani, G., Ciobanu, A. A., Ciolfi, R., Cipriano, F., Cirone, A., Clara, F., Clark, J. A., Clearwater, P., Cleva, F., Cocchieri, C., Coccia, E., Cohadon, P. F., Colgan, R., Colleoni, M., Collette, C. G., Collins, C., Cominsky, L. R., Constancio, M., J., Conti, L., Cooper, S. J., Corban, P., Corbitt, T. R., Cordero-Carrión, I., Corley, K. R., Cornish, N., Corsi, A., Cortese, S., Costa, C. A., Cotesta, R., Coughlin, M. W., Coughlin, S. B., Coulon, J. P., Countryman, S. T., Couvares, P., Covas, P. B., Cowan, E. E., Coward, D. M., Cowart, M. J., Coyne, D. C., Coyne, R., Creighton, J. D. E., Creighton, T. D., Cripe, J., Croquette, M., Crowder, S. G., Cullen, T. J., Cumming, A., Cunningham, L., Cuoco, E., Dal Canton, T., Dálya, G., Danilishin, S. L., D'Antonio, S., Danzmann, K., Dasgupta, A., Da Silva Costa, C. F., Datrier, L. E. H., Dattilo, V., Dave, I., Davis, D., Daw, E. J., DeBra, D., Deenadayalan, M., Degallaix, J., De Laurentis, M., Deléglise, S., Del Pozzo, W., DeMarchi, L. M., Demos, N., Dent, T., De Pietri, R., Derby, J., De Rosa, R., De Rossi, C., DeSalvo, R., de Varona, O., Dhurandhar, S., Díaz, M. C., Dietrich, T., Di Fiore, L., Di Giovanni, M., Di Girolamo, T., Di Lieto, A., Ding, B., Di Pace, S., Di Palma, I., Di Renzo, F., Dmitriev, A., Donovan, F., Dooley, K. L., Doravari, S., Dorrington, I., Downes, T. P., Drago, M., Driggers, J. C., Du, Z., Dupej, P., Dwyer, S. E., Easter, P. J., Edo, T. B., Edwards, M. C., Effler, A., Ehrens, P., Eichholz, J., Eikenberry, S. S., Eisenmann, M., Eisenstein, R. A., Estelles, H., Estevez, D., Etienne, Z. B., Etzel, T., Evans, M., Evans, T. M., Fafone, V., Fair, H., Fairhurst, S., Fan, X., Farinon, S., Farr, B., Farr, W. M., Fauchon-Jones, E. J., Favata, M., Fays, M., Fazio, M., Fee, C., Feicht, J., Fejer, M. M., Feng, F., Fernandez-Galiana, A., Ferrante, I., Ferreira, E. C., Ferreira, T. A., Ferrini, F., Fidecaro, F., Fiori, I., Fiorucci, D., Fisher, R. P., Fishner, J. M., Fitz-Axen, M., Flaminio, R., Fletcher, M., Flynn, E., Fong, H., Font, J. A., Forsyth, P. W. F., Fournier, J. D., Frasca, S., Frasconi, F., Frei, Z., Freise, A., Frey, R., Fritschel, P., Frolov, V. V., Fulda, P., Fyffe, M., Gabbard, H. A., Gadre, B. U., Gaebel, S. M., Gair, J. R., Gammaitoni, L., Ganija, M. R., Gaonkar, S. G.,

Garcia, A., García-Quirós, C., Garufi, F., Gateley, B., Gaudio, S., Gaur, G., Gayathri, V., Gemme, G., Genin, E., Gennai, A., George, D., George, J., Gergely, L., Germain, V., Ghonge, S., Ghosh, A., Ghosh, A., Ghosh, S., Giacomazzo, B., Giaime, J. A., Giardina, K. D., Giazotto, A., Gill, K., Giordano, G., Glover, L., Godwin, P., Goetz, E., Goetz, R., Goncharov, B., González, G., Gonzalez Castro, J. M., Gopakumar, A., Gorodetsky, M. L., Gossan, S. E., Gosselin, M., Gouaty, R., Grado, A., Graef, C., Granata, M., Grant, A., Gras, S., Grassia, P., Gray, C., Gray, R., Greco, G., Green, A. C., Green, R., Gretarsson, E. M., Groot, P., Grote, H., Grunewald, S., Guidi, G. M., Gulati, H. K., Guo, Y., Gupta, A., Gupta, M. K., Gustafson, E. K., Gustafson, R., Haegel, L., Halim, O., Hall, B. R., Hall, E. D., Hamilton, E. Z., Hammond, G., Haney, M., Hanke, M. M., Hanks, J., Hanna, C., Hannuksela, O. A., Hanson, J., Hardwick, T., Haris, K., Harms, J., Harry, G. M., Harry, I. W., Haster, C. J., Haughian, K., Hayes, F. J., Healy, J., Heidmann, A., Heintze, M. C., Heitmann, H., Hemming, G., Hendry, M., Heng, I. S., Hennig, J., Heptonstall, A. W., Hernandez Vivanco, F., Heurs, M., Hild, S., Hinderer, T., Hoak, D., Hochheim, S., Hofman, D., Holgado, A. M., Holland, N. A., Holt, K., Hopkins, P., Horst, C., Hough, J., Howell, E. J., Hoy, C. G., Hreibi, A., Huerta, E. A., Hughey, B., Hulko, M., Husa, S., Huttner, S. H., Huynh-Dinh, T., Idzkowski, B., Iess, A., Ingram, C., Inta, R., Intini, G., Irwin, B., Isa, H. N., Isac, J. M., Isi, M., Iyer, B. R., Izumi, K., Jacqmin, T., Jadhav, S. J., Jani, K., Janthalur, N. N., Jaranowski, P., Jenkins, A. C., Jiang, J., Johnson, D. S., Jones, A. W., Jones, D. I., Jones, R., Jonker, R. J. G., Ju, L., Junker, J., Kalaghatgi, C. V., Kalogera, V., Kamai, B., Kandhasamy, S., Kang, G., Kanner, J. B., Kapadia, S. J., Karki, S., Karvinen, K. S., Kashyap, R., Kasprzack, M., Katsanevas, S., Katsavounidis, E., Katzman, W., Kaufer, S., Kawabe, K., Keerthana, N. V., Kéfélian, F., Keitel, D., Kennedy, R., Key, J. S., Khalili, F. Y., Khan, H., Khan, I., Khan, S., Khan, Z., Khazanov, E. A., Khursheed, M., Kijbunchoo, N., Kim, C., Kim, J. C., Kim, K., Kim, W., Kim, W. S., Kim, Y. M., Kimball, C., King, E. J., King, P. J., Kinley-Hanlon, M., Kirchhoff, R., Kissel, J. S., Kleybolte, L., Klika, J. H., Klimenko, S., Knowles, T. D., Koch, P., Koehlenbeck, S. M., Koekoek, G., Koley, S., Kondrashov, V., Kontos, A., Koper, N., Korobko, M., Korth, W. Z., Kowalska, I., Kozak, D. B., Kringel, V., Krishnendu, N., Królak, A., Kuehn, G.,

Kumar, A., Kumar, P., Kumar, R., Kumar, S., Kuo, L., Kutynia, A., Kwang, S., Lackey, B. D., Lai, K. H., Lam, T. L., Landry, M., Lane, B. B., Lang, R. N., Lange, J., Lantz, B., Lanza, R. K., Lasky, P. D., Laxen, M., Lazzarini, A., Lazzaro, C., Leaci, P., Leavey, S., Lecoeuche, Y. K., Lee, C. H., Lee, H. K., Lee, H. M., Lee, H. W., Lee, J., Lee, K., Lehmann, J., Lenon, A., Letendre, N., Levin, Y., Li, J., Li, K. J. L., Li, T. G. F., Li, X., Lin, F., Linde, F., Linker, S. D., Littenberg, T. B., Liu, J., Liu, X., Lo, R. K. L., Lockerbie, N. A., London, L. T., Longo, A., Lorenzini, M., Loriette, V., Lormand, M., Losurdo, G., Lough, J. D., Lousto, C. O., Lovelace, G., Lower, M. E., Lück, H., Lumaca, D., Lundgren, A. P., Lynch, R., Ma, Y., Macas, R., Macfoy, S., MacInnis, M., Macleod, D. M., Macquet, A., Magaña Hernandez, I., Magaña-Sandoval, F., Magaña Zertuche, L., Magee, R. M., Majorana, E., Maksimovic, I., Malik, A., Man, N., Mandic, V., Mangano, V., Mansell, G. L., Manske, M., Mantovani, M., Marchesoni, F., Marion, F., Márka, S., Márka, Z., Markakis, C., Markosyan, A. S., Markowitz, A., Maros, E., Marquina, A., Marsat, S., Martelli, F., Martin, I. W., Martin, R. M., Martynov, D. V., Mason, K., Massera, E., Masserot, A., Massinger, T. J., Masso-Reid, M., Mastrogiovanni, S., Matas, A., Matichard, F., Matone, L., Mavalvala, N., Mazumder, N., McCann, J. J., McCarthy, R., McClelland, D. E., McCormick, S., McCuller, L., McGuire, S. C., McIver, J., McManus, D. J., McRae, T., McWilliams, S. T., Meacher, D., Meadors, G. D., Mehmet, M., Mehta, A. K., Meidam, J., Melatos, A., Mendell, G., Mercer, R. A., Mereni, L., Merilh, E. L., Merzougui, M., Meshkov, S., Messenger, C., Messick, C., Metzdorff, R., Meyers, P. M., Miao, H., Michel, C., Middleton, H., Mikhailov, E. E., Milano, L., Miller, A. L., Miller, A., Millhouse, M., Mills, J. C., Milovich-Goff, M. C., Minazzoli, O., Minenkov, Y., Mishkin, A., Mishra, C., Mistry, T., Mitra, S., Mitrofanov, V. P., Mitselmakher, G., Mittleman, R., Mo, G., Moffa, D., Mogushi, K., Mohapatra, S. R. P., Montani, M., Moore, C. J., Moraru, D., Moreno, G., Morisaki, S., Mours, B., Mow-Lowry, C. M., Mukherjee, A., Mukherjee, D., Mukherjee, S., Mukund, N., Mullavey, A., Munch, J., Muñiz, E. A., Muratore, M., Murray, P. G., Nardecchia, I., Naticchioni, L., Nayak, R. K., Neilson, J., Nelemans, G., Nelson, T. J. N., Nery, M., Neunzert, A., Ng, K. Y., Ng, S., Nguyen, P., Nichols, D., Nissanke, S., Nocera, F., North, C., Nuttall, L. K., Obergaulinger, M., Oberling, J., O'Brien, B. D., O'Dea, G. D., Ogin, G. H., Oh,

J. J., Oh, S. H., Ohme, F., Ohta, H., Okada, M. A., Oliver, M., Oppermann, P., Oram, R. J., O'Reilly, B., Ormiston, R. G., Ortega, L. F., O'Shaughnessy, R., Ossokine, S., Ottaway, D. J., Overmier, H., Owen, B. J., Pace, A. E., Pagano, G., Page, M. A., Pai, A., Pai, S. A., Palamos, J. R., Palashov, O., Palomba, C., Pal-Singh, A., Pan, H.-W., Pang, B., Pang, P. T. H., Pankow, C., Pannarale, F., Pant, B. C., Paoletti, F., Paoli, A., Parida, A., Parker, W., Pascucci, D., Pasqualetti, A., Passaquieti, R., Passuello, D., Patil, M., Patricelli, B., Pearlstone, B. L., Pedersen, C., Pedraza, M., Pedurand, R., Pele, A., Penn, S., Perez, C. J., Perreca, A., Pfeiffer, H. P., Phelps, M., Phukon, K. S., Piccinni, O. J., Pichot, M., Piergiovanni, F., Pillant, G., Pinard, L., Pirello, M., Pitkin, M., Poggiani, R., Pong, D. Y. T., Ponrathnam, S., Popolizio, P., Porter, E. K., Powell, J., Prajapati, A. K., Prasad, J., Prasai, K., Prasanna, R., Pratten, G., Prestegard, T., Privitera, S., Prodi, G. A., Prokhorov, L. G., Puncken, O., Punturo, M., Puppo, P., Pürrer, M., Qi, H., Quetschke, V., Quinonez, P. J., Quintero, E. A., Quitzow-James, R., Radkins, H., Radulescu, N., Raffai, P., Raja, S., Rajan, C., Rajbhandari, B., Rakhmanov, M., Ramirez, K. E., Ramos-Buades, A., Rana, J., Rao, K., Rapagnani, P., Raymond, V., Razzano, M., Read, J., Regimbau, T., Rei, L., Reid, S., Reitze, D. H., Ren, W., Ricci, F., Richardson, C. J., Richardson, J. W., Ricker, P. M., Riles, K., Rizzo, M., Robertson, N. A., Robie, R., Rocchi, A., Rolland, L., Rollins, J. G., Roma, V. J., Romanelli, M., Romano, R., Romel, C. L., Romie, J. H., Rose, K., Rosińska, D., Rosofsky, S. G., Ross, M. P., Rowan, S., Rüdiger, A., Ruggi, P., Rutins, G., Ryan, K., Sachdev, S., Sadecki, T., Sakellariadou, M., Salconi, L., Saleem, M., Samajdar, A., Sammut, L., Sanchez, E. J., Sanchez, L. E., Sanchis-Gual, N., Sandberg, V., Sanders, J. R., Santiago, K. A., Sarin, N., Sassolas, B., Saulson, P. R., Sauter, O., Savage, R. L., Schale, P., Scheel, M., Scheuer, J., Schmidt, P., Schnabel, R., Schofield, R. M. S., Schönbeck, A., Schreiber, E., Schulte, B. W., Schutz, B. F., Schwalbe, S. G., Scott, J., Scott, S. M., Seidel, E., Sellers, D., Sengupta, A. S., Sennett, N., Sentenac, D., Sequino, V., Sergeev, A., Shaddock, D. A., Shaffer, T., Shahriar, M. S., Shaner, M. B., Shao, L., Sharma, P., Shawhan, P., Shen, H., Shink, R., Shoemaker, D. H., Shoemaker, D. M., ShyamSundar, S., Siellez, K., Sieniawska, M., Sigg, D., Silva, A. D., Singer, L. P., Singh, N., Singhal, A., Sintes, A. M., Sitmukhambetov, S., Skliris, V., Slagmolen, B. J. J.,

Slaven-Blair, T. J., Smith, J. R., Smith, R. J. E., Somala, S., Son, E. J., Sorazu, B., Sorrentino, F., Souradeep, T., Sowell, E., Spencer, A. P., Srivastava, A. K., Srivastava, V., Staats, K., Stachie, C., Standke, M., Steer, D. A., Steinke, M., Steinlechner, J., Steinlechner, S., Steinmeyer, D., Stevenson, S. P., Stocks, D., Stone, R., Stops, D. J., Strain, K. A., Stratta, G., Strigin, S. E., Strunk, A., Sturani, R., Stuver, A. L., Sudhir, V., Summerscales, T. Z., Sun, L., Sunil, S., Sur, A., Suresh, J., Sutton, P. J., Swinkels, B. L., Szczepańczyk, M. J., Tacca, M., Tait, S. C., Talbot, C., Talukder, D., Tanner, D. B., Tápai, M., Taracchini, A., Tasson, J. D., Taylor, R., Thies, F., Thomas, M., Thomas, P., Thondapu, S. R., Thorne, K. A., Thrane, E., Tiwari, S., Tiwari, S., Tiwari, V., Toland, K., Tonelli, M., Tornasi, Z., Torres-Forné, A., Torrie, C. I., Töyrä, D., Travasso, F., Traylor, G., Tringali, M. C., Trovato, A., Trozzo, L., Trudeau, R., Tsang, K. W., Tse, M., Tso, R., Tsukada, L., Tsuna, D., Tuyenbayev, D., Ueno, K., Ugolini, D., Unnikrishnan, C. S., Urban, A. L., Usman, S. A., Vahlbruch, H., Vajente, G., Valdes, G., van Bakel, N., van Beuzekom, M., van den Brand, J. F. J., Van Den Broeck, C., Vander-Hyde, D. C., van Heijningen, J. V., van der Schaaf, L., van Veggel, A. A., Vardaro, M., Varma, V., Vass, S., Vasúth, M., Vecchio, A., Vedovato, G., Veitch, J., Veitch, P. J., Venkateswara, K., Venugopalan, G., Verkindt, D., Vetrano, F., Viceré, A., Viets, A. D., Vine, D. J., Vinet, J. Y., Vitale, S., Vo, T., Vocca, H., Vorvick, C., Vyatchanin, S. P., Wade, A. R., Wade, L. E., Wade, M., Walet, R., Walker, M., Wallace, L., Walsh, S., Wang, G., Wang, H., Wang, J. Z., Wang, W. H., Wang, Y. F., Ward, R. L., Warden, Z. A., Warner, J., Was, M., Watchi, J., Weaver, B., Wei, L. W., Weinert, M., Weinstein, A. J., Weiss, R., Wellmann, F., Wen, L., Wessel, E. K., Weßels, P., Westhouse, J. W., Wette, K., Whelan, J. T., Whiting, B. F., Whittle, C., Wilken, D. M., Williams, D., Williamson, A. R., Willis, J. L., Willke, B., Wimmer, M. H., Winkler, W., Wipf, C. C., Wittel, H., Woan, G., Woehler, J., Wofford, J. K., Worden, J., Wright, J. L., Wu, D. S., Wysocki, D. M., Xiao, L., Yamamoto, H., Yancey, C. C., Yang, L., Yap, M. J., Yazback, M., Yeeles, D. W., Yu, H., Yu, H., Yuen, S. H. R., Yvert, M., Zadrożny, A. K., Zanolin, M., Zelenova, T., Zendri, J. P., Zevin, M., Zhang, J., Zhang, L., Zhang, T., Zhao, C., Zhou, M., Zhou, Z., Zhu, X. J., Zimmerman, A., Zucker, M. E., Zweizig, J., LIGO Scientific Collaboration, and Virgo Collaboration

(2019). First Measurement of the Hubble Constant from a Dark Standard Siren using the Dark Energy Survey Galaxies and the LIGO/Virgo Binary-Black-hole Merger GW170814. *ApJ*, 876(1):L7.

Sobral, D., Best, P. N., Smail, I., Geach, J. E., Cirasuolo, M., Garn, T., and Dalton, G. B. (2011). The dependence of star formation activity on environment and stellar mass at z$\sim$ 1 from the HiZELS-Hα survey. *MNRAS*, 411(1):675–692.

Socolovsky, M., Almaini, O., Hatch, N. A., Wild, V., Maltby, D. T., Hartley, W. G., and Simpson, C. (2018). The enhancement of rapidly quenched galaxies in distant clusters at 0.5 ¡ z ¡ 1.0. *MNRAS*, 476(1):1242–1257.

Soltan, A. (1982). Masses of quasars. *MNRAS*, 200:115–122.

Somerville, R. S. and Primack, J. R. (1999). Semi-analytic modelling of galaxy formation: the local Universe. *MNRAS*, 310(4):1087–1110.

Sotillo-Ramos, D., Lara-López, M. A., Pérez-García, A. M., Pérez-Martínez, R., Hopkins, A. M., Holwerda, B. W., Liske, J., López-Sánchez, A. R., Owers, M. S., and Pimbblet, K. A. (2021). Galaxy and mass assembly (GAMA): The environmental impact on SFR and metallicity in galaxy groups. *MNRAS*, 508(2):1817–1830.

Sparre, M. and Springel, V. (2016). Zooming in on major mergers: dense, starbursting gas in cosmological simulations. *MNRAS*, 462(3):2418–2430.

Spergel, D., Gehrels, N., Baltay, C., Bennett, D., Breckinridge, J., Donahue, M., Dressler, A., Gaudi, B. S., Greene, T., Guyon, O., Hirata, C., Kalirai, J., Kasdin, N. J., Macintosh, B., Moos, W., Perlmutter, S., Postman, M., Rauscher, B., Rhodes, J., Wang, Y., Weinberg, D., Benford, D., Hudson, M., Jeong, W. S., Mellier, Y., Traub, W., Yamada, T., Capak, P., Colbert, J., Masters, D., Penny, M., Savransky, D., Stern, D., Zimmerman, N., Barry, R., Bartusek, L., Carpenter, K., Cheng, E., Content, D., Dekens, F., Demers, R., Grady, K., Jackson, C., Kuan, G., Kruk, J., Melton, M., Nemati, B., Parvin, B., Poberezhskiy, I., Peddie, C., Ruffa, J., Wallace, J. K., Whipple, A., Wollack, E., and Zhao, F. (2015). Wide-Field InfrarRed Survey Telescope-Astrophysics Focused Telescope Assets WFIRST-AFTA 2015 Report. *arXiv e-prints*, page arXiv:1503.03757.

Splawa-Neyman, J., Dabrowska, D. M., and Speed, T. P. (1990). On the Application of Probability Theory to Agricultural Experiments. Essay on Principles. Section 9. *Statistical Science*, 5(4):465 – 472.

Springel, V. (2010). E pur si muove: Galilean-invariant cosmological hydrodynamical simulations on a moving mesh. *MNRAS*, 401(2):791–851.

Springel, V. (2015). N-GenIC: Cosmological structure initial conditions. Astrophysics Source Code Library, record ascl:1502.003.

Springel, V., Pakmor, R., Pillepich, A., Weinberger, R., Nelson, D., Hernquist, L., Vogelsberger, M., Genel, S., Torrey, P., Marinacci, F., and Naiman, J. (2018). First results from the IllustrisTNG simulations: matter and galaxy clustering. *MNRAS*, 475(1):676–698.

Springel, V., White, S. D. M., Jenkins, A., Frenk, C. S., Yoshida, N., Gao, L., Navarro, J., Thacker, R., Croton, D., Helly, J., Peacock, J. A., Cole, S., Thomas, P., Couchman, H., Evrard, A., Colberg, J., and Pearce, F. (2005). Simulations of the formation, evolution and clustering of galaxies and quasars. *Nature*, 435(7042):629–636.

Springel, V., White, S. D. M., Tormen, G., and Kauffmann, G. (2001). Populating a cluster of galaxies - I. Results at [formmu2]z=0. *MNRAS*, 328(3):726–750.

Starobinsky, A. A. (1982). Dynamics of phase transition in the new inflationary universe scenario and generation of perturbations. *Physics Letters B*, 117(3-4):175–178.

Stensbo-Smidt, K., Gieseke, F., Igel, C., Zirm, A., and Steenstrup Pedersen, K. (2016). Sacrificing information for the greater good: how to select photometric bands for optimal accuracy. *MNRAS*, 464(3):2577–2596.

Stips, A., Macias, D., Coughlan, C., Garcia-Gorriz, E., and Liang, X. S. (2016). On the causal structure between co2 and global temperature. *Scientific reports*, 6(1):21691.

Storrie-Lombardi, M. C., Lahav, O., Sodré, L., J., and Storrie-Lombardi, L. J. (1992).

Morphological Classification of galaxies by Artificial Neural Networks. *MNRAS*, 259(1):8P–12P.

Strateva, I., Ivezić, Ž., Knapp, G. R., Narayanan, V. K., Strauss, M. A., Gunn, J. E., Lupton, R. H., Schlegel, D., Bahcall, N. A., Brinkmann, J., Brunner, R. J., Budavári, T., Csabai, I., Castander, F. J., Doi, M., Fukugita, M., Győry, Z., Hamabe, M., Hennessy, G., Ichikawa, T., Kunszt, P. Z., Lamb, D. Q., McKay, T. A., Okamura, S., Racusin, J., Sekiguchi, M., Schneider, D. P., Shimasaku, K., and York, D. (2001). Color Separation of Galaxy Types in the Sloan Digital Sky Survey Imaging Data. *AJ*, 122(4):1861–1874.

Suchyta, E., Huff, E. M., Aleksić, J., Melchior, P., Jouvel, S., MacCrann, N., Ross, A. J., Crocce, M., Gaztanaga, E., Honscheid, K., Leistedt, B., Peiris, H. V., Rykoff, E. S., Sheldon, E., Abbott, T., Abdalla, F. B., Allam, S., Banerji, M., Benoit-Lévy, A., Bertin, E., Brooks, D., Burke, D. L., Carnero Rosell, A., Carrasco Kind, M., Carretero, J., Cunha, C. E., D'Andrea, C. B., da Costa, L. N., DePoy, D. L., Desai, S., Diehl, H. T., Dietrich, J. P., Doel, P., Eifler, T. F., Estrada, J., Evrard, A. E., Flaugher, B., Fosalba, P., Frieman, J., Gerdes, D. W., Gruen, D., Gruendl, R. A., James, D. J., Jarvis, M., Kuehn, K., Kuropatkin, N., Lahav, O., Lima, M., Maia, M. A. G., March, M., Marshall, J. L., Miller, C. J., Miquel, R., Neilsen, E., Nichol, R. C., Nord, B., Ogando, R., Percival, W. J., Reil, K., Roodman, A., Sako, M., Sanchez, E., Scarpine, V., Sevilla-Noarbe, I., Smith, R. C., Soares-Santos, M., Sobreira, F., Swanson, M. E. C., Tarle, G., Thaler, J., Thomas, D., Vikram, V., Walker, A. R., Wechsler, R. H., Zhang, Y., and DES Collaboration (2016). No galaxy left behind: accurate measurements with the faintest objects in the Dark Energy Survey. *MNRAS*, 457(1):786–808.

Sugihara, G., May, R., Ye, H., Hsieh, C.-h., Deyle, E., Fogarty, M., and Munch, S. (2012). Detecting causality in complex ecosystems. *science*, 338(6106):496–500.

Tanaka, M., Coupon, J., Hsieh, B.-C., Mineo, S., Nishizawa, A. J., Speagle, J., Furusawa, H., Miyazaki, S., and Murayama, H. (2018). Photometric redshifts for Hyper Suprime-Cam Subaru Strategic Program Data Release 1. *PASJ*, 70:S9.

Tanaka, M., Goto, T., Okamura, S., Shimasaku, K., and Brinkmann, J. (2004). The Environmental Dependence of Galaxy Properties in the Local Universe:

Dependences on Luminosity, Local Density, and System Richness. *AJ*, 128(6):2677–2695.

Tasca, L. A. M., Le Fèvre, O., Hathi, N. P., Schaerer, D., Ilbert, O., Zamorani, G., Lemaux, B. C., Cassata, P., Garilli, B., Le Brun, V., Maccagni, D., Pentericci, L., Thomas, R., Vanzella, E., Zucca, E., Amorin, R., Bardelli, S., Cassarà, L. P., Castellano, M., Cimatti, A., Cucciati, O., Durkalec, A., Fontana, A., Giavalisco, M., Grazian, A., Paltani, S., Ribeiro, B., Scodeggio, M., Sommariva, V., Talia, M., Tresse, L., Vergani, D., Capak, P., Charlot, S., Contini, T., de la Torre, S., Dunlop, J., Fotopoulou, S., Koekemoer, A., López-Sanjuan, C., Mellier, Y., Pforr, J., Salvato, M., Scoville, N., Taniguchi, Y., and Wang, P. W. (2015). The evolving star formation rate: $M_\star$ relation and sSFR since $z \simeq 5$ from the VUDS spectroscopic survey. *A&A*, 581:A54.

Taylor, E., Almaini, O., Merrifield, M., Maltby, D., Wild, V., Hartley, W. G., and Rowlands, K. (2023). The role of mass and environment in the build-up of the quenched galaxy population since cosmic noon. *MNRAS*, 522(2):2297–2306.

Taylor, E. N., Hopkins, A. M., Baldry, I. K., Bland-Hawthorn, J., Brown, M. J. I., Colless, M., Driver, S., Norberg, P., Robotham, A. S. G., Alpaslan, M., Brough, S., Cluver, M. E., Gunawardhana, M., Kelvin, L. S., Liske, J., Conselice, C. J., Croom, S., Foster, C., Jarrett, T. H., Lara-Lopez, M., and Loveday, J. (2015). Galaxy And Mass Assembly (GAMA): deconstructing bimodality - I. Red ones and blue ones. *MNRAS*, 446(2):2144–2185.

Taylor, M. B. (2005). TOPCAT & STIL: Starlink Table/VOTable Processing Software. In Shopbell, P., Britton, M., and Ebert, R., editors, *Astronomical Data Analysis Software and Systems XIV*, volume 347 of *ASP Conf. Ser.*, page 29.

Teimoorinia, H., Bluck, A. F. L., and Ellison, S. L. (2016). An artificial neural network approach for ranking quenching parameters in central galaxies. *MNRAS*, 457(2):2086–2106.

The Dark Energy Survey Collaboration (2005). The Dark Energy Survey. *arXiv e-prints*, pages astro–ph/0510346.

The Dark Energy Survey Collaboration, Abbott, T., Abdalla, F. B., Aleksić, J., Allam, S., Amara, A., Bacon, D., Balbinot, E., Banerji, M., Bechtol, K., Benoit-Lévy, A., Bernstein, G. M., Bertin, E., Blazek, J., Bonnett, C., Bridle, S., Brooks, D., Brunner, R. J., Buckley-Geer, E., Burke, D. L., Caminha, G. B., Capozzi, D., Carlsen, J., Carnero-Rosell, A., Carollo, M., Carrasco-Kind, M., Carretero, J., Castander, F. J., Clerkin, L., Collett, T., Conselice, C., Crocce, M., Cunha, C. E., D'Andrea, C. B., da Costa, L. N., Davis, T. M., Desai, S., Diehl, H. T., Dietrich, J. P., Dodelson, S., Doel, P., Drlica-Wagner, A., Estrada, J., Etherington, J., Evrard, A. E., Fabbri, J., Finley, D. A., Flaugher, B., Foley, R. J., Fosalba, P., Frieman, J., García-Bellido, J., Gaztanaga, E., Gerdes, D. W., Giannantonio, T., Goldstein, D. A., Gruen, D., Gruendl, R. A., Guarnieri, P., Gutierrez, G., Hartley, W., Honscheid, K., Jain, B., James, D. J., Jeltema, T., Jouvel, S., Kessler, R., King, A., Kirk, D., Kron, R., Kuehn, K., Kuropatkin, N., Lahav, O., Li, T. S., Lima, M., Lin, H., Maia, M. A. G., Makler, M., Manera, M., Maraston, C., Marshall, J. L., Martini, P., McMahon, R. G., Melchior, P., Merson, A., Miller, C. J., Miquel, R., Mohr, J. J., Morice-Atkinson, X., Naidoo, K., Neilsen, E., Nichol, R. C., Nord, B., Ogando, R., Ostrovski, F., Palmese, A., Papadopoulos, A., Peiris, H. V., Peoples, J., Percival, W. J., Plazas, A. A., Reed, S. L., Refregier, A., Romer, A. K., Roodman, A., Ross, A., Rozo, E., Rykoff, E. S., Sadeh, I., Sako, M., Sánchez, C., Sanchez, E., Santiago, B., Scarpine, V., Schubnell, M., Sevilla-Noarbe, I., Sheldon, E., Smith, M., Smith, R. C., Soares-Santos, M., Sobreira, F., Soumagnac, M., Suchyta, E., Sullivan, M., Swanson, M., Tarle, G., Thaler, J., Thomas, D., Thomas, R. C., Tucker, D., Vieira, J. D., Vikram, V., Walker, A. R., Wechsler, R. H., Weller, J., Wester, W., Whiteway, L., Wilcox, H., Yanny, B., Zhang, Y., and Zuntz, J. (2016). The Dark Energy Survey: more than dark energy - an overview. *MNRAS*, 460(2):1270–1299.

Thoemmes, F. and Ong, A. D. (2016). A primer on inverse probability of treatment weighting and marginal structural models. *Emerging Adulthood*, 4(1):40–59.

Thomas, D., Maraston, C., Bender, R., and Mendes de Oliveira, C. (2005). The Epochs of Early-Type Galaxy Formation as a Function of Environment. *ApJ*, 621(2):673–694.

Thomas, D., Maraston, C., Schawinski, K., Sarzi, M., and Silk, J. (2010). Environment and self-regulation in galaxy formation. *MNRAS*, 404(4):1775–1789.

Tinsley, B. M. (1968). Evolution of the Stars and Gas in Galaxies. *ApJ*, 151:547.

Tinsley, B. M. (1972). Galactic Evolution. *A&A*, 20:383.

Tinsley, B. M. and Gunn, J. E. (1976). Evolutionary synthesis of the stellar population in elliptical galaxies. I. Ingredients, broad-band colors, and infrared features. *ApJ*, 203:52–62.

Tojeiro, R., Heavens, A. F., Jimenez, R., and Panter, B. (2007). Recovering galaxy star formation and metallicity histories from spectra using VESPA. *MNRAS*, 381(3):1252–1266.

Tomczak, A. R., Quadri, R. F., Tran, K.-V. H., Labbé, I., Straatman, C. M. S., Papovich, C., Glazebrook, K., Allen, R., Brammer, G. B., Cowley, M., Dickinson, M., Elbaz, D., Inami, H., Kacprzak, G. G., Morrison, G. E., Nanayakkara, T., Persson, S. E., Rees, G. A., Salmon, B., Schreiber, C., Spitler, L. R., and Whitaker, K. E. (2016). The SFR-M* Relation and Empirical Star-Formation Histories from ZFOURGE* at 0.5 ¡ z ¡ 4. *ApJ*, 817(2):118.

Tonnesen, S. and Cen, R. (2014). On the Reversal of Star formation Rate-Density Relation at z = 1: Insights from Simulations. *ApJ*, 788(2):133.

Toomre, A. (1977). Mergers and Some Consequences. In Tinsley, B. M. and Larson, Richard B. Gehret, D. C., editors, *Evolution of Galaxies and Stellar Populations*, page 401.

Toomre, A. and Toomre, J. (1972). Galactic Bridges and Tails. *ApJ*, 178:623–666.

Torrey, P., Vogelsberger, M., Genel, S., Sijacki, D., Springel, V., and Hernquist, L. (2014). A model for cosmological simulations of galaxy formation physics: multi-epoch validation. *MNRAS*, 438(3):1985–2004.

Tran, K.-V. H., Franx, M., Illingworth, G., Kelson, D. D., and van Dokkum, P. (2003). The Nature of E+A Galaxies in Intermediate-Redshift Clusters. *ApJ*, 599(2):865–885.

Tran, K.-V. H., Franx, M., Illingworth, G. D., van Dokkum, P., Kelson, D. D., Blakeslee, J. P., and Postman, M. (2007). A Keck Spectroscopic Survey of MS 1054-03 (z = 0.83): Forming the Red Sequence. *ApJ*, 661(2):750–767.

Tran, K.-V. H., Franx, M., Illingworth, G. D., van Dokkum, P., Kelson, D. D., and Magee, D. (2004). Field E+A Galaxies at Intermediate Redshifts (0.3 ¡ z ¡ 1). *ApJ*, 609(2):683–691.

Tran, K.-V. H., Papovich, C., Saintonge, A., Brodwin, M., Dunlop, J. S., Farrah, D., Finkelstein, K. D., Finkelstein, S. L., Lotz, J., McLure, R. J., Momcheva, I., and Willmer, C. N. A. (2010). Reversal of Fortune: Confirmation of an Increasing Star Formation-Density Relation in a Cluster at z = 1.62. *ApJ*, 719(2):L126–L129.

Treister, E., Schawinski, K., Urry, C. M., and Simmons, B. D. (2012). Major Galaxy Mergers Only Trigger the Most Luminous Active Galactic Nuclei. *ApJ*, 758(2):L39.

Treu, T., Ellis, R. S., Kneib, J.-P., Dressler, A., Smail, I., Czoske, O., Oemler, A., and Natarajan, P. (2003). A Wide-Field Hubble Space Telescope Study of the Cluster Cl 0024+16 at z = 0.4. I. Morphological Distributions to 5 Mpc Radius. *ApJ*, 591(1):53–78.

van den Bergh, S. (1976). A new classification system for galaxies. *ApJ*, 206:883–887.

van Dokkum, P. G., Kriek, M., and Franx, M. (2009). A high stellar velocity dispersion for a compact massive galaxy at z=2.2. *Nature*, 460:717.

VanderWeele, T. J. (2008). Ignorability and stability assumptions in neighborhood effects research. *Statistics in Medicine*, 27(11):1934–1943.

VanderWeele, T. J., Jackson, J. W., and Li, S. (2016). Causal inference and longitudinal data: a case study of religion and mental health. *Social psychiatry and psychiatric epidemiology*, 51(11):1457–1466.

Vansteelandt, S. and Joffe, M. (2015). Structural Nested Models and G-estimation: The Partially Realized Promise. *arXiv e-prints*, page arXiv:1503.01589.

Vergani, D., Scodeggio, M., Pozzetti, L., Iovino, A., Franzetti, P., Garilli, B., Zamorani, G., Maccagni, D., Lamareille, F., Le Fèvre, O., Charlot, S., Contini,

T., Guzzo, L., Bottini, D., Le Brun, V., Picat, J. P., Scaramella, R., Tresse, L., Vettolani, G., Zanichelli, A., Adami, C., Arnouts, S., Bardelli, S., Bolzonella, M., Cappi, A., Ciliegi, P., Foucaud, S., Gavignaud, I., Ilbert, O., McCracken, H. J., Marano, B., Marinoni, C., Mazure, A., Meneux, B., Merighi, R., Paltani, S., Pellò, R., Pollo, A., Radovich, M., Zucca, E., Bondi, M., Bongiorno, A., Brinchmann, J., Cucciati, O., de la Torre, S., Gregorini, L., Perez-Montero, E., Mellier, Y., Merluzzi, P., and Temporin, S. (2008). The VIMOS VLT Deep Survey. Tracing the galaxy stellar mass assembly history over the last 8 Gyr. *A&A*, 487(1):89–101.

Vergani, D., Zamorani, G., Lilly, S., Lamareille, F., Halliday, C., Scodeggio, M., Vignali, C., Ciliegi, P., Bolzonella, M., Bondi, M., Kovač, K., Knobel, C., Zucca, E., Caputi, K., Pozzetti, L., Bardelli, S., Mignoli, M., Iovino, A., Carollo, C. M., Contini, T., Kneib, J. P., Le Fèvre, O., Mainieri, V., Renzini, A., Bongiorno, A., Coppa, G., Cucciati, O., de la Torre, S., de Ravel, L., Franzetti, P., Garilli, B., Kampczyk, P., Le Borgne, J. F., Le Brun, V., Maier, C., Pello, R., Peng, Y., Perez Montero, E., Ricciardelli, E., Silverman, J. D., Tanaka, M., Tasca, L., Tresse, L., Abbas, U., Bottini, D., Cappi, A., Cassata, P., Cimatti, A., Guzzo, L., Koekemoer, A. M., Leauthaud, A., Maccagni, D., Marinoni, C., McCracken, H. J., Memeo, P., Meneux, B., Oesch, P., Porciani, C., Scaramella, R., Capak, P., Sanders, D., Scoville, N., and Taniguchi, Y. (2010). K+a galaxies in the zCOSMOS survey . Physical properties of systems in their post-starburst phase. *A&A*, 509:A42.

Verma, S., Boonsanong, V., Hoang, M., Hines, K. E., Dickerson, J. P., and Shah, C. (2020). Counterfactual Explanations and Algorithmic Recourses for Machine Learning: A Review. *arXiv e-prints*, page arXiv:2010.10596.

Vogelsberger, M., Genel, S., Sijacki, D., Torrey, P., Springel, V., and Hernquist, L. (2013). A model for cosmological simulations of galaxy formation physics. *MNRAS*, 436(4):3031–3067.

Vogelsberger, M., Genel, S., Springel, V., Torrey, P., Sijacki, D., Xu, D., Snyder, G., Bird, S., Nelson, D., and Hernquist, L. (2014a). Properties of galaxies reproduced by a hydrodynamic simulation. *Nature*, 509(7499):177–182.

Vogelsberger, M., Genel, S., Springel, V., Torrey, P., Sijacki, D., Xu, D., Snyder, G., Nelson, D., and Hernquist, L. (2014b). Introducing the Illustris Project:

simulating the coevolution of dark and visible matter in the Universe. *MNRAS*, 444(2):1518–1547.

Vogt, N. P., Koo, D. C., Phillips, A. C., Wu, K., Faber, S. M., Willmer, C. N. A., Simard, L., Weiner, B. J., Illingworth, G. D., Gebhardt, K., Gronwall, C., Guzmán, R., Im, M., Sarajedini, V., Groth, E. J., Rhodes, J., Brunner, R., Connolly, A., Szalay, A., Kron, R., and Blandford, R. (2005). The DEEP Groth Strip Survey. I. The Sample. *ApJS*, 159(1):41–59.

Vollmer, B., Cayatte, V., Balkowski, C., and Duschl, W. J. (2001). Ram Pressure Stripping and Galaxy Orbits: The Case of the Virgo Cluster. *ApJ*, 561(2):708–726.

Wadadekar, Y. (2005). Estimating photometric redshifts using support vector machines. *PASP*, 117(827):79–85.

Wager, S. and Athey, S. (2015). Estimation and Inference of Heterogeneous Treatment Effects using Random Forests. *arXiv e-prints*, page arXiv:1510.04342.

Walcher, J., Groves, B., Budavári, T., and Dale, D. (2011). Fitting the integrated spectral energy distributions of galaxies. *Ap&SS*, 331:1–52.

Wang, D., Hogg, D. W., Foreman-Mackey, D., and Schölkopf, B. (2016). A Causal, Data-driven Approach to Modeling the Kepler Data. *PASP*, 128(967):094503.

Way, M. J. and Klose, C. D. (2012). Can Self-Organizing Maps Accurately Predict Photometric Redshifts? *PASP*, 124(913):274.

Way, M. J. and Srivastava, A. N. (2006). Novel Methods for Predicting Photometric Redshifts from Broadband Photometry Using Virtual Sensors. *ApJ*, 647(1):102–115.

Wechsler, R. H. and Tinker, J. L. (2018). The Connection Between Galaxies and Their Dark Matter Halos. *ARA&A*, 56:435–487.

Weinberger, R., Springel, V., Hernquist, L., Pillepich, A., Marinacci, F., Pakmor, R., Nelson, D., Genel, S., Vogelsberger, M., Naiman, J., and Torrey, P. (2017). Simulating galaxy formation with black hole driven thermal and kinetic feedback. *MNRAS*, 465(3):3291–3308.

Weiner, B. J., Phillips, A. C., Faber, S. M., Willmer, C. N. A., Vogt, N. P., Simard, L., Gebhardt, K., Im, M., Koo, D. C., Sarajedini, V. L., Wu, K. L., Forbes, D. A., Gronwall, C., Groth, E. J., Illingworth, G. D., Kron, R. G., Rhodes, J., Szalay, A. S., and Takamiya, M. (2005). The DEEP Groth Strip Galaxy Redshift Survey. III. Redshift Catalog and Properties of Galaxies. *ApJ*, 620(2):595–617.

Weinmann, S. M., van den Bosch, F. C., Yang, X., and Mo, H. J. (2006). Properties of galaxy groups in the Sloan Digital Sky Survey - I. The dependence of colour, star formation and morphology on halo mass. *MNRAS*, 366(1):2–28.

Westera, P., Lejeune, T., Buser, R., Cuisinier, F., and Bruzual, G. (2002). A standard stellar library for evolutionary synthesis. III. Metallicity calibration. *A&A*, 381:524–538.

Westreich, D., Lessler, J., and Funk, M. J. (2010). Propensity score estimation: machine learning and classification methods as alternatives to logistic regression. *Journal of clinical epidemiology*, 63(8):826.

Whitaker, K. E., Franx, M., Leja, J., van Dokkum, P. G., Henry, A., Skelton, R. E., Fumagalli, M., Momcheva, I. G., Brammer, G. B., Labbé, I., Nelson, E. J., and Rigby, J. R. (2014). Constraining the Low-mass Slope of the Star Formation Sequence at 0.5 ¡ z ¡ 2.5. *ApJ*, 795(2):104.

Whitaker, K. E., van Dokkum, P. G., Brammer, G., and Franx, M. (2012). The Star Formation Mass Sequence Out to z = 2.5. *ApJ*, 754(2):L29.

White, S. D. M., Clowe, D. I., Simard, L., Rudnick, G., De Lucia, G., Aragón-Salamanca, A., Bender, R., Best, P., Bremer, M., Charlot, S., Dalcanton, J., Dantel, M., Desai, V., Fort, B., Halliday, C., Jablonka, P., Kauffmann, G., Mellier, Y., Milvang-Jensen, B., Pelló, R., Poggianti, B., Poirier, S., Rottgering, H., Saglia, R., Schneider, P., and Zaritsky, D. (2005). EDisCS - the ESO distant cluster survey. Sample definition and optical photometry. *A&A*, 444(2):365–379.

White, S. D. M. and Frenk, C. S. (1991). Galaxy Formation through Hierarchical Clustering. *ApJ*, 379:52.

White, S. D. M. and Rees, M. J. (1978). Core condensation in heavy halos: a two-stage theory for galaxy formation and clustering. *MNRAS*, 183:341–358.

Whitmore, B. C. and Gilmore, D. M. (1991). On the Interpretation of the Morphology-Density Relation for Galaxies in Clusters. *ApJ*, 367:64.

Whitmore, B. C., Gilmore, D. M., and Jones, C. (1993). What Determines the Morphological Fractions in Clusters of Galaxies? *ApJ*, 407:489.

Williamson, T. and Ravani, P. (2017). Marginal structural models in clinical research: when and how to use them? *Nephrology Dialysis Transplantation*, 32(suppl_2):ii84–ii90.

Willmer, C. N. A., da Costa, L. N., and Pellegrini, P. S. (1998). Southern Sky Redshift Survey: Clustering of Local Galaxies. *AJ*, 115(3):869–884.

Willmer, C. N. A., Faber, S. M., Koo, D. C., Weiner, B. J., Newman, J. A., Coil, A. L., Connolly, A. J., Conroy, C., Cooper, M. C., Davis, M., Finkbeiner, D. P., Gerke, B. F., Guhathakurta, P., Harker, J., Kaiser, N., Kassin, S., Konidaris, N. P., Lin, L., Luppino, G., Madgwick, D. S., Noeske, K. G., Phillips, A. C., and Yan, R. (2006). The Deep Evolutionary Exploratory Probe 2 Galaxy Redshift Survey: The Galaxy Luminosity Function to z˜1. *ApJ*, 647(2):853–873.

Wolf, C., Aragón-Salamanca, A., Balogh, M., Barden, M., Bell, E. F., Gray, M. E., Peng, C. Y., Bacon, D., Barazza, F. D., Böhm, A., Caldwell, J. A. R., Gallazzi, A., Häußler, B., Heymans, C., Jahnke, K., Jogee, S., van Kampen, E., Lane, K., McIntosh, D. H., Meisenheimer, K., Papovich, C., Sánchez, S. F., Taylor, A., Wisotzki, L., and Zheng, X. (2009). The STAGES view of red spirals and dusty red galaxies: mass-dependent quenching of star formation in cluster infall. *MNRAS*, 393(4):1302–1323.

Wolf, C., Meisenheimer, K., Rix, H. W., Borch, A., Dye, S., and Kleinheinrich, M. (2003). The COMBO-17 survey: Evolution of the galaxy luminosity function from 25 000 galaxies with 0.2¡ z ¡1.2. *A&A*, 401:73–98.

Wright, S. (1921). Correlation and causation. *Journal of agricultural research*, 20(7):557–585.

Wu, J. F. (2020). Connecting Optical Morphology, Environment, and H I Mass Fraction for Low-redshift Galaxies Using Deep Learning. *ApJ*, 900(2):142.

Wu, J. F. and Boada, S. (2019). Using convolutional neural networks to predict galaxy metallicity from three-colour images. *MNRAS*, 484(4):4683–4694.

Wu, P.-F., Gal, R. R., Lemaux, B. C., Kocevski, D. D., Lubin, L. M., Rumbaugh, N., and Squires, G. K. (2014). Star Formation Quenching in High-redshift Large-scale Structure: Post-starburst Galaxies in the Cl 1604 Supercluster at z ~0.9. *ApJ*, 792(1):16.

Wuyts, S., Franx, M., Cox, T. J., Hernquist, L., Hopkins, P. F., Robertson, B. E., and van Dokkum, P. G. (2009). Recovering Stellar Population Properties and Redshifts from Broadband Photometry of Simulated Galaxies: Lessons for SED Modeling. *ApJ*, 696(1):348–369.

Wyder, T. K., Martin, D. C., Schiminovich, D., Seibert, M., Budavári, T., Treyer, M. A., Barlow, T. A., Forster, K., Friedman, P. G., Morrissey, P., Neff, S. G., Small, T., Bianchi, L., Donas, J., Heckman, T. M., Lee, Y.-W., Madore, B. F., Milliard, B., Rich, R. M., Szalay, A. S., Welsh, B. Y., and Yi, S. K. (2007). The UV-Optical Galaxy Color-Magnitude Diagram. I. Basic Properties. *ApJS*, 173(2):293–314.

Xia, K., Lee, K.-Z., Bengio, Y., and Bareinboim, E. (2021). The Causal-Neural Connection: Expressiveness, Learnability, and Inference. *arXiv e-prints*, page arXiv:2107.00793.

Yang, T.-C. and South, S. J. (2018). Neighborhood effects on body mass: temporal and spatial dimensions. *Social science & medicine*, 217:45–54.

Yang, X., Mo, H. J., van den Bosch, F. C., Weinmann, S. M., Li, C., and Jing, Y. P. (2005). The cross-correlation between galaxies and groups: probing the galaxy distribution in and around dark matter haloes. *MNRAS*, 362(2):711–726.

Yang, Y., Zabludoff, A. I., Zaritsky, D., Lauer, T. R., and Mihos, J. C. (2004). E+A Galaxies and the Formation of Early-Type Galaxies at z~0. *ApJ*, 607(1):258–273.

Yang, Y., Zabludoff, A. I., Zaritsky, D., and Mihos, J. C. (2008). The Detailed Evolution of E+A Galaxies into Early Types. *ApJ*, 688(2):945–971.

Yano, M., Kriek, M., van der Wel, A., and Whitaker, K. E. (2016). The Relation

between Galaxy Structure and Spectral Type: Implications for the Buildup of the Quiescent Galaxy Population at 0.5 ¡ z ¡ 2.0. *ApJ*, 817(2):L21.

Yao, L., Chu, Z., Li, S., Li, Y., Gao, J., and Zhang, A. (2020). A Survey on Causal Inference. *arXiv e-prints*, page arXiv:2002.02770.

Yesuf, H. M., Faber, S. M., Trump, J. R., Koo, D. C., Fang, J. J., Liu, F. S., Wild, V., and Hayward, C. C. (2014). From Starburst to Quiescence: Testing Active Galactic Nucleus feedback in Rapidly Quenching Post-starburst Galaxies. *ApJ*, 792(2):84.

York, D. G., Adelman, J., Anderson, John E., J., Anderson, S. F., Annis, J., Bahcall, N. A., Bakken, J. A., Barkhouser, R., Bastian, S., Berman, E., Boroski, W. N., Bracker, S., Briegel, C., Briggs, J. W., Brinkmann, J., Brunner, R., Burles, S., Carey, L., Carr, M. A., Castander, F. J., Chen, B., Colestock, P. L., Connolly, A. J., Crocker, J. H., Csabai, I., Czarapata, P. C., Davis, J. E., Doi, M., Dombeck, T., Eisenstein, D., Ellman, N., Elms, B. R., Evans, M. L., Fan, X., Federwitz, G. R., Fiscelli, L., Friedman, S., Frieman, J. A., Fukugita, M., Gillespie, B., Gunn, J. E., Gurbani, V. K., de Haas, E., Haldeman, M., Harris, F. H., Hayes, J., Heckman, T. M., Hennessy, G. S., Hindsley, R. B., Holm, S., Holmgren, D. J., Huang, C.-h., Hull, C., Husby, D., Ichikawa, S.-I., Ichikawa, T., Ivezić, Ž., Kent, S., Kim, R. S. J., Kinney, E., Klaene, M., Kleinman, A. N., Kleinman, S., Knapp, G. R., Korienek, J., Kron, R. G., Kunszt, P. Z., Lamb, D. Q., Lee, B., Leger, R. F., Limmongkol, S., Lindenmeyer, C., Long, D. C., Loomis, C., Loveday, J., Lucinio, R., Lupton, R. H., MacKinnon, B., Mannery, E. J., Mantsch, P. M., Margon, B., McGehee, P., McKay, T. A., Meiksin, A., Merelli, A., Monet, D. G., Munn, J. A., Narayanan, V. K., Nash, T., Neilsen, E., Neswold, R., Newberg, H. J., Nichol, R. C., Nicinski, T., Nonino, M., Okada, N., Okamura, S., Ostriker, J. P., Owen, R., Pauls, A. G., Peoples, J., Peterson, R. L., Petravick, D., Pier, J. R., Pope, A., Pordes, R., Prosapio, A., Rechenmacher, R., Quinn, T. R., Richards, G. T., Richmond, M. W., Rivetta, C. H., Rockosi, C. M., Ruthmansdorfer, K., Sandford, D., Schlegel, D. J., Schneider, D. P., Sekiguchi, M., Sergey, G., Shimasaku, K., Siegmund, W. A., Smee, S., Smith, J. A., Snedden, S., Stone, R., Stoughton, C., Strauss, M. A., Stubbs, C., SubbaRao, M., Szalay, A. S., Szapudi, I., Szokoly,

G. P., Thakar, A. R., Tremonti, C., Tucker, D. L., Uomoto, A., Vanden Berk, D., Vogeley, M. S., Waddell, P., Wang, S.-i., Watanabe, M., Weinberg, D. H., Yanny, B., Yasuda, N., and SDSS Collaboration (2000). The Sloan Digital Sky Survey: Technical Summary. *AJ*, 120(3):1579–1587.

Young, J. S. and Scoville, N. Z. (1991). Molecular gas in galaxies. *ARA&A*, 29:581–625.

Zabludoff, A. I., Zaritsky, D., Lin, H., Tucker, D., Hashimoto, Y., Shectman, S. A., Oemler, A., and Kirshner, R. P. (1996). The Environment of "E+A" Galaxies. *ApJ*, 466:104.

Zanga, A., Ozkirimli, E., and Stella, F. (2022). A survey on causal discovery: theory and practice. *International Journal of Approximate Reasoning*, 151:101–129.

Zehavi, I., Blanton, M. R., Frieman, J. A., Weinberg, D. H., Mo, H. J., Strauss, M. A., Anderson, S. F., Annis, J., Bahcall, N. A., Bernardi, M., Briggs, J. W., Brinkmann, J., Burles, S., Carey, L., Castander, F. J., Connolly, A. J., Csabai, I., Dalcanton, J. J., Dodelson, S., Doi, M., Eisenstein, D., Evans, M. L., Finkbeiner, D. P., Friedman, S., Fukugita, M., Gunn, J. E., Hennessy, G. S., Hindsley, R. B., Ivezić, Ž., Kent, S., Knapp, G. R., Kron, R., Kunszt, P., Lamb, D. Q., Leger, R. F., Long, D. C., Loveday, J., Lupton, R. H., McKay, T., Meiksin, A., Merrelli, A., Munn, J. A., Narayanan, V., Newcomb, M., Nichol, R. C., Owen, R., Peoples, J., Pope, A., Rockosi, C. M., Schlegel, D., Schneider, D. P., Scoccimarro, R., Sheth, R. K., Siegmund, W., Smee, S., Snir, Y., Stebbins, A., Stoughton, C., SubbaRao, M., Szalay, A. S., Szapudi, I., Tegmark, M., Tucker, D. L., Uomoto, A., Vanden Berk, D., Vogeley, M. S., Waddell, P., Yanny, B., and York, D. G. (2002). Galaxy Clustering in Early Sloan Digital Sky Survey Redshift Data. *ApJ*, 571(1):172–190.

Zel'dovich, Y. B. (1970). Gravitational instability: An approximate theory for large density perturbations. *A&A*, 5:84–89.

Zhao, X., Mao, Y., and Wandelt, B. D. (2022). Implicit Likelihood Inference of Reionization Parameters from the 21 cm Power Spectrum. *ApJ*, 933(2):236.

Zhao, X., Mao, Y., Zuo, S., and Wandelt, B. D. (2023). Simulation-based Inference of Reionization Parameters from 3D Tomographic 21 cm Light-cone Images – II:

Application of Solid Harmonic Wavelet Scattering Transform. *arXiv e-prints*, page arXiv:2310.17602.

Zhou, X. and Kosorok, M. R. (2017). Causal nearest neighbor rules for optimal treatment regimes. *arXiv e-prints*, page arXiv:1711.08451.

Zhu, Y., Coffman, D. L., and Ghosh, D. (2015). A boosting algorithm for estimating generalized propensity scores with continuous treatments. *Journal of causal inference*, 3(1):25–40.

Ziegel, J. F. and Gneiting, T. (2014). Copula calibration. *Electron. J. Statist.*, 8(2):2619–2638.

Ziparo, F., Popesso, P., Finoguenov, A., Biviano, A., Wuyts, S., Wilman, D., Salvato, M., Tanaka, M., Nandra, K., Lutz, D., Elbaz, D., Dickinson, M., Altieri, B., Aussel, H., Berta, S., Cimatti, A., Fadda, D., Genzel, R., Le Floc'h, E., Magnelli, B., Nordon, R., Poglitsch, A., Pozzi, F., Portal, M. S., Tacconi, L., Bauer, F. E., Brandt, W. N., Cappelluti, N., Cooper, M. C., and Mulchaey, J. S. (2014). Reversal or no reversal: the evolution of the star formation rate-density relation up to z $\sim$ 1.6. *MNRAS*, 437(1):458–474.

Zurita, A., Relaño, M., Beckman, J. E., and Knapen, J. H. (2004). Ionized gas kinematics and massive star formation in NGC 1530. *A&A*, 413:73–89.

Zwaan, M. A., Kuntschner, H., Pracy, M. B., and Couch, W. J. (2013). The cold gas content of post-starburst galaxies. *MNRAS*, 432(1):492–499.

Zwicky, F. (1933). Die Rotverschiebung von extragalaktischen Nebeln. *Helvetica Physica Acta*, 6:110–127.

Zwicky, F. (1937). On the Masses of Nebulae and of Clusters of Nebulae. *ApJ*, 86:217.

Zwicky, F. (1938). On the Clustering of Nebulae. *PASP*, 50(296):218–220.

Zwicky, F. (1952). Dispersion in the Large-Scale Distribution of Galaxies. *PASP*, 64(380):247.